

Spectroscopic studies towards the understanding of CeO₂-based catalysts for chlorine production

vorgelegt von
Diplom Chemiker
Ramzi Farra
aus Aleppo, Syrien

Von der Fakultät II - Mathematik und Naturwissenschaften
der Technischen Universität Berlin
zur Erlangung des akademischen Grades
Doktor der Naturwissenschaften
Dr. rer. nat.
genehmigte Dissertation

Promotionsausschuss:

Vorsitzender: Prof. Dr. Matthias Driess

Berichter/Gutachter: Prof. Dr. Robert Schlögl

Berichter/Gutachter: Prof. Dr. Reinhard Schomäcker

Berichter/Gutachter: Prof. Dr. Nicola Pinna

Tag der wissenschaftlichen Aussprache: 20. Dezember 2013

Berlin 2013

D83

Abstract

The heterogeneously catalyzed gas-phase oxidation of HCl to Cl₂ (Deacon reaction) is an energy-efficient and sustainable route to recycle chlorine from HCl-containing industrial waste streams. This work investigates HCl oxidation over CeO₂ using *in situ* and *ex situ* characterization techniques, and provides molecular understanding of Deacon chemistry over ceria catalysts.

The reactivity and stability of CeO₂ in HCl oxidation were assessed by steady-state kinetic experiments, which indicate that CeO₂ is an efficient catalyst for Cl₂ recycling in the temperature range of 623-723 K. A structural-reactivity correlation obtained by the assessment of sample pretreatment effects, particularly calcination, on reactivity reveals that ceria samples calcined at mildly high temperature (1173 K) represent the best compromise between performance and stability. Calcination at this temperature optimizes both the number of vacancies and the structural stability of the catalyst. Because of the semiconductor nature of CeO₂, HCl oxidation over CeO₂ catalysts requires the redox chemistry of the catalyst as well, and thus O vacancies are expected to play a crucial role. X-ray diffraction and electron microscopy of samples exposed to reaction feeds with different O₂:HCl ratios provide evidence that CeO₂ does not suffer from bulk chlorination in O₂-rich feeds (O₂:HCl ≥ 0.75), while it does form chlorinated phases in stoichiometric or sub-stoichiometric feeds (O₂:HCl ≤ 0.25). The quantitative analysis of the chlorine uptake by thermogravimetry and X-ray photoelectron spectroscopy indicates that chlorination under O₂-rich conditions is confined to the surface and possibly one subsurface layer of CeO₂ particles. Density functional theory simulations reveal that Cl activation from vacancy positions to surface Ce atoms is the most energy-demanding step, although chlorine-oxygen competition for the available active sites may render re-oxidation as the rate-determining step.

Since the surface of CeO₂ is prone to chlorination upon exposure to the reaction gas mixture, and hence the active surface phase comprises Cl species in its structure, the stability and reactivity of CeOCl as a possible active phase for Deacon reaction were investigated using various feed compositions at 703 K. CeOCl was synthesized by the solid state reaction of cerium oxide and anhydrous cerium chloride. X-ray diffraction of post-reaction samples revealed that CeOCl is unstable, in both oxygen-rich and lean conditions. A complete transformation of CeOCl into CeO₂ was observed by applying oxygen over-stoichiometric feeds. Considerable HCl conversions were obtained only after this transformation, which confirms the essential role of bulk cerium oxide in this catalytic system, probably by facilitating efficient O₂ activation via bulk and surface O-vacancy dynamics.

The impact of surface chlorination on the acid/base properties of ceria (fresh and after reaction) was investigated by probe molecule adsorption (CO₂, NH₃, CO) applying micro-calorimetry, FTIR, TPD and DFT calculations. Micro-calorimetric experiments with CO₂ adsorption indicate that the basic character of CeO₂ has been essentially eliminated upon reaction in HCl oxidation indicating that most of the basic lattice O sites are exchanged by chlorine and that the OH groups formed are rather acidic. Thus, HCl adsorption is certainly retarded by the loss of basic (O²⁻) sites required for H abstraction during dissociative HCl adsorption. Furthermore, FTIR and TPD adsorption experiments using NH₃ and CO as probing molecules reveal that the density and the strength of surface acidic functions increased significantly upon reaction. EPR experiments were carried out on fresh and post-reaction samples using O₂ as probing molecule to assess the effect of surface chlorination on the amount surface O vacancies required for O₂ activation. The results strongly suggest that oxygen activation is inhibited by the high degree of surface chlorination.

The coverage of most abundant surface intermediates, OH and Cl, were monitored by *in situ* infrared spectroscopy and *in situ* PGAA under various conditions. Higher temperature and *p*(O₂) led to enhanced OH coverage, reduced Cl coverage and increased reactivity. Variation of *p*(HCl) gave rise to opposite correlations, while raising *p*(Cl₂) did not induce any measurable increase in the Cl coverage, despite the strong inhibition of the reaction rate. The results indicate that only a small fraction of surface sites is actively involved in the reaction, and

most of the surface species probed in the *in situ* observations are spectators. Kinetics of surface/bulk chlorination and dechlorination was investigated by means of *in situ* PGAA experiments. Using variable reaction conditions (T , p_i) the *in situ* PGAA studies revealed that the chlorination rate is independent of the pre-chlorination degree but increases at lower oxygen over-stoichiometry, while dechlorination is effective in O_2 -rich feeds, and its rate is higher for a more extensively pre-chlorinated ceria.

The role of trivalent (La, Sm, Gd, and Y) and tetravalent (Hf, Zr, and Ti) dopants in the catalytic, structural, and electronic properties of ceria was also investigated. Promoted ceria catalysts were synthesized by co-precipitation with ammonia and tested in HCl oxidation. The intrinsic reactivity of ceria was improved by a factor of 2 when doping with Hf and Zr in appropriate quantities, whereas trivalent dopants are detrimental. The effects of promoters on the electronic conductivity and the vacancy formation energy were studied by contactless conductivity experiments using the microwave cavity perturbation technique and by DFT calculations. In HCl oxidation, only the balanced reduction of both Cl and O vacancy formation energies allows for an enhanced reactivity. Promoters give rise to lattice contraction–expansion modifying vacancy formation energies, adsorption properties, and surface coverage.

Zusammenfassung

Die heterogen katalysierte Gasphasenoxidation von HCl zu Cl₂ (Deacon Reaktion) ist eine energieeffiziente und nachhaltige Methode, Chlor aus chlorwasserstoffhaltigen industriellen Abfallströmen zurückzugewinnen. Diese Arbeit untersucht die Oxidation von HCl über CeO₂ mit Hilfe von *in situ* und *ex situ* Charakterisierungsmethoden und liefert ein Verständnis zur Deacon Chemie über CeO₂ Katalysatoren auf molekularer Ebene.

Die Reaktivität und Stabilität von CeO₂ in der HCl-Oxidation wurde mit Hilfe von kinetischen Experimenten im stationären Zustand untersucht, welche zeigen, dass CeO₂ ein effizienter Katalysator für die Wiedergewinnung von Cl₂ im Temperaturbereich von 623-723 K ist. Eine Korrelation von Struktur und Reaktivität, welche durch die Untersuchung des Einflusses der Probenvorbehandlung, insbesondere der Kalzinierung, auf die Reaktivität erhalten wurde, zeigt, dass Proben von Ceroxid, kalziniert bei mäßig hoher Temperatur (1173 K), den optimalen Kompromiss zwischen Leistung und Stabilität darstellen. Die Kalzinierung bei dieser Temperatur optimiert die Zahl an Leerstellen und die strukturelle Stabilität des Katalysators. Da CeO₂ ein Halbleiter ist, bedarf es zusätzlich seiner Redoxchemie für die Oxidation von HCl und es wird angenommen, dass dabei O-Leerstellen eine entscheidende Rolle spielen. Die Röntgenbeugung und die Elektronenmikroskopie an Proben, welche Reaktionsgasgemischen mit unterschiedlichem O₂:HCl-Verhältnissen ausgesetzt wurden, zeigen, dass CeO₂ in O₂-reichen Gasgemischen (O₂:HCl ≥ 0.75) keiner Chlorierung des Volumens unterliegt, während in (sub)-stöchiometrischen Gasgemischen (O₂:HCl ≤ 0.25) chlorhaltige Phasen gebildet werden. Die qualitative Analyse der Chloraufnahme durch Thermogravimetrie und Röntgenphotoelektronenspektroskopie weist darauf hin, dass sich die Chlorierung unter O₂-reichen Bedingungen auf die Oberfläche und möglicherweise auf die erste Lage unterhalb der Oberfläche beschränkt. Rechnungen mit Hilfe der Dichtefunktionaltheorie stellen heraus, dass die Chloraktivierung von Leerstellenpositionen zu Ce-Oberflächenatomen der energieaufwändigste Schritt ist, obwohl die Konkurrenz von Chlor und Sauerstoff um die verfügbaren aktiven Zentren die Re-Oxidation als geschwindigkeitsbestimmende Schritt kennzeichnet.

Da die Oberfläche von CeO₂ in Anwesenheit des Reaktivgases zur Chlorierung neigt und damit Chlor in die Struktur der aktiven Oberfläche eingebaut wird, wurde die Stabilität und Reaktivität von CeOCl als mögliche aktive Phase für die Deacon Reaktion in unterschiedlichen Reaktivgasgemischen bei 703 K untersucht. CeOCl wurde mittels Festkörperreaktion zwischen Ceroxid und wasserfreiem Cerchlorid erhalten. Röntgenbeugungsmessungen an Ausbauproben zeigten, dass CeOCl sowohl unter sauerstoffreichen als auch unter mageren Bedingungen instabil ist. In, hinsichtlich Sauerstoff, überstöchiometrischem Gasgemischen wurde eine vollständige Umsetzung von CeOCl in CeO₂ beobachtet. Nur dann wurden nennenswerte Umsätze von HCl erhalten, was die essentielle Rolle des Volumens von CeO₂ in diesem katalytischem System bestätigt. Wahrscheinlich geschieht dies durch eine erleichterte, effiziente Aktivierung von O₂ durch die Dynamik von Volumen- und Oberflächenleerstellen des Sauerstoffs.

Der Einfluss der Oberflächenchlorierung auf die Säure-Base-Eigenschaften von Ceroxid wurde mittels Adsorption an Sondenmolekülen (CO₂, NH₃, CO) mit Mikrokolorimetrie, FTIR, TPD und DFT-Berechnungen sowohl an frischen Ceroxid als auch Ausbauproben untersucht. Mikrokolorimetrische Experimente mit Adsorption von CO₂ weisen darauf hin, dass der basische Charakter von CeO₂ während der HCl Oxidation im Wesentlichen verloren geht, was darauf hindeutet, dass der überwiegende Teil des Gittersauerstoffs durch Chlor ersetzt wurde und dass gebildete OH-Gruppen eher sauer reagieren. Damit wird die Adsorption von HCl höchstwahrscheinlich durch den Verlust basischer (O²⁻) Zentren, welche für die Abstraktion von H während der dissoziativen Adsorption benötigt werden, gehemmt. Weiterhin zeigen FTIR und TPD mit NH₃ und CO als Probemolekül, dass die Dichte und Stärke saurer Funktionalitäten auf der Oberfläche während der Reaktion zunimmt. EPR Experimente an frischen Proben und an Ausbauproben mit O₂ als Sondenmolekül wurden durchgeführt, um den Effekt der Oberflächenchlorierung auf die Menge von Sauerstoffleerstellen an der Oberfläche, welche zur

O₂-Aktivierung nötig sind, einschätzen zu können. Die Ergebnisse weisen darauf hin, dass die Sauerstoffaktivierung durch den hohen Grad an Chlorierung unterdrückt wird.

Die Bedeckungen der wichtigsten Oberflächenintermediate, OH und Cl, wurden durch *in situ* Infrarot-Spektroskopie und *in situ* PGAA verfolgt. Höhere Temperaturen und höhere $p(\text{O}_2)$ führen zu einer erhöhten Bedeckung mit OH, einer verminderten Bedeckung mit Cl und schließlich zu einer erhöhten Reaktivität. Die Änderung von $p(\text{HCl})$ führt zu entgegengesetzten Korrelationen, während die Erhöhung von $p(\text{Cl}_2)$, trotz starker Unterdrückung der Reaktionsrate, keine messbare Erhöhung der Cl Bedeckung bewirkt. Diese Ergebnisse lassen vermuten, dass nur ein kleiner Teil der Oberflächenzentren aktiv an der Reaktion teilnimmt, während die meisten der untersuchten Oberflächenspezies, welche unter *in situ* Bedingungen beobachtet wurden, unbeteiligt sind. Die Kinetik der Oberflächen- und Volumenchlorierung und Dechlorierung wurde mit Hilfe von *in situ* PGAA Experimenten untersucht. Die unter verschiedenen Reaktionsbedingungen ausgeführten Experimente zeigen, dass die Chlorierungsgeschwindigkeit unabhängig vom Grad der Vorchlorierung ist, jedoch bei niedrigerer Überstöchiometrie von Sauerstoff ansteigt, während die Dechlorierung in sauerstoffreichen Gasgemischen effektiv ist. Diese Geschwindigkeit ist höher für ein stärker vorchloriertes Ceroxid.

Die Rolle trivalenter (La, Sm, Gd und Y) und tetravalenter (Hf, Zr und Ti) Dotierungen für die katalytischen, strukturellen und elektronischen Eigenschaften von Ceroxid wurde ebenso untersucht. Promotiertes Ceroxid wurde mittel Co-Fällung mit Ammoniak dargestellt und in der HCl-Oxidation getestet. Die intrinsische Aktivität von Ceroxid wurde um Faktor 2 gesteigert, wenn mit Hf und Zr in adäquater Weise promotiert wurde, während sich trivalente Dotierungsmittel nachteilig auswirken.

Der Effekt der Promotoren auf die elektronische Leitfähigkeit und die Bildungsenergie der Fehlstellen wurde mittels kontaktfreien Leitfähigkeitsexperimenten mit Hilfe der „Microwave perturbation technique“ und mit DFT-Berechnungen geprüft. In der HCl-Oxidation begünstigt nur eine gleichzeitige Reduktion von Cl- und O-Leerstellenbildungsenergien eine erhöhte Reaktivität. Promotoren verursachen eine Gitterkontraktion oder Expansion, was die Leerstellenbildungsenergien, die Adsorptionseigenschaften und die Oberflächenbedeckung modifiziert.

Acknowledgement

I would like to express my special gratitude to Prof. Robert Schlögl for giving me the opportunity to do this work in an excellent working environment in the Department of Inorganic Chemistry at the Fritz Haber Institute of the Max Planck Society, for offering me an exciting research project, and for providing me with his scientific advice.

I am very grateful for the committee members of my thesis defense. Prof. Dr. Reinhard Schomäcker for hosting me as external student, Prof. Dr. Nicola Pinna for reviewing this thesis and Prof. Dr. Matthias Driess for taking the chair of the examination board.

My endless thanks go to Dr. Detre Teschner who has supervised my work and transferred a lot of his experience and knowledge to me. I would like to thank him for the wonderful time we spent together in discussing different matters on both an academic and a personal level. He helped me also in the final assessment of the thesis and in “catching my typos and mistakes”. I cannot imagine if I could have gone so far without his help and supervision. Thanks a lot!

All the members of my group, “Electronic structure”, deserve special thanks for the valuable discussions and encouraging. In particular, I thank Eugen Stotz for his help in designing the *in situ* IR cell I used for my work. Dr. Axel Knop-Gericke is acknowledged for supervising me during the period of the research stay at the FHI.

During my stay at the Fritz Haber Institute I have been enjoying the team-work atmosphere. A number of colleagues in the Department of Inorganic Chemistry contributed in performing experiments, technical assistance and discussions. I would like to acknowledge the following people (in no particular order): Dr. Frank Girgsdies and Jasmin Allan (XRD), Jutta Kröhnert (IR), Dr. Andrey Tarasov (TG), Dr. Sabine Wrabetz (microcalorimetry), Gisela Weinberg and Wiebke Frandsen (SEM-EDX), Gisela Lorenz and Maike Hashagen (N_2 physisorption), Dr. Manfred Schuster (HRTEM), Dr. Maik Eichelbaum (EPR and conductivity experiments), Patrick Kast (for allowing me the use his setup for CO oxidation experiments).

I also thank my officemates, Pia Kjær Nielsen, Dr. Kazuhiko Amakawa, Margherita Macino and Dr. Detre Teschner for the warm atmosphere and inspiring chat.

I thank Dr. László Szentmiklósi at the Centre for Energy Research (Budapest, Hungary) for introducing me to the PGAA setup and for performing the quantitative evaluation of the PGAA experiments. I thank Professor Dr. Núria López and her research group at the ICIQ (Tarragona, Spain) for performing the DFT calculations needed for this work. I thank Professor Javier Pérez-Ramírez and his research group at ETH Zürich (Switzerland) for the excellent collaboration and for conducting some of the kinetic experiments, TPR and XRD measurements presented in my thesis.

I thank my parents and relatives in Syria for enduring my long absence and for their unlimited non-stop encouragement.

Last but not least, I thank my own family; my dearest wife and my little angel Adam for continuing support, patience, love and for their standing by me in the difficult times.

Table of Contents

Table of Contents	i
List of Abbreviations	v
List of Figures	vi
List of Tables	xv
Chapter 1: Introduction	1
1.1 General introduction	1
1.2 Characterization of solid catalysts	2
1.3 Importance of chlorine	2
1.4 State of the art technologies for chlorine production	3
1.4.1 Electrolysis process.....	3
1.4.2 Gas phase oxidation of HCl.....	3
1.5 Aim of the work	7
1.6 Outline of the work	8
1.7 References	10
Chapter 2: Performance, structure, and mechanism of CeO₂ in HCl oxidation to Cl₂	13
Abstract	13
2.1 Introduction	14
2.2 Experimental	14
2.2.1 Catalysts.....	14
2.2.2 Characterization.....	15
2.2.3 Catalytic tests.....	16
2.2.4 <i>In situ</i> Fourier Transform Infrared spectroscopy (FTIR).....	16
2.2.5 Computational details.....	16
2.3 Results and discussion	17
2.3.1 Catalytic evaluation.....	17
2.3.2 Characterization.....	21
2.3.3 <i>In situ</i> Fourier Transform Infrared Spectroscopy.....	25
2.3.4 Molecular modeling.....	27
2.4 Conclusions	31
2.5 Supporting Information	32
2.6 References	41
Chapter 3: Synthesis and catalytic performance of CeOCl in Deacon reaction	43
Abstract	43
3.1 Introduction	44
3.2 Experimental	44
3.2.1 Sample preparation.....	44
3.2.2 Characterization methods.....	45
3.2.3 Catalytic test.....	45
3.3 Results and discussion	45
3.3.1 Synthesis and stability of CeOCl.....	45
3.3.2 Catalytic activity of CeOCl in HCl oxidation.....	47
3.4 Conclusion	49

3.5 References	50
Chapter 4: Understanding CeO₂ as a Deacon catalyst by probe molecule adsorption and <i>in situ</i> infrared characterizations	51
Abstract	51
4.1 Introduction	52
4.2 Experimental	52
4.2.1 Samples	52
4.2.2 HRTEM characterization	52
4.2.3 NH ₃ temperature programmed desorption	52
4.2.4 Micro-calorimetry	53
4.2.5 Probe molecule adsorption by FTIR	53
4.2.6 <i>In situ</i> FTIR in HCl oxidation	53
4.2.7 Density Functional Theory calculations (DFT) of probe molecule adsorption	54
4.3 Results and discussion	55
4.3.1 HRTEM	55
4.3.2 Micro-calorimetry and corresponding DFT analysis	56
4.3.3 Probe molecule adsorption by FTIR and corresponding DFT analysis	59
4.3.4 <i>In situ</i> FTIR under Deacon reaction	61
4.3.5 Mechanistic considerations	63
4.4 Conclusions	65
4.5 Supporting Information	66
4.6 References	70
Chapter 5: Do observations on surface coverage-reactivity correlations always describe the true catalytic process? A case study on ceria	73
Abstract	73
5.1 Introduction	74
5.2 Experimental	74
5.2.1 Catalysts	74
5.2.2 Basic characterization	75
5.2.3 <i>In situ</i> Prompt Gamma Activation Analysis (PGAA)	75
5.2.4 Catalytic evaluation	75
5.2.5 <i>In situ</i> Fourier Transform Infrared Spectroscopy	76
5.2.6 Electron Paramagnetic Resonance (EPR) experiments	76
5.3 Results	77
5.3.1 Kinetics of chlorination and dechlorination	77
5.3.2 Surface coverage analysis	80
5.3.3 EPR experiments of O ₂ adsorption	83
5.4 Discussion	85
5.5 Conclusions	86
5.6 Supporting Information	87
5.7 References	92
Chapter 6: Promoted ceria: a structural, catalytic and computational study	93
Abstract	93
6.1 Introduction	94
6.2 Experimental and computational methods	95
6.2.1 Preparation of catalysts	95
6.2.2 Basic characterization	95
6.2.3 Contactless conductivity experiments using a Microwave Cavity Perturbation Technique (MCPT)	95

6.2.4	<i>In situ</i> Prompt Gamma Activation Analysis	96
6.2.5	Catalytic tests	96
6.2.6	Computational details	96
6.3	Results	98
6.3.1	HCl oxidation.....	98
6.3.2	CO oxidation.....	100
6.3.3	Structural characterization of promoted ceria.....	101
6.3.4	Contactless conductivity experiments using the microwave cavity perturbation technique.....	104
6.3.5	DFT calculations.....	104
6.3.6	<i>In situ</i> PGAA	106
6.4	Discussion	108
6.5	Conclusions	111
6.6	Supporting Information	112
6.7	References	120
	Chapter 7: Conclusions	123
	Appendix A	127
	Appendix B	133
	Curriculum Vitae	141

List of Abbreviations

Abbreviation	Explanation
BET	adsorption isotherm model of Brunauer, Emmet and Teller
DFT	Density Functional Theory
BNC	Budapest Neutron Center
DRIFTS	Diffuse Reflectance Infrared Fourier Transform Spectroscopy
DSC	Differential Scanning Calorimetry
DSA	Dimensionally Stable Anode
EAL	Effective Attenuation Length
EDX	Energy Dispersive X-ray spectroscopy
EPR	Electron Paramagnetic Resonance
Fig.	Figure
FTIR	Fourier Transform Infrared Spectroscopy
FEP	Full-Energy Peak
GC	Gas Chromatography
HRTEM	High Resolution Transmission Electron Microscopy
HPGe	High Purity Germanium Crystal
ID	Inner Diameter
IMFP	Inelastic Mean Free Path
IR	Infrared Spectroscopy
MS	Mass Spectrometry
MIR	Mid-Infrared
MW	Microwave
MCPT	Microwave Cavity Perturbation Technique
NAA	Neutron Activation Analysis
NIR	Near-Infrared
OSC	Oxygen Storage capacity
PC	Polycarbonate
PGAA	Prompt Gamma Activation Analysis
PVC	Polyvinylchloride
PU	Polyurethane
SEM	Scanning Electron Microscopy
SI	Supporting Information
STEM	Scanning Transmission Electron Microscopy
STP	Standard Pressure
TAP	Temporal Analysis of Products
TEM	Transmission Electron Microscopy
TGA	Thermo Gravimetry Analysis
TOS	Time On Stream
TPO	Temperature Programmed Oxidation
TPR	Temperature Programmed Reduction
UHV	Ultra High Vacuum
WGS	Water Gas Shift
XPS	X-ray Photoelectron Spectroscopy
XRD	X-Ray Diffraction

List of Figures

- Figure 2.1** HCl conversion *versus* (a) surface area of fresh (open symbols) and used (solid symbols) CeO₂ samples and (b) OSC, measured at 573 K, of fresh CeO₂ samples. Conditions: inlet mixture of 10 vol.% HCl and 20 vol.% O₂ balanced in N₂, $T_{\text{bed}} = 703$ K, $W/F^0(\text{HCl}) = 11.2$ g h mol⁻¹, $P = 1$ bar, and time-on-stream = 3 h. 19
- Figure 2.2** HCl conversion *versus* feed O₂:HCl ratio at 703 K for CeO₂-1173-F. Conditions: inlet mixture of 10 vol.% HCl and 5-70 vol.% O₂ balanced in N₂, $T_{\text{bed}} = 703$ K, $W/F^0(\text{HCl}) = 11.2$ g h mol⁻¹, and $P = 1$ bar. 20
- Figure 2.3** HCl conversion *versus* time-on-stream over CeO₂-1173 using sequential HCl-rich/O₂-rich feed mixtures. (a) HCl-rich step with O₂:HCl = 0.25 followed by O₂-rich step with O₂:HCl = 2. (b) HCl-rich step with O₂:HCl = 0.25 followed by O₂-rich step with O₂:HCl = 7. (c) HCl-rich step with O₂:HCl = 0 followed by O₂-rich step with O₂:HCl = 7. Other conditions: $T_{\text{bed}} = 703$ K, $W/F^0(\text{HCl}) = 11.2$ g h mol⁻¹, and $P = 1$ bar. 20
- Figure 2.4** XRD patterns of CeO₂-1173 samples in fresh and used (at various O₂:HCl ratios) forms. The diffractogram of CeO₂-773-0 is included for comparison. The most intense reflections are due to CeO₂ (JCPDS 73-6328), while those within boxes belong to CeCl₃·6H₂O (JCPDS 01-0149). 22
- Figure 2.5** TEM of (a) CeO₂-773-F, (b) CeO₂-773-2, (c) CeO₂-773-0, and HRTEM of (d) CeO₂-773-2, revealing the surface of the CeO₂ particles. (e) A CeO₂-773-0 particle (surface termination in the inset) and (f) a CeO₂-773-0 particle showing an amorphous layer of CeCl₃·6H₂O on the surface. TEM of (g) CeO₂-1173-F, (h) CeO₂-1173-2, and (i) CeO₂-1173-0. Detailed imaging of (j) CeO₂-1173-2, showing CeO₂ particles with clean surface (inset) and of (k,l) CeO₂-1173-0, exhibiting both the (k) CeO₂ and (l) CeCl₃·6H₂O phases. 24
- Figure 2.6** Evolution of the stretching OH band region of CeO₂-773-F upon introducing 1 vol.% HCl into an O₂/N₂ (20/80) feed at 653 K. The dark-blue curve represents the starting state prior to HCl introduction, whereas the black spectrum shows the stabilized state after HCl has been turned off (both in O₂/N₂). The temporal evolution in the Deacon feed was as follows: light blue / brown / green / orange / red corresponding to time-on-stream of 85 / 170 / 220 / 270 / 1055 s, respectively. 26
- Figure 2.7** Structural model of a $p(2 \times 2)$ supercell of CeO₂(111): (a) regular surface, (b) surface vacancy, and (c) subsurface vacancy. Ce atoms are depicted in blue, surface O atoms in red, and subsurface O atoms in scarlet and small balls. 28
- Figure 2.8** Reaction energy profile for the Deacon process on CeO₂(111). The initial state in the profile is CeO₂(111) with a surface oxygen vacancy. The color codes in the bottom panels are as described in the caption of Figure 2.7. 29
- Figure S 2.1** H₂-TPR profiles of CeO₂ catalysts. All profiles are characterized by a main peak of hydrogen consumption centered at 1073-1150 K, due to the reduction of bulk CeO₂. Less intense peaks around 723-773 K are assigned to reduction of labile surface and near-surface oxygen species (Yao et al., J. Catal. 86 (1984) 254; Trovarelli, Catal. Rev. Sci. Eng. 38 (1996), 439). The profiles indicate that reduction of surface CeO₂ starts at *ca.* 573 K. 35
- Figure S 2.2** Oxygen storage capacity (OSC) of CeO₂-773-F measured at different temperatures. As HCl oxidation involves participation of the CeO₂ outermost surface layers, the temperature of the OSC measurement has to be selected so that

reduction would be mostly limited to the (near-)surface region. The H₂-TPR results (Fig. S 2.1) gave preliminary indication of a suitable temperature (573 K). OSC measurements carried out on CeO₂-773-F at temperatures between 573 and 873 K evidenced substantially similar OSC values in the temperature range of 523-773 K, suggesting reduction at the surface level only. However, a further temperature increase by 100 K enabled reduction of the bulk to some extent. This result is in line with literature reports (Trovarelli, Catal. Rev. Sci. Eng. 38 (1996) 439, Fornasiero et al., Appl. Catal., B 22 (1999) L11, Aneggi et al., J. Alloys Compd. 408-412 (2006) 1096). On the basis of these data, the OSC of the catalysts was measured at 573 K. 35

Figure S 2.3 Diagnostic to verify the absence of extra-particle and intra-particle diffusion limitations in the catalytic tests. HCl conversion *versus* volumetric flow rate (a) and particle size (b) over CeO₂-1173-F. Conditions: inlet mixture of 10 vol.% HCl and 20 vol.% O₂ balanced in N₂, $T_{\text{bed}} = 703$ K, $W/F^0(\text{HCl}) = 11.2$ g h mol⁻¹, $P = 1$ bar, and time-on-stream = 3 h. 36

Figure S 2.4 HCl conversion and total surface area *versus* time-on-stream for CeO₂-773-F. Conditions: inlet mixture of 10 vol.% HCl and 20 vol.% O₂ balanced in N₂, $T_{\text{bed}} = 703$ K, $W/F^0(\text{HCl}) = 11.2$ g h mol⁻¹, and $P = 1$ bar. The HCl conversion was practically constant at each measured point, whereas the S_{BET} halved already after 15 min on stream and further decreased up to 3 h, reaching a value that corresponds to about 25% of the original one (27 *versus* 106 m² g⁻¹). These results confirmed the observed independence of the activity on S_{BET} for values of the latter greater than 25 m² g⁻¹ and additionally indicated that the restructuring of high-surface area catalysts upon contact with the reaction mixture occurs rapidly. 36

Figure S 2.5 (a) Equilibrium HCl conversion *versus* reaction temperature at variable feed O₂:HCl ratio and total pressure. (b) HCl conversion *versus* time-on-stream over CeO₂-1173 using various residence times. Conditions: inlet mixture of O₂:HCl = 5, $T_{\text{bed}} = 673$ K, and $P = 1$ bar. High operating temperatures (613-703 K range) are required for CeO₂, and this implies not only a high energy input, but also thermodynamic restrictions to the attainable HCl conversion. Fig. S 2.5a shows that the equilibrium HCl conversion indeed decreases at higher temperatures, but that higher pressures and O₂:HCl ratios largely overcome these limitations, so that the HCl conversion level achieved can still make the development of a technical process feasible (HCl conversion > 80%). For instance, by using a feed mixture with O₂:HCl = 5 and by increasing the space time (at the limits of our current set-up), stable single-pass HCl conversion values of 40% were attained over CeO₂-1173-F at 673 K and 1 bar (Fig. S 2.5b). 37

Figure S 2.6 HCl conversion *versus* space time over CeO₂-1173-F at different feed O₂:HCl ratios. Conditions: inlet mixture of 10 vol.% HCl and 5-70 vol.% O₂ balanced in N₂, $T_{\text{bed}} = 703$ K, and $P = 1$ bar. 37

Figure S 2.7 Space time yield of Cl₂ *versus* feed HCl concentration and feed HCl:O₂ ratio over CeO₂-1173-F. Conditions: inlet mixture of 5-40 vol.% HCl and 10 vol.% O₂ balanced in N₂, $T_{\text{bed}} = 703$ K, and $P = 1$ bar. Upon raising the relative HCl content in the feed mixture, the Cl₂ production slightly increased at first and then progressively diminished. This unexpected result is not due to intrinsic kinetics. Low HCl concentrations limit Cl₂ production, while HCl excess causes a change in the catalyst composition at the surface and near-surface level (chlorination) that leads to activity loss. 38

Figure S 2.8 XRD patterns of CeO₂-1173 samples used at 703 K in the HCl-rich/O₂-rich flow experiments (Fig. 2.4). The O₂:HCl ratios used in the two stages and the duration

of each stage are reported on the right-hand side of the figure. The most intense reflections are specific to CeO_2 (JCPDS 73-6328, black lines). Minor amounts of $\text{CeCl}_3 \cdot 6\text{H}_2\text{O}$ (JCPDS 01-0149, gray lines; the relative reflections are visualized in the black boxes) were present for the sample exposed to $\text{O}_2:\text{HCl} = 2$ for the O_2 -rich stage. 38

Figure S 2.9 Thermogravimetric profiles of fresh and Deacon-used CeO_2 catalysts. Mass spectrometry profiles for H_2O (AMU 18) and for Cl (AMU 35) coupled to the TGA analysis of CeO_2 -773-0 are shown in the secondary y-axis. The peaks result identical for all the samples in terms of number and position, while their intensity differs according to the extents of weight loss. The weight loss of chlorinated samples occurred in several steps. Up to 400 K, removal of surface impurities, such as physically adsorbed water (peak 1), took place. This loss was observed for the fresh sample too. From 360 K up to 473 K, the water of crystallization of the $\text{CeCl}_3 \cdot 6\text{H}_2\text{O}$ phase was lost in three steps (peaks 2-4). Finally, chlorine removal took place between 473 and 700 K (peak 5). These assignments were made on the basis of literature reports (Wendlandt, J. Inorg. Nucl. Chem. 5 (1957) 118; Guo-Cai et al., Trans. Nonferrous Met. Soc. China, 13 (2003) 1454). The quantification of the chlorination degree of the samples was performed taking into account only the relevant partial weight losses, i.e. relative to structural water and chlorine. 39

Figure S 2.10 Ce 3d core level XPS spectra of CeO_2 -773 and CeO_2 -1173 samples in fresh form and after treatments under various reaction conditions. A difference spectrum (HCl treatment minus fresh sample) and a $\text{CeCl}_3 \cdot 6\text{H}_2\text{O}$ reference spectrum are included for comparison. 39

Figure S 2.11 First principles thermodynamics for the $\text{CeO}_2(111)$ $p(2 \times 2)$ surface containing different amounts of chlorine. The plane showing the lowest energy ΔG at a given set of pressures is the most likely equilibrium structure under reaction conditions. The employed temperature was set to $T = 703.15$ K. The code for the configurations is indicated in the lowest panel: black for pure $\text{CeO}_2(111)$; green for a single Cl occupying a vacancy on the surface; blue for a substituting Cl atom and a second Cl on top of a Ce site; and red for two Cl substituting two oxygen atoms on the surface. Grey spheres stand for Ce atoms, red for surface O atoms, scarlet for sub-surface O atoms, and green for Cl atoms. 40

Figure 3.1 XRD pattern of CeOCl materials. CeOCl-T after cleaning treatment; CeOCl-F before cleaning treatment and CeOCl-ref as a reference [21]. 46

Figure 3.2 SEM photographs of CeOCl-T. (a) and (b): before HCl oxidation, (c) and (d): after reaction ($\text{O}_2:\text{HCl} = 9:1$ at 703 K). 47

Figure 3.3 TGA-MS of CeOCl-T in Ar flow. (a) fresh material; (b) after 5 months exposure to ambient air 47

Figure 3.4 (a) X-ray powder diffraction patterns of CeOCl-T: after 5 months exposure to ambient air (reflections within boxes belong to $\text{Ce}(\text{OH})_2\text{Cl}$), after TGA treatment of CeOCl-T exposed to air for 5 month with the fresh CeOCl for comparison. (b) XRD spectra of CeOCl-T samples before and after reaction using different feed ratios, with added CeO_2 reference. 48

Figure 3.5 (a) reactivity of CeOCl-T at different feed ratios with time on stream. (b) comparison of Cl_2 productivity of CeOCl at different $\text{O}_2:\text{HCl}$ ratios with a theoretical 0.5 order dependence observed for CeO_2 . 48

Figure 4.1 Scheme of the *in situ* FTIR cell with gas inlet and outlet at the sides and three feedthroughs at the top (2 for thermocouples and one for heating). The investigated sample (red) is held in a heatable stage. 54

- Figure 4.2** TEM and HRTEM comparison of CeO₂ before (a, c) and after Deacon reaction (b, d). The sample after reaction was taken from the pellet used for the *in situ* FTIR experiments. 55
- Figure 4.3** Adsorption isotherms (a, c) and differential heat of adsorption data of CO₂ (a, b) and NH₃ (c, d) on fresh and post Deacon CeO₂ studied by micro-calorimetry. When indicated, a 2nd adsorption was carried out after desorption in UHV. $T = 313$ K. 56
- Figure 4.4** Schematic representation of adsorption sites on the CeO₂(111) surface. The different sites are highlighted by the circles. Light blue spheres represent Ce atoms, orange sub-surface O atoms, red O, green Cl and white H. CeO₂H (O_{lattice}H) corresponds to the OH group on the left and CeO₂H-OH is the water pair. 57
- Figure 4.5** NH₃-TPD profiles of fresh and post Deacon CeO₂ samples. 58
- Figure 4.6** (a) FTIR spectra of CO adsorbed at 77 K on fresh CeO₂; after admission of 1.860 mbar CO in equilibrium (black-spectrum), after various sequential steps of evacuation (rest). Inset: Difference spectrum of the sample before and after admission of CO; (b) FTIR spectra of CO adsorbed at 77 K on CeO₂-D; after admission of 1.306 mbar CO in equilibrium (black-spectrum), after sequential steps of evacuation (rest). Inset: zoom in for the band at 2186 cm⁻¹. 59
- Figure 4.7** *In situ* single beam FTIR spectra of CeO₂ under various conditions: activated (before HCl introduction) and in Deacon reaction. 62
- Figure 4.8** Evolution of integrated area of OH band at 3730 cm⁻¹ as a function of time on Deacon stream. Red points represent the standard conditions of O₂:HCl = 9:1 at 703 K and the black line is a fit to these data. Blue points represent various other conditions in Deacon feed during pO_2 , $pHCl$ and T variation. These are discussed in detail in Fig. 4.9-4.11. 62
- Figure 4.9** *In situ* results at 703 K during pO_2 variation. (a) Cl₂ production as a function of O₂ content of the feed. (b) Evolution of integrated OH area as a function of time on Deacon stream during pO_2 variation. OH variation is expressed as the difference of the OH area at 9:1:0 feed according to the fit at the corresponding time on stream and the actual measured area. 64
- Figure 4.10** *In situ* results at 703 K during $pHCl$ variation. (a) Cl₂ production as a function of HCl content of the oxygen-rich feed. (b) Evolution of integrated OH area as a function of time on Deacon stream during $pHCl$ variation. OH variation is expressed as the difference of the OH area at 9:1:0 feed according to the fit at the corresponding time on stream and the actual measured area. 64
- Figure 4.11** *In situ* results during temperature variation using a feed of O₂:HCl:N₂ = 9:1:0. (a) Arrhenius Plot. (b) Evolution of integrated OH area as a function of time on Deacon stream during T variation. OH variation is expressed as the difference of the OH area at 9:1:0 feed and 703 K according to the fit at the corresponding time on stream and the actual measured area. 64
- Figure S 4.1** Schematic representation of the clean CeO₂(111) surface (a), surface hydroxyl (b), surface on top hydroxyl (c) and chlorine substitution with a concomitant hydroxyl group (d). Ammonia adsorption on models (a-d) are represented in figures (e-h); CO₂ adsorption on figures (i-j) and adsorption on an oxygen vacancy (m) and CO adsorption on the (a-d) models shown in (n-q). Grey spheres represent Ce atoms, red O, blue H, yellow C and green Cl. 66
- Figure S 4.2** Thermogravimetric (TGA) profile of CeO₂-D coupled to mass spectrometry (MS) profiles for H₂O (AMU 18) and for Cl (AMU 35). The weight loss of the

equilibrated sample occurred in several steps. Up to 490 K, removal of surface impurities, such as physically adsorbed water, and the water of crystallisation of the $\text{CeCl}_3 \cdot 6\text{H}_2\text{O}$ phase took place. Weight loss between 490 and 660 K was attributed to chlorine removal. Similar assignments were made by Amrute et al. (J. Catal., 286 (2012) 287-297). 69

Figure S 4.3 An example of fitting the OH region of *in situ* FTIR spectra observed during Deacon reaction. The red peak is integrated and discussed in the main text. 69

Figure 5.1 Series of chlorination/dechlorination experiments over $\text{CeO}_2\text{-R}$ at 703 K by *in situ* PGAA. (a) Map of experiments with three series. Various $\text{O}_2\text{:HCl}$ feed ratios (10% HCl, 2.5–90% O_2 balanced in N_2) were probed. Measurements were performed from left to right consecutively, however, for different time periods. (b) Evolution of HCl conversion and Cl uptake (as Cl:Ce) in the experiments. The first data point is at 4% conversion. The lines guide the eyes to follow the order of experiments. (c) An example of Cl uptake over time-on-stream with a feed of $\text{O}_2\text{:HCl} = 0.25\text{:}1$. (d) Thickness growth ($\text{\AA}/\text{h}$) of chlorinated shell as a function of the feed oxygen content. The rate of Cl uptake was evaluated in a simple geometric model (with particle radius of 82 nm) and assuming a homogeneous growth of the chlorinated surface shell toward the particle core. The thickness growth describes the speed of the chlorinated front moving towards the core of the ceria particle. 78

Figure 5.2 Rejuvenation of the CeO_2 phase from CeCl_3 under Deacon conditions. (a) HCl conversion *versus* time-on-stream over CeCl_3 at various $\text{O}_2\text{:HCl}$ ratios and temperatures. Other conditions: 10 vol.% HCl and 20–90 vol.% O_2 balanced in N_2 , space time = $11.2 \text{ g h mol}^{-1}$, total volumetric flow = $166 \text{ cm}^3 \text{ STP min}^{-1}$, and 1 bar. (b) XRD patterns of fresh $\text{CeO}_2\text{-A}$, fresh CeCl_3 , and CeCl_3 samples resulted from the catalytic tests. The right panel lists the crystalline phases identified in the samples, with the predominant phase in bold: CeO_2 (JCPDS 73-6328), CeCl_3 (JCPDS 77-0154), $\text{CeCl}_3 \cdot 6\text{H}_2\text{O}$ (JCPDS 01-0149). 79

Figure 5.3 Evolution of the intensity of the mono-coordinated OH band at 3730 cm^{-1} as a function of (a) $p(\text{O}_2)$, (b) $p(\text{HCl})$, (c) temperature as measured by *in situ* FTIR on $\text{CeO}_2\text{-A}$. The absorbance spectra were fitted, and the area variation referenced to the condition $\text{O}_2\text{:HCl} = 9\text{:}1$ at 703 K was plotted. (d) Reaction rate measured in parallel by iodometric titration, *versus* the intensity of the OH band under different conditions. 81

Figure 5.4 *In situ* PGAA experiments on $\text{CeO}_2\text{-R}$ showing the reaction rate evolution as a function of Cl:Ce ratio under various conditions. In (a), the feed oxygen content (at 703 K), in (b) the temperature (at $\text{O}_2\text{:HCl} = 9\text{:}1$) and in (c), the feed HCl content (at 703 K) was varied. (d) Cl:Ce ratio as a function of various amounts of Cl_2 co-dosed to a 9:1 feed at 703 K. In SI, corresponding $p(\text{O}_2)$ and T dependences on $\text{CeO}_2\text{-A}$ are shown to be identical to those given here. Table 5.1 suggests that over $\text{CeO}_2\text{-R}$ and $\text{CeO}_2\text{-A}$, both reactivity and Cl uptake are similar when normalized to the corresponding BET surface area. 82

Figure 5.5 Influence of Cl_2 co-feeding on the rate of HCl oxidation over $\text{CeO}_2\text{-A}$. Conditions: 10 vol.% HCl and 90 vol.% O_2 , 703 K, space time = 5.6 g h mol^{-1} , total volumetric flow = $166 \text{ cm}^3 \text{ STP min}^{-1}$, 1 bar, and dwelling time under each condition = 1.5 h. 83

Figure 5.6 EPR signals of superoxide species produced by O_2 adsorbed at RT on pre-reduced samples (a) $\text{CeO}_2\text{-A}$ and (b) $\text{CeO}_2\text{-D}$. Signal marked with * is due to highly EPR-active Mn^{2+} impurities in the ceria. (c) The amount of superoxide was quantified by double integration of signals assigned to superoxides. 84

- Figure S 5.1** *In situ* PGAA experiments on CeO₂-A showing the reaction rate (conversion) evolution as a function of Cl/Ce ratio under various conditions: varying the feed oxygen content at 703 K (O₂:HCl= 9:1, 4:1, 2:1, 1:1 and 0.5:1), and the temperature at O₂:HCl = 9:1 ($T = 673$ -593 K). 87
- Figure S 5.2** A photo of the *in situ* PGAA experiment. 88
- Figure S 5.3** A typical PGAA spectrum of the CeO₂ catalyst 89
- Figure S 5.4** Peak fitting of the Ce (top) and Cl lines (bottom). The panel in purple displays the uncertainties of the fitted quantities. 90
- Figure 6.1** Side view of the M-doped CeO₂ bulk structures (a) and side and top views of the different M-doped CeO₂ (111) and (110) surfaces (b) employed for the DFT calculations. 97
- Figure 6.2** (a) Stability test. Normalized HCl conversion over CeHf-10 vs time on stream. Conditions: 703 K, 9:1 O₂:HCl ratio, catalyst weight of 0.25 g. (b) HCl conversion (■) over CeHf-10 vs the reactor loading expressed in weight and surface area. Conditions: 703 K, 9:1 O₂:HCl ratio. A hypothetical other catalyst (□) is also shown. The intrinsic reactivity of the samples (i.e. the efficiency to provide a certain number of turnovers to occur) is compared on the basis of the actual surface area (SA^{Act}) of the sample and the equivalent surface area (SA^{Eq}) by SA^{Eq}/SA^{Act}. Please note that the fit shown (---) does not correspond to the 0.5 order power fit because of the slowly approaching equilibrium above 60% HCl conversion. Instead, a mathematically better fitting can be obtained for the whole 0–64% conversion range using an Exponential Decay 2 function (in Origin Pro), which is shown here and was used to calculate SA^{Eq}. 99
- Figure 6.3** (a) CO oxidation light-off profiles of selected catalysts at a 1:1:98 O₂:CO:He mixture, and (b) temperatures allowing 20, 50, and 90% CO conversion. Catalyst weight of 0.2 g and flow rate of 100 cm³ min⁻¹. 100
- Figure 6.4** SEM of CeHf-10 as prepared (a and b) and after a 100 h stability test in HCl oxidation (c and d). 102
- Figure 6.5** (a) Plot of the lattice parameter as a function of effective ionic radius of the guest ion for fresh materials and those used in HCl oxidation. The ionic radius is an effective radius of Shannon [71], with a coordination number of 8. (b) Plot of the lattice parameter as a function of guest ion concentration of Zr and Hf. Error bars correspond to ±3 times the estimated standard uncertainties. 102
- Figure 6.6** Microwave (MW) conductivity at 9.2 GHz of undoped and doped CeO₂ powder samples in different gas mixtures as indicated, with N₂ as the residual gas. As for CeO₂, between 170 and 350 min time on stream (TOS) the sample was treated in mixtures containing 2–20% O₂ in N₂ (not directly labeled), but no conductivity changes were observed. 103
- Figure 6.7** Calculated formation energies for oxygen and chlorine surface defects as a function of the x and y -lattice expansion in an undoped p(2 × 2) CeO₂(111) surface. 105
- Figure 6.8** O and Cl vacancy formation energies with respect to gas-phase oxygen or chlorine (E_{O} or E_{Cl}), for the different undoped CeO₂ and M-doped surfaces. The relative positions of the dopant and the vacancy are indicated as follows: s for surface position, ss for subsurface position, and NN and NNN for the vacancy being the nearest and next nearest neighbor to M, respectively. See Figure 6.1 for further details. 107
- Figure 6.9** Intrinsic reactivity as a function of (a) the Cl uptake per surface area as measured by *in situ* PGAA and (b) the lattice parameter after HCl oxidation. The

normalized intrinsic reactivity is based on the description provided in the legend of Figure 6.2b; however, the numbers are scaled to provide CeO₂ an intrinsic reactivity value of 1. Error bars assume for the lattice parameter ± 3 times the estimated standard uncertainties and for Cl uptake and normalized intrinsic reactivity $\pm 10\%$ of the actual value. The $\pm 10\%$ error is an estimate of the convoluted error of reactivity + the BET value and the PGAA accuracy + the BET value.

- Figure S 6.1** A typical LabMax® protocol on the example of the synthesis of Ce_{0.95}Hf_{0.05}O₂. The protocol reads as follows; (1) increasing the reactor temperature till 318 K; (2) basification to pH = 8.95; (3) addition of metal salt solution (7 cm³ min⁻¹) while keeping the pH constant at 9 by adding appropriate amounts of ammonia solution (10 wt.%); (4) aging for 1 hour accompanied by increasing the rotation speed to 375 rpm. 110
- Figure S 6.2** Ln(SigmaT) plot as a function of inverse temperature for CeHf-5, as deduced from the temperature dependent MW conductivity experiment. 113
- Figure S 6.3** (a) Constable-Cremer relationship for HCl oxidation over doped and undoped CeO₂ catalysts. The Arrhenius parameters were determined in the temperature range of 643–703 K with a reaction mixture O₂:HCl:N₂ = 9:1:0 and a catalyst loading of 0.25 g. The rate was plotted as “mol Cl₂ g⁻¹ min⁻¹” in the Arrhenius diagram. (b) Oxygen partial pressure dependence (at constant HCl and total flow rate) with CeHf-10 at 703 K. 113
- Figure S 6.4** (a) Arrhenius plot for CO oxidation (CO:O₂:He = 1:1:98) over CeSm-5 and CeHf-5. (b) Constable-Cremer relationship for CO oxidation over the studied catalysts. The Arrhenius parameters were determined in the smooth conversion range of ~5–40 % with excellent linear fit. The rate was plotted as “CO conversion” in the Arrhenius diagram. (c) CO conversion in heating and cooling section showing very little difference in reactivity over CeHf-5. At 550 K cooling was stopped and the feed O₂ content was varied. (d) Oxygen partial pressure dependence (at constant CO and total flow rate) with CeHf-5 and CeLa-5 at 550 K. 114
- Figure S 6.5** The XRD pattern of CeHf-20 with its fitting showing the two cubic phases present. 116
- Figure S 6.6** Strain (a) and crystallite size (b) as a function of Zr and Hf dopant concentration, as derived by the Double-Voigt pattern analysis [6]. Error bars correspond to ± 3 -times the estimated standard uncertainties. 116
- Figure S 6.7** Side and top views of the calculated diffusion barriers for the oxygen vacancy in the M-doped-CeO₂(111) surface (M = Hf, La). Notice that when moving the vacancy a rearrangement of the associated electrons takes place. 117
- Figure S 6.8** Plot of the calculated oxygen vacancy formation energy for the M-doped-CeO₂(110) surface *versus* the M-doped-CeO₂(111) surface. 117
- Figure A 1** The transmission spectrum of Si window in the mid and far infrared regions. 131
- Figure A 2** Cross section views of the *in situ* transmission FTIR cell. 131
- Figure A 3** The lid and the heatable stage (sample holder) of the *in situ* FTIR cell. 132
- Figure B 1** Unsuppressed (red) and Compton suppressed (black) PGAA spectra of ¹⁷Cl. 137
- Figure B 2** A photo of the *in situ* PGAA setup. 138
- Figure B 3** The iodometric titration tools. 138
- Figure B 4** Shielding materials used for the *in situ* PGAA setup. 139

List of Tables

Table 2.1	Description of catalysts' codes.	15
Table 2.2	Characterization and catalytic activity data.	18
Table 2.3	Quantification by different models of the surface Cl uptake from XPS measurements.	25
Table 2.4	Energy (ΔE) in eV and Gibbs free energy (ΔG^0) in $\text{kJ mol}^{-1} \text{ M}$ ($\text{M} = \text{Ce}, \text{Ru}$) atom for the complete chlorination of CeO_2 and RuO_2 by Cl_2 or HCl . ^a	31
Table S 2.1	Configurations and calculated frequencies, in cm^{-1} , for H_2O -related species adsorbed on a regularly terminated CeO_2 surface, or a CeO_2 surface with vacancies, and/or with neighboring adsorbed chlorine atoms. ^{a,b,c}	33
Table 4.1	Summary of the experimental and calculated adsorption, E in kJ mol^{-1} , and vibrational frequencies, ν in cm^{-1} , of probe molecules together with the corresponding model.	60
Table S 4.1	Vibrational frequencies for hydroxyl groups on CeO_2 , ν in cm^{-1} , for vibrations higher than 800 cm^{-1} . Frequency assignment labels: (s) OH stretching; (b) bending modes. μ_{B} : Bohr magneton.	66
Table S 4.2	Adsorption energies, E_{ads} in kJ mol^{-1} , of ammonia on different CeO_2 configurations (with respect to different model surfaces and gas-phase NH_3) and corresponding vibrational frequencies, ν in cm^{-1} (for the vibrations stronger than 800 cm^{-1}). Frequency assignment labels: symmetric stretching (ν_{s}), asymmetric stretching (ν_{a}), bending (δ modes). The labelling follows that of ref. [1] pages 117 and 131. μ_{B} : Bohr magneton.	67
Table S 4.3	Adsorption energies, E_{ads} in kJ mol^{-1} , of CO_2 on different CeO_2 configurations and corresponding vibrational frequencies, ν in cm^{-1} (for the vibrations stronger than 800 cm^{-1}). Negative adsorption energies indicate endothermic processes. Frequency assignment labels: symmetric stretching (ν_{s}), asymmetric stretching (ν_{a}), bending (δ modes). The labelling follows that of ref. [1] page 108.	68
Table S 4.4	Adsorption energies, E_{ads} in kJ mol^{-1} , of CO on different CeO_2 configurations and corresponding vibrational frequencies, ν in cm^{-1} (for the vibrations stronger than 800 cm^{-1}). Negative adsorption energies indicate endothermic processes. Frequency assignment labels: stretching (s), bending (b). μ_{B} : Bohr magneton.	68
Table 5.1	Comparison of characterization and activity for the ceria catalysts. Notice, the two CeO_2 catalysts exhibit similar intrinsic reactivity.	80
Table S 5.1	Characteristics of the EPR signals for $\text{CeO}_2\text{-A}$ and $\text{CeO}_2\text{-D}$ obtained upon oxygen adsorption at 298 K.	87
Table S 5.2	Peak energies, cross-sections and count rates of primary lines for Ce and Cl.	90
Table 6.1	Samples with their Codes, BET surface areas, and Cl_2 space time yields under standard conditions.	99
Table 6.2	Steady-state microwave conductivity data for selected doped and undoped CeO_2 measured under different conditions as shown in Figure 6.6.	103
Table 6.3	Segregation energies, E_{seg} in eV, for M-doped- CeO_2 (111) and (110) surfaces.	105

- Table S 6.1** Calculated formation energy (in eV) of an oxygen surface defect in a p(3×3) CeO₂(111) surface imposing a ferromagnetic (FM) and an antiferromagnetic (AFM) spin states. 118
- Table S 6.2** Calculated formation energies of an oxygen surface defect in a p(3×3) CeO₂(111) surface, $\Delta E_{\text{Os}}^{(111)}$ in eV, with different locations of the pair of Ce³⁺ ions. In parenthesis, reported values for comparison. 118
- Table S 6.3** Calculated formation energy of an oxygen surface defect in a p(3×3) CeO₂(111) surface, $\Delta E_{\text{Os}}^{(111)}$ in eV, with and without adding a U_{eff} term for the O(2p) states. 118
- Table S 6.4** Relevant distances (in Å) for the CeO₂(111) surface with no oxygen defects, and the CeO₂(111) and M_s-doped-CeO₂(111) (M = Hf, La) surfaces with an oxygen surface defect. 118
- Table S 6.5** Calculated polaron energy, E_{pol} in eV, oxygen diffusion barriers, E_a in eV for different M-doped bulk structures. Notice that when moving the anions a homogeneous distribution of dopants is employed. NN: nearest neighbor, NNN: next nearest neighbor, >NNN: further away from M. 118

Chapter 1: Introduction

1.1 General introduction

The role of heterogeneous catalysts for our society has been increasing steadily and it became indispensable like any other key element of our life. Although the science related to heterogeneous catalysis might be too involved for everyman, many people are nowadays aware of the role of the catalyst in cleaning up exhaust of automobiles. On the other hand, it might be for some even surprising to know that the fertilizer generated from ammonia, which is produced by the Haber-Bosch process (in which nitrogen gas extracted from air is fixed and converted into ammonia over a solid catalyst), is estimated to be responsible for sustaining one third of earth's population [1-2]. In fact, the importance of heterogeneous catalysis exceeds these two particular examples, which definitely reflect the vital role of catalysis in our daily life. Heterogeneous catalysts are crucial to energy conversion, chemical industry and environmental technology. It has been estimated that over 90% of all industrial chemical processes make use of heterogeneous catalysts [3]. In fact, many chemical products may not have been possible to commercialize without the aid of solid catalysts. Furthermore, the environmental impact of catalysis is clearly evident by reducing the amount of energy and raw materials needed for fuels and chemical manufacture [4].

Catalyst by definition is a material that converts reactants into products, through a series of elementary steps, in which the catalyst participates while being recovered in its original form at the end of each reaction cycle during its lifetime [3]. The catalyst provides an alternative, energetically favorable mechanism to the non-catalytic reaction. The overall change in free energy for the catalytic reaction equals that of the non-catalyzed reaction, i.e., the catalyst increases the rate of reaction without modifying the overall standard Gibbs energy change during the reaction. And hence, if the considered reaction is thermodynamically unfavorable the catalyst cannot change this situation. In simple words, the catalyst changes the kinetics but not the thermodynamics.

On the *macroscopic* level, the heterogeneous catalytic process is a simple phenomenon, in which reactants introduced to the reactor are transformed into products over a solid catalyst that has *macroscopic* dimensions too. But on the *microscopic* level the catalytic route is much more complicated and comprises plenty of elementary steps happening at the molecular level. The reactant must diffuse through the catalyst pores, adsorb on its surface, travel to the active site, form the reactive complex with the catalyst and produce the desired product that desorbs back to the gas phase. Moreover, bond-rupturing of reactants and bond-forming of products are *nanoscopic* events taking place on the surface of the catalysts. Thus, the sole *macroscopic* observation of catalytic performance does not provide understanding on the underlying mechanisms at a *microscopic* level. The importance of the latter scale goes without saying as it determines the intrinsic reactivity and selectivity of the catalyst. Despite this fact, most industrial catalytic achievements were attained using the Edisonian approach of try and error. Nevertheless, discovering of mechanistic details and the set of elementary reactions that comprise the catalytic turnover can make the rational design of improved catalysts more feasible. This in-depth understanding of heterogeneous catalysis will not just make a great contribution to the fundamental science but also our life will benefit through improvements of catalysts by rational design. This approach however is challenging and may require the most advanced experimental techniques available.

1.2 Characterization of solid catalysts

Solid catalysts might be compared to a living organism having a life cycle with their creation, their life during reaction and their death when the catalysts are deactivated. Adequate information about the parameters and factors affecting each stage and in-depth understanding of the nature of that organism are prerequisite for finding the best means and tools ensuring healthy and long life. The conventional approach of characterizing solid catalysts under static conditions, i.e., before and after reaction, does not provide sufficient knowledge on the physicochemical processes occurring under dynamic conditions at the molecular level. To overcome this limitation many surface and bulk characterization techniques (e.g., XPS, XRD, UPS, IR, Raman, etc.) have been improved to investigate catalysts under reaction conditions (*in situ*), and hence a better understanding of how a heterogeneous catalyst operates can be obtained. In this sense, it is worth noting that the major drawback of using surface science characterization techniques (XPS, UPS, LEED, STM etc.), which very often require ultra-high vacuum (UHV) conditions, is the possibility that surface reconstruction, segregation or even phase transformation might occur under reaction conditions and thus, the catalyst (surface) under investigation is not mimicking that one under real reaction conditions (e.g., elevated pressures and temperatures). Therefore, bridging the pressure gap is an important issue in the field of heterogeneous catalysis. Moreover, developing new chemical analysis techniques (e.g., based on nuclear methods) [5] with the potential of being used under real catalytic reaction conditions is highly desirable. The ultimate goals of catalyst's characterization are to determine the nature and the amount of active sites, to unravel the mechanism of a catalytic turnover and to establish correlation between the structure/composition of catalytic solids and their functions including activity, selectivity and stability. However, thus far, the first two objectives have rarely been achieved (if at all) for any heterogeneous catalytic system.

1.3 Importance of chlorine

With 0.017% of natural abundance of chlorine, it is ranked 11th among the constituent elements of the earth's crust. In nature, molecular chlorine (Cl₂) does not exist as such due to its high reactivity, rather, it is found in combination with other elements. Approximately 2000 naturally occurring chlorine-based compounds have been identified [6], which are indispensable for many useful biological functions of different living organisms.

From the industrial point of view, chlorine derives its importance from being a key building block for the manufacture of most important basic products in the chemical industry. A large number of chemicals require chlorine in their production processes; de facto about 55% of the chemical industry turnover depends on chlorine. A sound description of chlorine's industrial importance has been made by Peter Schmittinger, who stated that "the chlorine worldwide production of a country is an indicator of the state of development of its chemical industry"[7].

Chlorine has numerous applications in a variety of fields including construction, electronics, transport, healthcare, textile, etc. Engineering materials, like versatile plastics or elastomers, are so far the main consumers of chlorine. About 33.6% of all produced chlorine in Europe is used for the synthesis of polyvinylchloride (PVC), followed by isocyanates and oxygenates with 29.4% [8]. Polyurethanes (PU) and polycarbonates (PC) are chlorine free end-products using molecular chlorine as a reactant during the manufacturing chain for the synthesis of intermediates or precursors like phosgene (COCl₂) required for the process. Chlorine in turn ends up forming chlorine-containing by-product, namely hydrogen chloride.

The remarkable tendency towards chlorine-free products, e.g. polycarbonates or polyurethanes (annual growth rate of 5% for PU and 6-7% for PC) [9] on the cost of chlorine containing products e.g. polyvinylchloride (expected annual growth of only 2%) [10], will compel the industry to deal with huge quantities of the undesirable toxic hydrogen chloride resulting in a

toxic-waste disposal problem if there were no efficient technologies available for chlorine recycling.

1.4 State of the art technologies for chlorine production

Chlorine manufacturing has a long past of mutation and development starting from the DEACON [11] process in 1866 through the first large scale application of electrolysis process in 1892 by SIEMENS [12] and the application of *dimensionally stable anodes* (DSA) in 1965 by H.B. Beer [13,14] turning back to the DEACON-like process by SUMITOMO-Chemicals in 2004 [15] and Bayer MaterialScience in 2007 [16–18]. The latter achievements from the last decade represent a true breakthrough in recent catalysis research. Based on the above list, nowadays two main technologies can be effectively used to recycle chlorine from chloride containing compounds (NaCl or HCl), the electrolysis process and the Deacon-like heterogeneous catalytic oxidation process.

1.4.1 Electrolysis process

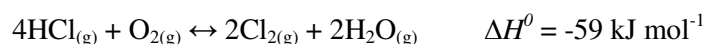
The electrolysis process improved by Bayern & DeNora [19] was till 2004 the most efficient procedure known for producing chlorine from NaCl brine or HCl. However, it is still hitherto the dominant industrial technology for Cl₂ production. Basically, Cl₂ is produced on the anode surface of the electrochemical cell by passing an electric current through an aqueous NaCl solution. H₂ and NaOH are produced as by-products. There are three basic processes for the electrolytic production of chlorine: (1) the diaphragm cell process, (2) the mercury cell process and (3) the membrane cell process. The latter is the most energy efficient and economic process producing the desired products (Cl₂ and caustic soda) with high purity. In 2011 the membrane cell capacity accounted for 51% of total installed chlorine production capacity in Europe [8]. The so called *dimensionally stable anodes*, consisting of a conductive substrate of titanium coated with mixed oxide of RuO₂-TiO₂ (30 mol%-70 mol%), are used in both diaphragm and membrane processes. The composition mentioned above can be considered as standard, in which the catalytic layer RuO₂ has been partially substituted with TiO₂ which increases the adhesion of the noble metal oxide onto the titanium substrate and thus resulting in increased durability. During the course of chlorine and oxygen evolution reactions the titanium substrate is usually covered by a thin insulating layer of titanium oxide brought about by the passivation of the Ti substrate. Hence, titanium oxide from the coating layer is binding to titanium oxide from the Ti substrate resulting in increased durability. However, with extended usage in electrolytic chlorine cells, the chlorine overpotential increases by a factor of 7 [19] and the anode is then considered to have become deactivated. The main reasons of this deactivation are the surface depletion of the active catalytic oxide (RuO₂) and the build-up of thicker nonconductive layer of TiO₂ at the Ti substrate/coating interface [19]. Many attempts using different approaches have been reported to enhance the resistance properties of the DSA anodes [20–30]. Doping the electrocatalytic layer (RuO₂-TiO₂) with metal oxides of the same crystal structure as for the RuO₂ [31] (rutile type), like, IrO₂ [32–36] and SnO₂ [22,37–40] has proven to be the best way for producing DSA anodes of better catalytic performance, longer service life and lower Ru loss. Nevertheless, it must be emphasized that the electrochemical Cl₂ production represents one of the most energy demanding processes in the chemical industry and almost half of the production costs are accounted for the power supply. Consequently, economic and environmental reasons have met together to raise the importance of finding an alternative technology for a sustainable chlorine recycling.

1.4.2 Gas phase oxidation of HCl

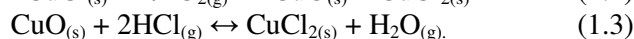
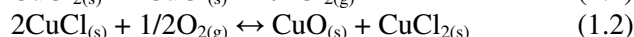
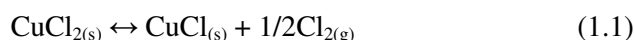
The gas phase oxidation of HCl (Deacon process) represents an attractive route for chlorine recovery due to its relative ease of application, low power consumptions and relative low thermal requirements. In 1866, chemist Henry DEACON [11] developed a process based on the

oxidation of the hydrogen chloride gas by atmospheric oxygen in the presence of a copper salt (CuCl_2) placed on pumice as a catalyst and obtained yields up to 65% of the theoretical value.

The gas phase oxidation of hydrogen chloride is a slightly exothermic and equilibrium-controlled reaction, that is, high total pressure and low temperatures are the favoured reaction conditions for high equilibrium conversion of HCl.



The reaction steps comprising the catalytic cycle over copper chloride catalyst are predicted as follows:



Equation (1.3) represents the chlorination step, in which CuO abstracts two HCl molecules and forms thereby CuCl_2 and the couple product H_2O , whereas equations (1.2) represents the oxidation step, in which original oxide catalyst is recovered by the oxidation of CuCl intermediate by molecular oxygen. In equation (1.1) the desired product is obtained by the decomposition of CuCl_2 to CuCl and Cl_2 . From the energy point of view the reaction can be decomposed into two consecutive steps: exothermic (chlorination of the oxide catalyst) and endothermic (reoxidation of the chlorinated catalyst) steps.

Several drawbacks hindered Deacon to the industrial application of his process: rapid deactivation of the copper-based catalyst due to the volatilization of the active metal species above 673 K, high oxygen separation costs and severe corrosion problems brought about by unreacted HCl in the presence of H_2O [41].

Many efforts were undertaken since then to overcome these major problems. Some works were devoted to find an effective and more robust catalyst than the original copper-based Deacon one [42,43]. For instance, IG Farben used the molten sodium (or potassium) and iron chloride as a catalyst for the gas-phase HCl oxidation process [44]. In 1960s, the Shell-Chlor process was established using a copper-didymium-potassium chloride combination as a catalyst in fluidized bed reactor [45,46]. As a result of the molten salt formed by CuCl_2 and KCl, higher HCl conversion at lower operation temperatures and better stability of the active materials in comparison to the original Deacon process were achieved [47]. At about the same time, Kellogg established the Kel-Chlor process [48] for Cl_2 manufacturing using nitrogen oxides (NO and NO_2) as a homogeneous type catalyst with sulfuric acid as circulating medium. In 1980s, Mitsui Chemicals proposed the MT-Chlor process using $\text{Cr}_2\text{O}_3/\text{SiO}_2$ as a catalyst in a fluidized reactor [49,50]. In contrast to the copper-based Deacon catalysts used in Shell-Chlor process, the Cr_2O_3 catalyst inclines to preserve its bulk structure under reaction conditions, and hence, it is believed that the reaction proceeds through a surface redox catalytic cycle rather than going through the bulk chloride-oxide reaction route of copper-based catalysts. Consequently, the stability of the catalyst was considerably enhanced compared with the Shell-Chlor process. However, most of the above proposed processes were either not stable or not active enough or even being curtailed due to environmental concerns. Some other works focused on the optimization of the reaction process from a technical point of view, so that ~100% recovery of Cl_2 was attained by conducting the reaction over copper based catalysts using a two stage cyclic fluidized bed process [51–53] and hence corrosion problems brought about by the coexistence of unreacted HCl and H_2O in the effluent stream could be minimized to a great extent. In this process the reaction is subdivided into two steps: 1) the exothermic chlorination, in which HCl reacts with CuO and converts it to CuCl_2 and H_2O vapor, 2) the endothermic oxidation, in which the chlorinated catalyst is reoxidised by air or O_2 to release the desired product Cl_2 . Actually, in this

two-stage process the catalyst acts as a chlorine storage medium. This storage effect helps to overcome the chemical equilibrium limitation in HCl oxidation (ca. 84% HCl conversion at 623 K) and hence full HCl conversion could be attained. However, the two-stage process suffered (as expected) from catalyst deactivation due to copper chloride volatilization.

The limited success of the above proposed processes highlighted the importance of finding indicators or descriptors that allows ranking relative activity as well as stability of catalysts in the Deacon reaction. The selection criteria used to identify the potential Deacon catalyst was based on thermodynamic analysis of the energies associated with both processes comprising the proposed catalytic steps of chlorination and reoxidation. Essentially, this approach implies that the potential Deacon catalyst must display a moderate exothermicity upon chlorination which leads to a modest endothermicity for the reoxidation step. Hisham and Benson [54] utilized this approach to assess the catalytic activity of a large number of main group and transition metal oxides for the Deacon process. They concluded that CuO is the only metal oxide that fulfills the requirements of a complete catalytic cycle below 700 K. It is worthwhile to mention, that the thermochemistry data given in that study is bulk phase related, and it is expected that for the surface where the heterogeneously catalyzed reaction takes place would be different. Moreover, as the authors mentioned in their original study, although the thermodynamic approach might be useful, it can only provide constraints on possible catalytic reactions. In practice, kinetic parameters and physical properties may dominate. In searching for a simple descriptor, Allen [55] was the first one who recognized that the reoxidation step of the chlorinated catalyst (metal oxide) must not be too demanding, and hence, it is a prerequisite to consider potential catalysts for Deacon reaction. In this context, Studt et al. [56,57] evaluated various rutile oxide surfaces in HCl oxidation using density functional theory (DFT) calculations and found that the dissociative adsorption energy of O₂ is a good descriptor to assess the activity of oxide surfaces in Deacon reaction. Recently, Over and Schomäcker [58] compiled experimental reactivity data and suggested a similar volcano dependence as a function of the same descriptor. In both studies the reactivity of ruthenium oxide catalyst lies close to the optimum of the volcano trend.

Indeed, ruthenium-based materials have been successfully implemented for large scale Cl₂ production by Sumitomo Chemicals [15] and Bayer MaterialScience [16–18] (RuO₂/SiO₂/TiO₂ by Sumitomo and RuO₂/SnO₂-Al₂O₃ by Bayer). The use of ruthenium based catalysts was regarded as a major breakthrough in Cl₂ production via HCl oxidation, since the catalysts applied overcame almost all critical points encountered by the original copper-based Deacon catalysts. The main advantage of these catalysts is that RuO₂ exhibits a remarkable high activity in HCl oxidation that allows conducting the reaction at relatively low temperatures (about 573 K). Moreover, chlorination is confined to the upper surface layer; i.e. ruthenium oxide preserves its structure upon contact with the aggressive Deacon gas mixture. Nonetheless, the time required for this discovery is somewhat surprising, since the catalytic materials used are seemingly similar to those applied for decades as *dimensionally stable anodes* in the electrolysis process! [25]. This reflects the lack of deep understanding into mechanistic details controlling the catalytic processes (electro- and heterogeneous catalysis) [59]. Recently, RuO₂-based catalysts have been investigated extensively [60–73] using variety of characterization techniques and theoretical calculations to elucidate key features on the molecular level. This includes the reaction mechanism, the reactive catalytic phase, effects of supports and binders and the reason of deactivation. Experiments were conducted on RuO₂-model surfaces under ultra-high vacuum conditions (UHV) as well as on polycrystalline supported or bulk RuO₂ catalysts at pressures more relevant to the real catalysis [60–62]. *In situ* surface studies on the RuO₂ (110) surface [62] have revealed that bridging O atoms (O_{br}) are selectively replaced by chlorine atoms forming thereby strongly bonded bridging Cl atoms (Cl_{br}). Furthermore, it is suggested that the reaction proceeds one dimensionally [61] over isolated rows of coordinatively unsaturated Ru atoms (Ru_{cus}) where the reaction between HCl and O₂ takes place. The superior catalytic performance and the robust character of RuO₂ under Deacon conditions were assigned to the self-limiting nature of surface chlorination that facilitates in turn Cl₂

evolution and surface re-oxidation [60,62]. The latter allows thus low temperature operations. The $\text{RuO}_{2-x}\text{Cl}_x$ (110) surface was regarded as the catalytic active phase [62] and the catalytic reaction proceeds according to the Langmuir-Hinshelwood mechanism [60,61], in which surface chlorine recombination was defined as the most energy demanding step [61]. However, because of the high Cl coverage O_2 activation was identified as the rate determining step [71]. In addition, HRTEM experiments revealed that the epitaxial growth of RuO_2 on rutile-phase supports (like rutile- TiO_2 or rutile- SnO_2) is beneficial from the point view of reactivity and stability, since lattice matching effects increase the active metal distribution and enhance the active phase – support bonding strength, as well [64,71]. Sintering effects were responsible for the deactivation behavior of supported RuO_2 catalysts [71], while adding Al_2O_3 (to Bayer catalyst $\text{RuO}_2/\text{TiO}_2$) [73] and SiO_2 (for Sumitomo catalyst, $\text{RuO}_2/\text{TiO}_2$) [64] as binder materials filling interstitial spaces between RuO_2 particles plays an essential role in protecting support materials from severe chlorination and hence volatilization as well as in suppressing RuO_2 agglomeration.

Despite the pronounced success of the implementation of RuO_2 -based catalysts in pilot trials and plant installations, the high and fluctuating price of Ru as long as the steady increase of its application in the technology fields, not to mention being precious metal with limited abundance are all disadvantageous for the wide application of this technology. Hence, efforts were directed to search for alternative cost-effective and especially stable catalytic materials [43]. Unfortunately fundamental studies on the mechanism of Deacon reaction over a wide range of metal oxides are scarce [54]. However, recent studies led to the recognition of CeO_2 as promising alternative to the industrially implemented RuO_2 based catalysts. Amrute et al. [74] studied Deacon catalytic activity of a series of metal oxides, namely, RuO_2 , Cr_2O_3 , CeO_2 , CuO and MnO_2 using temporal analysis of products (TAP) technique. CeO_2 ranked third beyond RuO_2 according to the activity order given. Interestingly, the oxide bulk phase was retained upon exposure to a certain reaction feed mixture in the case of CeO_2 and Cr_2O_3 . The latter oxide however is less interesting for large scale applications due to environmental concerns associated with the use of chromium-based materials. These observations were the driving force to investigate Deacon chemistry over CeO_2 on the molecular level and to assess its reactivity and long-term stability before possible adaption for large scale applications. This is especially valid here, since history has proven that the main reason of the limited success of other Deacon-type processes was the lack of detailed understanding of the catalytic reaction mechanism associated with this process.

CeO_2 (having a fluorite structure) [75] has been employed in numerous catalytic processes as support, additive and active phase. It is a key component in automotive exhaust catalysis [76], in Diesel soot oxidation [77], in water-gas shift (WGS) catalysis [78], in oxidative halogenations [79] and in preferential oxidation of CO (PROX) reactions [80]. The key features making CeO_2 such an important catalytic material, particularly in redox reactions, is the mobility of its lattice oxygen ions and the easy formation of oxygen vacancies. Furthermore, structural stability improvements as well as higher catalytic turnovers can be achieved by doping ceria catalysts with specific amounts of different elements [81,82]. In this context, ceria represents an exceptionally advantageous catalytic material for investigation.

1.5 Aim of the work

The work presented in this thesis investigates Deacon chemistry on CeO₂-based catalysts at the molecular level using state of the art characterization techniques. Novel questions related to the microscopic understanding of key parameters affecting the catalytic performance of CeO₂-based catalysts are highlighted and discussed. First, we addressed the basic question, what makes CeO₂ as a good alternative to the industrially implemented RuO₂ catalyst. In order to provide answer to this question, two critical aspects must be assessed, namely, the reactivity and longevity of CeO₂ in Deacon reaction. In addition, reaction condition variables (T , p_i) have to be thoroughly explored to find out the most appropriate conditions in which the optimum reactivity of CeO₂ can be achieved.

The effect of catalyst preparation and pretreatment on the physico-chemical properties (e.g. rigidity, surface area, porosity, etc.) and in turn on reactivity are common issues in heterogeneous catalysis and need to be addressed in the case of using CeO₂ for HCl oxidation.

Since bulk chlorination and hence the formation of volatile chloride species was often the main reason of catalyst deactivation (losing the active phase), and the remarkable stability of RuO₂-based catalysts was assigned to the self-limiting nature of surface chlorination, we need to assess whether CeO₂ suffer from any bulk chlorination and whether this chlorination, if any, influence the catalytic turnover. Furthermore, we need to define reaction conditions at which Cl diffusion to the bulk takes place. Because the surface of CeO₂ gets likely chlorinated upon exposure to the reaction feeds (as the case of most proposed Deacon catalysts), the initial basic character of CeO₂ surface will be altered upon this chlorination. This raises the questions as to which extent the distribution as well as the nature of acid-base surface species on ceria will be altered upon surface chlorination in HCl oxidation, and whether mechanistic insights could be derived from the analysis of these changes? On the other hand, it is worth to investigate whether the sole existence of Cl and O species on the surface is enough to ensure catalytic reactivity of ceria catalysts, or the co-existence of bulk oxide phase is a prerequisite factor in this catalytic system. Based on the previous assumption of surface chlorination, one may ask how surface chlorination affects the catalytic turnover. In this respect, it is very informative to study the surface coverage impact on the catalytic turnover. Furthermore, this may allow clarifying the role of adsorbed surface species or intermediates (Cl or OH groups) in the reaction mechanism. Ceria is well-known for its relative ease with which oxygen vacancies can be formed and eliminated, and hence it is reasonable to assume that oxygen vacancy defects at the cerium oxide surface play a crucial role in determining its catalytic activity in redox reactions, as HCl oxidation over ceria. Accordingly, knowing the nature and distribution of such defective sites as well as how surface chlorination may alter the propensity of CeO₂ to activate molecular oxygen is highly desirable. Moreover, mechanistic insights concerning the identification of the rate determining step could be obtained by this assessment of the role of oxygen vacancies in the reaction mechanism.

In many catalytic reaction systems in which ceria serves as active material or carrier, catalytic performance improvements in terms of stability or intrinsic reactivity were achieved by the addition of promoters (dopants). In this context, we intended to investigate whether doping of ceria with selected elements could enhance its reactivity in HCl oxidation. Furthermore, structural and electronic changes associated with the doping process must be assessed to understand the real role of dopants in the catalytic reaction.

1.6 Outline of the work

After this short introduction, the major findings of the present work are summarized and discussed in context to the literature.

This work represents also a successful scientific collaboration between different research institutions and the Inorganic Chemistry Department of the Fritz-Haber Institute in Berlin. The group of Professor N ria L pez from the ICIQ in Tarragona contributed with DFT calculations in the publications this thesis is based upon. The group of Professor Javier P rez-Ram rez from ETH Z rich, Switzerland contributed with kinetic experiments, TPR and some XRD measurements, mainly presented in Chapter 2 of this work, whereas Dr. L szl  Szentmikl si, Centre for Energy Research, Hungarian Academy of Sciences performed the quantitative evaluation of the *in situ* PGAA experiments. Personally, I have contributed by the evaluation or conduction of the rest of experiments (except microscopy) performed at the Fritz-Haber Institute or at the Budapest Neutron Centre and presented in this work. The results are presented in the chapter structure as follows:

In Chapter 2, kinetic experiments under various Deacon feed compositions followed by X-ray diffraction analysis of post-reaction samples reveal that CeO₂ suffers from bulk chlorination and hence deactivation when stoichiometric or sub-stoichiometric feed compositions are used [83]. The reactivity however can be restored by exposing deactivated samples to O₂-rich feeds. Catalyst pretreatment effects, in particular calcination, are systematically studied, and hence a structure-reactivity correlation is established. X-ray photoelectron spectroscopy experiments on post-reaction samples exposed to O₂-rich feeds indicate that chlorination is limited to the surface and maybe a subsurface layer. Based on DFT calculations on the most stable (111) surface, the reaction mechanism as well as the energetically most demanding step is proposed.

In Chapter 3, CeOCl was synthesized by solid state reaction of cerium oxide with anhydrous cerium chloride [84]. According to the findings given in Chapter 2, the surface of CeO₂ is chlorinated upon exposure to the reaction gas mixture; surface chlorination was proven even for the samples exposed to oxygen rich feed compositions. Thus, the active phase of the catalyst is certainly not pure CeO₂, rather a chlorinated surface or phase. Consequently, the stability and reactivity of CeOCl as a possible active phase are tested in HCl oxidation using various feed compositions. The importance of bulk oxide phase in this catalytic system is emphasized.

In Chapter 4, a comprehensive characterization of acid-base properties of ceria samples, before and after chlorination in HCl oxidation, using multiple spectroscopic techniques is demonstrated [85]. Micro-calorimetric CO₂ adsorption experiments revealed that the basic character of CeO₂ has been completely eliminated upon reaction in HCl oxidation. In addition, FTIR and micro-calorimetric experiments were conducted using NH₃ and CO as probing molecules to assess surface acidity changes induced by surface chlorination. The negative impact of surface chlorine on HCl dissociative adsorption is highlighted. NH₃ temperature programmed desorption experiments were conducted on fresh and post-reaction ceria samples to investigate the impact of surface chlorination on the strength of the acid sites available on the surface of CeO₂. DFT calculations performed on the lowest energy surface, CeO₂ (111), assess adsorption energies and vibrational frequencies associated with different degrees of surface hydroxylation and/or chlorination. The evolution and density of OH groups on ceria were investigated during HCl oxidation by means of *in situ* transmission FTIR experiments. OH-density-reactivity correlations at various reaction conditions (*T*, *p_i*) are established. The reaction mechanism is discussed in view of the above mentioned observations.

In Chapter 5, Electron Paramagnetic Resonance (EPR) experiments performed on fresh and chlorinated samples using O₂ as probing molecule are presented. A quantitative assessment of the surface chlorination impact on the oxygen activation on ceria was attained [86]. Since OH groups and adsorbed Cl constitute the most abundant species on the surface, a quantitative assessment of their surface density under various reaction conditions was accomplished and thus surface coverage-reactivity correlations were established. For this purpose, *in situ* Prompt

Gamma Activation Analysis (PGAA) was implemented to record the Cl uptake of catalysts during HCl oxidation, and *in situ* transmission FTIR spectroscopy for OH groups (More information about the fundamentals and experimental requirements of these techniques is given in Appendix A and B). Kinetics of chlorination and de-chlorination processes was studied in an elaborate way, in which Cl uptake/release rates were determined using *in situ* PGAA. Product co-feeding experiments (Cl_2) were carried out to prove whether product inhibition is relevant to this catalytic system. Moreover, these experiments (product co-feeding) allow us to test the reliability of surface coverage-reactivity correlation obtained, and to make a sound estimation concerning the amount of surface sites that can be regarded as “active sites”.

In Chapter 6, intrinsic reactivity improvements were achieved by doping ceria with a certain amount of Hf and Zr [87]. Long-term stability test (100 hours) of the best promoted catalyst was carried out, and followed by morphological (by SEM) and composition (by EDX) inspections to find out whether dopant was leaching during HCl oxidation. A series of dopants, namely, La, Sm, Gd, Y, Hf, Zr and Ti, was used to investigate electronic and structural changes induced to corresponding doped ceria catalysts. The effect of promoters on the electronic conductivity and vacancy formation energy was studied by DFT calculations and by contactless conductivity measurements under oxidative, inert and reductive atmospheres using the microwave cavity perturbation technique (MCPT). The positive impact of the balanced reduction of both Cl and O vacancy formation energies on reactivity is highlighted. Lattice parameter changes (expansion and contraction) of promoted ceria catalysts were attained and correlated to the intrinsic reactivity of corresponding catalysts. The effect of promoters on lattice contraction/expansion and hence on adsorption properties, surface coverage and vacancy formation energies are presented.

1.7 References

- [1] V. Smil, *Ambio* **2002**, *31*, 126–131.
- [2] T. Hager, *The Alchemy of Air: A Jewish Genius, a Doomed Tycoon, and the Scientific Discovery That Fed the World But Fueled the Rise of Hitler*, Harmony Books, **2008**.
- [3] G. Ertl, Ed., *Handbook of Heterogeneous Catalysis: 8 Volumes*, WILEY-VCH, Weinheim, **2008**.
- [4] P. Barbaro, C. Bianchini, Eds., *Catalysis for Sustainable Energy Production*, Wiley-VCH, Weinheim, **2009**.
- [5] R. M. Lindstrom, *Journal of Research of the National Institute of Standards and Technology* **1993**, *98*, 127.
- [6] N. Winterton, *Green Chem.* **2000**, *2*, 173–225.
- [7] P. Schmittinger, *Chlorine: Principles and Industrial Practice*, Wiley-VCH, **2000**.
- [8] “Euro Chlor - The Chlorine Industry Review 2011-2012,” can be found under <http://www.eurochlor.org/download-centre/the-chlorine-industry-review.aspx>, **n.d.**
- [9] J. Pérez-Ramírez, C. Mondelli, T. Schmidt, O. F.-K. Schlueter, A. Wolf, L. Mleczko, T. Dreier, *Energy Environ. Sci.* **2011**, *4*, 4786–4799.
- [10] *Additives for Polymers* **2009**, 2009, 10–11.
- [11] H. Deacon, *Improvement in Manufacture of Chlorine*, **1875**, U.S. Patent 165802.
- [12] J. Eidern, L. Lunevall, *Extended Abstracts of Industrial Electrolytic Division*, The Chlorine Institute, San Francisco, **1974**.
- [13] H. B. Beer, *Improvements in or Relating to Electodes for Electrolysis*, **1965**, U.S. Patent GB1147442.
- [14] H. B. Beer, *Improvements in or Relating to the Manufacture of Electrodes.*, **1967**, U.S. Patent GB1195871.
- [15] K. Iwanaga, K. Seki, T. Hibi, K. Issoh, T. Suzuta, M. Nakada, Y. Mori, T. Abe, *Sumitomo Kagaku* **2004**, *1*, 1–11.
- [16] A. Wolf, L. Mleczko, O. Schlueter, S. Schubert, *Method for Producing Chlorine by Gas Phase Oxidation*, **2007**, U.S. Patent WO2007134772 (A1).
- [17] A. Wolf, L. Mleczko, S. Schubert, O. F. Schluter, *Processes and Apparatus for the Production of Chlorine by Gas Phase Oxidation*, **2007**, U.S. Patent US2007274901 (A1).
- [18] A. Wolf, J. Kintrup, O. F. Schluter, L. Mleczko, *Processes for the Preparation of Chlorine by Gas Phase Oxidation*, **2007**, U.S. Patent US2007292336 (A1).
- [19] F. Gestermann, A. Ottaviani, *Modern Chlor-Alkali Technology*, Wiley-Blackwell, **2001**.
- [20] J. Cook, *Anode for Electrolytic Processes*, **1975**, U.S. Patent US3882002 (A).
- [21] C. J. H., *Anode for Electrolytic Processes*, **1976**, U.S. Patent DE2532553 (A1) Abstract of corresponding document: US3882002 (A).
- [22] L. K. O., *Partial Replacement of Ruthenium with Tin in Electrode Coatings*, **1973**, U.S. Patent US3776834 (A).
- [23] V. V. Panic, B. Z. Nikolic, *Journal of the Serbian Chemical Society* **2008**, *73*, 1083–1112.
- [24] V. Panic, A. Dekanski, V. B. Miskovic-Stankovic, S. Milonjic, B. Nikolic, *Journal of Electroanalytical Chemistry* **2005**, *579*, 67–76.
- [25] V. V. Panic, A. Dekanski, S. K. Milonjic, R. T. Atanasoski, B. Z. Nikolic, *Colloids and Surfaces A: Physicochemical and Engineering Aspects* **1999**, *157*, 269–274.
- [26] V. Panic, A. Dekanski, S. Milonjic, R. Atanasoski, B. Nikolic, *Journal of the Serbian Chemical Society* **2000**, *65*, 649–660.
- [27] V. V. Gorodetskii, V. A. Neburchilov, *Russian journal of Electrochemistry* **2003**, *39*, 1111–1115.
- [28] S. Saito, A. KAZUHIDE, K. MAKOTO, N. AKIO, *Process for Preparing Insoluble Electrode*, **1980**.
- [29] P. Shrivastava, M. S. Moats, *J. Electrochem. Soc.* **2008**, *155*, E101–E107.

- [30] L. M. Da Silva, J. F. C. Boodts, L. A. De Faria, *Electrochimica Acta* **2001**, *46*, 1369–1375.
- [31] O. De Nora, *Chemie Ing. Techn.* **1970**, *42*, 222–226.
- [32] V. V. Gorodetskii, V. A. Neburchilov, *Russian journal of Electrochemistry* **2007**, *43*, 223–228.
- [33] V. V. Gorodetskii, V. A. Neburchilov, *Russian journal of Electrochemistry* **2003**, *39*, 1116–1123.
- [34] V. Gorodetskii, V. Neburchilov, *Russian journal of Electrochemistry* **2005**, *41*, 971–978.
- [35] V. V. Gorodetskii, V. A. Neburchilov, V. I. Alyab'eva, *Russian journal of Electrochemistry* **2005**, *41*, 1111–1117.
- [36] Z. Yi, C. Kangning, W. Wei, J. Wang, S. Lee, *Ceramics International* **2007**, *33*, 1087–1091.
- [37] L. Nanni, S. Polizzi, A. Benedetti, A. De Battisti, *J. Electrochem. Soc.* **1999**, *146*, 220–225.
- [38] J. F. C. Boodts, S. Trasatti, *J. Electrochem. Soc.* **1990**, *137*, 3784–3789.
- [39] L. Vázquez-Gómez, E. Horváth, J. Kristóf, A. De Battisti, *Thin Solid Films* **2006**, *515*, 1819–1824.
- [40] M. Ito, Y. Murakami, H. Kaji, K. Yahikozawa, Y. Takasu, *J. Electrochem. Soc.* **1996**, *143*, 32–36.
- [41] H. Y. Pan, R. G. Minet, S. W. Benson, T. T. Tsotsis, *Industrial & Engineering Chemistry Research* **1994**, *33*, 2996–3003.
- [42] V. E. Tarabanko, N. V. Tarabanko, N. V. Koropachinskaya, *Catal. Ind.* **2010**, *2*, 259–265.
- [43] C. Mondelli, A. P. Amrute, T. Schmidt, J. Pérez-Ramírez, *Chem. Commun.* **2011**, *47*, 7173–7175.
- [44] *Ullmann's Encyclopedia of Industrial Chemistry*.
- [45] A. J. Johnson, A. J. Cherniavsky, *Chlorine Production*, **1951**, U.S. Patent US2542961 (A).
- [46] W. F. Engel, F. Wattimena, *Process for the Production of Chlorine*, **1965**, U.S. Patent US3210158 (A).
- [47] F. Wattimena, W. M. H. Sachtler, in *Studies in Surface Science and Catalysis* (Ed.: T. S. Eiyama and K. Tanabe), Elsevier, **1981**, pp. 816–827.
- [48] A. Oblad, *Industrial and Engineering Chemistry* **1969**, *61*, 23–&.
- [49] H. Itoh, Y. Kono, M. Ajioka, S. Takenaka, M. Kataita, *Production Process of Chlorine*, **1989**, U.S. Patent US4803065 (A).
- [50] T. Kiyoura, Y. Kogure, T. Nagayama, K. Kanaya, *Manufacturing Process of Chlorine*, **1989**, U.S. Patent US4822589 (A) Abstract of corresponding document: EP0272332 (A1).
- [51] M. Mortensen, R. G. Minet, T. T. Tsotsis, S. Benson, *Chem. Eng. Sci.* **1996**, *51*, 2031–2039.
- [52] M. Mortensen, R. G. Minet, T. T. Tsotsis, S. W. Benson, *Chem. Eng. Sci.* **1999**, *54*, 2131–2139.
- [53] U. Nieken, O. Watzenberger, *Chem. Eng. Sci.* **1999**, *54*, 2619–2626.
- [54] M. W. M. Hisham, S. W. Benson, *J. Phys. Chem.* **1995**, *99*, 6194–6198.
- [55] J. A. Allen, *Journal of Applied Chemistry* **1962**, *12*, 406–412.
- [56] F. Studt, F. Abild-Pedersen, H. Hansen, I. Man, J. Rossmeisl, T. Bligaard, *ChemCatChem* **2010**, *2*, 98–102.
- [57] A. Toftelund, I. C. Man, H. A. Hansen, F. Abild-Pedersen, T. Bligaard, J. Rossmeisl, F. Studt, *ChemCatChem* **2012**, *4*, 1856–1861.
- [58] H. Over, R. Schomaecker, *ACS Catal.* **2013**, *3*, 1034–1046.
- [59] H. Over, *Electrochim. Acta* **2013**, *93*, 314–333.

- [60] S. Zweidinger, D. Crihan, M. Knapp, J. P. Hofmann, A. P. Seitsonen, C. J. Weststrate, E. Lundgren, J. N. Andersen, H. Over, *The Journal of Physical Chemistry C* **2008**, *112*, 9966–9969.
- [61] N. López, J. Gómez-Segura, R. P. Marín, J. Pérez-Ramírez, *Journal of Catalysis* **2008**, *255*, 29–39.
- [62] D. Crihan, M. Knapp, S. Zweidinger, E. Lundgren, C. Weststrate, J. Andersen, A. Seitsonen, H. Over, *Angewandte Chemie International Edition* **2008**, *47*, 2131–2134.
- [63] M. A. G. Hevia, A. P. Amrute, T. Schmidt, J. Pérez-Ramírez, *Journal of Catalysis* **2010**, *276*, 141–151.
- [64] K. Seki, *Catal Surv Asia* **2010**, *14*, 168–175.
- [65] J. P. Hofmann, S. Zweidinger, A. P. Seitsonen, A. Farkas, M. Knapp, O. Balmes, E. Lundgren, J. N. Andersen, H. Over, *Phys. Chem. Chem. Phys.* **2010**, *12*, 15358.
- [66] S. Zweidinger, J. P. Hofmann, O. Balmes, E. Lundgren, H. Over, *Journal of Catalysis* **2010**, *272*, 169–175.
- [67] A. P. Seitsonen, H. Over, *J. Phys. Chem. C* **2010**, *114*, 22624–22629.
- [68] A. P. Amrute, C. Mondelli, M. A. G. Hevia, J. Pérez-Ramírez, *J. Phys. Chem. C* **2011**, *115*, 1056–1063.
- [69] C. Mondelli, A. P. Amrute, F. Krumeich, T. Schmidt, J. Pérez-Ramírez, *ChemCatChem* **2011**, n/a–n/a.
- [70] D. Teschner, G. Novell-Leruth, R. Farra, A. Knop-Gericke, R. Schloegl, L. Szentmiklosi, M. Gonzalez Hevia, H. Soerijanto, R. Schomaecker, J. Perez-Ramirez, et al., *Nat. Chem.* **2012**, *4*, 739–745.
- [71] D. Teschner, R. Farra, L. Yao, R. Schlögl, H. Soerijanto, R. Schomäcker, T. Schmidt, L. Szentmiklósi, A. P. Amrute, C. Mondelli, et al., *Journal of Catalysis* **2012**, *285*, 273–284.
- [72] H. Over, *J. Phys. Chem. C* **2012**, *116*, 6779–6792.
- [73] A. P. Amrute, C. Mondelli, T. Schmidt, R. Hauert, J. Pérez-Ramírez, *ChemCatChem* **2013**, *5*, 748–756.
- [74] A. P. Amrute, C. Mondelli, M. A. G. Hevia, J. Perez-Ramirez, *ACS Catal.* **2011**, *1*, 583–590.
- [75] R. W. G. Wyckoff, *Crystal Structures*, Interscience Publ., New York, NY U.a., **1965**.
- [76] A. TROVARELLI, *Catalysis Reviews* **1996**, *38*, 439–520.
- [77] E. Aneghi, C. de Leitenburg, J. Llorca, A. Trovarelli, *Catalysis Today* **2012**, *197*, 119–126.
- [78] Q. Fu, H. Saltsburg, M. Flytzani-Stephanopoulos, *Science* **2003**, *301*, 935–938.
- [79] J. He, T. Xu, Z. Wang, Q. Zhang, W. Deng, Y. Wang, *Angewandte Chemie International Edition* **2012**, *51*, 2438–2442.
- [80] O. Pozdnyakova, D. Teschner, A. Wootsch, J. Kröhnert, H. Sauer, L. Toth, F. C. Jentoft, A. Knop-Gericke, Z. Paál, et al., *Journal of Catalysis* **2006**, *237*, 1–16.
- [81] L. Katta, G. Thrimurthulu, B. M. Reddy, M. Muhler, W. Gruenert, *Catal. Sci. Technol.* **2011**, *1*, 1645–1652.
- [82] B. M. Reddy, P. Bharali, P. Saikia, A. Khan, S. Loridant, M. Muhler, W. Grünert, *J. Phys. Chem. C* **2007**, *111*, 1878–1881.
- [83] A. P. Amrute, C. Mondelli, M. Moser, G. Novell-Leruth, N. Lopez, D. Rosenthal, R. Farra, M. E. Schuster, D. Teschner, T. Schmidt, et al., *J. Catal.* **2012**, *286*, 287–297.
- [84] R. Farra, F. Girgsdies, W. Frandsen, M. Hashagen, R. Schlögl, D. Teschner, *Catal Lett*, in press
- [85] R. Farra, S. Wrabetz, M. E. Schuster, E. Stotz, N. G. Hamilton, A. P. Amrute, J. Pérez-Ramírez, N. López, D. Teschner, *Phys. Chem. Chem. Phys.* **2013**, *15*, 3454–3465.
- [86] R. Farra, M. Eichelbaum, R. Schloegl, L. Szentmiklosi, T. Schmidt, A. P. Amrute, C. Mondelli, J. Perez-Ramirez, D. Teschner, *J. Catal.* **2013**, *297*, 119–127.
- [87] R. Farra, M. García-Melchor, M. Eichelbaum, M. Hashagen, W. Frandsen, J. Allan, F. Girgsdies, L. Szentmiklósi, N. López, D. Teschner, *ACS Catal.* **2013**, 2256–2268.

Chapter 2: Performance, structure, and mechanism of CeO₂ in HCl oxidation to Cl₂

Amol P. Amrute, Cecilia Mondelli, Maximilian Moser, Gerard Novell-Leruth, Núria López, Dirk Rosenthal, Ramzi Farra, Manfred E. Schuster, Detre Teschner, Timm Schmidt, Javier Pérez-Ramírez

Abstract

Experimental and theoretical studies reveal performance descriptors and provide molecular-level understanding of HCl oxidation over CeO₂. Steady-state kinetics and characterization indicate that CeO₂ attains a significant activity level, which is associated with the presence of oxygen vacancies. Calcination of CeO₂ at 1173 K prior to reaction maximizes both the number of vacancies and the structural stability of the catalyst. X-ray diffraction and electron microscopy of samples exposed to reaction feeds with different O₂:HCl ratios provide evidence that CeO₂ does not suffer from bulk chlorination in O₂-rich feeds (O₂:HCl ≥ 0.75), while it does form chlorinated phases in stoichiometric or sub-stoichiometric feeds (O₂:HCl ≤ 0.25). Quantitative analysis of the chlorine uptake by thermogravimetry and X-ray photoelectron spectroscopy indicates that chlorination under O₂-rich conditions is limited to few surface and subsurface layers of CeO₂ particles, in line with the high energy computed for the transfer of Cl from surface to subsurface positions. Exposure of chlorinated samples to a Deacon mixture with excess oxygen rapidly restores the original activity levels, highlighting the dynamic response of CeO₂ outermost layers to feeds of different composition. Density functional theory simulations reveal that Cl activation from vacancy positions to surface Ce atoms is the most energy-demanding step, although chlorine-oxygen competition for the available active sites may render re-oxidation as the rate-determining step. The substantial and remarkably stable Cl₂ production and the lower cost of CeO₂ make it an attractive alternative to RuO₂ for catalytic chlorine recycling in industry.

Acknowledgements

We thank Bayer MaterialScience for permission to publish these results.

2.1 Introduction

The heterogeneously catalyzed gas-phase oxidation of HCl to Cl₂ (Eq. (2.1)) is a sustainable route to recycle chlorine from by-product HCl streams derived from the manufacture of polyurethanes and polycarbonates with low energy input [1,2]. The amount of waste HCl raises due to the growing demand for these versatile plastics. As selling the HCl excess is unfeasible, and the neutralization option is unattractive, its catalytic conversion to Cl₂ is receiving an increasing interest.



Since its introduction and till recent times, the industrialization of HCl oxidation has suffered from many failed attempts to obtain sufficiently active and durable catalysts. The CuCl₂/pumice catalyst patented by Henry Deacon in 1868 [3] exhibited fast deactivation due to volatilization of the active phase in the form of copper chlorides. Other examples of processes of limited success are the Shell-Chlor process (based on CuCl₂-KCl/SiO₂) [4] and the Mitsui-Toatsu process (based on Cr₂O₃/SiO₂) [5]. Only recently, ruthenium supported on specific carriers was successfully developed for large-scale chlorine recycling [1]. In particular, Sumitomo has applied RuO₂/SiO₂/TiO₂-rutile in a plant producing 100 kton Cl₂ per year [2,6], while Bayer's RuO₂/SnO₂-Al₂O₃ catalyst has been piloted and is ready for industrial use [7,8]. The distinctive features of RuO₂-based catalysts are the high activity at low temperature and the remarkable stability against bulk chlorination [9-11].

The implementation of the catalytic HCl oxidation technology would expand if cheaper, but comparably stable, alternatives to RuO₂-based catalysts were developed. The high and fluctuating market price of ruthenium indeed reflects the large costs for new plants [12]. These considerations have constituted the driving force to search for alternative cost-effective catalytic materials. A first step in this direction is the recent design of a copper delafossite (CuAlO₂) catalyst, which exhibited stable performance for more than 1200 h on stream [13]. However, this catalyst experienced significant copper loss.

CeO₂ (fluorite structure [14]) attracted our interest in view of its wide use in redox processes in many research fields [15-21], and oxidation reactions in particular [22-26]. In oxidations, it has been employed both as catalyst and co-catalyst. The success of CeO₂ stems from the easy generation of oxygen vacancies [22,27,28] that facilitate activation and transport of oxygen species. Nevertheless, only a few works have derived quantitative correlations between its oxidation activity and this structural peculiarity, typically measured in terms of oxygen storage capacity (OSC). Furthermore, comparisons have been preferably reported between CeO₂ and solid solutions of CeO₂ with ZrO₂ or SiO₂ [29], or between ceria-containing catalysts including supported (active) metal phases [30].

CeO₂-based materials have been claimed in the patent literature as catalysts potentially suited for HCl oxidation [31-33]. However, there are no studies gathering a fundamental understanding of the Deacon chemistry on CeO₂. Only the detailed assessment of CeO₂ activity and stability will determine its potential as an alternative to RuO₂-based catalysts for chlorine recycling.

Herein we report on the use of CeO₂ in HCl oxidation, as well as on the fundamental knowledge derived by means of a multi-technique approach. Performance-structure-mechanism relationships are established, collecting information from extensive kinetic tests in a flow reactor at ambient pressure, detailed characterization (in relation to the catalyst activation procedure and the operating conditions), and mechanistic investigations using *in situ* infrared spectroscopy and density functional theory calculations.

2.2 Experimental

2.2.1 Catalysts

CeO₂ (Aldrich, nanopowder, code 544841) was calcined in static air at various temperatures in the range of 573-1373 K using a heating rate of 10 K min⁻¹ and a dwell time of 5 h prior to use.

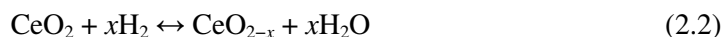
These samples are referred to as “fresh”. A complete list of all sample-codes used along the manuscript, together with their description, is reported in Table 2.1.

Table 2.1 Description of catalysts’ codes.

<i>Catalyst code</i>	<i>Calcination temperature (K)</i>	<i>Catalyst state (-)</i>	<i>Feed O₂:HCl ratio (mol mol⁻¹)</i>
CeO ₂ -573-F	573	fresh	-
CeO ₂ -773-F	773	fresh	-
CeO ₂ -1023-F	1023	fresh	-
CeO ₂ -1173-F	1173	fresh	-
CeO ₂ -1273-F	1273	fresh	-
CeO ₂ -1373-F	1373	fresh	-
CeO ₂ -573-2	573	used	2
CeO ₂ -773-2	773	used	2
CeO ₂ -1023-2	1023	used	2
CeO ₂ -1173-2	1173	used	2
CeO ₂ -1273-2	1273	used	2
CeO ₂ -1373-2	1373	used	2
CeO ₂ -773-0	773	used	0
CeO ₂ -1173-0	1173	used	0
CeO ₂ -1173-0.25	1173	used	0.25
CeO ₂ -1173-0.75	1173	used	0.75
CeO ₂ -1173-0.25-2	1173	used	0.25 followed by 2
CeO ₂ -1173-0.25-7	1173	used	0.25 followed by 7
CeO ₂ -1173-0-7	1173	used	0 followed by 7

2.2.2 Characterization

All the samples were subjected to basic characterization prior to and after catalytic testing. More extensive characterization was performed on CeO₂-773 and CeO₂-1173. In particular, fresh samples of these two catalysts were compared to samples exposed to reaction mixtures with feed O₂:HCl ratios equal to 2, 0.75, 0.25, or 0 (see Section 2.2.3 for detailed testing conditions). Standard characterization of the samples was performed by powder X-ray diffraction (XRD), nitrogen adsorption at 77 K, and temperature-programmed reduction with hydrogen (H₂-TPR). The oxygen storage capacity (OSC) was measured by estimating the H₂ uptake of the samples (after a similar pre-treatment in inert gas as prior to the catalytic evaluation), as this represents an indirect quantification of the oxygen that the samples can store (Eq. (2.2)) [34-36].



This method was chosen among others reported in the literature [37], as the straightforward approach of determining the OSC by pulse chemisorption of oxygen [38] did not provide reproducible results on our samples. In order to select the appropriate temperature (573 K), at which the OSC would be evaluated in relation to a few outermost surface layers of CeO₂, the H₂ uptake was first separately measured at various temperatures (523-873 K), defined on the basis of the H₂-TPR profiles (Figs. S 2.1-S 2.2 in the SI). The degree of bulk chlorination of selected catalysts after HCl oxidation was determined by thermogravimetric analysis coupled to mass spectrometry (TGA-MS). The structure, morphology, and composition of the catalyst particles were studied by high-resolution transmission electron microscopy (HRTEM). X-ray photoelectron spectroscopy (XPS) was applied to determine the degree of chlorination of the used CeO₂ catalysts. Three different layer models were employed to calculate the number of layers in CeO₂ that experienced chlorination. The first model was based on the inelastic mean free path (IMFP) and on 100% Cl occupation, the second on 80% of IMFP for practical effective attenuation length (EAL) and on 100% Cl occupation, and the third 80% of IMFP for

practical EAL and on 75% Cl occupation. For details on the characterization techniques, the reader is referred to the supporting information (SI).

2.2.3 Catalytic tests

The oxidation of HCl with O₂ was carried out at ambient pressure in a quartz fixed-bed micro-reactor (8 mm i.d.) using 0.5 g of catalyst (particle size = 0.4-0.6 mm), a total flow of 166 cm³ STP min⁻¹, a bed temperature (T_{bed}) of 703 K, and reaction times up to 3 h. The catalyst was kept at 703 K for 30 min in N₂ flow before admitting a mixture containing 10 vol.% HCl (Messer, purity 2.8, anhydrous) and 20 vol.% O₂ (Pan Gas, purity 5.0), balanced in N₂ (Pan Gas, purity 5.0).

Steady-state kinetic studies were performed on CeO₂-1173-F. First of all, it was experimentally verified that, under our experimental conditions, the reaction was not limited by extra- and/or intra-particle diffusion limitations. For this purpose, we varied (i) the total flow rate (83-250 cm³ STP min⁻¹) at constant space time ($W/F^0(\text{HCl}) = 11.2 \text{ g h mol}^{-1}$, defined as the ratio of the catalyst mass to the inlet molar flow of HCl) and (ii) the particle size (0.075-0.6 mm) with other conditions constant, respectively (Fig. S 2.3 in the SI). The kinetic experiments included changes of the feed composition at different temperatures and space times. In particular, the feed O₂:HCl ratio was varied in the range of 0.5-7 at constant feed HCl concentration (10 vol.%) and in the range 0.25-2 at constant feed O₂ concentration (10 vol.%) at $T_{\text{bed}} = 603, 653, \text{ and } 703 \text{ K}$ and space times of 5.6, 9, and 11.2 g h mol⁻¹. CeO₂-1173-F samples exposed to O₂:HCl = 0, 0.25, or 0.75, and CeO₂-773-F treated in O₂:HCl = 0 (only HCl) at 703 K for 3 h were collected for characterization, after switching the feed to N₂ and allowing the reactor to cool down. In addition, experiments were carried out at 703 K combining a HCl-rich step, in which the catalyst was exposed to a feed composition O₂:HCl = 0 or 0.25 (causing bulk chlorination), and a O₂-rich step, in which substantial oxygen excess was supplied (O₂:HCl = 2 or 7). Cl₂ quantification at the reactor outlet was carried out by iodometric titration in a Mettler Toledo G20 Compact Titrator, using the protocol reported elsewhere [39]. HCl conversion was determined from the Cl₂ produced, taking into account the reaction stoichiometry.

2.2.4 *In situ* Fourier transform infrared spectroscopy

A home-made transmission cell, especially designed to withstand the corrosive HCl oxidation mixture, was used for *in situ* Fourier transform infrared (FTIR) spectroscopy measurements. The sample in powder form was pressed into a self-supporting disc (15 mg cm⁻²) under 30 bar for 10 s. The wafer, having a thickness of 50 μm, was placed in the sample holder, which also serves as the heating system. Inlet gases were analytical grade and controlled by mass flow controllers. The sample was heated in 20 vol.% O₂ in N₂ (100 cm³ STP min⁻¹) up to 653 K (5 K min⁻¹), and allowed to stabilize. After ca. 1 h, 1 vol.% HCl was introduced into the O₂/N₂ flow to mimic a diluted Deacon feed condition. Spectra were recorded with a Varian-670 FTIR spectrometer at 653 K and with 4 cm⁻¹ resolution.

2.2.5 Computational details

Density functional theory (DFT) simulations were applied to CeO₂ slabs. The calculations were performed with the 5.2 version of the VASP code [40]. The functional of choice was a GGA+U scheme to account in an approximate way for the complexity arising from the presence of *f*-electrons in cerium. The GGA was PBE [41], the U parameter chosen was set to 4.5 [42,43], and the inner electrons were replaced by PAW pseudopotentials [44]. The 12 valence electrons of Ce atoms in the 5*s*, 5*p*, 6*s*, 4*f*, and 5*d* states and the 6 valence electrons of O atoms in the 2*s*, and 2*p* states were considered explicitly. The valence electrons were expanded in plane waves with a cutoff energy of 400 eV. For the bulk, the k-point sampling was 9×9×9 [45]. The cell parameter obtained was 5.486 Å, in good agreement with experimental results and previous calculations [42,43]. The (111) facet was selected as it is known to be the lowest energy surface

[43]. The chosen slab corresponds to a $p(2\times 2)$ reconstruction and contains three layers. The k-point sampling was set to $3\times 3\times 1$ in this case. The calculated surface energy for this structure was 0.013 eV \AA^{-2} . For this surface, several vacancy structures were considered and benchmarked against more accurate calculations in the literature employing hybrid methods [43]. When forming a vacancy or adsorbing on this surface, the systems were allowed to relax in all directions, except for the last layer of the slab. In all cases, the slabs were interleaved by 10 \AA and decoupled from electronic interactions due to spurious polarizations given the asymmetry of the adsorption configuration. Spin-polarized calculations were performed when required. The CI-NEB method [46] was employed to locate the transition states, and the vibrational analysis of the potential transition state structures was performed to fully characterize the saddle points. In the calculation of vibrational frequencies, only the adsorbed structures of intermediates or transition states were considered. The numerical Hessian was calculated with two steps of 0.02 \AA for each degree of freedom and then diagonalized to obtain the corresponding eigenvalues and eigenmodes.

2.3 Results and discussion

2.3.1 Catalytic evaluation

2.3.1.1 Influence of calcination temperature on activity

CeO₂ samples calcined at different temperatures were tested in the gas-phase catalytic oxidation of HCl in a continuous-flow fixed-bed reactor operated at ambient pressure and under isothermal conditions. XRD analysis showed that the fresh samples exhibited the characteristic reflections of cerium (IV) oxide. The HCl conversion over the samples ranged from 2% to 29% (Table 2.2), remaining essentially constant in the course of the 3-h test. Interestingly, the CeO₂ samples calcined at temperatures between 573 K and 1173 K were similarly active, achieving the highest conversion levels, while higher calcination temperatures led to a progressive and almost complete depletion of the activity. These findings have been related to changes in the textural and structural properties of the materials and are first discussed on the basis of N₂ adsorption results. For the fresh catalysts, higher calcination temperatures led to lower total surface area (S_{BET}) values (Table 2.2). This result is expected, as higher temperatures favor sintering of the particles. The dependence of the HCl conversion on the S_{BET} of the fresh samples is shown in Fig. 2.1a (open symbols). For S_{BET} values $> 25\text{ m}^2\text{ g}^{-1}$ (i.e. calcination temperature below 1173 K), the activity is independent of the S_{BET} , while for S_{BET} values $< 25\text{ m}^2\text{ g}^{-1}$ (i.e. calcination temperature above 1173 K), it strongly depends on the surface area. In particular, CeO₂-1273-F ($S_{\text{BET}} = 12\text{ m}^2\text{ g}^{-1}$) and CeO₂-1373-F ($S_{\text{BET}} = 1\text{ m}^2\text{ g}^{-1}$) respectively exhibited 14% and 2% HCl conversion, i.e. 2 and ca. 15 times lower activity than the other catalysts. Exposure of the catalysts to reaction conditions generally led to a drop in S_{BET} (Table 2.2). The change is significant for CeO₂-573-2, CeO₂-773-2, and CeO₂-1023-2, and evidences that substantial sintering of the CeO₂ particles occurred during HCl oxidation. In contrast, the S_{BET} values of CeO₂-1173-2, CeO₂-1273-2, and CeO₂-1373-2 were hardly affected, indicating that calcination at or above 1173 K resulted in stabilized materials in HCl oxidation. Calcination of the starting CeO₂ nanopowder at 1173 K provides the best compromise between performance and stability against sintering. Generally, the slope-plateau relation used to depict the dependence of activity on the S_{BET} of fresh samples turned out to be a good description for the used catalysts too (Fig. 2.1a, solid symbols). An experiment showing practically constant HCl conversion over CeO₂-773-F in contrast to a strongly decreasing S_{BET} with time-on-stream further supports the observed independence of the activity on S_{BET} for values of the latter greater than $25\text{ m}^2\text{ g}^{-1}$ (Fig. S 2.4 in the SI). It was accordingly concluded that another descriptor is needed to rationalize the HCl oxidation activity of CeO₂.

Table 2.2 Characterization and catalytic activity data.

<i>Catalyst</i>	S_{BET}^a ($\text{m}^2 \text{g}^{-1}$)		X_{HCl}^b (%)	OSC^c ($\mu\text{g O g}_{\text{cat}}^{-1}$)
	<i>fresh</i>	<i>used</i>		
CeO ₂ -573	117	46	29	-
CeO ₂ -773	106	27	25	390
CeO ₂ -1023	53	39	25	382
CeO ₂ -1173	30	25	27	376
CeO ₂ -1273	12	11	14	237
CeO ₂ -1373	1	1	2.1	78

^a Total surface area, BET method.

^b HCl conversion at O₂:HCl = 2, $T_{\text{bed}} = 703 \text{ K}$, $P = 1 \text{ bar}$, $W/F^0(\text{HCl}) = 11.2 \text{ g h mol}^{-1}$.

^c Oxygen storage capacity measured at 573 K.

As mentioned in the introduction, the successful application of CeO₂-based materials in (electro) catalysis has been related to its capability to generate oxygen vacancies in the lattice [19,27]. Therefore, our CeO₂ samples were measured to assess their oxygen storage capacities (OSC), according to a method reported elsewhere [34]. On the basis of the values obtained (Table 2.2), the dependence of HCl conversion on OSC followed a linear trend (Fig. 2.1b). For CeO₂-773-F, CeO₂-1023-F, and CeO₂-1173-F, i.e. samples showing the highest (and similar) activity, the OSC was estimated at ca. 390 $\mu\text{g O g}_{\text{cat}}^{-1}$. For CeO₂-1273-F and CeO₂-1373-F, which exhibit decreasing HCl conversion levels, diminishing OSC values were measured, respectively equal to 237 and 78 $\mu\text{g O g}_{\text{cat}}^{-1}$. Based on these results, the OSC proved to be a suitable parameter to rationalize the activity differences. Nevertheless, an influence of S_{BET} on OSC and/or a combined role of OSC and S_{BET} , when the latter is below 20 $\text{m}^2 \text{g}^{-1}$, on the catalytic activity could be considered. In this regard, Terribile et al. [47] showed that OSC, as measured for the bulk, was independent of S_{BET} . The outcome of this study might not be directly applicable to our case, in which OSC has to be considered limitedly to the outermost surface and subsurface layers of CeO₂, where the catalytic process takes place (vide infra). More generally, the OSC could be described as $\text{OSC} = S_{\text{BET}} \times \rho$, where ρ corresponds to the density of surface or near-surface oxygen vacancies. At higher temperatures, the Gibbs energy for vacancy formation decreases (see DFT results), thus favoring an increased generation of vacancies in the corresponding equilibrium conditions, but S_{BET} drops. This explains why a larger OSC, i.e. more active CeO₂, is found for samples calcined at 573-1173 K.

The activity of CeO₂ is significantly lower than that of RuO₂. A 40 K higher light-off temperature for Cl₂ evolution was determined over CeO₂-1173 by temperature-programmed reaction according to the protocol described in [39]. In view of a practical use, high-temperature operation is detrimental due to thermodynamic constraints that limit the equilibrium HCl conversion [48]. Nevertheless, these restrictions can be overcome by employing higher pressures and inlet O₂:HCl ratios, so that the degree of HCl conversion achieved still makes the development of a technical process feasible. Profiles of equilibrium HCl conversion at different total pressures and O₂:HCl ratios have been included in the SI (Fig. S 2.5a). Our experiments and calculations (vide infra) conclude that oxygen vacancies determine the activity of CeO₂ in HCl oxidation. More active ceria-based catalysts may be obtained enhancing its oxygen storage capacity, e.g. by the addition of dopants. However, this aspect was beyond the scope of the present manuscript.

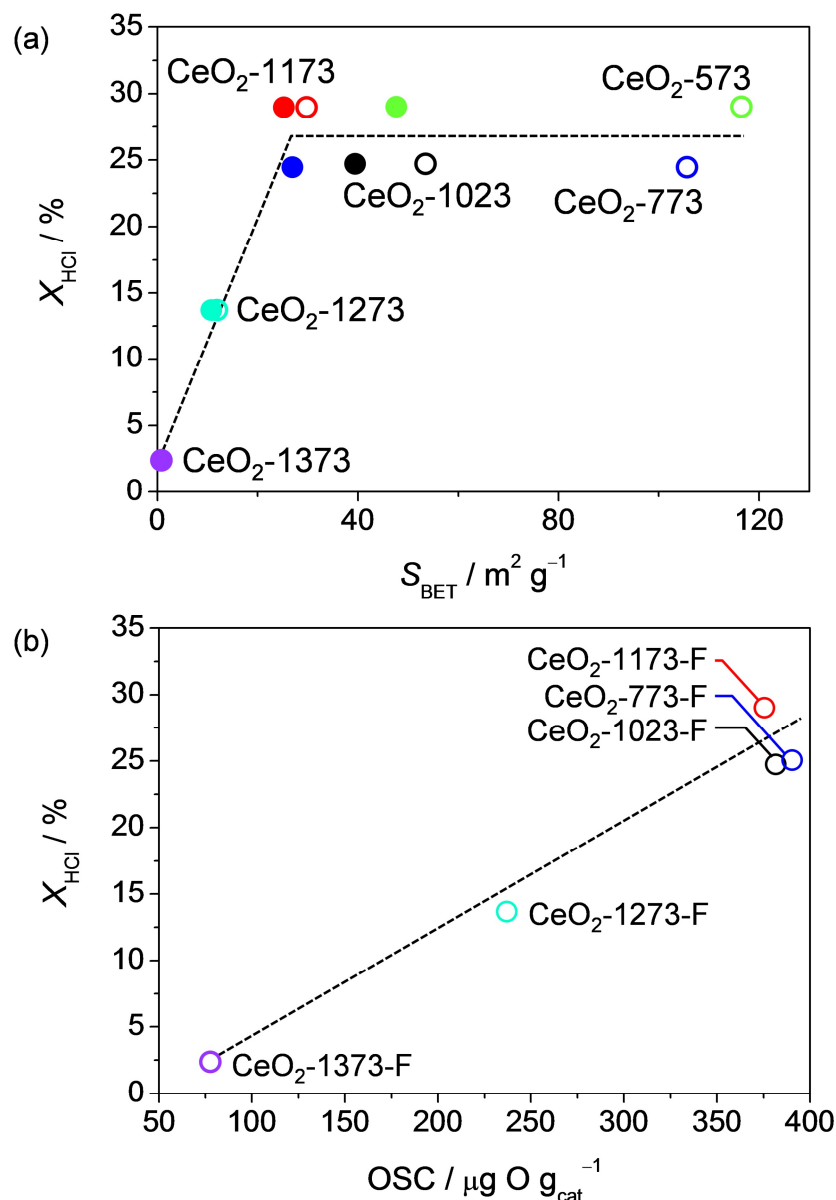


Figure 2.1 HCl conversion *versus* (a) surface area of fresh (open symbols) and used (solid symbols) CeO₂ samples and (b) OSC, measured at 573 K, of fresh CeO₂ samples. Conditions: inlet mixture of 10 vol.% HCl and 20 vol.% O₂ balanced in N₂, $T_{\text{bed}} = 703 \text{ K}$, $\text{W/F}^0(\text{HCl}) = 11.2 \text{ g h mol}^{-1}$, $P = 1 \text{ bar}$, and time-on-stream = 3 h.

2.3.1.2 Kinetic analysis

The influence of the O₂:HCl ratio on the activity was examined over CeO₂-1173-F at 703 K (Fig. 2.2). The HCl conversion increased upon raising the relative O₂ content in the feed mixture. The reaction order on O₂, calculated using a power equation fitting, was 0.5. This result suggests that oxygen-assisted chlorine evolution (re-oxidation) is the rate-limiting step, hence favored at a higher partial O₂ pressure. This point is further discussed in Section 2.3.4.3. Remarkably, the HCl conversion profiles derived from measurements in which the feed O₂ content was step-wise changed so to vary the O₂:HCl ratio from the lowest (0.5-7, Fig.2.2, black symbols) or from the highest (7-0.5, Fig 2.2, gray symbols) value evidence very little hysteresis (Fig. 2.2). This outcome indicates that the catalyst reversibly responds to variations of the feed mixture, and highlights the dynamic character of the CeO₂ surface. The HCl conversion increased upon raising the space time for different feed O₂:HCl ratios (Fig. S 2.6 in the SI). On

the contrary, the Cl₂ production decreased upon increasing the relative feed HCl content (Fig. S 2.7 in the SI), thus suggesting a change in the catalyst composition at the (near-) surface level (later addressed by characterization) that leads to activity loss. With regard to the dependency of CeO₂ activity on the reaction temperature, the HCl conversion level varied from 1% to 18% between 603 and 703 K at O₂:HCl = 2. The apparent activation energy was estimated at ca. 90 kJ mol⁻¹. In addition, a catalytic test using a feed mixture with O₂:HCl = 5 and an increased space time (at the limit of our current setup) was conducted. Fig. S 2.5b in the SI shows that a significant single-pass HCl conversion of 40% was reached over CeO₂ at 673 K and 1 bar.

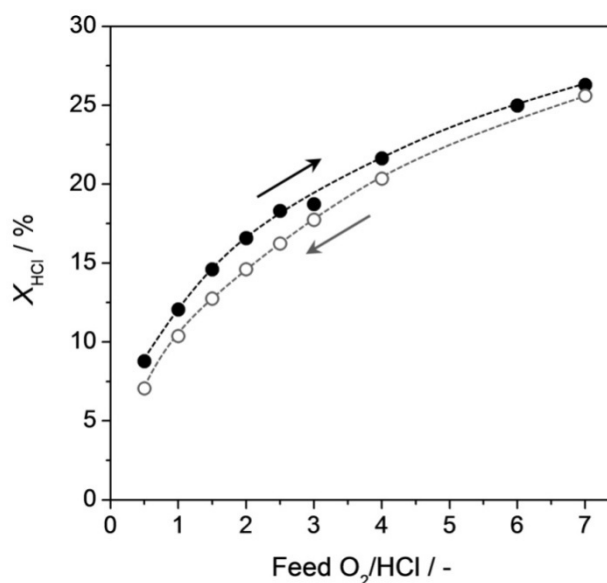


Figure 2.2 HCl conversion *versus* feed O₂:HCl ratio at 703 K for CeO₂-1173-F. Conditions: inlet mixture of 10 vol.% HCl and 5-70 vol.% O₂ balanced in N₂, $T_{\text{bed}} = 703$ K, $W/F^0(\text{HCl}) = 11.2$ g h mol⁻¹, and $P = 1$ bar.

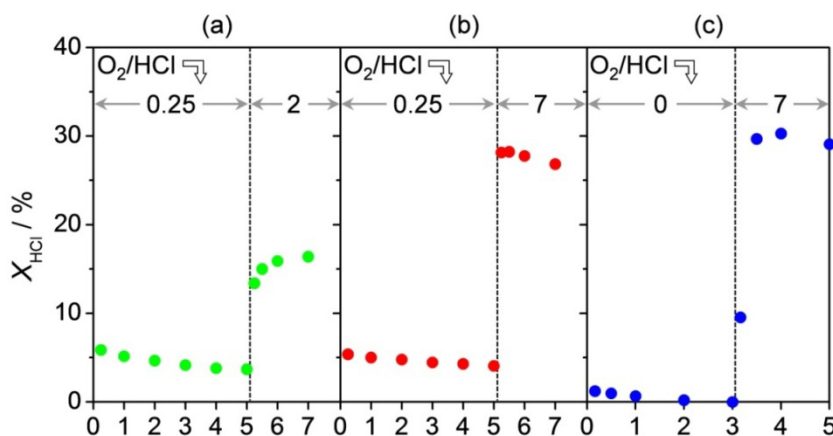


Figure 2.3 HCl conversion *versus* time-on-stream over CeO₂-1173 using sequential HCl-rich/O₂-rich feed mixtures. (a) HCl-rich step with O₂:HCl = 0.25 followed by O₂-rich step with O₂:HCl = 2. (b) HCl-rich step with O₂:HCl = 0.25 followed by O₂-rich step with O₂:HCl = 7. (c) HCl-rich step with O₂:HCl = 0 followed by O₂-rich step with O₂:HCl = 7. Other conditions: $T_{\text{bed}} = 703$ K, $W/F^0(\text{HCl}) = 11.2$ g h mol⁻¹, and $P = 1$ bar.

As operation in industry would be more economic lowering the inlet partial pressure of O₂ down to the stoichiometric amount (O₂:HCl = 0.25), we have investigated to which extent a stoichiometric or excess amount of HCl can negatively impact the catalytic activity. Some effort

was also made to explore whether activity recovery is possible and to determine the re-oxidation kinetics. Fig. 2.3 displays the HCl conversion profiles obtained for CeO₂-1173-F in sequential HCl-rich/O₂-rich experiments.

The HCl-rich step was conducted at 703 K using O₂:HCl = 0 or 0.25 for 3 or 5 h, followed by the O₂-rich step using O₂:HCl = 2 or 7 for 2 h. As shown in Fig. 2.3a, a slight decrease in HCl conversion was observed when the reaction was carried out with O₂:HCl = 0.25. Upon increasing the O₂ content in the feed (O₂:HCl = 2), a gradual increase in activity was obtained. The HCl conversion expected for an O₂:HCl = 2 feed composition (ca. 17%, Fig. 2.2) was approached in 2 h (Fig. 2.3a). In view of the slow re-oxidation kinetics, the experiment was repeated at a higher O₂:HCl ratio for the O₂-rich step. Using O₂:HCl = 7, the HCl conversion level immediately rose (Fig. 2.3b) to the expected value (ca. 27%, Fig. 2.2). When repeating this two-step experiment with the HCl-rich phase at O₂:HCl = 0 and the O₂-rich at O₂:HCl = 7, a similar profile was obtained (Fig. 2.3c). The data show that upon treating the catalyst with HCl in the absence of gas-phase O₂, the HCl conversion was completely depleted due to excessive chlorination (*vide infra*). Nevertheless, upon switching to O₂:HCl = 7, the original activity was fully restored within 1 h.

2.3.2 Characterization

2.3.2.1 X-ray diffraction and thermogravimetry

In order to relate the activity loss in HCl-rich feeds to modifications of the catalyst structure and/or composition, CeO₂-1173-F samples treated at 703 K for 3 h using various O₂:HCl feed ratios were analyzed by XRD (Fig. 2.4). The diffractogram of CeO₂-773-HCl is also included for comparison purposes. For the samples exposed to O₂:HCl = 0 or 0.25, CeCl₃·6H₂O (JCPDS 01-0149) reflections were detected, thus pointing to bulk chlorination as the main cause for the observed catalyst deactivation. From the intensity of the cerium chloride reflections, the samples could be sequenced according to the extent of bulk chlorination as follows: CeO₂-773-0 > CeO₂-1173-0 > CeO₂-1173-0.25. The fact that CeO₂-1173-0 was less altered than CeO₂-773-0 is probably related to the better stabilization achieved by high-temperature calcination, thus not only rendering lower sintering upon use, but also a higher resistance against chlorination. The presence of stoichiometric amounts of O₂ did not fully prevent structural alterations, but the degree of chlorination was smaller than for O₂-free runs. Samples treated in O₂:HCl = 0.75 or 2 did not suffer from detectable bulk chlorination. Accordingly, the choice of O₂:HCl feed ratio is of great importance, and should be equal or higher than 0.75 to avoid activity deterioration of CeO₂-based catalysts. The inhibiting effect of excess HCl on the conversion (Fig. S 2.7 in the SI) can be also related to bulk chlorination. Deactivation does not appear to be induced by the volatilization of the active phase in form of the metal chlorides produced *in situ*, as in the case of copper-based catalysts [13,39]. Analysis of the condensate at the reactor outlet by ICP-OES did not show appreciable cerium loss. On the basis of the result of the catalytic test on CeCl₃ (HCl conversion = 2%, at 703 K and O₂:HCl = 2), the activity loss is assigned to the inactivity of cerium chloride for HCl oxidation.

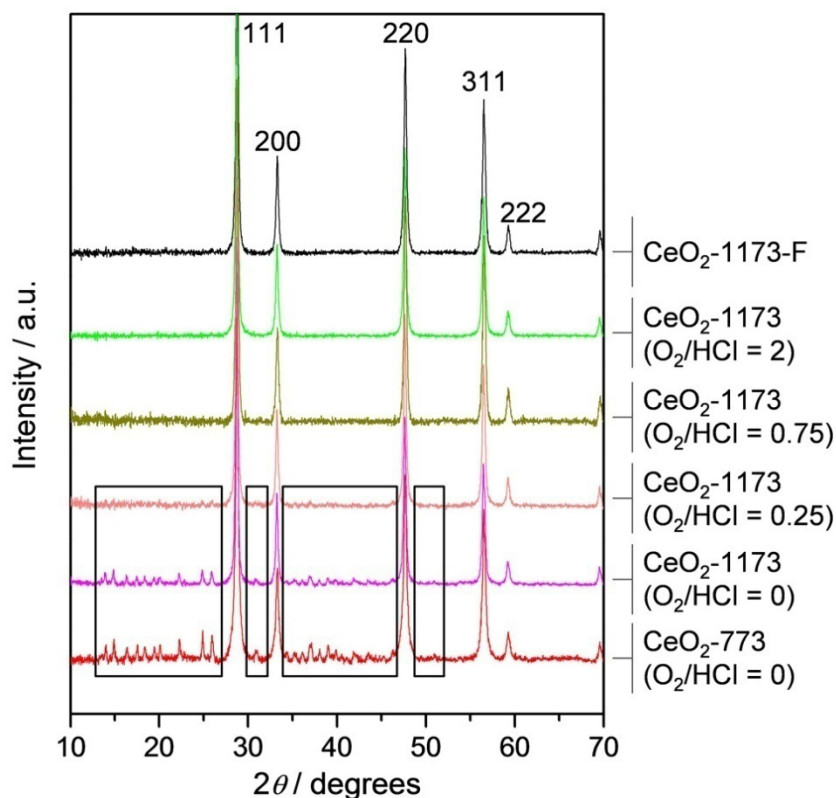


Figure 2.4 XRD patterns of CeO₂-1173 samples in fresh and used (at various O₂:HCl ratios) forms. The diffractogram of CeO₂-773-0 is included for comparison. The most intense reflections are due to CeO₂ (JCPDS 73-6328), while those within boxes belong to CeCl₃·6H₂O (JCPDS 01-0149).

XRD analysis of the samples exposed to the HCl-rich/O₂-rich mixtures (Fig. S 2.8 in the SI) evidenced that activity recovery was indeed induced by the removal of chlorine at higher partial pressures of O₂. In the case of the samples treated with O₂:HCl = 7, the original CeO₂ phase was restored, while traces of CeCl₃·6H₂O were still observed for the sample exposed to a lower oxygen excess (O₂:HCl = 2). These evidences are in line with the activity pattern described above.

Quantification of the chlorination degree was estimated by TGA-MS studies of the used catalysts. The weight loss and MS profiles as a function of the temperature are reported in Fig. S 2.9 in the SI. According to these data, the values for molar Cl/Ce ratio were 0.38, 0.30, and 0.08 for CeO₂-773-0, CeO₂-1173-0, and CeO₂-1173-0.25, respectively. These results support the trend qualitatively derived by XRD.

In contrast to the extensive bulk alteration reported for CuO and MnO₂ already upon exposure to an O₂-rich feed (O₂:HCl = 2) [39,49], chlorination of CeO₂ occurs only under stoichiometric feed conditions or in excess HCl and to a very limited extent. Consequently, the behavior of CeO₂ resembles more that of RuO₂, and this is directly related to the high stability of the latter two oxides in the Deacon reaction.

2.3.2.2 High-resolution transmission electron microscopy

TEM micrographs of CeO₂-773-F reveal a bimodal particle size distribution (Fig. 2.5a). Small CeO₂ particles of approximately 10 nm are scattered around larger particles reaching up to 300 nm. Exposure to O₂:HCl = 2 induced a significant change in particle size (CeO₂-773-2), which attained a range of 20-40 nm (Fig. 2.5b). Under Deacon conditions, the smaller particles agglomerated and the bigger particles “cracked”, thus not being detectable in the used sample. While sintering is expected to occur upon use, the latter phenomenon is tentatively explained on

the basis of a different activity/stability of the crystal facets, where one (or more) might be unstable under reaction conditions. It cannot be excluded that the mechanical strain applied in the pressing step during preparation of the sieve fraction may be the origin of the disruption of the bigger grains. Nevertheless, the significantly reduced S_{BET} of CeO₂-773-2 implies that the loss in surface area determined by the agglomeration of the small particles clearly surpasses the increase due to the breaking up of few big grains. High-resolution imaging of the surface of CeO₂ nanoparticles after exposure to Deacon conditions shows clean surfaces exhibiting several steps (Fig. 2.5d). The analysis of CeO₂-773-0 reveals some clear changes due to the treatment in HCl only. While the size of the nanoparticles does not seem to differ significantly from CeO₂-773-2 (Fig. 2.5c), the treatment had a considerable effect on the particle structure. Besides rounded nanoparticles of CeO₂-773-0 (Fig. 2.5e), revealing numerous “clean” atomic steps on the surface (magnified in the inset of Fig. 2.5e), nanoparticles covered with an amorphous layer are now evidenced (Fig. 2.5f). SAED (selected area electron diffraction) analysis of such particles suggests that the structure can fit to CeCl₃·6H₂O, in agreement with the phase assigned by XRD (Fig. 2.4). The high vacuum conditions of the TEM could result in the removal of crystal water from the CeCl₃·6H₂O particles, leading to a collapse of the structural order in the near-surface region. This would explain the amorphous layer covering the particles. The coexistence of clean CeO₂ particles and particles made of CeCl₃·6H₂O substantiates that certain crystallographic planes of CeO₂ are less prone to chlorination while others favor the formation of the chloride phase. The catalyst morphology within the complete “1173”-series (Fig. 2.5g-i) looks substantially similar, with the particle size ranging between 20 and 40 nm in all the samples. The fresh catalyst does not contain considerable amounts of bigger particles as in CeO₂-773-F. Thus, the particle size was stabilized already during calcination at the higher temperature, an effect that apparently occurred for the CeO₂-773-F sample only after exposure to Deacon conditions. The only assigned phase in CeO₂-1173-2 was CeO₂ (Fig. 2.5j). In CeO₂-1173-0 both CeO₂ (Fig. 2.5k) and CeCl₃·6H₂O (Fig. 2.5l) were present. SAED analysis showed that CeO₂ is the dominant structure in the CeO₂-1173-0 sample with a minor CeCl₃·6H₂O contribution. This result also agrees with XRD (Fig. 2.4).

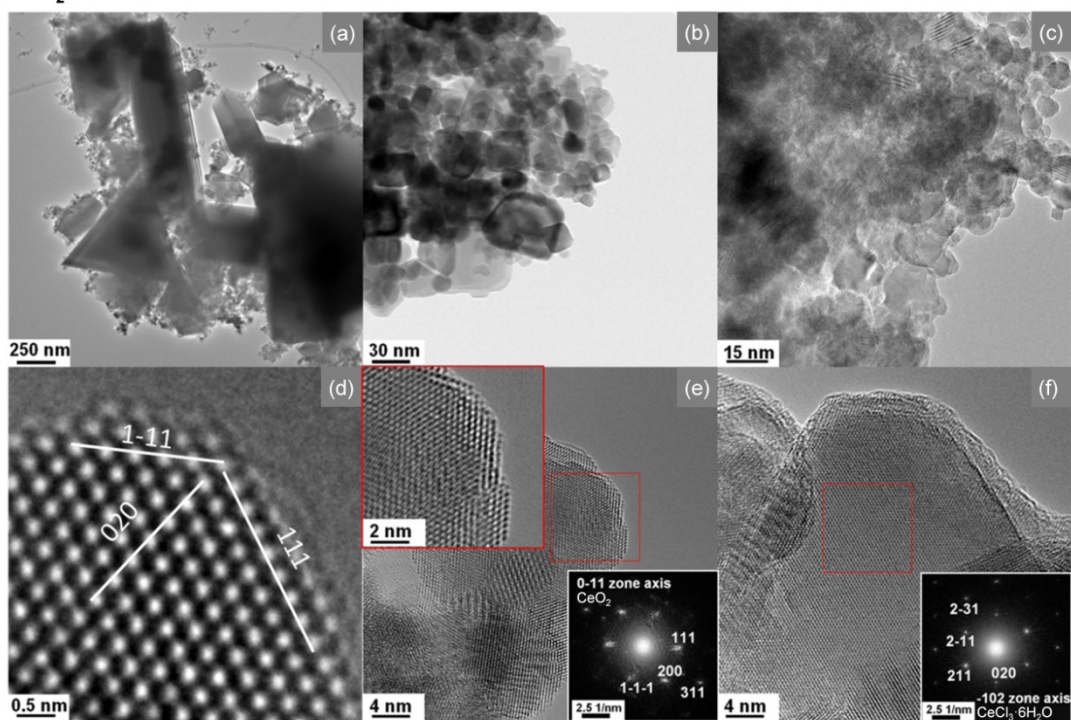
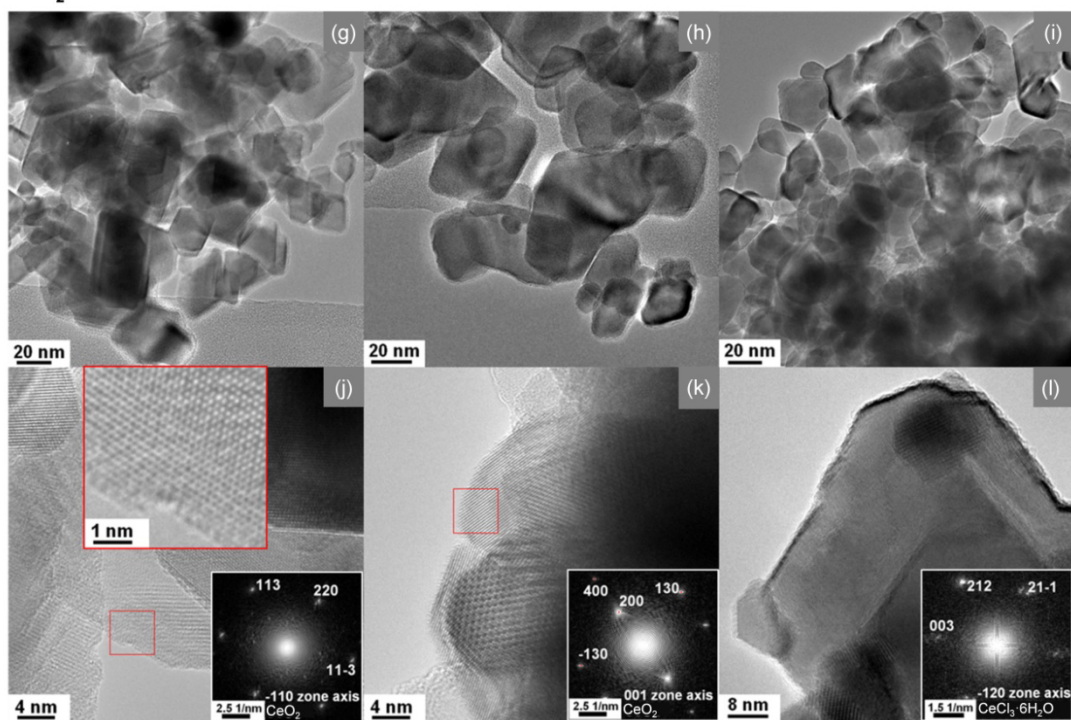
CeO₂-773CeO₂-1173

Figure 2.5 TEM of (a) CeO₂-773-F, (b) CeO₂-773-2, (c) CeO₂-773-0, and HRTEM of (d) CeO₂-773-2, revealing the surface of the CeO₂ particles. (e) A CeO₂-773-0 particle (surface termination in the inset) and (f) a CeO₂-773-0 particle showing an amorphous layer of CeCl₃·6H₂O on the surface. TEM of (g) CeO₂-1173-F, (h) CeO₂-1173-2, and (i) CeO₂-1173-0. Detailed imaging of (j) CeO₂-1173-2, showing CeO₂ particles with clean surface (inset) and of (k,l) CeO₂-1173-0, exhibiting both the (k) CeO₂ and (l) CeCl₃·6H₂O phases.

2.3.2.3 X-ray photoelectron spectroscopy

XPS was applied to selected catalysts to assess the degree of surface chlorination. Table 2.3 compiles the experimentally determined Cl/Ce ratios. In general, CeO₂-773-F was more prone to chlorination than CeO₂-1173-F. Moreover, exposure to HCl gave rise to a more extended chlorination than the exposure to HCl+O₂. Both findings are in line with XRD analysis. To translate the Cl/Ce stoichiometry numbers that assume homogeneous distribution of Cl in the information depth into the number of near-surface layers containing Cl various models were applied (see details in the SI). Thus, a more realistic layered structure was constructed (Cl occupation preference from top inwards) giving rise to the same signal ratio as determined by XPS. As Table 2.3 indicates, Cl occupies approximately 1-1.5 layers in the samples used under Deacon conditions and 2.5 to 6 layers after HCl conditioning. Nevertheless, one should remember that after exposure to the mixture, the samples were quenched in N₂, thus it is reasonable to assume that the Cl atoms adsorbed on external Ce atoms could desorb and hence are not counted in XPS. This assumption is in line with DFT simulations (Section 2.3.4.3). Based on the XPS data, it can be concluded that during the HCl oxidation, Cl atoms can occupy surface sites as well as lattice oxygen vacancies. This is in contrast to the RuO₂ case, where chlorination was confined to the surface layer [9,10,51]. Since XRD after HCl treatment detected traces of CeCl₃·6H₂O, the higher Cl uptake in the near-surface region for CeO₂-1173-0 and CeO₂-773-0 can be explained by the presence of the chloride phase. The Ce 3*d* difference spectrum (Fig. S 2.10 in the SI) between 773-0 and 773-F confirms the presence of CeCl₃·6H₂O. The calculation, indicating 8% of chloride phase (corresponding to an increase in Cl/Ce by ca. 0.24), is in reasonable agreement with the observed increase in Cl/Ce by 0.36, and the difference might be due to additional subsurface Cl occupation. In addition, Fig. S 2.10 in the SI suggests that calcination at 773 K is not sufficient to produce fully oxidized cerium (CeO₂), an extra 10% of Ce³⁺ state being estimated after this milder calcination.

Table 2.3 Quantification by different models of the surface Cl uptake from XPS measurements.

Catalyst	Cl/Ce stoichiometry ^a	Number of layers occupied by Cl		
		Model 1 IMFP ^b	Model 2 EAL ^c	Model 3 EAL, 75% Cl ^d
CeO ₂ -773-F	-	-	-	-
CeO ₂ -773-2	0.19	1.5	1.2	1.6
CeO ₂ -773-0	0.55	5.7	4.6	6.1
CeO ₂ -1173-F	-	-	-	-
CeO ₂ -1173-2	0.14	1.0	0.8	1.1
CeO ₂ -1373-0	0.29	2.4	1.9	2.6

^a Based on homogeneous distribution of elements.

^b Inelastic mean free path (by TPP-2M [50]): 22 Å.

^c Effective attenuation length, 0.8×IMFP was used.

^d Additionally to the EAL model, 75% Cl occupation of possible sites was considered, in line with the DFT calculations.

2.3.3 In situ Fourier transform infrared spectroscopy

In situ FTIR experiments were carried out to study the chlorination mechanism indirectly, that is, following the evolution of the OH stretching bands upon introducing a diluted Deacon feed. A detailed description based on our DFT calculations of different configurations of OH/H₂O-related species adsorbed on CeO₂(111) and of the corresponding vibrational frequencies is presented in the SI (Table S 2.1). The CeO₂-773-F sample was activated by heating in O₂/N₂ up to 653 K, and holding at this temperature till no spectral changes were observed. The spectrum at the end of this stage (Fig. 2.6, dark blue) shows two main bands at 3713 cm⁻¹ and 3632 cm⁻¹,

which are respectively assigned to mono-coordinated (OH-I) and bridging (OH-IIB) hydroxyls [52-54]. Another absorption band at 3684 cm⁻¹, due to water, as well as a band at 3660 cm⁻¹, attributed to a different bridging hydroxyl species (OH-IIA), vanished during the activation process. The existence of two types of bridged hydroxyl groups was first reported by Badri et al. [52], who assigned the red-shifted band to bridged hydroxyl groups next to oxygen vacancies created by water elimination. According to our DFT calculations on CeO₂(111), the mono-coordinate OH band should appear at 3729 cm⁻¹, but threefold coordinated OH species with surface O being part of the lattice can also give rise to bands in the range of 3750-3732 cm⁻¹. Note that the calculation tends to overestimate the stretching frequency by 15-30 cm⁻¹, when benchmarked against gas-phase water molecules. Additionally, OH-II species seem to be unstable on the (111) and (100) facets. On the other hand, bands related to water with a neighboring hydroxyl group are expected to fall around 3682-3646 cm⁻¹; thus they may give rise to the low-frequency absorption.

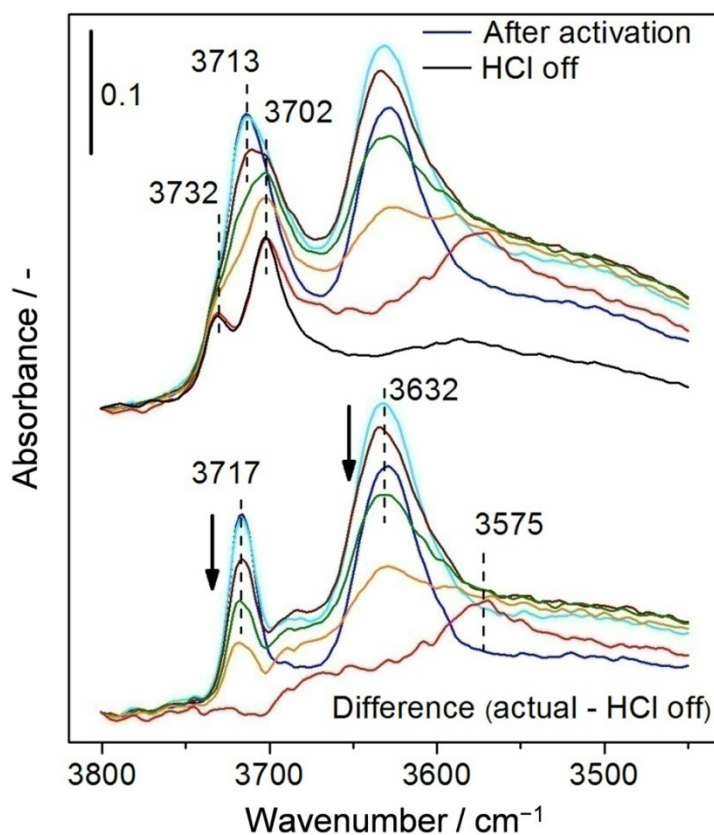


Figure 2.6 Evolution of the stretching OH band region of CeO₂-773-F upon introducing 1 vol.% HCl into an O₂/N₂ (20/80) feed at 653 K. The dark-blue curve represents the starting state prior to HCl introduction, whereas the black spectrum shows the stabilized state after HCl has been turned off (both in O₂/N₂). The temporal evolution in the Deacon feed was as follows: light blue / brown / green / orange / red corresponding to time-on-stream of 85 / 170 / 220 / 270 / 1055 s, respectively.

Two shoulders at 3732 cm⁻¹ and 3702 cm⁻¹ are visible on both sides of the high-frequency OH band. Upon introducing HCl in the O₂/N₂ feed, these shoulders became more resolved. According to Table S 2.1, they can be attributed to threefold coordinated hydroxyl groups, as well as to mono-coordinated OH groups with different neighboring species coexisting on the surface. During HCl oxidation, significant changes were observed in the spectra, as the intensity of the peak at 3632 cm⁻¹ decreased gradually till it was completely depleted at later stages (Fig. 2.6, light-blue till red). According to the bands assignment in the OH stretching region suggested by our DFT-calculated vibrational frequencies, this would indicate that the initial

H₂O-OH pairs progressively disappeared, likely due to the partial occupation of the vacancies by Cl. OH-Cl pairs showed OH vibration at 3739 cm⁻¹, just in the middle of the OH band of threefold and adsorbed OH. In parallel, the baseline in the whole spectral region first increased (light blue/brown/green), and, then declined to reach the level shown by the red spectrum. This modulation of the baseline reflects the rapid evolution, desorption, and stabilization of the hydrogen-bonded water structure as HCl dissociatively adsorbs on the ceria surface. The broad signal at 3575 cm⁻¹ (red spectrum), developed when the hydrogen-bonded water structure reached low enough concentration, can be assigned to isolated adsorbed water species produced during the reaction (in line with the theoretical value at 3591 cm⁻¹), since it diminished after stopping the HCl flow (black line). To visualize the changes occurring in the high-frequency OH band, the ‘‘HCl off’’ curve was subtracted from all other spectra. This illustration suggests that the changes in this band were not due to band shift, but rather related to the gradual disappearance of one OH species at 3717 cm⁻¹ in parallel with the depletion of the band at 3632 cm⁻¹. This experiment suggests that surface chlorination occurs *via* dissociative HCl adsorption (baseline modulation) and consumption of OH groups, and thus through the displacement of surface oxygen species of different coordination by Cl.

2.3.4 Molecular modeling

2.3.4.1 Vacancy formation, diffusion, and healing

The surface energy to cleave the (111) plane of CeO₂(111) is 0.013 eV Å⁻². The inward relaxation of the external atoms is 0.090 and 0.097 Å for Ce and O atoms, respectively. The material is known to be easily reducible and, thus, can accommodate oxygen vacancies [55]. The formation of surface vacancies, thereafter denoted as □, in 0.25 ML (monolayers) in the *p*(2×2) cell is endothermic by 3.25 eV. This is a very small value when compared to ionic materials [56] or to other reducible oxides like SrTiO₃ [57]. The electronic structure of the surface vacancy corresponds to an anti-ferromagnetic solution, where the two electrons left end up in the next and next nearest surface Ce atoms, as described by Ganduglia-Pirovano et al. [43]. The electronic structure, electron localization, and formation energy are in good agreement with previous calculations with both PBE+U and HSE06 functionals [43]. The latter is supposed to be more accurate for strongly localized *f*-electrons. However, the energy difference with other configurations is rather small and dynamic re-ordering of the electronic structure through polaronic effects is likely to occur [58,59].

Oxygen vacancies can be present in near-surface layers (Fig. 2.7c). Indeed, the formation energy for subsurface defects turns out to be lower than for surface defects, 2.93 eV, in agreement with previous theoretical estimates [43]. The energy requirement for surface to subsurface vacancy diffusion is small, 0.30 eV, in line with reported values for bulk diffusion, 0.50 eV [60]. Vacancy agglomeration has also been evidenced by scanning tunneling microscopy (STM) investigations [28]. From our calculations on a *p*(4×2) supercell, surface vacancy agglomeration at a constant concentration of 0.25 ML is weakly exothermic, by 0.13 eV, in agreement with STM images.

As for the surface re-oxidation, oxygen adsorption does not take place on a non-defective CeO₂(111) surface, but occurs on surface oxygen vacancies, □, leading to a superoxo-like species, in which one of the two O atoms fills the hole, and the O-O distance is 1.453 Å.

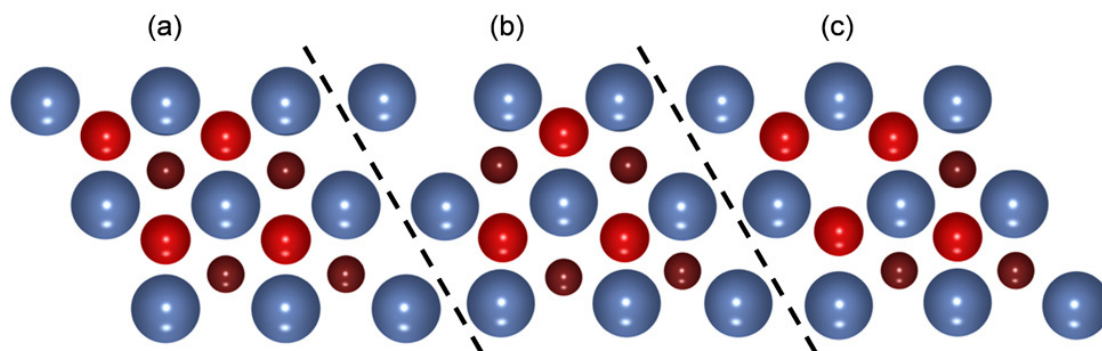


Figure 2.7 Structural model of a $p(2\times 2)$ supercell of CeO₂(111): (a) regular surface, (b) surface vacancy, and (c) subsurface vacancy. Ce atoms are depicted in blue, surface O atoms in red, and subsurface O atoms in scarlet and small balls.

Dissociation of this bond heals the defect and leaves a surface O atom, but it is uphill by 1.80 eV. Nevertheless, the dynamics of oxygen vacancies in oxides can be enhanced by the presence of gas-phase O₂ [61]. Aggregation of oxygen defects at the surface or near-surface is energetically favored. Indeed, surface vacancy diffusion takes place by penetration to the subsurface layer and ejection toward the surface in neighboring lattice position. The first step is exothermic by 0.72 eV with a barrier of 0.24 eV, while the second is mildly endothermic (0.59 eV) with a barrier of 0.64 eV. Once the defect dimer is present on the surface, gas-phase oxygen molecules can interact healing both vacancies and liberating about 6 eV.

2.3.4.2 Chlorination

In order to assess the stability of CeO₂(111), we have employed first-principles thermodynamics [62] to consider the effect of partial oxygen and chlorine pressures on the state of the surface. The stability problem is considerable and was simplified by exclusively considering a reactant (O₂) and a product (Cl₂), for which no crossing between the associated chemical potentials appears in the equations. The excess surface energy can be calculated from the following equation:

$$\Delta G_X \approx E_X - E_{\text{CeO}_2} + N_{\text{O}_2}/2\mu_{\text{O}_2} - N_{\text{Cl}_2}/2\mu_{\text{Cl}_2} \quad (2.3)$$

where ΔG_X is the Gibbs energy associated with the configuration X with respect to the energy of regularly terminated CeO₂, E_{CeO_2} , N_{O_2} and N_{Cl_2} are the number of oxygen and chlorine molecules, and μ is the corresponding gas-phase chemical potential. The ability of HCl to form chlorides is somehow higher than that of Cl₂, but the present model serves as a guide to evaluate the degree of chlorination of the material. The Gibbs potentials of solids including 40 different X configurations, E_X , and of the regular surface, E_{CeO_2} , were taken from DFT calculations and the chemical potentials of Cl₂ and O₂ were calculated through statistical thermodynamics [63]. Fig. S 2.11 in the SI shows that, at extremely low oxygen and chlorine chemical potentials, the surface is regularly terminated. When increasing the Cl₂ pressure, partial chlorination can take place by substitution of an oxygen atom from the surface (Fig. S 2.11 in the SI, green configuration). At relatively low oxygen pressures (for $\log(p_{\text{O}_2})$ and $\log(p_{\text{Cl}_2})$ in the range -1 to 2), the clean surface, mono-substituted Cl, and multiple substituted Cl structures lie very close in energy and are likely present on the catalyst surface. If the chlorine pressure is much higher ($\log(p_{\text{Cl}_2}) = 0$), lattices with Cl in lattice oxygen positions become more stable. The maximum oxygen substitution achievable in this way corresponds to 50% of the surface oxygen atoms. If the oxygen pressure is raised up to the 0.1 bar regime, as in our catalytic tests, then the most likely configuration corresponds to the clean surface. Finally, the thermodynamic penalty to introduce a Cl atom occupying a vacancy site (Cl□) to inner layers is about 3 eV. Accordingly, it is implied that Cl preferentially stays in the near-surface region, and that high HCl or Cl₂

pressures might account for lattice disruption and formation of CeCl₃-related phases (Section 2.3.2), as Cl cannot be accommodated in the bulk of CeO₂.

2.3.4.3 Reaction mechanism

The reaction profile of the HCl oxidation on CeO₂ is presented in Fig. 2.8. The main elementary steps derived for the Deacon process comprise: (i) hydrogen abstraction from HCl by basic surface O atoms, to form hydroxyl groups and leave chlorine atoms on the surface, (ii) reaction of the hydroxyl groups with new incoming HCl molecules and/or hydroxyl group recombination on the surface to form water, (iii) water removal, (iv) re-oxidation, and (v) recombination of chlorine atoms.

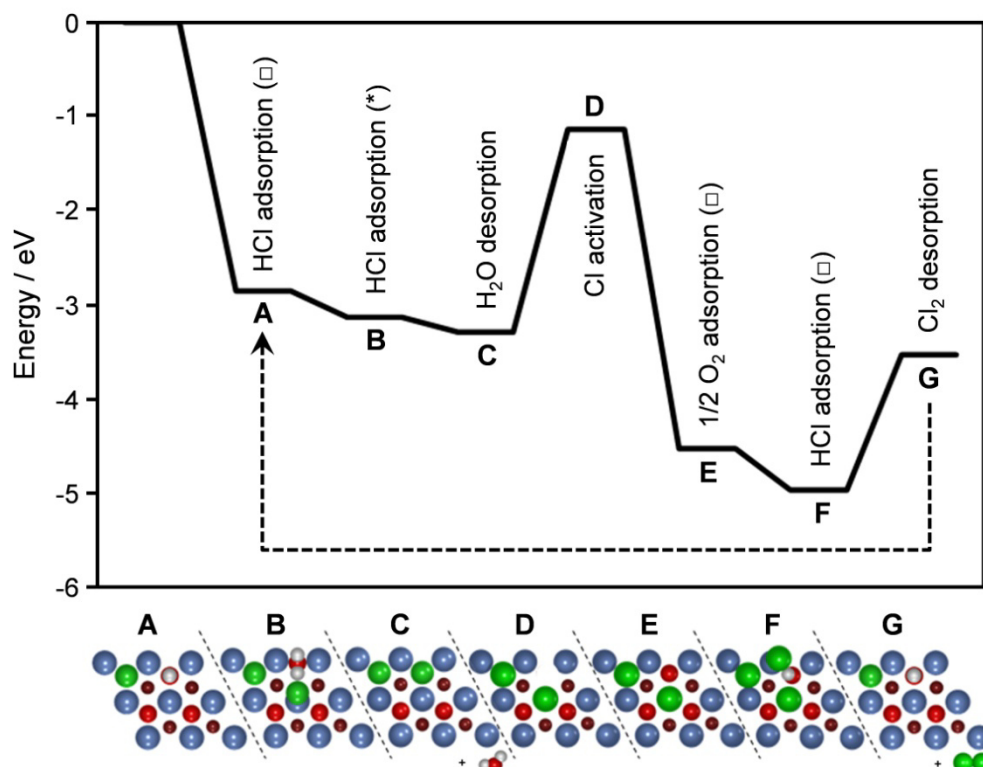
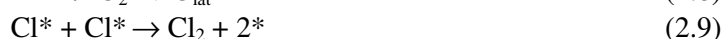
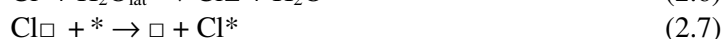
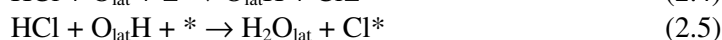


Figure 2.8 Reaction energy profile for the Deacon process on CeO₂(111). The initial state in the profile is CeO₂(111) with a surface oxygen vacancy. The color codes in the bottom panels are as described in the caption of Figure 2.7.

The Deacon reaction starts by the adsorption of HCl near the basic centers on the surface (lattice oxygen atoms, O_{lat}). The reaction is energetically favored provided that a surface vacancy exists, where the Cl atom can be accommodated (Fig. 2.8, step A). In this process, HCl adsorption is exothermic by 2.84 eV and leads to a surface O_{lat}H group and a Cl atom at the surface vacancy. Care should be taken as both O_{lat} and adsorbed O atoms can give rise to the OH-I and OH-II vibrational bands described in Section 2.3.3. At the transition state, the H-Cl and O_{lat}-H distances are 3.590 and 2.121 Å, respectively. A second HCl molecule can adsorb, forming a water molecule and leaving a Cl atom on top of a Ce atom on the surface, Cl* (Fig. 2.8, step B). This second process is also exothermic, but only by 0.29 eV. The external Cl* atom can push the already formed water molecule H₂O_{lat} out of the lattice and fill the nascent vacancy, thus becoming Cl□. This process is almost thermo-neutral (Fig. 2.8, step C). Then, one of the oxygen atoms from the subsurface layer can diffuse toward the surface, pushing a Cl□ atom toward the outer surface, i.e. converting Cl□ in Cl* (Fig. 2.8, step D). The energy required for this elementary step is 2.15 eV and forms an oxygen vacancy at a subsurface position, □_{ss}. Re-oxidation can take place by the complex diffusion-reaction mechanism described in Section

2.3.4.1 to release nearly 3.4 eV (Fig. 2.8, step E). Still, HCl can adsorb on this surface releasing 0.42 eV to form a O_{lat}H and a Cl* (Fig. 2.8, step F). Three chlorine atoms are then adsorbed on the surface, one Cl* and two Cl_□, respectively. Cl₂ evolution toward the gas-phase takes place from this structure; the energy required is 1.42 eV (Fig. 2.8, step G). As it can be noticed in Fig. 2.8, states A and G correspond to the active states of the catalyst. Therefore, the catalytic cycle runs between steps A and G.

The list of elementary steps in the mechanism can be summarized by the following reactions:



It is important to notice that, although the reaction scheme on CeO₂ resembles that of RuO₂, some important differences are found. First, the reaction on RuO₂ occurs at almost full coverage of the under-coordinated Ru_{cus} positions, as nearly all available sites are occupied by Cl [9]. For CeO₂, under-coordinated cerium atoms only exist when oxygen vacancies are present in the surface or near-surface regions. These are the only active sites for the reaction, in agreement with the linearity found between activity and OSC (Fig. 2.1b). As a consequence, the reaction profile for CeO₂ is much more abrupt (involves higher energy requirements) than that of RuO₂. This correlates with the higher temperatures needed to run the Deacon reaction on CeO₂ (vide supra). The most energy-demanding step of HCl oxidation on RuO₂ is related to the formation and evolution of Cl₂. Due to the high energy required for Cl₂ elimination on RuO₂, Cl self-poisoning is observed and, thus, re-oxidation turns out to be the rate-determining step under relevant conditions, as shown by the positive dependence of the activity on the partial pressure of O₂ [51]. For CeO₂, the activation of Cl atoms from lattice vacancies to surface positions is the most energy-demanding step.

The similar activity enhancement observed at higher partial O₂ pressures (Fig. 2.2) can be rationalized on the basis of the chlorine and oxygen competition for the same active sites, which tightly couples chlorine elimination to oxygen re-adsorption. When Cl atoms occupy most of the active positions, very few active sites exist for re-oxidation, thus producing less Cl₂. In extreme cases, this leads to catalyst deactivation.

Regarding the stability against the harsh reaction conditions employed, while the experimental data indicate that RuO₂ and CeO₂ are quite similar, the DFT analysis points out some differences. The RuO₂ surface is known to be partially chlorinated, but this chlorination is confined to the under-coordinated O and Ru positions at the external surface. Comparing surface Cl contents, the situation is such that the amount of Cl on the surface of RuO₂ is very large, as the under-coordinated positions in the lattice are very prone to adsorb reactants (Cl in particular). This effect is less evident on CeO₂, given the relative inertness of Ce atoms on the surface. Indeed, most of the Cl is sitting at oxygen vacancies on the surface and not directly on top of the active Ce sites. In addition, the penetration of Cl atoms to deeper layers is hindered in both RuO₂ and CeO₂ systems by more than 2 eV. This energy is somewhat larger for CeO₂ (3 eV). Nevertheless, owing to vacancy diffusion, and thus oxygen supply to the surface, ceria will be more prone to subsurface and bulk chlorination in pure HCl or sub-stoichiometric Deacon feeds. In line with this, we have compared the energy required for the bulk chlorination and lattice disruption in both Ru and Ce cases, see Table 2.4. The energy requirement for the chlorination of CeO₂ is smaller than the corresponding value for RuO₂, in agreement with the greater chlorination detected in the CeO₂ experiments in HCl-rich feeds.

Table 2.4 Energy (ΔE) in eV and Gibbs free energy (ΔG^0) in kJ mol⁻¹ M (M = Ce, Ru) atom for the complete chlorination of CeO₂ and RuO₂ by Cl₂ or HCl.^a

Chlorination equation	ΔG^0		
	ΔE	573 K	703 K
$\text{CeO}_2 + 3/2\text{Cl}_2 \rightarrow \text{CeCl}_3 + \text{O}_2$	15.82	92.95	112.18
$\text{CeO}_2 + 4\text{HCl} \rightarrow \text{CeCl}_3 + 2\text{H}_2\text{O} + 1/2\text{Cl}_2$	-115.99	60.61	97.95
$\text{RuO}_2 + 3/2\text{Cl}_2 \rightarrow \text{RuCl}_3 + \text{O}_2$	101.86	178.98	198.22
$\text{RuO}_2 + 4\text{HCl} \rightarrow \text{RuCl}_3 + 2\text{H}_2\text{O} + 1/2\text{Cl}_2$	-29.95	146.65	183.98

^a Calculated using the PBE (RuO₂) and PBE+U (CeO₂) functionals.

2.4 Conclusions

In this study we present a fundamental understanding of HCl oxidation on bulk CeO₂ combining catalyst testing, steady-state kinetics, characterization, and DFT simulations. Due to its remarkable activity and stability, CeO₂ constitutes a promising alternative to highly expensive RuO₂-based catalysts for industrial chlorine recycling. The activity is related to the presence of oxygen vacancies in the material. The stability arises from the remarkable resistance of cerium oxide against chlorination. Limited bulk chlorination, that is detection of CeCl₃ by XRD, takes place under HCl-rich conditions ($\text{O}_2:\text{HCl} \leq 0.25$). The bulk chloride phase rapidly and completely disappears when the catalyst is exposed to O₂-rich conditions. Under $\text{O}_2:\text{HCl} \geq 0.75$, only the outermost surface layers of CeO₂ contain chlorine. Density functional theory simulations reveal that Cl activation from vacancy positions to surface Ce atoms is the most energy-demanding step, although chlorine-oxygen competition for the available active sites may render re-oxidation as the rate-determining step. Current studies focus on developing a proper strategy to support the active phase on a suitable carrier preserving the catalytic properties of bulk CeO₂.

2.5 Supporting Information

Description of characterization techniques

Powder X-ray diffraction (XRD) was measured in a PANalytical X'Pert PRO-MPD diffractometer. Data were recorded in the 10-70° 2θ range with an angular step size of 0.017° and a counting time of 0.26 s per step. Nitrogen adsorption was measured at 77 K in a Quantachrome Quadrasorb-SI gas adsorption analyzer. Prior to the measurement, the samples were degassed in vacuum at 473 K for 10 h. Temperature-programmed reduction with hydrogen (H₂-TPR) was measured in a Thermo TPDRO 1100 unit equipped with a thermal conductivity detector. The samples were loaded in the quartz micro-reactor (11 mm i.d.), pre-treated in He (20 cm³ STP min⁻¹) at 473 K for 30 min, and cooled to 323 K in He. The analysis was carried out in 5 vol.% H₂/N₂ (20 cm³ STP min⁻¹), ramping the temperature from 323 to 1173 K at 10 K min⁻¹. Oxygen storage capacity (OSC) measurements were also conducted in the Thermo TPDRO 1100 unit. The samples (20 mg) were pre-treated in He (20 cm³ STP min⁻¹) at 773 K (10 K min⁻¹) for 30 min and then exposed to 5 vol.% H₂ in N₂ (20 cm³ STP min⁻¹) at 573 K and until no H₂ consumption was observed anymore. The obtained OSC values are expressed in micrograms of O per gram of catalyst. Thermogravimetric analysis was performed in a Mettler Toledo TGA/DSC 1 Star system analyzer connected to a Pfeiffer Vacuum ThermoStar GSD 320 T1 Gas Analysis System. Analyses were performed in N₂ (40 cm³ STP min⁻¹), ramping the temperature from 298 to 1173 K at 10 K min⁻¹. AMU 32 (O₂), 35 (Cl), 18 (H₂O), and 71 (Cl₂) were continuously monitored. High-resolution transmission electron microscopy (HRTEM) investigations were undertaken in a Titan 80-300 Cs-corrected microscope equipped with a Gatan Tridiem Image Filter. Prior to the measurement, selected samples were deposited on a Cu-TEM grid via dry preparation. Crystalline phases were assigned according to ICSD database using the following structures: JCPDS 73-6328 for CeO₂, JCPDS 75-1891 for CeCl₃, JCPDS 52-1843 for CeOCl, and JCPDS 01-0149 for CeCl₃·6H₂O. X-ray photoelectron spectroscopy (XPS) was performed at room temperature using non-monochromatized Al Kα (1486.6 eV) excitation and a hemispherical analyzer (Phoibos 150, SPECS). Samples were transferred to the spectrometer chamber under regular air exposure. The binding energy scale was calibrated by internally referencing to the Ce 3d U'''' (916.7 eV) hybridization state of Ce⁴⁺ to correct for charging effects. The chlorine content of the samples was calculated from the Cl 2p and Ce 4d states after Shirley background subtraction. The values are thus related to a situation in which chlorine is homogeneously distributed in the information depth. Since this is unlikely, 3 different layer models were employed to calculate the number of layers in CeO₂ that experienced chlorination, assuming that Cl atoms are either adsorbed on the surface or substituting lattice O atoms. For layer thickness, 3.12 Å was considered, which is the lattice parameter of the most prominent [111] surface facet. First, the inelastic mean free path (IMFP) value was estimated for ceria using the Tanuma, Powell, and Penn algorithm (Tanuma *et al.*, Surf. Interface Anal. 21 (1994) 165), and used this in the first model. For the Cl 2p and Ce 4d electrons used for the quantification, the IMFP was calculated as 21.1 and 22.0 Å, respectively. Elastic scattering causes the attenuation length to be typically between 10% and 25% shorter than IMFPs, depending on the type of material and the kinetic energy of the electrons (Cumpson *et al.*, Surf. Interface Anal. 25 (1997) 430). Therefore, in our second model, 80% of IMFP for practical effective attenuation length (EAL) at normal electron emission was assumed. Based on DFT simulations (section 2.2.5), only 3/4 Cl occupation was considered in the third model. Calculation of the layer thickness was in all three cases based on the equation:

$$d = \text{EAL} \cos\theta \ln(1 + I_{\text{Cl-Ce}} / (R (I_{\text{Ce4d}} - I_{\text{Cl-Ce}}))) \quad (\text{S } 2.1)$$

This equation is equivalent to that used to calculate the layer thickness of SiO₂ over Si (Seah *et al.*, Surf. Interface Anal. 41 (2009) 430). θ is the electron emission angle (zero in our case), $I_{\text{Cl-Ce}}$ is the Ce 4d intensity equivalent to the recorded Cl 2p signal, and R is the relative intensity of Ce 4d of pure materials (overlayer: ceria with incorporated Cl; substrate: CeO₂). R was assumed equal to 1, as we considered that Cl atoms replaced lattice O atoms (if not adsorbed on the

surface). $I_{\text{Ce}4d}$ is the recorded Ce 4d signal. Note that in the model of only inelastic events, model 1, IMFP substitutes EAL.

Table S 2.1 Configurations and calculated frequencies, in cm⁻¹, for H₂O-related species adsorbed on a regularly terminated CeO₂ surface, or a CeO₂ surface with vacancies, and/or with neighboring adsorbed chlorine atoms.^{a,b,c}

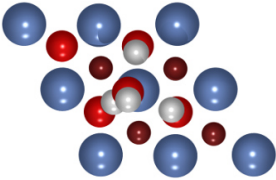
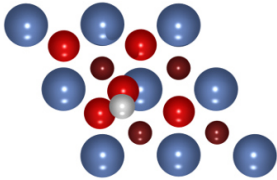
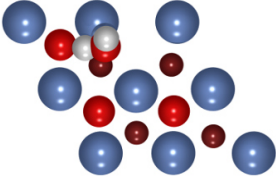
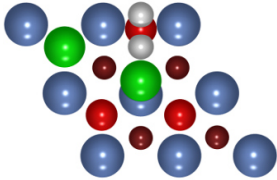
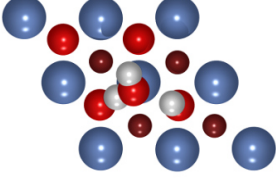
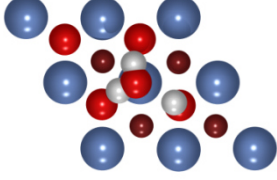
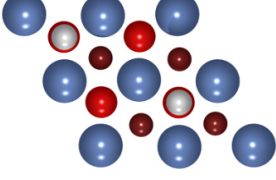
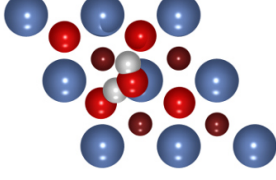
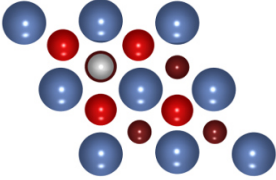
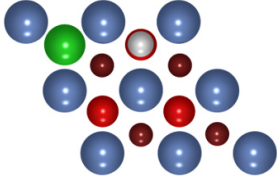
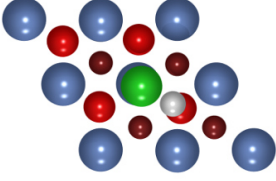
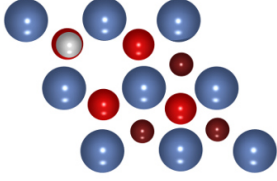
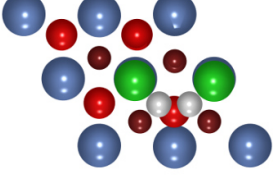
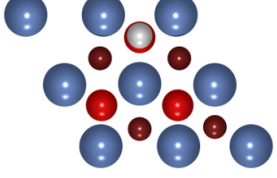
	H₂O* + 2O_{lat}H 3783 3711 3552 2708 1572		O*H 3729
	H₂O* + □ 3764 2630 1559		H₂O_{lat} + Cl□ + Cl* 3716 2456 1522
	H₂O + O_{lat}H 3759 3646 2892 1565		H₂O* + O_{lat}H 3682 3582 3309 1581
	2O_{lat}H 3751 3750		H₂O* 3591 3317 1570

Table S 2.1 Configurations and calculated frequencies, in cm⁻¹, for H₂O-related species adsorbed on a regularly terminated CeO₂ surface, or a CeO₂ surface with vacancies, and/or with neighboring adsorbed chlorine atoms.^{a,b,c}

	O_{lat,ss}H 3377		O_{lat}H + Cl□ 3739
	O_{lat}H + Cl* 3183		O_{lat}H + □_{ss} 3732
	H₂O_{lat} + 2Cl* 2591 2371 1520		O_{lat}H + □ 3744

^a Color code in the structural models: blue (Ce), red (surface O), scarlet (subsurface O), white (H), and green (Cl).

^b Notations: lat = lattice, * = Ce site, □ = surface vacancy, □_{ss} = subsurface vacancy, ss = subsurface.

^c The calculation tends to overestimate the stretching frequency by 15-30 cm⁻¹, when benchmarked with the same approach for gas-phase water molecules.

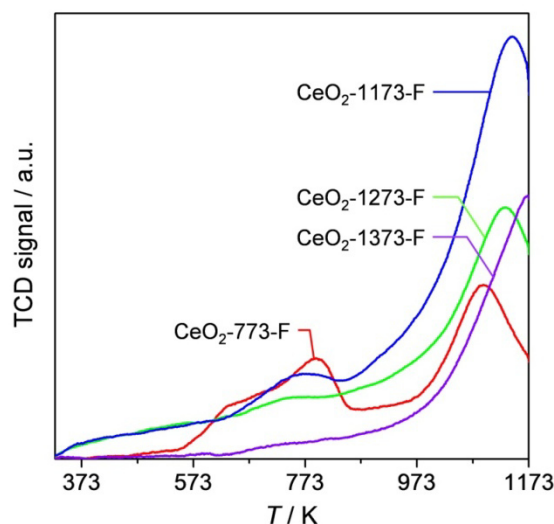


Figure S 2.1 H₂-TPR profiles of CeO₂ catalysts. All profiles are characterized by a main peak of hydrogen consumption centered at 1073-1150 K, due to the reduction of bulk CeO₂. Less intense peaks around 723-773 K are assigned to reduction of labile surface and near-surface oxygen species (Yao et al., J. Catal. 86 (1984) 254; Trovarelli, Catal. Rev. Sci. Eng. 38 (1996), 439). The profiles indicate that reduction of surface CeO₂ starts at *ca.* 573 K.

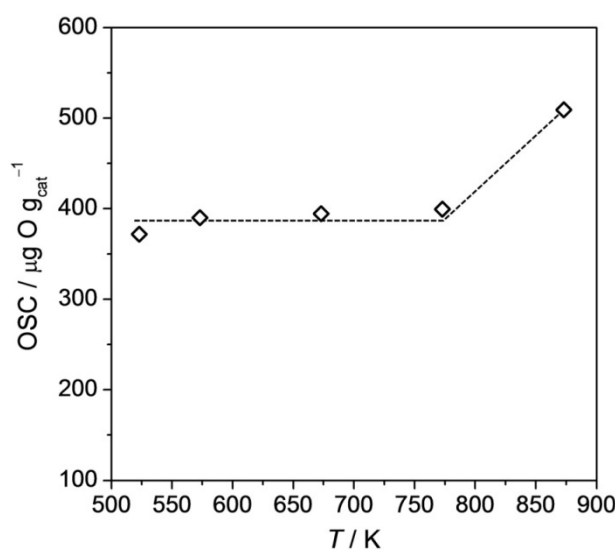


Figure S 2.2 Oxygen storage capacity (OSC) of CeO₂-773-F measured at different temperatures. As HCl oxidation involves participation of the CeO₂ outermost surface layers, the temperature of the OSC measurement has to be selected so that reduction would be mostly limited to the (near-)surface region. The H₂-TPR results (Fig. S 2.1) gave preliminary indication of a suitable temperature (573 K). OSC measurements carried out on CeO₂-773-F at temperatures between 573 and 873 K evidenced substantially similar OSC values in the temperature range of 523-773 K, suggesting reduction at the surface level only. However, a further temperature increase by 100 K enabled reduction of the bulk to some extent. This result is in line with literature reports (Trovarelli, Catal. Rev. Sci. Eng. 38 (1996) 439, Fornasiero et al., Appl. Catal., B 22 (1999) L11, Aneggi et al., J. Alloys Compd. 408-412 (2006) 1096). On the basis of these data, the OSC of the catalysts was measured at 573 K.

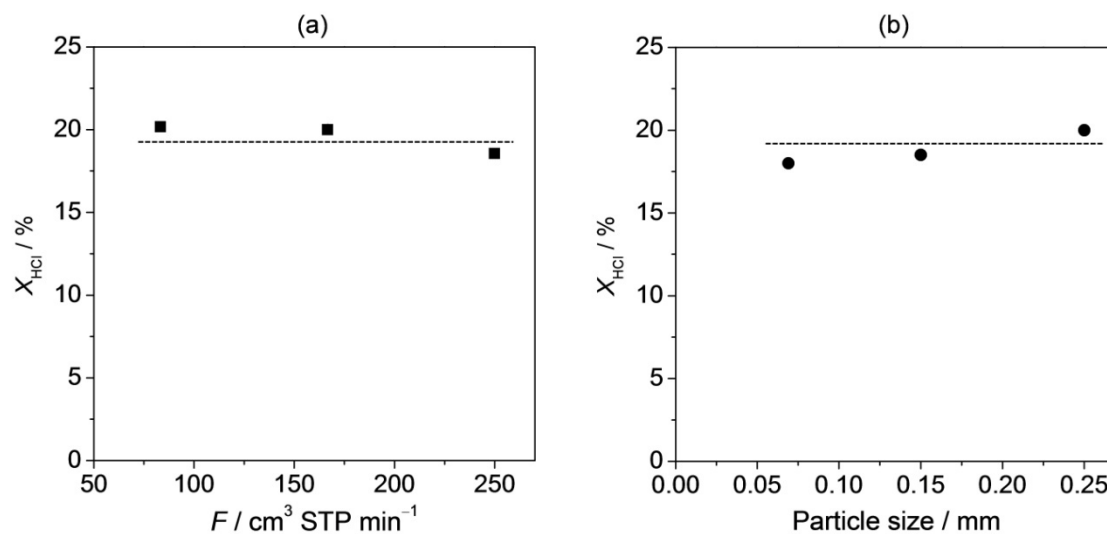


Figure S 2.3 Diagnostic to verify the absence of extra-particle and intra-particle diffusion limitations in the catalytic tests. HCl conversion *versus* volumetric flow rate (a) and particle size (b) over CeO₂-1173-F. Conditions: inlet mixture of 10 vol.% HCl and 20 vol.% O₂ balanced in N₂, $T_{\text{bed}} = 703 \text{ K}$, $W/F^0(\text{HCl}) = 11.2 \text{ g h mol}^{-1}$, $P = 1 \text{ bar}$, and time-on-stream = 3 h.

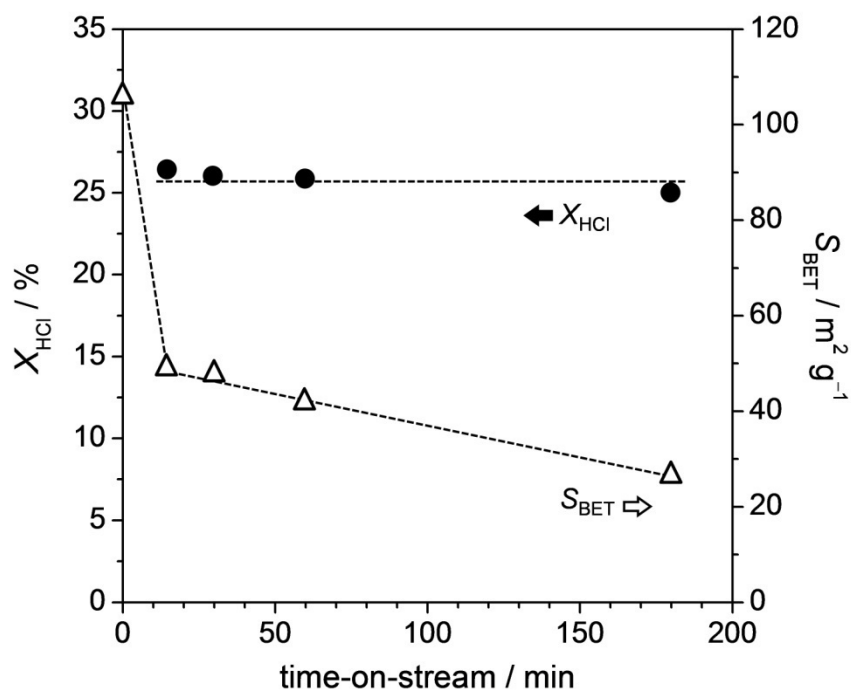


Figure S 2.4 HCl conversion and total surface area *versus* time-on-stream for CeO₂-773-F. Conditions: inlet mixture of 10 vol.% HCl and 20 vol.% O₂ balanced in N₂, $T_{\text{bed}} = 703 \text{ K}$, $W/F^0(\text{HCl}) = 11.2 \text{ g h mol}^{-1}$, and $P = 1 \text{ bar}$. The HCl conversion was practically constant at each measured point, whereas the S_{BET} halved already after 15 min on stream and further decreased up to 3 h, reaching a value that corresponds to about 25% of the original one (27 *versus* 106 $\text{m}^2 \text{ g}^{-1}$). These results confirmed the observed independence of the activity on S_{BET} for values of the latter greater than 25 $\text{m}^2 \text{ g}^{-1}$ and additionally indicated that the restructuring of high-surface area catalysts upon contact with the reaction mixture occurs rapidly.

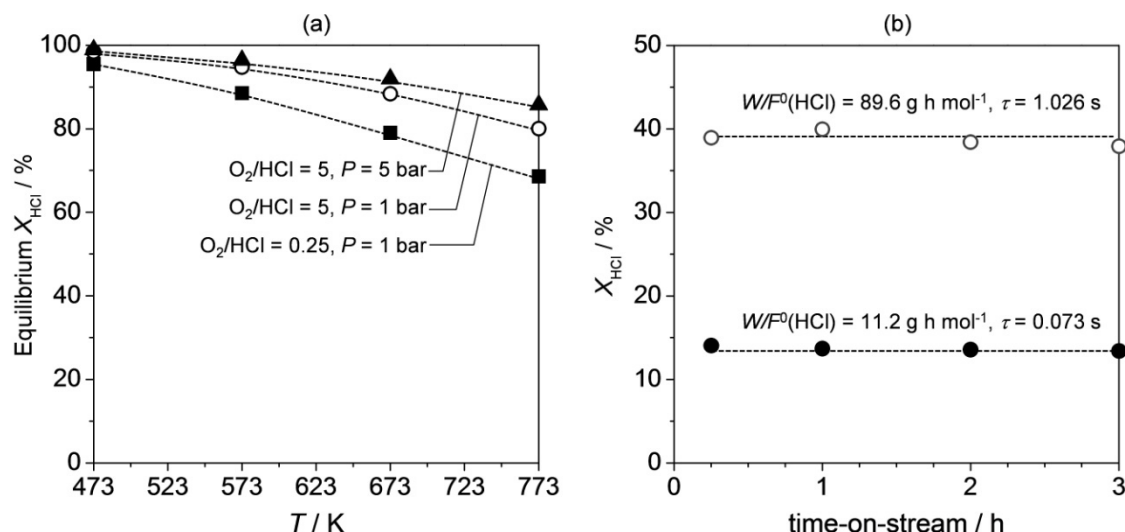


Figure S 2.5 (a) Equilibrium HCl conversion *versus* reaction temperature at variable feed O₂:HCl ratio and total pressure. (b) HCl conversion *versus* time-on-stream over CeO₂-1173 using various residence times. Conditions: inlet mixture of O₂:HCl = 5, $T_{\text{bed}} = 673 \text{ K}$, and $P = 1 \text{ bar}$. High operating temperatures (613-703 K range) are required for CeO₂, and this implies not only a high energy input, but also thermodynamic restrictions to the attainable HCl conversion. Fig. S 2.5a shows that the equilibrium HCl conversion indeed decreases at higher temperatures, but that higher pressures and O₂:HCl ratios largely overcome these limitations, so that the HCl conversion level achieved can still make the development of a technical process feasible (HCl conversion > 80%). For instance, by using a feed mixture with O₂:HCl = 5 and by increasing the space time (at the limits of our current set-up), stable single-pass HCl conversion values of 40% were attained over CeO₂-1173-F at 673 K and 1 bar (Fig. S 2.5b).

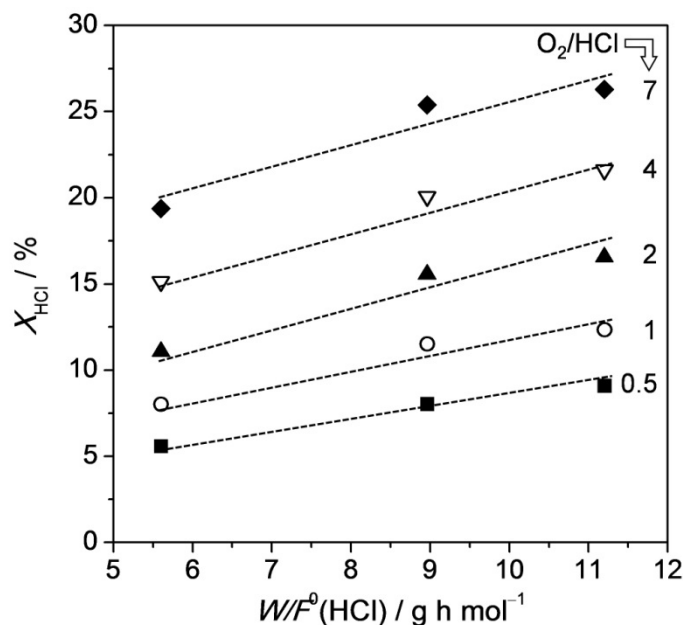


Figure S 2.6 HCl conversion *versus* space time over CeO₂-1173-F at different feed O₂:HCl ratios. Conditions: inlet mixture of 10 vol.% HCl and 5-70 vol.% O₂ balanced in N₂, $T_{\text{bed}} = 703 \text{ K}$, and $P = 1 \text{ bar}$.

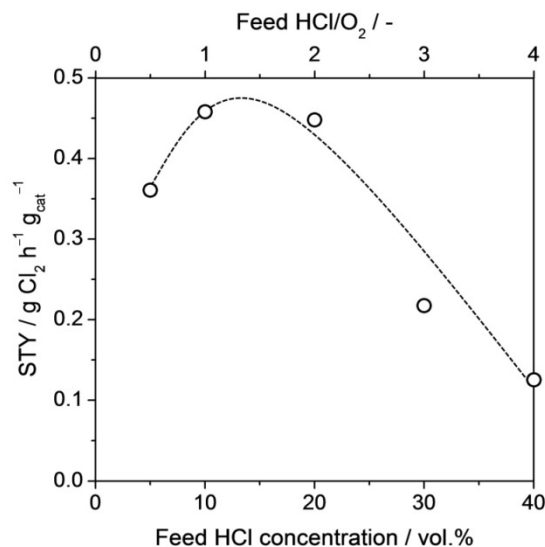


Figure S 2.7 Space time yield of Cl₂ *versus* feed HCl concentration and feed HCl:O₂ ratio over CeO₂-1173-F. Conditions: inlet mixture of 5-40 vol.% HCl and 10 vol.% O₂ balanced in N₂, $T_{\text{bed}} = 703$ K, and $P = 1$ bar. Upon raising the relative HCl content in the feed mixture, the Cl₂ production slightly increased at first and then progressively diminished. This unexpected result is not due to intrinsic kinetics. Low HCl concentrations limit Cl₂ production, while HCl excess causes a change in the catalyst composition at the surface and near-surface level (chlorination) that leads to activity loss.

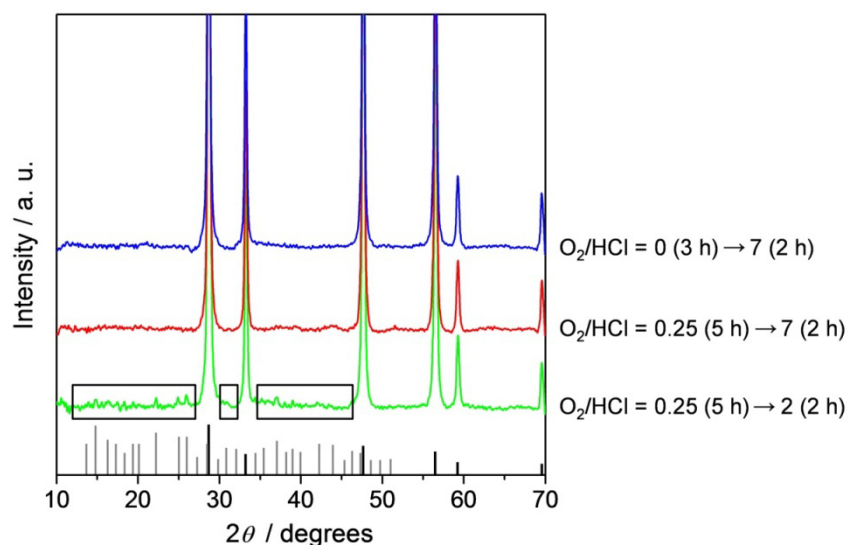


Figure S 2.8 XRD patterns of CeO₂-1173 samples used at 703 K in the HCl-rich/O₂-rich flow experiments (Fig. 2.4). The O₂:HCl ratios used in the two stages and the duration of each stage are reported on the right-hand side of the figure. The most intense reflections are specific to CeO₂ (JCPDS 73-6328, black lines). Minor amounts of CeCl₃·6H₂O (JCPDS 01-0149, gray lines; the relative reflections are visualized in the black boxes) were present for the sample exposed to O₂:HCl = 2 for the O₂-rich stage.

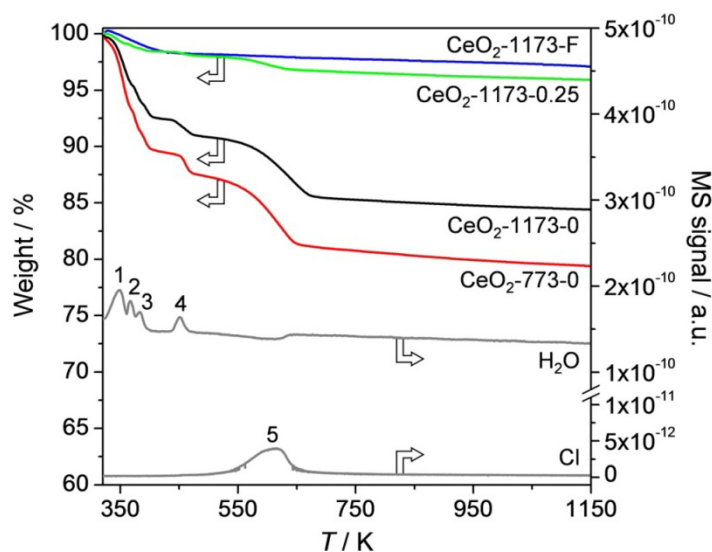


Figure S 2.9 Thermogravimetric profiles of fresh and Deacon-used CeO₂ catalysts. Mass spectrometry profiles for H₂O (AMU 18) and for Cl (AMU 35) coupled to the TGA analysis of CeO₂-773-0 are shown in the secondary y-axis. The peaks result identical for all the samples in terms of number and position, while their intensity differs according to the extents of weight loss. The weight loss of chlorinated samples occurred in several steps. Up to 400 K, removal of surface impurities, such as physically adsorbed water (peak 1), took place. This loss was observed for the fresh sample too. From 360 K up to 473 K, the water of crystallization of the CeCl₃·6H₂O phase was lost in three steps (peaks 2-4). Finally, chlorine removal took place between 473 and 700 K (peak 5). These assignments were made on the basis of literature reports (Wendlandt, J. Inorg. Nucl. Chem. 5 (1957) 118; Guo-Cai et al., Trans. Nonferrous Met. Soc. China, 13 (2003) 1454). The quantification of the chlorination degree of the samples was performed taking into account only the relevant partial weight losses, i.e. relative to structural water and chlorine.

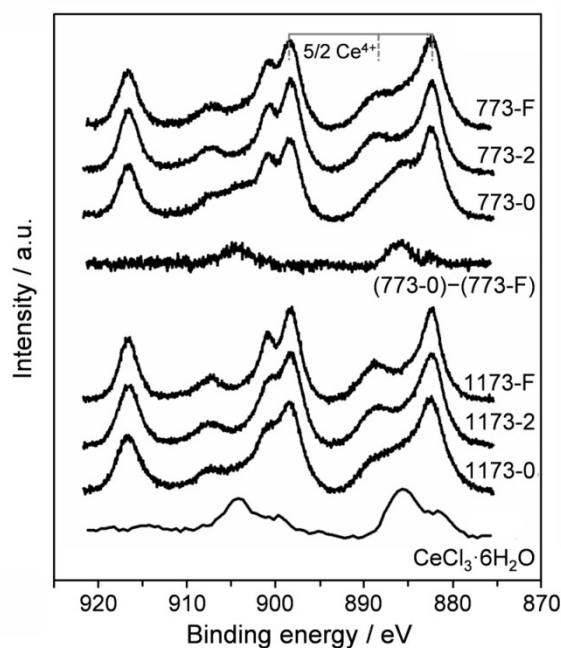


Figure S 2.10 Ce 3d core level XPS spectra of CeO₂-773 and CeO₂-1173 samples in fresh form and after treatments under various reaction conditions. A difference spectrum (HCl treatment minus fresh sample) and a CeCl₃·6H₂O reference spectrum are included for comparison.

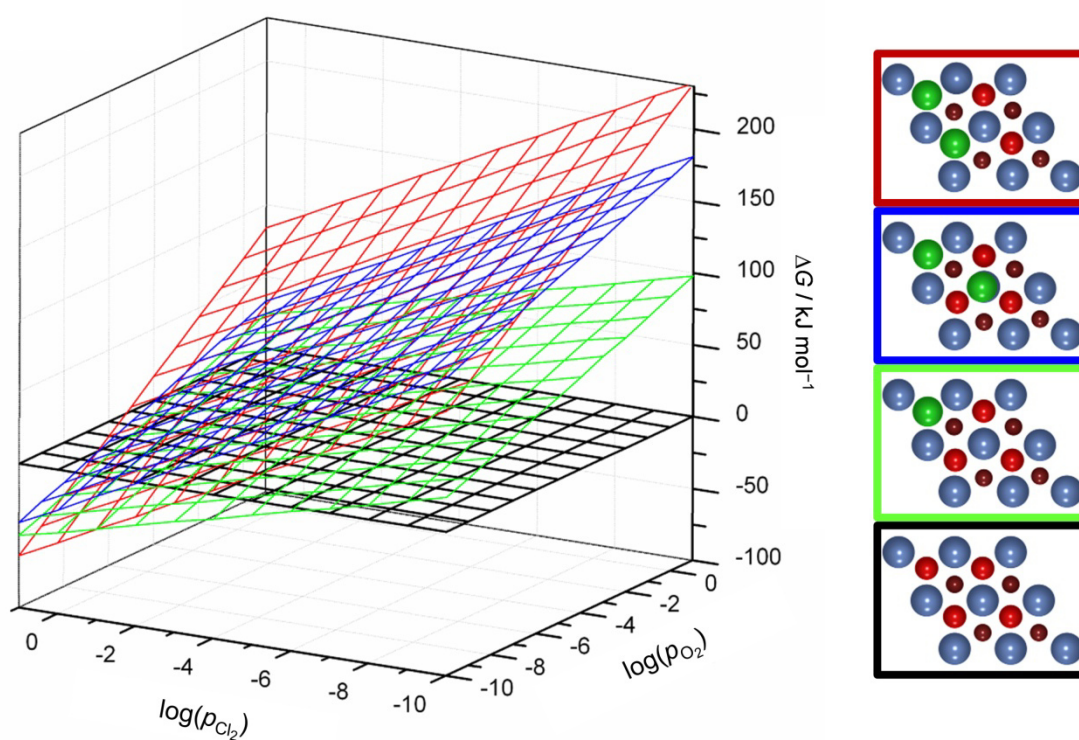


Figure S 2.11 First principles thermodynamics for the CeO₂(111) $p(2 \times 2)$ surface containing different amounts of chlorine. The plane showing the lowest energy ΔG at a given set of pressures is the most likely equilibrium structure under reaction conditions. The employed temperature was set to $T = 703.15$ K. The code for the configurations is indicated in the lowest panel: black for pure CeO₂(111); green for a single Cl occupying a vacancy on the surface; blue for a substituting Cl atom and a second Cl on top of a Ce site; and red for two Cl substituting two oxygen atoms on the surface. Grey spheres stand for Ce atoms, red for surface O atoms, scarlet for sub-surface O atoms, and green for Cl atoms.

2.6 References

- [1] J. Pérez-Ramírez, C. Mondelli, T. Schmidt, O.F.-K. Schlüter, A. Wolf, L. Mleczko, T. Dreier, *Energy Environ. Sci.* 4 (2011) 4786.
- [2] K. Seki, *Catal. Surv. Asia* 14 (2010) 168.
- [3] H. Deacon, U.S. Patent 85,370, 1868, assigned to Gaskell, Deacon and Co.
- [4] A.J. Johnson, A.J. Cherniavsky, U.S. Patent 2,542,961, 1951, assigned to Shell Development Company.
- [5] T. Kiyoura, N. Fujimoto, M. Ajioka, T. Suzuki, Y. Kogure, K. Kanaya, T. Nagayama, EP184413-A, 1984, assigned to Mitsui Chemicals.
- [6] T. Hibi, H. Nishida, H. Abekawa, U.S. Patent 5,871,707, 1999, assigned to Sumitomo Chemical Company.
- [7] C. Mondelli, A.P. Amrute, F. Krumeich, T. Schmidt, J. Pérez-Ramírez, *ChemCatChem* 3 (2011) 657.
- [8] A. Wolf, L. Mleczko, O.F. Schlüter, S. Schubert, EP2026905, 2006, assigned to Bayer Material Science.
- [9] M.A.G Hevia, A.P. Amrute, T. Schmidt, J. Pérez-Ramírez, *J. Catal.* 276 (2010) 141.
- [10] D. Crihan, M. Knapp, S. Zweidinger, E. Lundgren, C.J. Weststrate, J.N. Andersen, A.P. Seitsonen, H. Over, *Angew. Chem. Int. Ed.* 47 (2008) 2131.
- [11] J.P. Hofmann, S. Zweidinger, A.P. Seitsonen, A. Farkas, M. Knapp, O. Balmes, E. Lundgren, J.N. Andersen, H. Over, *Phys. Chem. Chem. Phys.* 12 (2010) 15358.
- [12] Retrieved from <http://www.platinum.matthey.com/pgm-prices>.
- [13] C. Mondelli, A.P. Amrute, T. Schmidt, J. Pérez-Ramírez, *Chem. Commun.* (2011) 7173.
- [14] R.W.G. Wyckoff, *Crystal Structures*, Interscience, New York, 1965.
- [15] R.J. Gorte, *AIChE J.* 56 (2010) 1126.
- [16] Q. Fu, H. Saltsburg, M. Flytzani-Stephanopoulos, *Science* 301 (2003) 935.
- [17] A. Primo, T. Marino, A. Corma, R. Molinari, H. Garcia, *J. Am. Chem. Soc.* 133 (2011) 6930.
- [18] Y.S. Chaudhary, S. Panigrahi, S. Nayak, B. Sarpati, S. Bhattacharjee, N. Kulkarni, *J. Mater. Chem.* 20 (2010) 2381.
- [19] M. Mogensen, N.M. Sammes, G.A. Tompsett, *Solid State Ionics* 129 (2000) 63.
- [20] B. Zhu, M.D. Mat, *Int. J. Electrochem. Sci.* 1 (2006) 383.
- [21] F. Zhou, X. Zhao, H. Xu, C. Yuan, *J. Phys. Chem. C* 111 (2007) 1651.
- [22] A. Trovarelli, *Catal. Rev. -Sci. Eng.* 38 (1996) 439.
- [23] A. Gómez-Cortés, Y. Márquez, J. Arenas-Alatorre, G. Díaz, *Catal. Today* 133-135 (2008) 743.
- [24] A. Martínez-Arias, A.B. Hungría, G. Munuera, D. Gamarra, *Appl. Catal., B* 65 (2006) 207.
- [25] W. Shin, C. Jung, J. Han, S. Nam, T. Lim, S. Hong, H. Lee, *J. Ind. Eng. Chem.* 10 (2004) 302.
- [26] T.X.T. Sayle, S.C. Parker, C.R.A. Catlow, *Surf. Sci.* 316 (1994) 329.
- [27] H.C. Yao, Y.F.Y. Yao, *J. Catal.* 86 (1984) 254.
- [28] F. Esch, S. Fabris, L. Zhou, T. Montini, C. Africh, P. Fornasiero, G. Comelli, R. Rosei, *Science* 309 (2005) 752.
- [29] N. Laosiripojana, W. Sutthisripok, P. Kim-Lohsoontorn, S. Assabumrungrat, *Int. J. Hydrogen Energy* 35 (2010) 6747.
- [30] R. Di Monte, J. Kašpar, *Top. Catal.* 28 (2004) 47.
- [31] A. Hagemeyer, P. Trübenbach, C.W. Rieker, M. Wünsch, O. Watzernberger, EP patent 0761594-A1, 1997.
- [32] A. Wolf, L. Mleczko, O.F. Schlüter, S. Schubert, WO2010133313-A1, 2010.
- [33] G. Lee, S.W. Lee, I. Sohn, Y.C. Kwon, J. Song, C.-S. Son, WO2009035234-A2, 2009.

- [34] G. Dutta, U.V. Waghmare, T. Baidya, M.S. Hegde, K.R. Priolkar, P.R. Sarode, *Chem. Mater.* 18 (2006) 3249.
- [35] G.R. Rao, B.G. Mishra, *Bull. Catal. Soc. India* 2 (2003) 122.
- [36] H.A. Al-Madfaa, M.M. Khader, *Mater. Chem. Phys.* 86 (2004) 180.
- [37] B.M. Reddy, P. Bharali, P. Saikia, *J. Phys. Chem. C* 112 (2008) 11729.
- [38] F. Deganello, A. Martorana, *J. Solid State Chem.* 163 (2002) 527.
- [39] A.P. Amrute, C. Mondelli, M.A.G. Hevia, J. Pérez-Ramírez, *J. Phys. Chem. C* 115 (2011) 1056.
- [40] G. Kresse, J. Hafner, *Phys. Rev. B* 47 (1993) 558.
- [41] J.-P. Perdew, K. Burke, M. Ernzerhof, *Phys. Rev. Lett.* 77 (1996) 3865.
- [42] M. Cococcioni, S. Gironcoli, *Phys. Rev. B* 71 (2005) 035105 and references therein.
- [43] M.V. Ganduglia-Pirovano, J.L.F. Da Silva, J. Sauer, *Phys. Rev. Lett.* 102 (2009) 026101 and references therein.
- [44] P.E. Blöchl, *Phys. Rev. B* 50 (1994) 17953.
- [45] H.J. Monkhorst, J.D. Pack, *Phys. Rev. B* 13 (1976) 5188.
- [46] G. Henkelman, B.P. Uberuaga, H. Jonsson, *J. Chem. Phys.* 113 (2000) 9901.
- [47] D. Terribile, A. Trovarelli, C. de Leitenburg, G. Dolcetti, J. Llorca, *Chem. Mater.* 9 (1997) 2676.
- [48] M.W.M. Hisham, S.W. Benson, *J. Phys. Chem.* 99 (1995) 6194.
- [49] A.P. Amrute, C. Mondelli, M.A.G. Hevia, J. Pérez-Ramírez, *ACS Catal.* 1 (2011) 583.
- [50] S. Tanuma, C.J. Powell, D.R. Penn, *Surf. Interface Anal.* 21 (1994) 165.
- [51] D. Teschner, R. Farra, L.-D. Yao, R. Schlogl, H. Soerijanto, R. Schomaecker, T. Schmidt, L. Szentmiklósi, A.P. Amrute, C. Mondelli, J. Pérez-Ramírez, G. Novell-Leruth, N. Lopez, *J. Catal.* 285 (2012) 273.
- [52] A. Badri, C. Binet, J. Lavalley, *Faraday Trans.* 92 (1996) 4669.
- [53] A. Laachir, V. Perrichon, A. Badri, J. Lamotte, E. Catherine, J.C. Lavalley, J. El Fallah, L. Hilaire, F. Le Normand, E.E. Quéméré, G.N. Sauvion, O. Touret, *Faraday Trans.* 87 (1991) 1601.
- [54] C. Binet, M. Daturi, J. Lavalley, *Catal. Today* 50 (1999) 207.
- [55] T.B. Lindemer, J. Brynestad, *J. Am. Ceram. Soc.* 69 (1986) 867.
- [56] J. Carrasco, N. Lopez, F. Illas, *Phys. Rev. Lett.* 93 (2004) 225502.
- [57] J. Carrasco, F. Illas, N. Lopez, E.A. Kotomin, Y.F. Zhukovskii, R.A. Evarestov, Y.A. Mastrikov, S. Piskunov, J. Maier, *Phys. Rev. B* 73 (2006) 064106.
- [58] P.M. Kowalski, M.F. Camellone, N.N. Nair, B. Meyer, D. Marx, *Phys. Rev. Lett.* 105 (2010) 146405.
- [59] S. Chretien, H. Metiu, *J. Phys. Chem. C* 115 (2011) 4696.
- [60] P.P. Dholabhai, J.B. Adams, P. Crozier, R. Sharma, *J. Chem. Phys.* 132 (2010) 094104.
- [61] N. Lopez, J.D. Prades, F. Hernandez-Ramirez, J.R. Morante, J. Pan, S. Mathur, *Phys. Chem. Chem. Phys.* 12 (2010) 2401.
- [62] X.G. Wang, A. Chaka, M. Scheffler, *Phys. Rev. Lett.* 84 (2000) 3650.
- [63] D.A. McQuarrie, J.D. Simon, *Molecular Thermodynamics*, University Science Books, Sausalito California, 1999.

Chapter 3: Synthesis and catalytic performance of CeOCl in Deacon reaction

Ramzi Farra, Frank Girgsdies, Wiebke Frandsen, Maike Hashagen, Robert Schlögl, Detre Teschner

Abstract

Surface chlorinated CeO₂ is an efficient material for HCl oxidation, which raises the question whether an oxychloride phase could be also active in the same reaction. CeOCl was synthesized by solid state reaction of cerium oxide with anhydrous cerium chloride and tested in HCl oxidation using various feed compositions at 703 K. X-ray diffraction of post-reaction samples revealed that CeOCl is unstable, in both oxygen-rich and -lean conditions. Applying oxygen over-stoichiometric feeds led to complete transformation of CeOCl into CeO₂. Considerable HCl conversions were obtained only after this transformation, which confirms the essential role of bulk cerium oxide in this catalytic system.

3.1 Introduction

The formation of CeOCl phase under reaction conditions or during sample preparation treatments has been experimentally verified in various heterogeneous catalytic systems [1–4]. In most cases, however, the formation of CeOCl is unintentional. This phase results from the interaction of cerium oxide with chlorine atoms. The origin and function of the components building up the cerium oxychloride differ according to the catalytic system used. For example, CeO₂ is utilized as a carrier in various catalytic systems (i.e. Pd/CeO₂, Rh/CeO₂). In this case Cl atoms may originate from chlorine-containing metal precursors (RhCl₃ or PdCl₂). Kepinski et al. [5] have studied by means of X-ray diffraction (XRD) and High Resolution Electron Microscopy (HREM) the mechanism of CeOCl formation in Pd/CeO₂ catalyst prepared from PdCl₂. They found that Cl atoms adsorbed on the surface of the ceria support are progressively incorporated into the oxygen vacancies as the reduction temperature increased. Ceria can be used also as a bulk catalytic material. In this case, chlorine-containing reactants (HCl or CCl₄) can dissociatively adsorb onto it, and consequently, Cl atoms may incorporate into cerium oxide and forming the CeOCl phase [1,6,7].

A comprehensive understanding of ceria-chlorine interaction and the nature of the halogenated oxide surface have drawn more attention recently, due to the newest findings of utilizing CeO₂ as a catalyst for the oxidative halogenation of CH₄ [8,9].

CeO₂ has been identified recently also as an efficient catalyst for HCl oxidation to chlorine (the Deacon reaction) [10] in the temperature range of 623–723 K [11,12]. Our previous studies have shown that CeO₂ suffers from bulk chlorination and hence deactivation when it is exposed to stoichiometric or sub-stoichiometric Deacon feeds (O₂:HCl ≤ 0.25) [11,13]. Furthermore, conducting the reaction at relatively low temperatures (<683 K) induces bulk chlorination too, even if over-stoichiometric feeds were applied [13]. The formation of the inactive CeCl₃·6H₂O phase was assigned as the main cause of losing reactivity upon bulk chlorination [11]. However, the quantitative analysis of the chlorine uptake studied by X-ray photoelectron spectroscopy has suggested that even if the catalyst was exposed to O₂-rich feeds (O₂:HCl = 2) at high temperature (703 K) chlorination in the very first subsurface layer could take place. Chlorine atoms can occupy surface sites as well as lattice oxygen vacancies, but yet no structural details are available for this chlorinated surface phase. This raises the question as to whether the bulk CeO₂ material has any influence on the catalytic performance or solely the coexistence of chlorine and oxygen species on the surface is an essential prerequisite for the reactivity of the catalyst. Moreover, using *in situ* techniques LaOCl was identified as an active intermediate phase catalyzing the destruction of chlorinated hydrocarbons with steam over lanthanide oxide-based catalysts [14]. Thus, similarly CeOCl may be also a candidate for an active surface phase in HCl oxidation. To answer these questions we have synthesized cerium oxychloride to assess its stability and catalytic performance under different Deacon reaction conditions. This phase has chlorine and oxygen species present in bulk and surface, as well, which can facilitate the assessment of the role of the surface O/Cl species and of the bulk CeO₂.

3.2 Experimental

3.2.1 Sample preparation

The polycrystalline CeOCl sample was prepared by solid state reaction between cerium oxide (Aldrich, 99%) and anhydrous cerium chloride (Aldrich, 99.9%). Excess amount of chloride was used to force the reaction to completion. A powder mixture of CeO₂ and CeCl₃ (molar ratio CeO₂:CeCl₃ = 1:2) was pressed into small pellets and placed in a horizontal quartz reactor tube surrounded by an oven. The solid state reaction was carried out in Ar flow (100 cm³ min⁻¹) at 1023 K for 10 hours, then cooled down to room temperature in Ar flow. The pellets retained their form (not melted), and their yellowish color turned white after reaction. The product was ground and washed using distilled water in order to dissolve the unreacted excess quantity of CeCl₃. Thereafter, the precipitate was filtered and dried in air at 353 K for 15 h. The CeOCl

(untreated) and CeOCl (after washing and drying treatment) will be referred hereafter as CeOCl-F and CeOCl-T, respectively. To the best of our knowledge, this is first time CeOCl has been intentionally synthesized from cerium chloride and cerium oxide via solid state reaction.

3.2.2 Characterization methods

XRD data were collected using a Bruker AXS D8 Advance Theta–theta diffractometer in Bragg–Brentano geometry, equipped with a Cu anode, a secondary graphite monochromator ($\text{CuK}\alpha_{1+2}$ radiation) and a scintillation counter. Patterns were recorded between 10 and $100^\circ 2\theta$ with a step width of 0.02° and a counting time of 15 s per step. The specific surface area was determined by nitrogen adsorption at 77 K using a Quantachrome 6 port BET system. Prior to the measurements the samples were evacuated for 5 h at 423 K. Thermogravimetric experiments (TGMS) were done on a NETZSCH Jupiter thermobalance in flowing argon ($100 \text{ cm}^3 \text{ min}^{-1}$). The gas evolution was measured with a quadrupole mass spectrometer (Pfeiffer Vacuum, Omnistar). Scanning electron microscopy (SEM) was conducted with a Hitachi S-4800 FEG and the micrographs were taken in the secondary electron (SE) mode at an accelerating voltage of 1.5 kV.

3.2.3 Catalytic test

The gas phase oxidation of hydrogen chloride was studied at ambient pressure at 703 K. Freshly prepared cerium oxychloride samples were utilized to investigate the catalytic activity of this phase under different O_2 to HCl feed ratios. 0.5 g of polycrystalline CeOCl was loaded in the tubular reactor (8 mm i.d.) and pretreated in N_2 at 703 K for 30 min. Thereafter, the reaction gases were introduced at a total flow of $166 \text{ cm}^3 \text{ min}^{-1}$. Various feed compositions were tested, which can be sorted out into two categories according to the oxygen partial pressure used: oxygen-rich ($\text{O}_2:\text{HCl} = 9$ and 2) and oxygen-lean conditions ($\text{O}_2:\text{HCl} = 0.5$ and 0.25). 5 h tests were carried out with fresh loads of CeOCl-T for each $\text{O}_2:\text{HCl}$ ratio. Post-reaction samples were collected for BET, SEM and XRD characterizations after rapidly cooling down the reactor to room temperature in a flow of N_2 . Reactivity was followed by means of iodometric titration.

3.3 Results and discussion

3.3.1 Synthesis and stability of CeOCl

Several synthesis routes to prepare rare-earth oxychlorides are known based on different ways to introduce the chlorine atom in the structure. Ammonium chloride has been used most frequently as chlorinating agent [15–18]. The solid state reaction of rare-earth oxide with NH_4Cl is taking place at temperatures (973 – 1273 K) [17] much higher than the ammonium chloride's sublimation temperature (611 K). Therefore, excess amount of NH_4Cl must be used at controlled temperature and flow. First, we have taken this approach for the synthesis of CeOCl. The primary results obtained from thermal gravimetric analysis (TGA) experiments were promising in terms of phase purity, but our attempts failed in scaling up this procedure.

Depner et al. [19] have developed a new route to synthesis CeOCl nanocrystals based on the condensation of cerium alkoxides with cerium halides. Depending on the alkoxide and halide precursors used it is possible to tune the composition and the size of the obtained nanocrystals. LaOCl was synthesized by mechano-chemical grinding of the corresponding oxide and chloride compounds [20].

Our CeOCl sample was prepared by solid state reaction of cerium oxide with excess amount of anhydrous cerium chloride, as detailed in section 3.2.1. The XRD patterns of CeOCl-T, CeOCl-F samples are shown in Figure 3.1 and compared to the pattern of CeOCl reference [21]. The diffractograms confirm the solid state reaction, and CeO_2 reflections are not obviously visible in either sample. However, fitting of the CeOCl-T diffractogram suggests 3% minority CeO_2 phase still present in the final material. The major impurity, as additional peaks with minor intensity, in the untreated sample (CeOCl-F) can be assigned to $\text{CeCl}_3 \cdot 7\text{H}_2\text{O}$ from the unreacted

excess of CeCl_3 precursor. This was washed out by water to obtain the final material. CeOCl has a PbFCL type crystal structure (tetragonal space group $P4/nmm$) with $a = 4.08$, $c = 6.83$ Å [20]. In this structure, the cerium has a 9-fold (capped square anti-prismatic) coordination environment, with four oxygen atoms forming the smaller basal square and 4+1 chlorine atoms a larger, mono-capped square plane.

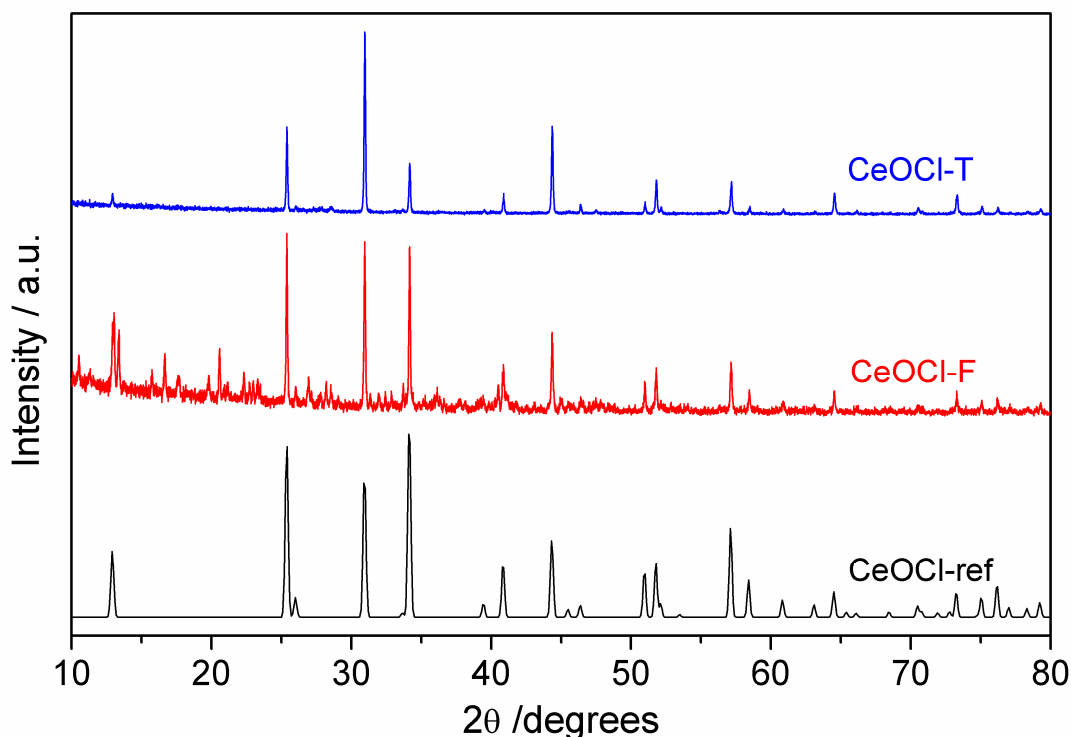


Figure 3.1 XRD pattern of CeOCl materials. CeOCl-T after cleaning treatment; CeOCl-F before cleaning treatment and CeOCl-ref as a reference [21].

Furthermore, the relative intensities of the CeOCl-T reflections indicate a pronounced preferred orientation, while this effect is only weakly developed in the sample before treatment. This indicates that a re-crystallization process took place during the cleaning process, producing more anisotropic crystallite morphology. The SEM photographs (Fig. 3.2a) of CeOCl-T confirm this observation and clearly display a plate-like morphology of the CeOCl-T particles with an average thickness of 2-3 μm and a particle size ranging from 5 to 20 μm . The BET surface area of CeOCl is relatively low ($8.7 \text{ m}^2\text{g}^{-1}$). The stability of CeOCl has been tested by means of thermogravimetric analysis coupled to mass spectroscopy (TGA-MS). The sample was heated up to 973 K (2 K min^{-1}) in Ar flow ($100 \text{ cm}^3 \text{ min}^{-1}$). The TGA curve (Fig. 3.3a) shows that the sample is essentially stable over the whole temperature range studied, and the minor weight loss of 0.5% at 573 K could be assigned according to the corresponding MS signal to the desorption of water molecules. Aging effect has been studied, in which the CeOCl-T sample was left exposed to ambient atmosphere over a long period of time (5 months), and thereafter its XRD spectrum was measured again. Over time water molecules adsorbed on the surface interact with CeOCl giving rise to phase transformation partially into $\text{Ce}(\text{OH})_2\text{Cl}$ (Fig. 3.4a). However, the original CeOCl phase can easily be restored by heating the sample in inert gas (Ar) (Fig. 3.4a), in which the evolution of water is observed at 570 K (Fig. 3.3b). No further decomposition was found at higher temperatures.

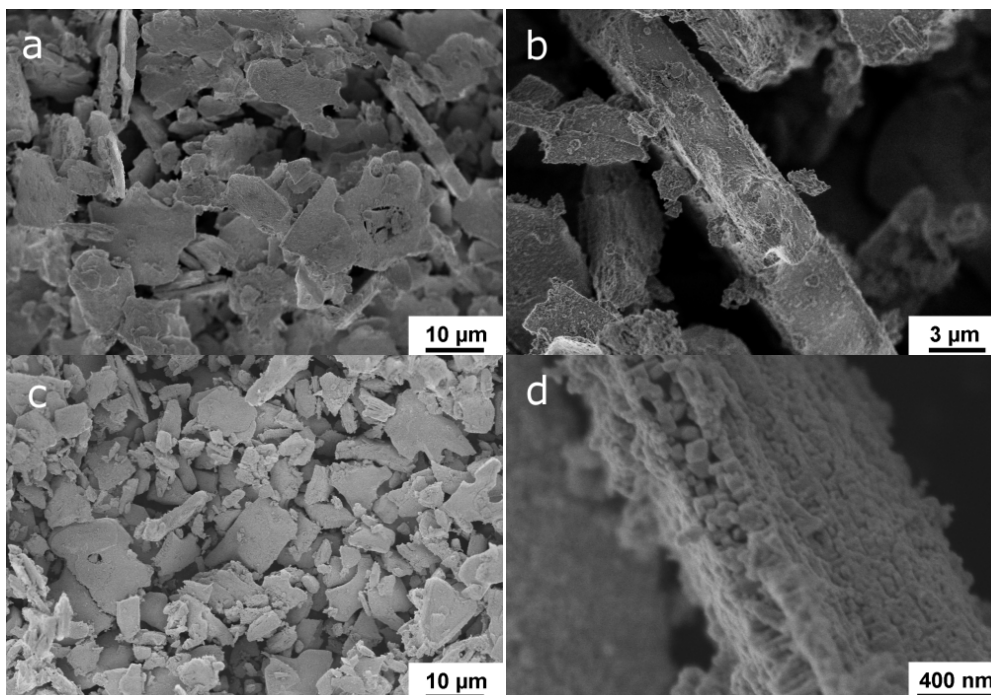


Figure 3.2 SEM photographs of CeOCl-T. (a) and (b): before HCl oxidation, (c) and (d): after reaction ($O_2:HCl = 9:1$ at 703 K).

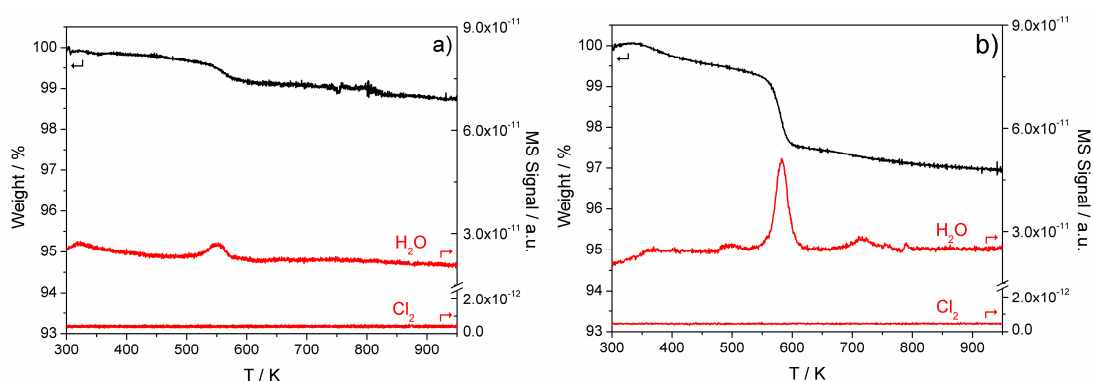


Figure 3.3 TGA-MS of CeOCl-T in Ar flow. (a) fresh material; (b) after 5 months exposure to ambient air

3.3.2 Catalytic activity of CeOCl in HCl oxidation

Freshly prepared CeOCl samples were tested as Deacon catalyst by exposing them to reaction feeds with different $O_2:HCl$ ratios at 703 K (Fig. 3.5a). The used samples were analyzed afterwards by XRD (Fig. 3.4b). In O_2 -lean regime ($O_2:HCl = 0.25$ or 0.5) HCl conversion was very low ($< 3\%$). The lowest $O_2:HCl = 0.25$ ratio led to the complete deactivation of the catalyst over time, whereas at $O_2:HCl = 0.5$ a very slight increase in reactivity trend was observed.

Beside CeOCl, CeO_2 , $CeCl_3 \cdot 3H_2O$ and $CeCl_3 \cdot 6H_2O$ were observed in the used sample exposed to the lowest feed ratio $O_2:HCl = 0.25$, CeO_2 being a significant component. CeO_2 was the dominant phase in the case of $O_2:HCl = 0.5$. These results reveal that chlorination and dechlorination are competing processes under these conditions, and furthermore the phase transformation to chloride is more likely passing through the formation of the corresponding oxide first.

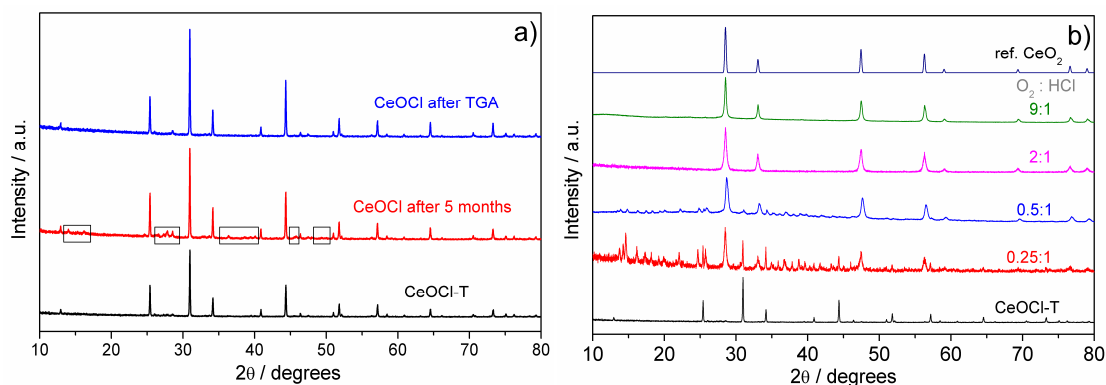


Figure 3.4 (a) X-ray powder diffraction patterns of CeOCl-T: after 5 months exposure to ambient air (reflections within boxes belong to $\text{Ce}(\text{OH})_2\text{Cl}$), after TGA treatment of CeOCl-T exposed to air for 5 month with the fresh CeOCl for comparison. (b) XRD spectra of CeOCl-T samples before and after reaction using different feed ratios, with added CeO_2 reference.

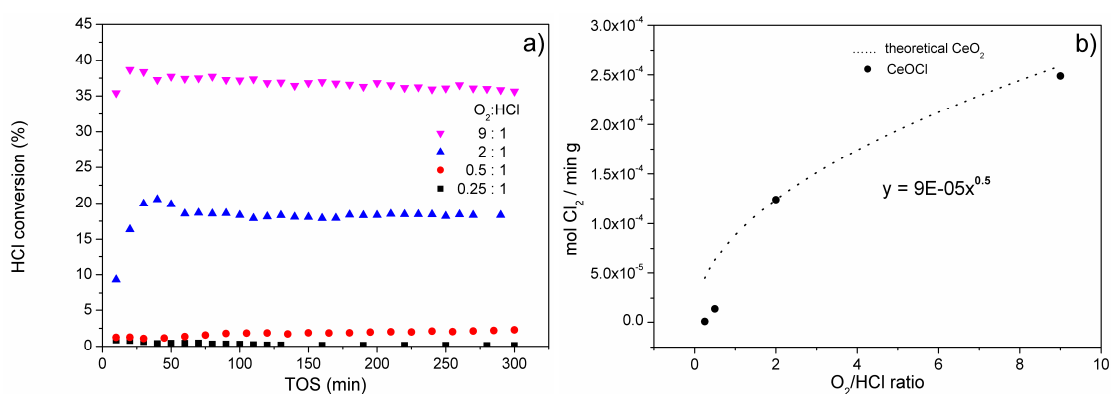


Figure 3.5 (a) reactivity of CeOCl-T at different feed ratios with time on stream. (b) comparison of Cl_2 productivity of CeOCl at different $\text{O}_2:\text{HCl}$ ratios with a theoretical 0.5 order dependence observed for CeO_2 .

Samples exposed to relatively high feed ratio, $\text{O}_2:\text{HCl} = 2$ and 9 , have shown that the original CeOCl was fully transformed into CeO_2 (Fig. 3.4b). At $\text{O}_2:\text{HCl} = 2$, the initially low HCl conversion progressively increased, reaching the activity level exhibited by a pure reference ceria at identical conditions [11]. Furthermore, $\text{CeCl}_3 \cdot 6\text{H}_2\text{O}$ transformed also to CeO_2 under these conditions reaching similar reactivity [13]. The highest HCl conversion ($\sim 37\%$) was achieved by using excess of O_2 at feed ratio $\text{O}_2:\text{HCl} = 9$. An overshooting of HCl conversion observed at the beginning of the reaction can be plausibly assigned to the additional contribution of Cl_2 produced during the transformation of CeOCl to CeO_2 and the high exothermicity of this transformation. This process depends on the $p(\text{O}_2)$ used in the feed, and hence is faster for CeOCl sample exposed to higher $\text{O}_2:\text{HCl}$ ratio. The SEM photograph (Fig. 3.2c) of the used sample ($\text{O}_2:\text{HCl} = 9$) shows that the plate-like morphology is retained but the particles themselves consist of compact agglomeration of very fine particles (Fig. 3.2d). This is in line with the surface area increase of the samples after reaction (BET = $28 \text{ m}^2/\text{g}$ for $\text{O}_2:\text{HCl} = 9$). The average Cl_2 productivity of CeOCl samples measured at different $\text{O}_2:\text{HCl}$ feed ratios ($\text{O}_2:\text{HCl} = 0.25, 0.5, 2$ and 9) is plotted in Fig. 3.5b. It is known that the apparent O_2 reaction order of pure CeO_2 is ~ 0.5 [11]. Since XRD suggested the formation of CeO_2 , a theoretical 0.5 order curve representative of CeO_2 is also included in Fig. 3.5b, and is aligned at $\text{O}_2:\text{HCl} = 2$ with the measured dataset. Not surprisingly, the data point at $\text{O}_2:\text{HCl} = 9$ follows reasonably the trend. However, the oxygen lean points are clearly inferior. This discrepancy can be partially

rationalized considering that the surface area of the CeO₂ is larger than that of CeOCl, and the partially formed chloride phase is inactive in Deacon conditions.

Since CeOCl is not stable in either O₂-rich or lean conditions, its intrinsic catalytic performance could not be assessed. Nevertheless, the results suggest that the sole existence of surface O and Cl species in the oxychloride matrix is not enough to maintain stable HCl oxidation reactivity and the existence of the bulk cerium oxide phase seems to be a prerequisite to ensure efficient and stable catalytic performance. The bulk oxide structure offers oxygen vacancies that are required for the O₂ activation process. Furthermore, its surface can withstand high degree of chlorination without phase transformation into chloride if oxygen over-stoichiometry is maintained. In spite of the catalytic reaction taking place on the surface, the co-existence of a slightly oxygen deficient bulk phase (CeO₂ with O vacancies) facilitating the mobility of vacancies between bulk and surface seems to be indispensable in this system.

3.4 Conclusion

Cerium oxide is now a well-established HCl oxidation catalyst with a high degree of surface chlorination. Since HCl oxidation requires both HCl and O₂ activation, both reactants need to coexist on the catalyst surface. Here, we synthesized and tested CeOCl in HCl oxidation in order to assess the importance of bulk oxide phase in the ceria system and to find out whether the sole presence of surface O and Cl species incorporated into the catalyst surface is enough to achieve stable and efficient catalytic performance. Our experiments have shown that CeOCl is not stable in HCl oxidation, neither in oxygen-lean nor in oxygen-rich conditions. The results suggest that the bulk oxide phase plays a significant role in the cerium oxide based HCl oxidation system, probably facilitating efficient O₂ activation via bulk and surface O-vacancy dynamics with the ability to dissociatively adsorb HCl, without giving rise to phase transition in an oxygen over-stoichiometric reaction feed.

3.5 References

- [1] Weckhuysen, B. M.; Rosynek, M. P.; Lunsford, J. H. *Phys. Chem. Chem. Phys.* **1999**, *1*, 3157–3162.
- [2] Fajardie, F.; Tempere, O.; Manoli, J.-M.; Djega-Mariadassou, G.; Blanchard, G. *J. Chem. Soc., Faraday Trans.* **1998**, *94*, 3727–3735.
- [3] Kepiński, L.; Wołczyrz, M.; Okal, J. *J. Chem. Soc., Faraday Trans.* **1995**, *91*, 507–515.
- [4] Le Normand, F.; Barrault, J.; Breault, R.; Hilaire, L.; Kiennemann, A. *J. Phys. Chem.* **1991**, *95*, 257–269.
- [5] Kepinski, L.; Okal, J. *J. Catal.* **2000**, *192*, 48–53.
- [6] De Rivas, B.; Lopez-Fonseca, R.; Gutierrez-Ortiz, M. A.; Gutierrez-Ortiz, J. I. *Appl. Catal. B-Environ.* **2011**, *104*, 373–381.
- [7] Farra, R.; Wrabetz, S.; Schuster, M. E.; Stotz, E.; Hamilton, N. G.; Amrute, A. P.; Pérez-Ramírez, J.; López, N.; Teschner, D. *Phys. Chem. Chem. Phys.* **2013**, *15*, 3454–3465.
- [8] He, J.; Xu, T.; Wang, Z.; Zhang, Q.; Deng, W.; Wang, Y. *Angew. Chem.-Int. Edit.* **2012**, *51*, 2438–2442.
- [9] Hu, Z.; Metiu, H. *J. Phys. Chem. C* **2012**, *116*, 6664–6671.
- [10] Pérez-Ramírez, J.; Mondelli, C.; Schmidt, T.; Schlueter, O. F.-K.; Wolf, A.; Mleczko, L.; Dreier, T. *Energy Environ. Sci.* **2011**, *4*, 4786–4799.
- [11] Amrute, A. P.; Mondelli, C.; Moser, M.; Novell-Leruth, G.; Lopez, N.; Rosenthal, D.; Farra, R.; Schuster, M. E.; Teschner, D.; Schmidt, T.; Pérez-Ramírez, J. *J. Catal.* **2012**, *286*, 287–297.
- [12] Moser, M.; Mondelli, C.; Schmidt, T.; Girgsdies, F.; Schuster, M. E.; Farra, R.; Szentmiklosi, L.; Teschner, D.; Pérez-Ramírez, J. *Appl. Catal. B-Environ.* **2013**, *132*, 123–131.
- [13] Farra, R.; Eichelbaum, M.; Schloegl, R.; Szentmiklosi, L.; Schmidt, T.; Amrute, A. P.; Mondelli, C.; Perez-Ramirez, J.; Teschner, D. *J. Catal.* **2013**, *297*, 119–127.
- [14] Weckhuysen, B. M. *Phys. Chem. Chem. Phys.* **2003**, *5*, 4351–4360.
- [15] Hölsä, J.; Niinistö, L. *Thermochimica Acta* **1980**, *37*, 155–160.
- [16] Song, K.; Kauzlarich, S. M. *Chem. Mater.* **1994**, *6*, 386–394.
- [17] Hölsä, J.; Lahtinen, M.; Lastusaari, M.; Valkonen, J.; Viljanen, J. *Journal of Solid State Chemistry* **2002**, *165*, 48–55.
- [18] Zhu, G. C.; Li, F. P.; Xiao, M. G. *Trans. Nonferrous Met. Soc. China* **2003**, *13*, 1454–1458.
- [19] Depner, S. W.; Kort, K. R.; Jaye, C.; Fischer, D. A.; Banerjee, S. *J. Phys. Chem. C* **2009**, *113*, 14126–14134.
- [20] Lee, J.; Zhang, Q.; Saito, F. *Journal of Solid State Chemistry* **2001**, *160*, 469–473.
- [21] Wołczyrz, M.; Kepinski, L. *Journal of Solid State Chemistry* **1992**, *99*, 409–413.

Chapter 4: Understanding CeO₂ as a Deacon catalyst by probe molecule adsorption and *in situ* infrared characterizations

Ramzi Farra, Sabine Wrabetz, Manfred E. Schuster, Eugen Stotz, Neil G. Hamilton, Amol P. Amrute, Javier Pérez-Ramírez, Núria López, Detre Teschner

Abstract

CeO₂ has been identified as an efficient catalyst for HCl oxidation in the temperature range of 623–723 K provided that the oxygen content in the feed mixture was sufficiently high to avoid bulk chlorination and thus deactivation. Here we characterize ceria in its fresh and post-reaction states by adsorption of CO₂, NH₃ and CO. Micro-calorimetry, FTIR and TPD experiments are complemented by DFT calculations, which assess adsorption energies and vibrational frequencies. The calculations were performed on the lowest energy surface, CeO₂(111), with perfect termination and with various degrees of hydroxylation and/or chlorination. Both experiments and calculations suggest that the basic character of the ceria surface has been eliminated upon reaction in HCl oxidation, indicating that most of the basic lattice O sites are exchanged by chlorine and that the OH groups formed are rather acidic. The density and the strength of surface acidic functions increased significantly upon reaction. An *in situ* FTIR reaction cell has been designed and constructed to study the evolution of OH group density of the ceria surface during HCl oxidation. The effect of experimental variables, such as *p*O₂, *p*HCl and temperature, has been investigated. We found that the OH group density positively correlated with the reactivity in the *p*O₂ and temperature series, whereas negative correlation was observed when *p*HCl was varied. Implications of the above observations to the reaction mechanism are discussed.

Acknowledgements

Bayer MaterialScience, the ICIQ Foundation, MICINN (CTQ2009-07753/BQU), BSC-RES are acknowledged for financial support. We thank Bayer MaterialScience for permission to publish these results.

4.1 Introduction

Chlorine is manufactured on the large scale by electrolysis of aqueous NaCl or HCl solutions. The heterogeneously catalysed gas phase HCl oxidation (Deacon reaction) over supported RuO₂ materials offers a viable alternative route to produce Cl₂ [1-7]. Despite its recent implementation, the quest for cheaper catalysts led to the recognition of CeO₂ as a highly stable HCl oxidation catalyst [8]. Our performance and characterization results [8] showed that mildly high-temperature (1173 K) calcined material represents an optimum between stabilised surface and unacceptable loss of surface area. The surface of ceria is chlorinated during the reaction and inactive cerium chloride may form when the oxygen over-stoichiometry of the reaction feed is low. As opposed to the metallic nature of RuO₂, ceria requires redox chemistry and thus oxygen vacancies impact the catalytic activity. In a simplified view, the mechanism of Deacon reaction involves reactive HCl adsorption via proton abstraction in the formation of OH and surface Cl, recombination of these species (H₂O and Cl₂) and surface re-oxidation by dissociative oxygen activation. It is suggested that several of these steps require an anionic vacancy.

Infrared spectroscopy (FTIR) offers the possibility to characterize surface acid/base properties that can be regarded as a crucial parameter in the adsorption energetics but also in the surface reaction steps of HCl oxidation. Moreover, infrared techniques enable observation of surface species under reaction conditions. *In situ* studies of surface species using FTIR, determination of surface sites and the various cell designs available for these studies have been recently reviewed [9-11]. Ceria is used as a carrier or additive in various catalytic processes, and *in situ* FTIR has been regularly utilised to extract mechanistic details in reactions such as the water-gas shift [12-15], reverse-WGS [16,17], low-temperature CO oxidation [18-20], and PROX [21,22]. *In situ* FTIR studies on ceria as the main catalytic material are, however, much scarcer [23,24].

In this manuscript, we aim at understanding how the surface acid/base properties of fresh ceria are modified by HCl oxidation. For this purpose, FTIR and micro-calorimetric characterization of probe molecules (CO₂, NH₃ and CO) in combination with DFT calculations have been applied. Furthermore, we have designed an *in situ* FTIR cell to study ceria under Deacon reaction in the transmission geometry. This cell withstands the corrosive ambient represented by the reaction gas mixture containing HCl, O₂, Cl₂ and H₂O. In the *in situ* experiments we tried to quantify OH groups formed under HCl oxidation and understand their role in the overall mechanism.

4.2 Experimental

4.2.1 Samples

Unsupported CeO₂ (Aldrich) was calcined in static air at 1173 K (10 K min⁻¹) for 5 h. This sample, either as fresh (hereafter denoted as CeO₂-F) or after Deacon reaction (treated at various feed conditions, ending with O₂:HCl= 9:1 at 593 K, hereafter denoted as CeO₂-D) was used for characterizations.

4.2.2 HRTEM characterization

High resolution transmission microscopy with aberration correction (FEI Titan Cs 800-300) was utilised to assess the morphology of the ceria particles.

4.2.3 NH₃ temperature programmed desorption

NH₃-TPD was measured in a Thermo TPDRO 1100 unit equipped with a thermal conductivity detector. The samples (300 mg) were loaded in the quartz micro-reactor (11 mm i.d.), pre-treated in He (20 cm³ STP min⁻¹) at 573 K for 3 h, and cooled to 373 K in He. NH₃ was chemisorbed at 373 K in three consecutive cycles of saturation with 10 vol.% NH₃/He (20 cm³ STP min⁻¹) for 30 min followed by purging with He (20 cm³ STP min⁻¹) at the same

temperature for 30 min. Desorption of NH₃ was monitored in the range of 323-1273 K using a heating rate of 20 K min⁻¹ and a He flow of 20 cm³ STP min⁻¹.

4.2.4 Micro-calorimetry

Micro-calorimetric experiments were carried out in a Calvet calorimeter (SETARAM MS70) combined with a high vacuum system, which enables the dosage of probe molecules within a range of 0.02 μmol. The samples were pre-treated according to the following procedure: CeO₂-F was exposed to synthetic air at 773 K for 5 h, whereas CeO₂-D (after Deacon) was only degassed under UHV at 423 K for 5 h. The pre-treatment was conducted in a separate chamber connected to the calorimetric cell. The final pressure in the degassed cell was approximately 10⁻⁶ mbar. The cell was cooled to room temperature, placed inside the calorimeter, and connected to the micro-calorimetric gas-adsorption system. Subsequently, CO₂ or NH₃ were dosed stepwise at 313 K. Pressure, adsorption temperature, and the heat signals were recorded during all dosing and desorption steps. Desorption was performed at adsorption temperature in UHV. In all calorimetric sections positive energy corresponds to an exothermic process.

4.2.5 Probe molecule adsorption by FTIR

Fourier transform infrared spectroscopic measurements were carried out using a Perkin-Elmer Pe100 spectrometer equipped with a MCT detector. The spectra were recorded with a resolution of 2 cm⁻¹ and accumulation of 64 scans. Self-supported wafers were prepared by pressing the sample under a pressure of 230 bar. The samples were activated first *in situ* prior to IR measurements. The cell is connected to a vacuum system with a residual pressure of ca. 1x10⁻⁷ mbar. Background spectrum of the empty cell was used to subtract the CO adsorption spectra of the sample. CO was initially dosed at 77 K up to equilibrium pressure (1.86 mbar for non-chlorinated and 1.31 mbar for chlorinated ceria). Then, the gas was evacuated in sequential steps in order to study the coverage dependence.

4.2.6 *In situ* FTIR in HCl oxidation

An *in situ* transmission FTIR cell (Fig. 4.1) has been designed to enable investigating Deacon catalysts under reaction condition. Details to the cell design will be discussed in the Results section.

CeO₂-F sample was pressed into a self-supporting disc (31.8 mg cm⁻²) and placed in the sample holder in the center of the furnace of the IR cell. The sample was heated in flowing synthetic air up to 723 K (10 K min⁻¹) and allowed to stabilise for 90 min. Spectra were recorded with a Varian-670 FTIR spectrometer at the reaction conditions indicated. A resolution of 4.0 cm⁻¹ was used throughout the investigation and in most cases 512 scans were averaged to achieve a satisfactory signal-to-noise ratio. Reactivity was followed by means of iodometric titration. Reaction feed, at constant 100 cm³ STP min⁻¹ total flow, was supplied by mass flow controllers. The Deacon reaction was started in an oxygen-rich atmosphere with a feed composition O₂:HCl:N₂ = 9:1:0 at 703 K. The reaction was maintained at this condition for 16 h before starting to investigate the effects of various reaction conditions (p_i , T). During the O₂ partial pressure dependence, the HCl flow was kept constant at 10 cm³ STP min⁻¹ and the O₂ flow was varied according to the following feed composition sequence: O₂:HCl:N₂ = 9:1:0, 4:1:5, 2:1:7, 1:1:8 and 0.5:1:8.5. During the measurement of HCl partial pressure dependence, the O₂ flow was kept constant at 20 cm³ STP min⁻¹ and the HCl flow was changed as follows: 10, 6, 3 and 1 cm³ STP min⁻¹. The time interval for each of the above steps was ~5 h, and the temperature was kept constant at 703 K. The temperature effect was studied at an oxygen-rich feed composition of O₂:HCl:N₂ = 9:1:0 by reducing the temperature, stepwise by 20 K, starting from 703 K and ending at 623 K. The time interval for each step was ~4 h.

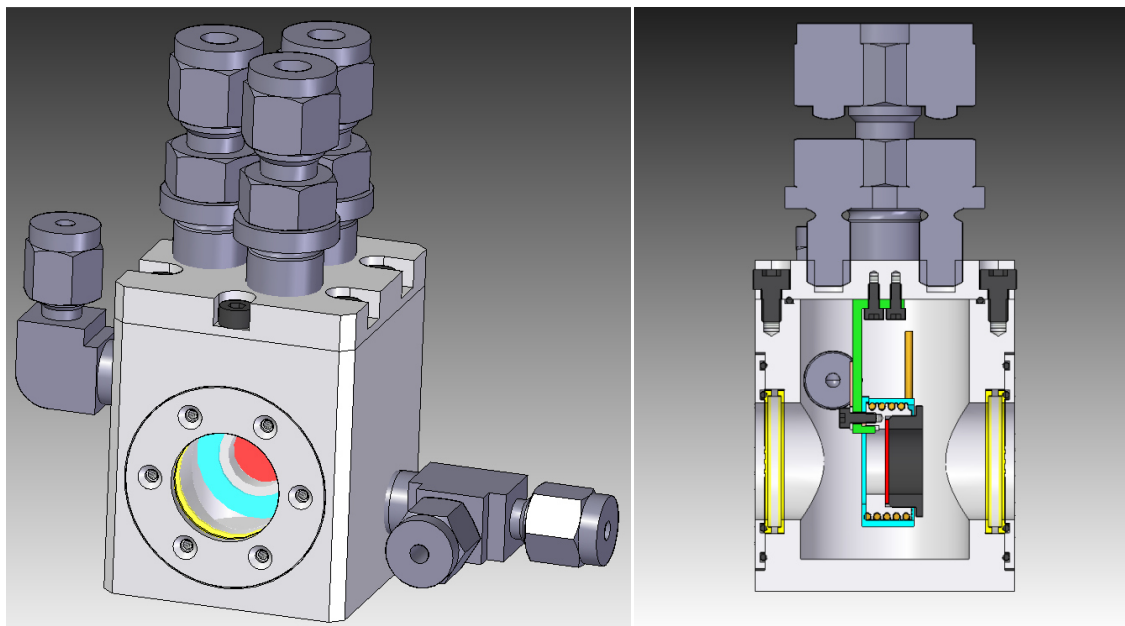


Figure 4.1 Scheme of the *in situ* FTIR cell with gas inlet and outlet at the sides and three feedthroughs at the top (2 for thermocouples and one for heating). The investigated sample (red) is held in a heatable stage.

4.2.7 Density Functional Theory (DFT) calculations of probe molecule adsorption

Density functional theory (DFT) simulations have been applied to CeO₂ slabs. The calculations were performed with the 5.2.12 version of the VASP code [25]. The functional of choice was PBE+U [26], to partially account for self-interaction issues in the f-electrons. The U parameter chosen was set to 4.5 [27-29]. Inner electrons were replaced by PAW pseudopotentials [30] while the 12 valence electrons of Ce atoms in the 5s, 5p, 6s, 4f, 5d states and the 6 valence electrons of O atoms were considered explicitly. The valence electrons were expanded in plane waves with a cut off energy of 400 eV. For further details the reader is referred to ref. [8]. The lowest energy surface, CeO₂(111) was taken as representative of the material. The chosen slab corresponds to a p(2 × 2) reconstruction and contains 3 layers. The k-point sampling was set to 5 × 5 × 1 [31]. Slabs were interleaved by 10 Å and artificial polarisation interactions due to the asymmetry of the adsorption configuration were removed by standard procedures. Spin polarised calculations were performed when needed. Vibrational frequencies were calculated through the diagonalisation of the numerical Hessian obtained by displacements of ±0.02 Å for each degree of freedom. A description of how good theoretical methods are at analysing acid-base properties of surfaces can be found elsewhere [32]. The full tables with adsorption energy and frequency calculations and spin states are presented in the Supporting Information and only the most representative features are described in the main text.

4.3 Results and discussion

4.3.1 HRTEM

HRTEM analysis of the CeO₂-F sample mostly revealed well faceted particles in the range of 20-50 nm with a few larger particles around 100 nm (Fig. 4.2). Many particles show (111) lattice fringes with a well faceted surface, suggesting the formation of energetically stable surface orientations. The sample after 80 h in the Deacon reaction revealed some changes in the morphology of the particles. The overview micrographs show the relatively broad particle size distribution being conserved, though many of the sharp corners of the CeO₂ particles seem to be smoothed and rounded upon the reaction. Despite the smoothen of edges, the crystalline structure remains that of CeO₂.

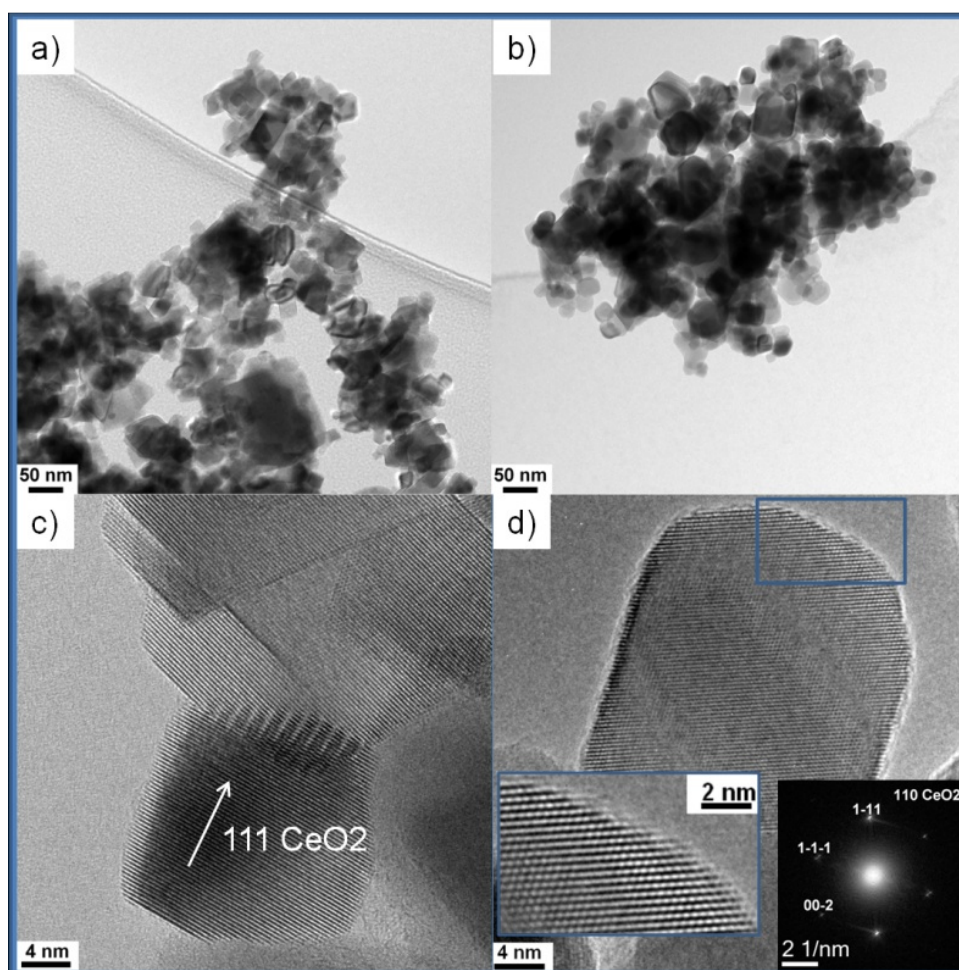


Figure 4.2 TEM and HRTEM comparison of CeO₂ before (a, c) and after Deacon reaction (b, d). The sample after reaction was taken from the pellet used for the *in situ* FTIR experiments.

4.3.2 Micro-calorimetry and corresponding DFT analysis

The pressure-controlled dosing system of the calorimeter with calibrated volume enables the quantification of adsorbed molecules (adsorption isotherm) as well as the differential heat of adsorption; and gives the possibility to elucidate the distribution of the adsorption sites along the range of adsorption heats. These results (Fig. 4.3) are compared with the modelling obtained through DFT in order to unravel the nature of the adsorption sites. It has been shown that the Deacon reaction gives rise to surface chlorination [8], thus, it is expected that acid-base properties of the surface are modified. Ceria is an amphoteric compound showing both surface acidity and basicity. Therefore, NH₃ and CO₂ probe molecules were used to assess acidic and basic properties of the samples, respectively, before and after reaction. For comparison, calculations were performed on different models representing the local structures in Fig. 4.4. Adsorption of probe molecules using DFT calculations has been performed on a model CeO₂ (111) surface and with different degrees of hydroxylation and/or defects involved, Fig. 4.4. (For the configurations with adsorbates see Fig. S 4.1). Finally, a summary with the assignments based on either adsorption energies or frequencies is proposed, (Table 4.1).

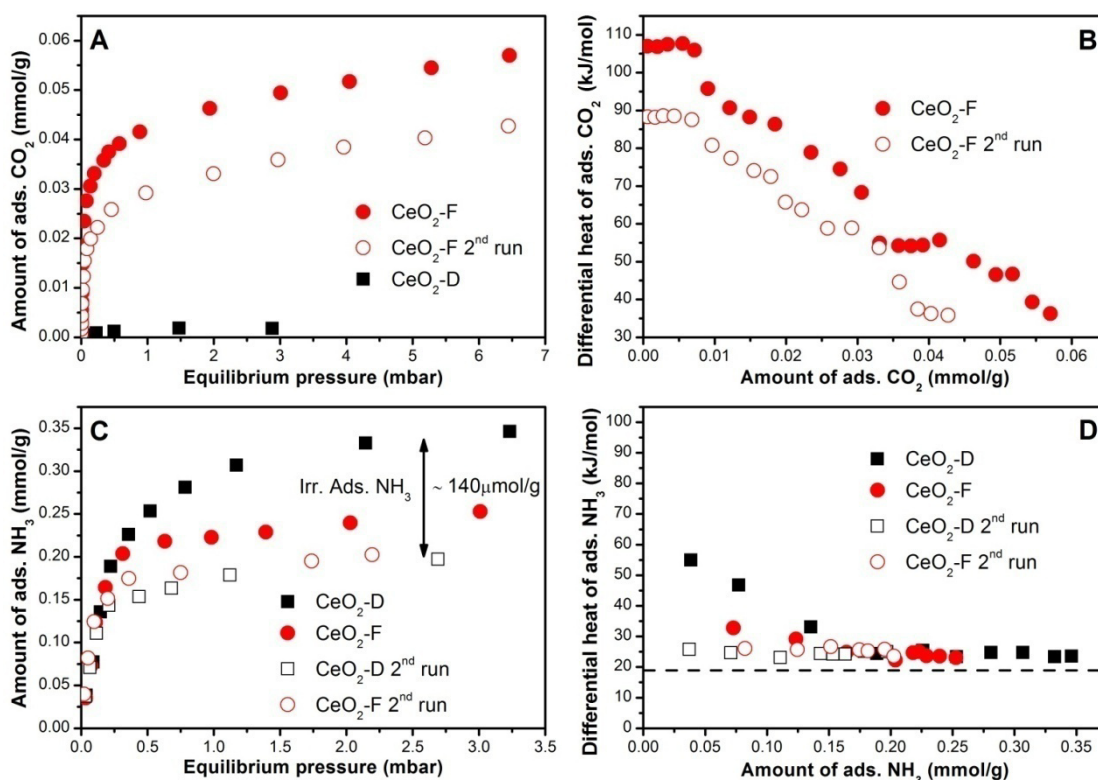


Figure 4.3 Adsorption isotherms (a, c) and differential heat of adsorption data of CO₂ (a, b) and NH₃ (c, d) on fresh and post Deacon CeO₂ studied by micro-calorimetry. When indicated, a 2nd adsorption was carried out after desorption in UHV. T = 313 K.

CO₂ adsorption was performed at 313 K in order to derive information from the pure adsorption process by suppressing secondary reactions, which have been shown to occur at higher temperatures [33]. The results are depicted in Fig. 4.3a,b. The differential heat of adsorption profile as a function of CO₂ uptake for the CeO₂-F demonstrates energetically wide distribution of basic interacting sites. Nevertheless, two distinct sites exhibited uniformity, as can be recognised by two plateaus at very low and relatively high pressures (Fig. 4.3b). The amount of these two energetically homogeneous sites (*ca.* 7 μmol g⁻¹ CO₂ adsorbed for each plateau) is small in comparison to the whole available basic sites on the surface. The initial heat of adsorption is about 110 kJ mol⁻¹. These adsorption energies were suggested to correspond to

structural defects such as edges in nanoparticles [34] or vacancies in more open facets such as (110) [35]. In our calculations, multiple (3) CO₂ adsorption on a single vacancy site could account for a large average adsorption energy > 100 kJ mol⁻¹ (see Table S 4.3). The adsorption energy profile in Fig. 4.3b decreases gradually with coverage until reaching the second plateau at about 55 kJ mol⁻¹. This energy plateau can be assigned to the formation of carbonate species (our calculation: 43 kJ mol⁻¹) with the basic O atoms on the surface (Fig. S 4.1 (i)). In Fig. 4.3b, small amount of CO₂ adsorbed with lower heat of adsorption values. Indeed, the calculations show that the interaction with partially hydroxylated surfaces is weaker (18 kJ mol⁻¹ and lower) and similar values are retrieved for oxygen vacancies when one of the O atoms of the CO₂ molecule fills the vacancy. Repeated adsorption experiment after desorption (at 313 K, UHV) revealed a certain degree of irreversible adsorption; either related to strong adsorption on low coordination sites and/or carbonate formation. The decrease of the heat of adsorption at the first plateau may be explained by the repulsive interaction of CO₂ with the irreversibly adsorbed species. By considering the wide range of heats of adsorption, it can be conveniently concluded that both Lewis and Brønsted basic sites are present in the non-chlorinated sample.

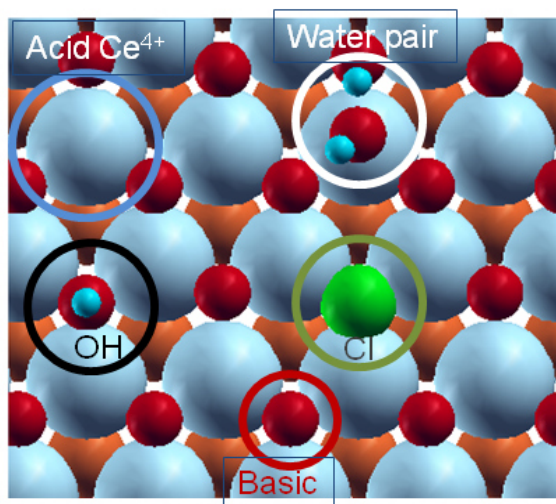


Figure 4.4 Schematic representation of adsorption sites on the CeO₂(111) surface. The different sites are highlighted by the circles. Light blue spheres represent Ce atoms, orange sub-surface O atoms, red O, green Cl and dark blue H. CeO₂H (O_{lattice}H) corresponds to the OH group on the left and CeO₂H-OH is the water pair.

In contrast to CeO₂-F, CO₂ does not show any considerable interaction with the chlorinated surface, even at relatively high CO₂ pressures (Fig. 4.3a). Indeed, very weak adsorption energies were calculated on the models for the partially chlorinated surfaces (see Table S 4.3). Therefore, we can confidently infer that during the reaction CeO₂ lost basicity due to surface chlorination and acidic hydroxyl formation (detailed in latter sections). In other words, the population of Lewis sites seem to be greatly attenuated [36] and Brønsted sites (OH groups) do not possess basic properties anymore.

NH₃ was employed to investigate acidic properties of the samples. Due to stainless steel tubing applied in our micro-calorimetric setup, the determination of the initial differential heat of adsorption values was not straightforward. Hence, initial values at very low NH₃ pressures were not analysed. The ammonia adsorption results are illustrated in Fig. 4.3c,d. The chlorinated sample gave rise to enhanced interaction up to ~150 μmol g⁻¹ adsorption, after which both samples reach a plateau at ~ 25 kJ mol⁻¹. The isotherm and heat of adsorption values demonstrate an increased acidity of the chlorinated surface. Re-adsorption evidences a significantly higher amount (~×3) of irreversibly held ammonia on the sample after Deacon reaction. The concomitant presence of high proton density, leading to a larger

number of NH₄⁺ groups, and high polarisability of the chlorine atoms on the surface that increases the electrostatic interactions can be responsible for the enhanced ammonia adsorption in the post-reaction sample.

FTIR spectra for ammonia adsorption on fresh and chlorinated samples (not shown) also reveal a stronger interaction of NH₃ with the chlorinated sample, as the peaks that are believed to correspond to the interaction with Brønsted (1396 cm⁻¹) and Lewis (1557 cm⁻¹) [37] acid sites are both shifted to the higher frequencies in this case. This is indeed seen from the calculations as the direct interaction to Ce⁴⁺ sites is calculated to give a main peak at 1593 cm⁻¹, which shifted upon chlorination to 1615-1612 cm⁻¹. Other bands in the same region may correspond to NH₃ adsorption to hydroxyl groups on the surface, 1566, 1562 (CeO₂H) and 1583 cm⁻¹ (CeO₂H-OH).

The acid strength distribution on the CeO₂ samples related to the *irreversible* NH₃ adsorption in the micro-calorimetry was studied further by NH₃-TPD in the range of 323-1273 K (Fig. 4.5). The distribution of acid sites on the fresh CeO₂ is broad, indicating the presence of both medium and strong acid sites. The medium acid sites appear to be much more abundant than strong ones. These results are in good agreement with previous literature reporting on the acidity/basicity of rare-earth oxides [38]. For the CeO₂-D sample new TPD peak centered at *ca.* 555 K and a large peak in the broad range of 800-1000 K appeared. These peaks cannot be due to chlorine desorption from the catalyst surface as the TGA-MS analysis showed a very small amount of chlorine leaving the surface (in the range of 500-660 K, Fig. S 4.2). Accordingly, these peaks are attributed to the generation of new medium and strong acid sites during HCl oxidation. Integration of the TDS signal yields an approximately 3-times higher response for the CeO₂-D sample in good agreement with the observed ratio of irreversible NH₃ adsorption by microcalorimetry (see Fig. 4.3c).

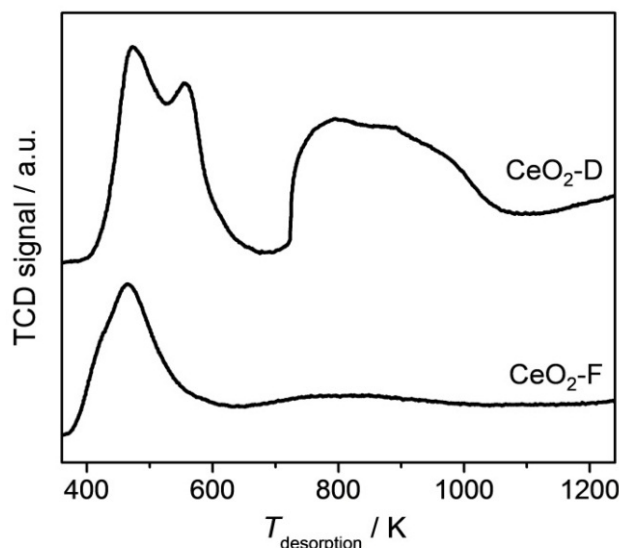


Figure 4.5 NH₃-TPD profiles of fresh and post Deacon CeO₂ samples.

When comparing to the computed results, within the PBE+U approach, the adsorption of ammonia with the N-down configuration on the Ce⁴⁺ site of undefective surface is 50 kJ mol⁻¹ (see Figure S3.1 (e)). (A second configuration with the three H atoms interacting with 3 neighbouring Lewis basic sites, i.e. O anions, leads to mere 9 kJ mol⁻¹.) Adsorbed on Brønsted acids (OH models), the adsorption is slightly weaker (31-39 kJ mol⁻¹). Using the model with partial chlorination and concomitant neighbouring Brønsted (OH) sites on the surface the interaction is stronger (about 60 kJ mol⁻¹) in agreement with the experimental

observations. These values are somehow smaller than the 500 K desorption peak would indicate, but they will be largely affected by the coordination of the Ce⁴⁺ cations. Likely the structure at higher desorption temperatures found in TPD arises from breaking the NH₄⁺ binding to the surface (see Table S 4.2 for the configurations). With surface hydroxylation two different configurations may exist: one with OH...NH₃ interactions, where the H is still bonded to oxygen on the surface, or ammonia can strip the H from some of these centers to generate NH₄⁺ species that can wander on the surface (see e.g. Fig. S 4.1(g)). Electrostatic interaction of NH₄⁺ with polarised surface Cl will further strengthen ammonia adsorption. The elimination of this species in the form of ammonia likely requires more energy than any other NH₃ desorption process, but it is unfortunately not well-reproduced by the calculations due to the charge displacement, the total charge state and the periodic boundary conditions employed in the simulations.

4.3.3 Probe molecule adsorption by FTIR and corresponding DFT analysis

CO is one of the most frequently used probe molecules in IR spectroscopy. Owing to its specific properties (sensitivity, accessibility and high extinction coefficient) crucial information can be obtained in terms of identification of adsorbing sites (Brønsted and Lewis) and definition of oxidation states [39]. In comparison to experiments, the DFT calculations underestimate the CO stretching frequency and thus only shifts are usually discussed to analyse the results. It is worthwhile mentioning here that σ -bond and electrostatic interactions cause hypsochromic frequency shifts, and the electrical field strength of metal ions is not only dependent on the formal charge but also the contribution of the metal ions' environment to the effective charge must be taken into account [39]. Hence, the effect of surface chlorination on the acid-base properties was further studied by monitoring shifts of CO vibrational frequencies at 77 K on both fresh and chlorinated samples. The former was pre-treated in batch at 200 mbar oxygen and 823 K for 5 h, O₂ had been replaced every 30 min to prevent re-adsorption of desorbing contaminants. The chlorinated sample was pre-treated in O₂ (200 mbar) at only 473 K for 5 h, as the surface after chlorination and thus replacement of O₂⁻ anions is now less prone to the formation of carbonate species [36]. Further, this minimises dechlorination. The samples were subsequently evacuated during cooling down. CO adsorption spectra on CeO₂-F are shown in Fig. 4.6a. After equilibration with 1.86 mbar CO at 77 K, two close and overlapping peaks at 2150 and 2155 cm⁻¹ with two shoulders at 2172 and 2140 cm⁻¹ appeared.

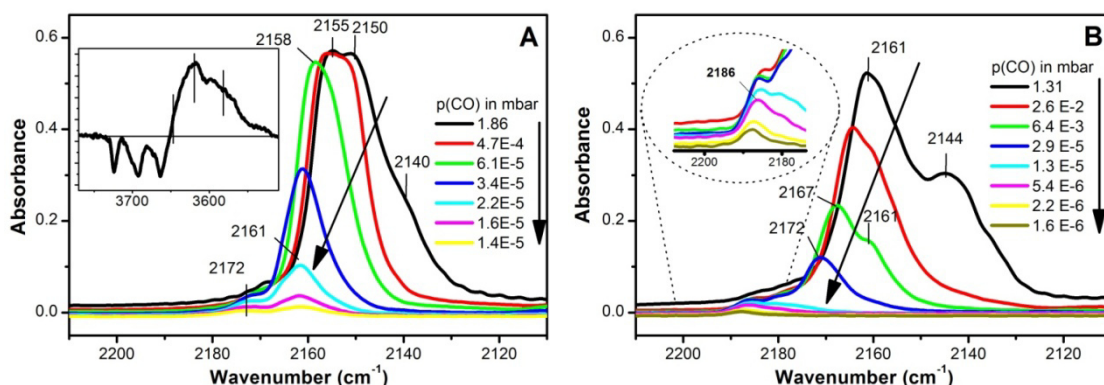


Figure 4.6 (a) FTIR spectra of CO adsorbed at 77 K on fresh CeO₂; after admission of 1.860 mbar CO in equilibrium (black-spectrum), after various sequential steps of evacuation (rest). Inset: Difference spectrum of the sample before and after admission of CO; (b) FTIR spectra of CO adsorbed at 77 K on CeO₂-D; after admission of 1.306 mbar CO in equilibrium (black-spectrum), after sequential steps of evacuation (rest). Inset: zoom in for the band at 2186 cm⁻¹.

Table 4.1 Summary of the experimental and calculated adsorption, E in kJ mol^{-1} , and vibrational frequencies, ν in cm^{-1} , of probe molecules together with the corresponding model.

<i>Molecule</i>	E^{exp}	ν^{exp}	E^{calc}	ν^{calc}	<i>Species</i>	<i>Model</i>
CO ₂	110				CO ₃ ²⁻	Multiple adsorption at vacancies
	55		43		CO ₃ ²⁻	Regular surf.
NH ₃	--	1394	--	1416-1382	NH ₄ ⁺	Brønsted
	--	1557	50	1593-1566	NH ₃ /NH ₄ ⁺	Lewis
	--	1414		1615-1612	NH ₄ ⁺	Chlorinated surface
CO	--	2155		2112		(O _{lattice} H)
	--	2161		2127		(O _{lattice} H..OH) chlorinated
	--	2186		2157		(O _{lattice} H...Cl)

Taking the IR frequency of gas phase CO (2143 cm^{-1}) as a reference, we can attribute the aforementioned bands and shoulders as follows: (i) the shoulder at 2140 cm^{-1} can be assigned to the physisorbed CO, since it is the closest one to the reference value, and it desorbs easily upon evacuation, (ii) the bands at 2150 and 2155 cm^{-1} , which are slightly up-shifted, can be attributed to CO hydrogen-bonded to OH groups of different acid strengths. This carbonyl band is accompanied by intensity perturbation and redshift of the $\nu(\text{OH})$ bands (see inset in Fig. 4.6a). Further evacuation gives rise to the disappearance of the band at 2150 cm^{-1} , which seems to have weaker interaction with the surface OH groups, whereas the band at 2155 cm^{-1} was decreasing gradually and shifting to higher wavenumbers with increasing vacuum. This shift is attributed to the diminishing intermolecular interactions at lower coverage [40]. By considering CO as weak electron donor molecule, the higher the positive shift of $\Delta(\text{CO})$, the stronger is the interaction with surface sites. The minor shoulder at 2172 cm^{-1} can be assigned to the CO interaction with Ce^{4+} sites [41,42], in agreement with the stronger adsorption of CO on the cationic site. However, DFT adsorption energies on *cus* Ce^{4+} is mere 18 kJ mol^{-1} , and therefore this band is more likely related to adsorption on more open surface sites.

Calculations are not fully conclusive at this stage. Indeed, adsorption energies have previously been calculated with different approximations leading to a range of $16\text{-}25 \text{ kJ mol}^{-1}$ [43], and the presence of hydroxyl groups, although induces CO shifts of $+40 \text{ cm}^{-1}$, reduces the adsorption energy further (O_{lattice}H model). Partially water covered surfaces (the CeO₂H-OH water pair model) might be responsible for stronger adsorption, about 48 kJ mol^{-1} , with the CO shift being dependent on the type of surface site (lattice or on top OH) CO interacting with (see Table S 4.4). The frequency shift is about $+10 \text{ cm}^{-1}$ when adsorption takes place close to the Ce^{4+} cations.

FTIR spectra of CO adsorption on chlorinated sample are illustrated in Fig. 4.6b. The main peak at high coverage is situated at 2161 cm^{-1} . According to the calculations this can be assigned to CO interacting with hydroxyls on the surface where the CO molecule is basically sitting with the C-down close to a Ce atom (see figure S 4.1 (o)). As these sites are not blocked in the Deacon reaction they seem to be rather stable when compared to the clean surface. There is an additional shoulder at 2144 cm^{-1} and a small band at 2186 cm^{-1} . Upon evacuation, the band at 2144 cm^{-1} , which is very close to the gas phase $\nu(\text{CO})$ disappeared. At lower pressures, the intensity of the main band further decreases and shifts to the higher wavenumber and splits up into two peaks. All bands, with exception of physisorbed CO at 2144 cm^{-1} , are blue shifted by $\sim 10 \text{ cm}^{-1}$ in comparison with those from the non-chlorinated sample. This blue shift indicates an overall increase of the acidity of the surface upon chlorination. The extent of the redshift of the OH band upon interaction with CO (inset in Fig. 4.6a) has often been utilised to evaluate the strength of surface Brønsted acid sites [39,40,44-46]. The magnitude of OH shifts was $\sim 75 \text{ cm}^{-1}$ for the fresh CeO₂. The

calculated value for CO-induced shifts of $\text{O}_{\text{lattice}}\text{H}$ is about 100 cm^{-1} . Whereas, it is in the range between 137 to 164 cm^{-1} for ceria after Deacon reaction, corroborating the enhanced acidity of the Brønsted sites. This latter value is not reproduced in the calculations and one of the reasons for the discrepancy might be high surface water content.

4.3.4 *In situ* FTIR under Deacon reaction

4.3.4.1 Cell design

For a successful *in situ* cell design, several aspects should be taken into consideration, such as small void volume, suitable IR-windows and construction materials, especially when it comes to such highly corrosive gaseous conditions, as for the Deacon reaction.

Our cell (Fig. 4.1) consists of two main parts. The cell body is provided with two IR transparent Si windows and two 1/8 in. tubing for the inlet- and outlet of the reactant gases and products. Si windows (20mm id, 1mm thickness) were fixed between two PTFE gaskets and sealed with Kalrez o-rings, which are chemically resistant at relatively high temperatures. The body of the cell is made of stainless steel; however a galvanic silver coating was applied on the inner walls. Silver is resistant to dry and moist chlorine at room temperature. A compact film of silver chloride is expected to form during the exposure of silver to molecular chlorine. This chloride layer is responsible for the resistance of the silver [47]. The lid is provided with a cylindrical oven (sample holder) and thermocouple for monitoring the temperature of the sample. Hastelloy C-22 was used as constructing material for the lid, which is coated afterwards with a special inert Si-based coating (SilcolloyTM1000) using CVD procedure. The sample holder serves as heating system that operates in the temperature range from 300 to 823 K . The internal volume of the cell is *ca.* 20 cm^3 .

4.3.4.2 *In situ* experiments

It has been proposed recently [8] that the mechanism of the Deacon reaction on CeO₂ includes two elementary steps that describe the formation and consumption of OH groups during the reaction. These results were based on DFT calculations. IR spectroscopy is among the best spectroscopic techniques known for monitoring the changes of OH groups under reaction conditions. Therefore, *in situ* IR experiments were carried out at different feed compositions and temperatures in the hope that mechanistic information could be extracted and to correlate the abundance of OH species with the catalytic activity of the sample.

CeO₂-F was activated *in situ* by heating in synthetic air up to 703 K and holding at this temperature for 90 min . Two main bands were observed at the end of this stage at 3700 and 3620 cm^{-1} , which are assigned, respectively, to mono-coordinated (OH-I) and bridging (OH-II) OH, see Table S 4.1 [48]. In our recent work with ceria calcined at only 773 K , these bands were slightly shifted to higher frequencies (*ca.* 10 cm^{-1}) and the band at 3730 cm^{-1} , which was considered as a shoulder, is better resolved now. Our current sample was calcined at higher temperature (1173 K), which results in a decreased density of the OH groups as well as a better Deacon performance despite the lower BET surface area [8].

HCl was introduced in the feed ratio $\text{O}_2:\text{HCl}=9:1$ at 703 K . Similar changes (Fig. 4.7) were observed at the early stages of the reaction as with the lower temperature calcined CeO₂ and strongly diluted Deacon feed [8]. Both OH bands at 3621 and 3700 cm^{-1} have vanished upon HCl introduction, the band at 3730 cm^{-1} was better resolved, and a broad band near 3500 cm^{-1} developed. This latter is related to surface water [8, 49]. A pronounced increase of the band at 3730 cm^{-1} was observed in advanced stages of the reaction, (see Fig. 4.7, black spectrum), whereas another low intensity band at 3676 cm^{-1} , which is observed only after introducing HCl to the feed, does not show remarkable variation with time. Since the initial changes under Deacon conditions were very fast, the single beam spectrum after 32 s on

Deacon feed (blue spectrum) was used as background to follow the evolution of the band at 3730 cm⁻¹. The time evolution of absorbance spectra were fitted (see Fig S 4.3 as an example) and we analyse the evolution of the abundance of the mono-coordinated OH component. The integral area of this peak at 3730 cm⁻¹ increased very rapidly at the beginning of the reaction (Fig. 4.8). Then, changes slowed down appreciably, though no plateau was reached even after 16 h on stream. This phenomenon may be interpreted based on structural evolution of the surface during the reaction, with sharp facets becoming more rounded. This morphological transformation may require the extended time experienced in the IR experiment.

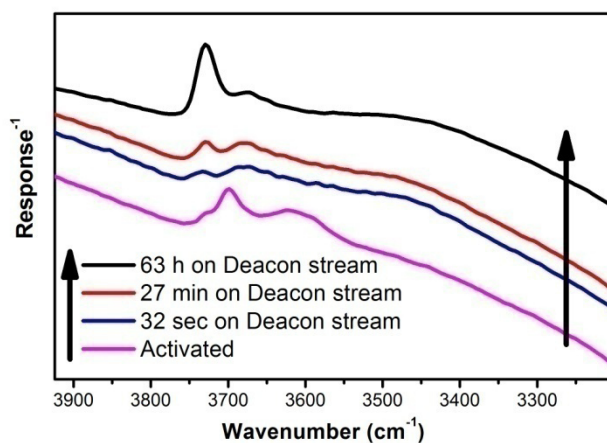


Figure 4.7 *In situ* single beam FTIR spectra of CeO₂ under various conditions: activated (before HCl introduction) and in Deacon reaction.

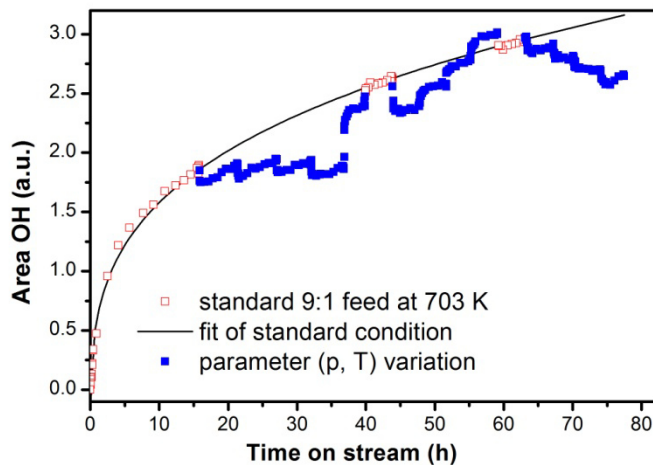


Figure 4.8 Evolution of integrated area of OH band at 3730 cm⁻¹ as a function of time on Deacon stream. Red points represent the standard conditions of O₂:HCl = 9:1 at 703 K and the black line is a fit to these data. Blue points represent various other conditions in Deacon feed during *p*O₂, *p*HCl and *T* variation. These are discussed in detail in Fig. 4.9-4.11.

The reaction conditions (*p_i*, *T*) were varied individually to study the influence of each parameter on the concentration of the OH groups. Fig. 4.8 shows the integration data for the whole experiment, in which first *p*O₂, then *p*HCl and lastly temperature was varied. Due to the non-steady nature of OH even after 16 h, we repeated the same reaction conditions twice to control the effect related to this. These data were fitted with a mathematical function and the actual OH abundance has been corrected with the hypothetical value given by the fit at the corresponding time on stream.

4.3.4.2.1 O₂ dependence

The effect of various pO_2 contents in the feed on the reaction rate level and the OH concentration compared to that in the standard feed of O₂:HCl = 9:1 is illustrated in Fig. 4.9. Increasing oxygen content gives rise to increasing reactivity that can be fitted to a formal pO_2 dependence of ~ 0.4 . In parallel, the OH concentration is the highest at the most oxygen rich feed and decreases continuously when pO_2 is lowered. The major changes in the OH concentration occur fast, usually within 2-3 min, thus the surface rapidly responds to the changes in the feed stream. In this experiment we observe a positive relationship between OH concentration and the reactivity, in the sense that higher OH coverage results in higher conversion.

4.3.4.2.2 HCl dependence

Before starting the investigation of $pHCl$ dependence, the sample was reactivated by switching to O₂ rich feed compositions (O₂:HCl = 4:1 then 9:1, 3 h for each), since feeds with low oxygen content was shown to induce deactivation [8].

According to the proposed mechanism [8], HCl dissociation on the surface is a fundamental reaction step, which is responsible for the compensation of OH group's loss during the formation of the by-product H₂O. Thus, one may assume that by reducing the inlet $pHCl$, OH concentration will decrease. Fig. 4.10 demonstrates exactly the opposite behaviour, that is, by reducing $pHCl$ (from 10 to 1 cm³ STP min⁻¹ in always constant 100 cm³ STP min⁻¹ total flow) and keeping also pO_2 constant (20 cm³ STP min⁻¹), OH concentration has steadily increased. In parallel, the Cl₂ productivity decreased, and therefore in this experiment the higher reaction rate correlates with decreasing OH concentration.

4.3.4.2.3 T dependence

Temperature influence was studied by reducing the temperature stepwise (20 K for each step) in the range from 703 to 623 K. Decreasing reaction temperature induces a loss of activity according to the Arrhenius law. The calculated apparent activation energy is 70 kJ mol⁻¹. Fig. 4.11b indicates that decreasing temperature and reactivity correlates with lower OH concentration, similar to that found in pO_2 dependence.

4.3.5 Mechanistic considerations

Micro-calorimetric experiments with CO₂ adsorption suggested a loss of basic character of ceria surface after reaction in Deacon conditions. That is, most of the basic lattice O surface sites are exchanged to surface (lattice) Cl and the OH groups are no more Lewis basic, but rather Brønsted acidic. Surface chlorination is in line with our previous XPS characterization [8]. H abstraction during dissociative HCl adsorption requires basic sites, and hence HCl adsorption is certainly retarded by the loss of basic character. Ammonia and CO adsorption studies by micro-calorimetry, FTIR, and TPD, confirmed the increase in the acidic character after Deacon reaction, at likely both the *cus* Ce⁴⁺ and OH positions. The calculated adsorption energies and vibrational frequencies by DFT were, generally, in accordance with the experiments. Due to the lack of other surface orientations considered and the partial sampling of potential defects, the DFT picture of CO and CO₂ adsorption and agreement to experiment is far from perfect. However, the major changes in acid/base character are satisfactorily deduced.

Although HRTEM is not statistically conclusive, there is nevertheless an indication that the well-faceted surface of CeO₂ becomes rounded during the course of the reaction. The evolution of the OH band intensity at ~ 3730 cm⁻¹ may be related to this morphological modification of the surface. Nevertheless, no activation corresponding to the increase in OH density was observed with our CeO₂ catalyst, and therefore a direct correspondence between the overall OH intensity and the reactivity should be excluded.

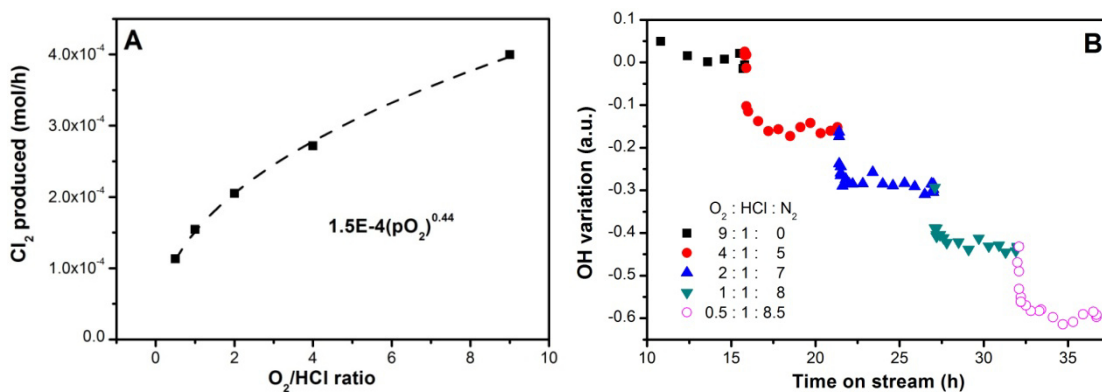


Figure 4.9 *In situ* results at 703 K during pO_2 variation. (a) Cl₂ production as a function of O₂ content of the feed. (b) Evolution of integrated OH area as a function of time on Deacon stream during pO_2 variation. OH variation is expressed as the difference of the OH area at 9:1:0 feed according to the fit at the corresponding time on stream and the actual measured area.

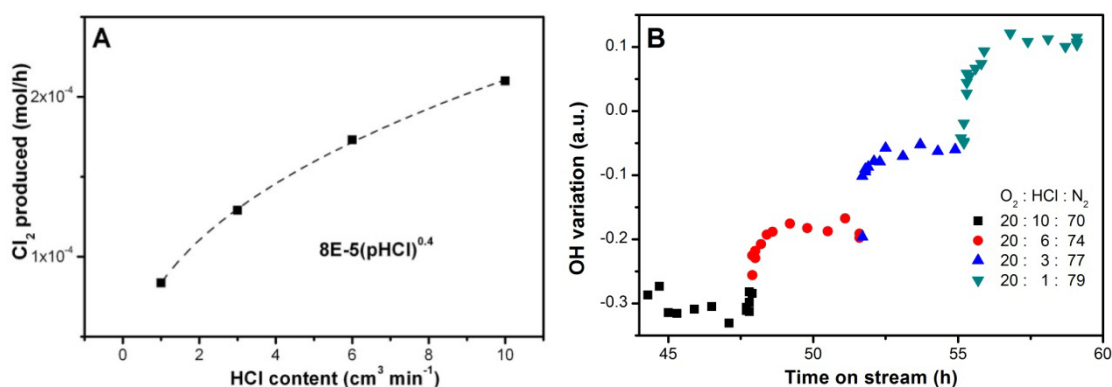


Figure 4.10 *In situ* results at 703 K during $pHCl$ variation. (a) Cl₂ production as a function of HCl content of the oxygen-rich feed. (b) Evolution of integrated OH area as a function of time on Deacon stream during $pHCl$ variation. OH variation is expressed as the difference of the OH area at 9:1:0 feed according to the fit at the corresponding time on stream and the actual measured area.

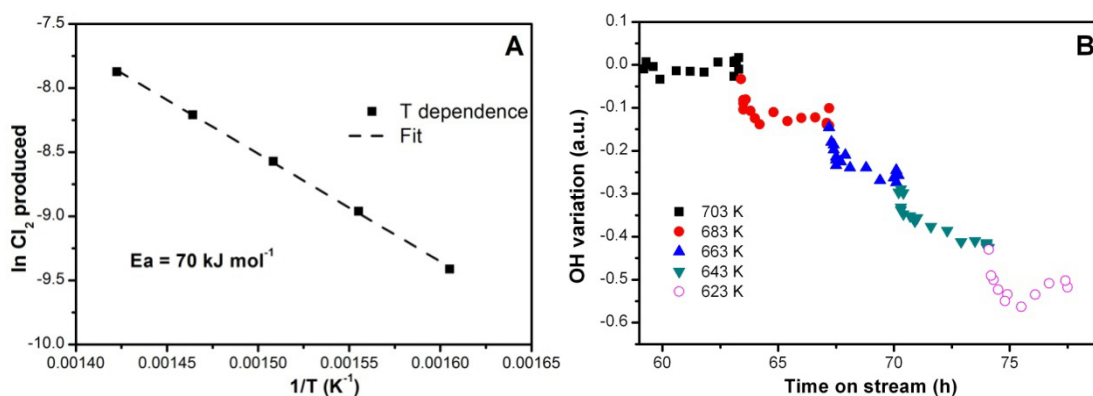


Figure 4.11 *In situ* results during temperature variation using a feed of O₂:HCl:N₂ = 9:1:0. (a) Arrhenius Plot. (b) Evolution of integrated OH area as a function of time on Deacon stream during T variation. OH variation is expressed as the difference of the OH area at 9:1:0 feed and 703 K according to the fit at the corresponding time on stream and the actual measured area.

The oxygen pressure dependence of HCl oxidation over CeO₂ shows a positive ~0.4-0.5 formal reaction order, even at high oxygen over-stoichiometry. Conversely, the effect of p_{HCl} is positive (0.2-0.4) in high O₂ excess and gets negative for $p_{\text{HCl}}/p_{\text{O}_2}$ higher than ~1.5 [8]. This indicates that HCl activation is also an issue at low $p_{\text{HCl}}/p_{\text{O}_2}$, but O₂ activation is always difficult, essentially at all feed mixtures studied. Due to surface chlorination, low Cl coverage is likely not a factor for reactivity. Rather, if Cl coverage is high and/or Cl is too strongly bound, it blocks sites for elementary steps as HCl or O₂ activation.

The OH evolution in the p_{O_2} and T dependent *in situ* FTIR experiment indicated that higher p_{O_2} and T will increase the OH density, and concomitantly the reaction rate increased. This might be interpreted as lowering surface Cl concentration by opening up sites capable of abstracting H from HCl and shifting equilibrium coverage toward higher OH density. On the other hand, even in those feed conditions, under which increasing p_{O_2} would give rise to rate enhancement, p_{HCl} was shown to increase reactivity with concomitant decrease of OH density. These apparently opposite observations may be reconciled assuming the importance of repulsive lateral interactions (e.g. for HCl adsorption) in decreasing the heat of adsorption of surface species and thereby facilitating recombination and product desorption. An alternative explanation may be related to surface restructuring as a function of $p_{\text{HCl}}/p_{\text{O}_2}$, which if facile could allow two parameters (structure and coverage) to control reactivity. Despite the rapid changes in the OH density following the variation in the parameter field studied, the above results and discussion suggest that one cannot assign the OH concentration *per se* as the main descriptor of HCl oxidation reactivity. Further studies correlating surface OH and Cl concentration may clarify details in HCl oxidation over ceria not accessible from this work.

4.4 Conclusions

Ceria is widely used as support, catalyst, or co-catalyst for various catalytic processes. We utilised ceria as the main active phase for the heterogeneous catalytic HCl oxidation. Here we compared the acid/base properties of bulk ceria in its fresh and post-reaction state by probe molecule adsorption (CO₂, NH₃, CO) applying micro-calorimetry, FTIR, TPD and DFT calculations. The results indicate that the basic character of the ceria surface has been essentially eliminated upon reaction in HCl oxidation. This can be explained with the replacement of surface lattice O with Cl species and that the OH groups formed are rather acidic in nature. An *in situ* FTIR reaction cell has been developed in order to follow the evolution of OH groups during HCl oxidation. OH groups are reaction intermediates in HCl oxidation. The effect of experimental variables as the reactant partial pressure and the reaction temperature were investigated. We find a good linear correlation of OH group density with the reactivity when T or p_{O_2} is varied. Nevertheless, an opposite trend is observed when p_{HCl} is investigated, suggesting that the reactivity cannot be assigned to this sole surface parameter.

4.5 Supporting Information

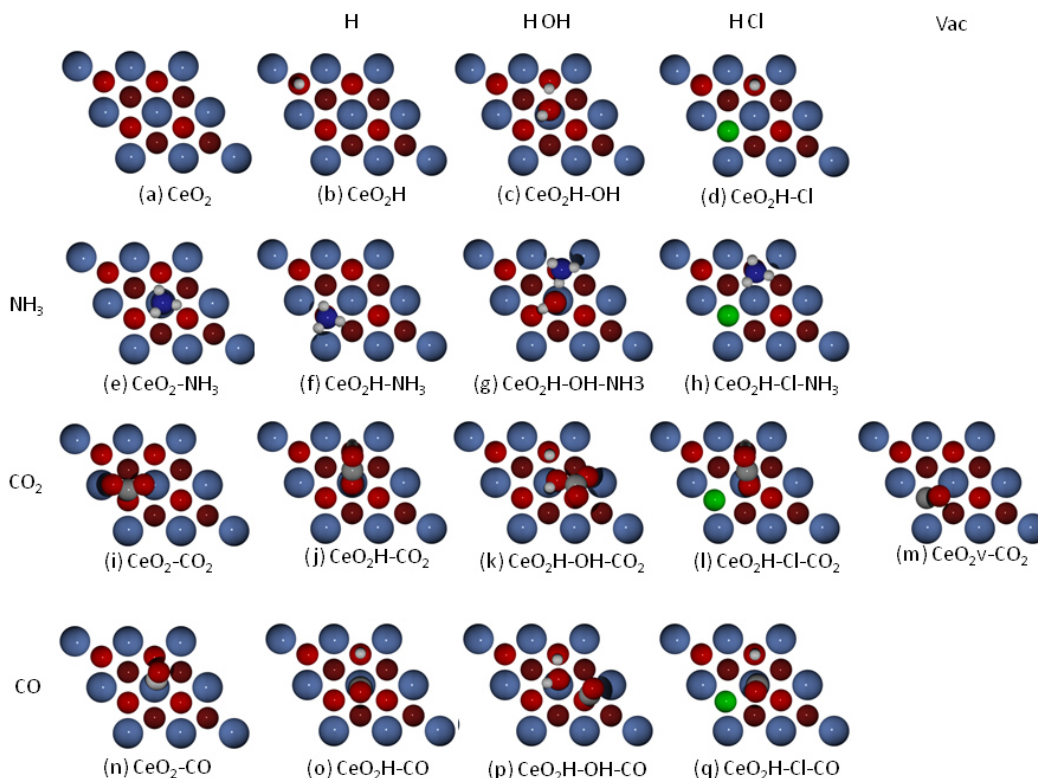


Figure S 4.1 Schematic representation of the clean CeO₂(111) surface (a), surface hydroxyl (b), surface on top hydroxyl (c) and chlorine substitution with a concomitant hydroxyl group (d). Ammonia adsorption on models (a-d) are represented in figures (e-h); CO₂ adsorption on figures (i-j) and adsorption on an oxygen vacancy (m) and CO adsorption on the (a-d) models shown in (n-q). Grey spheres represent Ce atoms, red O, blue H, yellow C and green Cl.

Table S 4.1 Vibrational frequencies for hydroxyl groups on CeO₂, ν in cm⁻¹, for vibrations higher than 800 cm⁻¹. Frequency assignment labels: (s) OH stretching; (b) bending modes. μ_B : Bohr magneton

	<i>CeO₂H</i>	<i>CeO₂-OH_{top}</i>	<i>CeO₂-OH_{bridge}</i>	<i>CeO₂H-OH_{top}</i>	<i>CeO₂H-Cl</i>
μ_B	0.5	1.0	1.0	0.0	2.0
1	3741 (s)	3714 (s)	3691 (s)	3786 (s)	3756 (s)
2				2953 (s)	
3				986 (b)	
4				890 (b)	

Table S 4.2 Adsorption energies, E_{ads} in kJ mol^{-1} , of ammonia on different CeO₂ configurations (with respect to different model surfaces and gas-phase NH₃) and corresponding vibrational frequencies, ν in cm^{-1} (for the vibrations stronger than 800 cm^{-1}). Frequency assignment labels: symmetric stretching (ν_s), asymmetric stretching (ν_a), bending (δ modes). The labelling follows that of ref. [1] pages 117 and 131. μ_B : Bohr magneton

	Site	μ_B	Fig. S4.1	E_{ads} (kJ mol^{-1})	ν (cm^{-1})
Gas-phase NH ₃	--	0.0		--	3509 (ν_a), 3506 (ν_a), 3370 (ν_s) 1627 δ_d (HNN), 1626 δ_d (HNN), 1021 δ_s (HNN)
Gas-phase NH ₄ ⁺	--	0.0		--	2873 (ν_a), 2866 (ν_a), 2862 (ν_a), 2812 (ν_s), 1536 δ_d (HNN), 1532 δ_d (HNN), 1271 δ_d (HNN), 1265 δ_d (HNN), 1260 δ_d (HNN)
CeO ₂	Ce N _{down}	0.0	(e)	50	3534 (ν_a), 3529 (ν_a), 3397 (ν_s), 1603 δ_d (HNN), 1593 δ_d (HNN), 1018 δ_s (HNN)
CeO ₂	O ₃ H _{down}	0.0		9	3690 (ν_a), 3550 (ν_a), 3290 (ν_s), 1648 δ_d (HNN), 1582 δ_d (HNN)
CeO ₂ H	H N _{down}		(f)	39	3385 (ν_a), 3376 (ν_a), 3367 (ν_a), 1566 δ_d (HNN), 1562 δ_d (HNN), 997 δ_s (HNN), 948 δ_s (HNN)
CeO ₂ H-OH	H N _{down}	0.5	(g)	31	3662 (OH _s), 3552 (ν_a), 3476 (ν_a), 3119 (ν_s), 2559 (HOH), 1632 δ_d (HNN), 1583 δ_d (HNN) 1145 δ_s (HNN), 1131 δ_s (HNN), 1021 δ_s (HNN)
CeO ₂ -H-Cl	H N _{down}	2.0	(h)	59	3513 (OH _s), 3510 (ν_a), 3393 (ν_a), 2948 (ν_s), 1615 δ_d (HNN), 1612 δ_d (HNN), 1096 δ_s (HNN), 972 δ_s (HNN), 954 δ_s (HNN)
CeO ₂ -H	NH ₄ O	at 0.0		-113	3257 (ν_a), 3250 (ν_a), 3173 (ν_a), 2974 (ν_s), 1639 δ_d (HNN), 1637 δ_d (HNN), 1416 δ_d (HNN), 1408 δ_d (HNN), 1340 δ_d (HNN)
CeO ₂ -H-Cl	NH ₄ Cl	at 0.0		-118	3583 (ν_a), 3476 (ν_a), 3271 (ν_a), 2213 (ν_s), 1618 δ_d (HNN), 1611 δ_d (HNN), 1415 δ_d (HNN), 1382 δ_d (HNN), 1274 δ_d (HNN)

[1] K. Nakamoto, Infrared and Raman spectra of inorganic and coordination compounds 4th Edition Wiley and Sons, New York, 1986

Table S 4.3 Adsorption energies, E_{ads} in kJ mol^{-1} , of CO₂ on different CeO₂ configurations and corresponding vibrational frequencies, ν in cm^{-1} (for the vibrations stronger than 800 cm^{-1}). Negative adsorption energies indicate endothermic processes. Frequency assignment labels: symmetric stretching (ν_s), asymmetric stretching (ν_a), bending (δ modes). The labelling follows that of ref. [1] page 108.

	Site	μ_B	Fig. S4.1	E_{ads} (kJ mol^{-1})	ν (cm^{-1})
Gas-phase	--	0.0	--	--	2342 (ν_a), 1310 (ν_s)
CO ₂					
Gas-phase	--	0.0	--	--	1519 (ν_a), 1425 (ν_a)
CO ₃ ²⁻					
Gas-phase	--	0.0	--	--	3511(OH), 1874 (ν_s)
HCO ₃ ⁻					
CeO ₂	O carbonate	0.0	(i)	43	1527 (ν_a), 1057 (ν_a), 829 ($\pi(\text{CO}_3)$)
CeO _{2-x}	Multiple adsorption (3)*	0.0	(m)	>120	--
CeO _{2-x}	Vacancy O-CO	0.0	(m)	14	1889(ν_a), 1105 (ν_s)
CeO ₂ H	Hydrocarbonate	1.0	(j)	-10	3720 (OH _s), 2344 (ν_a), 1307 (ν_s)
CeO ₂ H-OH	Hydrocarbonate	0.0	(k)	18	3618 (OH _s), 3588 (OH _s), 1769(ν_s), 1242 (ν_s), 1132 (ν_s)
CeO ₂ H-Cl	Hydrocarbonate	2.0	(l)	1	3717 (OH _s), 2247 (ν_a), 1252 (ν_s)

*Multiple adsorption on oxygen vacancies leads to large binding energies linked to the position of the vacancy states, as those are poorly reproduced by PBE+U only a tentative assignment is presented. μ_B : Bohr magneton.

[1] K. Nakamoto, Infrared and Raman spectra of inorganic and coordination compounds 4th Edition Wiley and Sons, New York, 1986

Table S 4.4 Adsorption energies, E_{ads} in kJ mol^{-1} , of CO on different CeO₂ configurations and corresponding vibrational frequencies, ν in cm^{-1} (for the vibrations stronger than 800 cm^{-1}). Negative adsorption energies indicate endothermic processes. Frequency assignment labels: stretching (s), bending (b). μ_B : Bohr magneton

	Site	μ_B	Fig. S4.1	E_{ads} (kJ mol^{-1})	ν (cm^{-1})
Gas-phase	CO	--	--	--	2105 (\square)
CeO ₂	Ce ⁴⁺ C _{down}	0.0	(n)	18	2086 (s)
CeO ₂ H	Ce ⁴⁺ C _{down}	0.5	(o)	12	3843 (OH _s), 2127 (s)
CeO ₂ H-OH	O C _{down}	0.0	(p)	48	3781 (OH _s), 2898 (OH _s), 2113(s), 957(b), 881(b)
CeO ₂ H-Cl	Ce ⁴⁺ C _{down}	2.0	(q)	23	3634 (OH _s), 2157 (s)

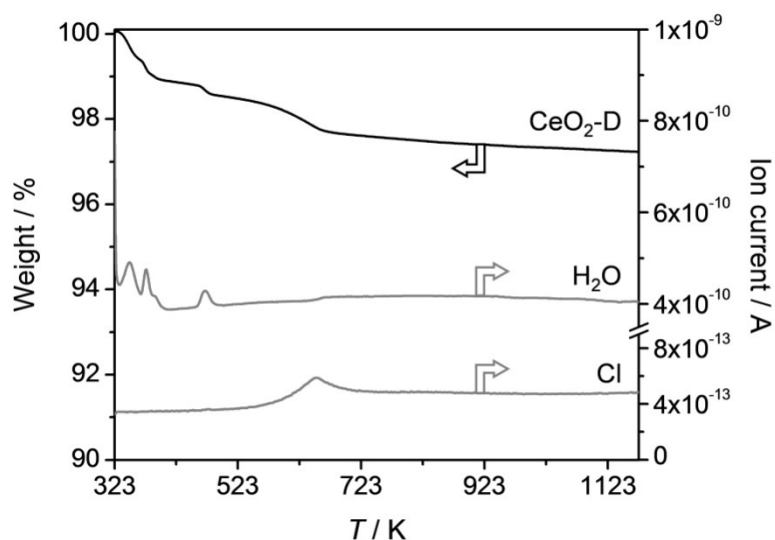


Figure S 4.2 Thermogravimetric (TGA) profile of CeO₂-D coupled to mass spectrometry (MS) profiles for H₂O (AMU 18) and for Cl (AMU 35). The weight loss of the equilibrated sample occurred in several steps. Up to 490 K, removal of surface impurities, such as physically adsorbed water, and the water of crystallisation of the CeCl₃·6H₂O phase took place. Weight loss between 490 and 660 K was attributed to chlorine removal. Similar assignments were made by Amrute *et al.* (*J. Catal.*, **286** (2012) 287-297).

Procedure: Thermogravimetric analysis was performed in a Mettler Toledo TGA/DSC 1 Star system analyser connected to a Pfeiffer Vacuum ThermoStar GSD 320 T1 Gas Analysis System. Analyses were performed in He (20 cm³ STP min⁻¹), ramping the temperature from 323 to 1273 K at 20 K min⁻¹. AMU 32 (O₂), 35 (Cl), 18 (H₂O), and 71 (Cl₂) were continuously monitored.

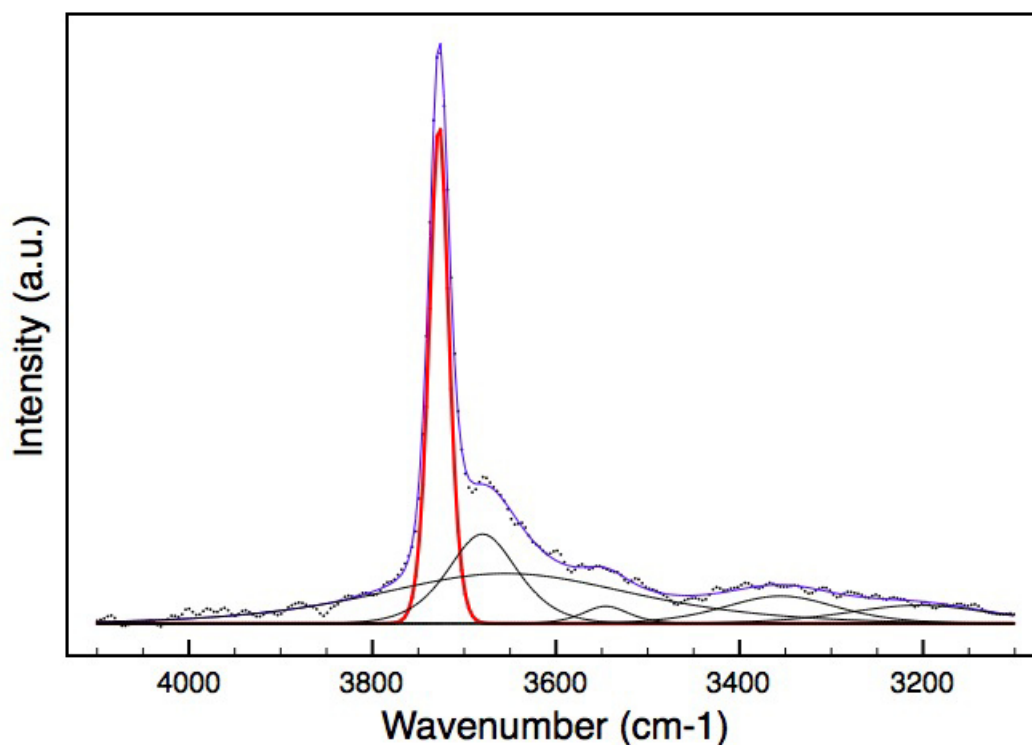


Figure S 4.3 An example of fitting the OH region of *in situ* FTIR spectra observed during Deacon reaction. The red peak is integrated and discussed in the main text.

4.6 References

- [1] T. Hibi, H. Abekawa, K. Seki, T. Suzuki, T. Suzuta, K. Iwanaga and T. Oizumi, *EP936184*, 1999.
- [2] T. Hibi, H. Nishida and H. Abekawa, *U.S. Patent 5,871,707*, 1999.
- [3] T. Hibi, T. Okuhara, K. Seki, H. Abekawa and H. Hamamatsu, *WO200110550-A1*, 2001.
- [4] A. Wolf, J. Kintrup, O. F. Schlüter and L. Mleczko, *EP2027062*, 2006.
- [5] A. Wolf, L. Mleczko, O. F. Schlüter and S. Schubert, *EP2026905*, 2006.
- [6] A. Wolf, L. Mleczko, S. Schubert and O. F. Schlüter, *EP2027063*, 2006.
- [7] J. Pérez-Ramírez, C. Mondelli, T. Schmidt, O. F. K. Schlüter, A. Wolf, L. Mleczko and T. Dreier, *Energy and Environmental Science*, 2011, **4**, 4786-4799.
- [8] A. P. Amrute, C. Mondelli, M. Moser, G. Novell-Leruth, N. Lopez, D. Rosenthal, R. Farra, M. E. Schuster, D. Teschner, T. Schmidt and J. Pérez-Ramírez, *Journal of Catalysis*, 2012, **286**, 287-297.
- [9] J. Ryczkowski, *Catalysis Today*, 2001, **68**, 263-381.
- [10] A. Vimont, F. Thibault-Starzyk and M. Daturi, *Chemical Society Reviews*, 2010, **39**, 4928-4950.
- [11] F. C. Meunier, *Catalysis Today*, 2010, **155**, 164-171.
- [12] G. Jacobs, L. Williams, U. Graham, G. A. Thomas, D. E. Sparks and B. H. Davis, *Applied Catalysis A*, 2003, **252**, 107-118.
- [13] R. Leppelt, B. Schumacher, V. Plzak, M. Kinne and R. J. Behm, *Journal of Catalysis*, 2006, **244**, 137-152.
- [14] T. Shido and Y. Iwasawa, *Journal of Catalysis*, 1993, **141**, 71-81.
- [15] X. Q. Wang, J. A. Rodriguez, J. C. Hanson, D. Gamarra, A. Martinez-Arias and M. Fernandez-Garcia, *Journal of Physical Chemistry B*, 2006, **110**, 428-434.
- [16] A. Goguet, F. C. Meunier, D. Tibiletti, J. P. Breen and R. Burch, *Journal of Physical Chemistry B*, 2004, **108**, 20240-20246.
- [17] D. Tibiletti, A. Goguet, D. Reid, F. C. Meunier and R. Burch, *Catalysis Today*, 2006, **113**, 94-101.
- [18] J. D. Grunwaldt, M. Maciejewski, O. S. Becker, P. Fabrizioli and A. Baiker, *Journal of Catalysis*, 1999, **186**, 458-469.
- [19] X.-S. Huang, H. Sun, L.-C. Wang, Y.-M. Liu, K.-N. Fan and Y. Cao, *Applied Catalysis B*, 2009, **90**, 224-232.
- [20] F. Romero-Sarria, L. M. Martinez, M. A. Centeno and J. A. Odriozola, *Journal of Physical Chemistry C*, 2007, **111**, 14469-14475.
- [21] O. Pozdnyakova, D. Teschner, A. Wootsch, J. Krohnert, B. Steinhauer, H. Sauer, L. Toth, F. C. Jentoft, A. Knop-Gericke, Z. Paal and R. Schlögl, *Journal of Catalysis*, 2006, **237**, 1-16.
- [22] O. Pozdnyakova-Tellinger, D. Teschner, J. Kroehnert, F. C. Jentoft, A. Knop-Gericke, R. Schlögl and A. Wootsch, *Journal of Physical Chemistry C*, 2007, **111**, 5426-5431.
- [23] M. A. Hasan, M. I. Zaki and L. Pasupulety, *Applied Catalysis A*, 2003, **243**, 81-92.
- [24] Z. L. Wu, M. J. Li and S. H. Overbury, *Journal of Catalysis*, 2012, **285**, 61-73.
- [25] G. Kresse and J. Hafner, *Physical Review B*, 1993, **47**, 558-561.
- [26] J. P. Perdew, K. Burke and M. Ernzerhof, *Physical Review Letters*, 1996, **77**, 3865-3868.
- [27] M. Cococcioni and S. de Gironcoli, *Physical Review B*, 2005, **71**, 035105.
- [28] S. Fabris, G. Vicario, G. Balducci, S. de Gironcoli and S. Baroni, *The Journal of Physical Chemistry B*, 2005, **109**, 22860-22867.
- [29] M. V. Ganduglia-Pirovano, J. L. F. Da Silva and J. Sauer, *Physical Review Letters*, 2009, **102**, 026101.
- [30] P. E. Blöchl, *Physical Review B*, 1994, **50**, 17953-17979.
- [31] H. J. Monkhorst and J. D. Pack, *Physical Review B*, 1976, **13**, 5188-5192.

- [32] H. Metiu, S. Chrétien, Z. Hu, B. Li and X. Sun, *The Journal of Physical Chemistry C*, 2012, **116**, 10439-10450.
- [33] C. Li, Y. Sakata, T. Arai, K. Domen, K.-i. Maruya and T. Onishi, *Journal of the Chemical Society, Faraday Transactions*, 1989, **85**, 929-943.
- [34] G. N. Vayssilov, M. Mihaylov, P. S. Petkov, K. I. Hadjiivanov and K. M. Neyman, *The Journal of Physical Chemistry C*, 2011, **115**, 23435-23454.
- [35] M. Nolan, S. C. Parker and G. W. Watson, *Physical Chemistry Chemical Physics*, 2006, **8**, 216-218.
- [36] A. Badri, C. Binet and J.-C. Lavalley, *The Journal of Physical Chemistry*, 1996, **100**, 8363-8368.
- [37] X. Gu, J. Ge, H. Zhang, A. Auroux and J. Shen, *Thermochimica Acta*, 2006, **451**, 84-93.
- [38] V. R. Choudhary and V. H. Rane, *Journal of Catalysis*, 1991, **130**, 411-422.
- [39] K. I. Hadjiivanov and G. N. Vayssilov, in *Advances in Catalysis*, Academic Press 2002, vol. Volume 47, pp. 307-511.
- [40] O. V. Manoilova, S. G. Podkolzin, B. Tope, J. Lercher, E. E. Stangland, J.-M. Goupil and B. M. Weckhuysen, *J. Phys. Chem. B*, 2004, **108**, 15770-15781.
- [41] C. Binet, M. Daturi and J.-C. Lavalley, *Catalysis Today*, 1999, **50**, 207-225.
- [42] G. A. H. Mekhemer and M. I. Zaki, *Adsorption Science & Technology*, 1997, **15**, 377-389.
- [43] M. Huang and S. Fabris, *The Journal of Physical Chemistry C*, 2008, **112**, 8643-8648.
- [44] G. Busca, *Physical Chemistry Chemical Physics*, 1999, **1**, 723-736.
- [45] G. Busca, in *Metal Oxide Catalysis*, eds. S. D. Jackson and J. S. J. Hargreaves, Wiley VCH 2009, pp. 95-175.
- [46] J. A. Lercher, C. Gründling and G. Eder-Mirth, *Catalysis Today*, 1996, **27**, 353-376.
- [47] K. Hauffe, H. Puschmann, K. Hauffe and H. Puschmann, in *Corrosion Handbook, Corrosion Handbook*, Wiley VCH Frankfurt (Main) 2008.
- [48] A. Badri, C. Binet and J.-C. Lavalley, *J. Chem. Soc., Faraday Trans.*, 1996, **92**, 4669-4673.
- [49] D. Fernández-Torre, K. Kośmider, J. Carrasco, M. V. Ganduglia-Pirovano and R. Pérez, *The Journal of Physical Chemistry C*, 2012, **116**, 13584-13593.

Chapter 5: Do observations on surface coverage-reactivity correlations always describe the true catalytic process? A case study on ceria

Ramzi Farra, Maik Eichelbaum, Robert Schlögl, László Szentmiklósi, Timm Schmidt, Amol P.

Amrute, Cecilia Mondelli, Javier Pérez-Ramírez, Detre Teschner

Abstract

In situ (operando) investigations aim at establishing structure-function and/or coverage-reactivity correlations. Herein, we investigated the gas-phase HCl oxidation ($4\text{HCl} + \text{O}_2 \rightarrow 2\text{Cl}_2 + 2\text{H}_2\text{O}$) over ceria. Despite its remarkable performance, under low oxygen over-stoichiometry, this oxide is prone to a certain extent to subsurface/bulk chlorination, which leads to deactivation. *In situ* Prompt Gamma Activation Analysis (PGAA) studies evidenced that the chlorination rate is independent of the pre-chlorination degree but increases at lower oxygen over-stoichiometry, while dechlorination is effective in oxygen-rich feeds, and its rate is higher for a more extensively pre-chlorinated ceria. Even bulk CeCl_3 could be transformed into CeO_2 under oxygen excess. Electron Paramagnetic Resonance experiments strongly suggested that oxygen activation is inhibited by a high surface chlorination degree. The coverage of most abundant surface intermediates, OH and Cl, were monitored by *in situ* infrared spectroscopy and PGAA under various conditions. Higher temperature and $p(\text{O}_2)$ led to enhanced OH coverage, reduced Cl coverage, and increased reactivity. Variation of $p(\text{HCl})$ gave rise to opposite correlations, while raising $p(\text{Cl}_2)$ did not induce any measurable increase in the Cl coverage, despite the strong inhibition of the reaction rate. The results indicate that only a small fraction of surface sites is actively involved in the reaction, and most of the surface species probed in the *in situ* observation are spectators. Therefore, when performing *in situ* steady-state experiments, a large set of variables should be considered to obtain accurate conclusions.

Acknowledgements

The authors acknowledge support from BMBF Project 033R018A, Bayer MaterialScience, ETH Zurich, the EU FP7 NMI3 Access Program, the NAP VENEUS Grant (OMFB-00184/2006) and the cooperation project between the Fritz-Haber Institute and the former Institute of Isotopes funded by the MPG. Bayer MaterialScience is acknowledged for permission to publish this article. Núria López is thanked for valuable discussions.

5.1 Introduction

Heterogeneous catalysis is a kinetically driven phenomenon, and the reaction rate is proportional to the coverage of *at least one* reactant, or surface species or by the number of free sites. Nevertheless, the dependence can be fairly complex, and the extent of sites occupied by blocking species crucially affects the catalyst's efficiency. The coverage of reactants, intermediates, and products strongly depends on their heat of adsorption at the relevant active surface site and on the barriers related to the formation and elimination of these surface species. The quantitative information on the surface coverage plays an important role in identifying reaction mechanisms, designing alternative catalysts, or validating purely computational approaches. Thus, the knowledge of the surface coverage at meaningful catalytic turnover is critical and has motivated extensive experimental efforts [1-3]. Unfortunately, only a very few number of experimental techniques are capable of deriving such information, the most important ones being the various forms of vibrational spectroscopies. In this manuscript, we will experimentally assess the coverage of surface species under catalytic turnover and correlate these with the reactivity. The catalytic HCl oxidation (Deacon reaction) over bulk ceria will serve as our example.

The heterogeneously catalyzed HCl oxidation is a sustainable route to manufacture chlorine, and the current technology is based on RuO₂ catalysts [4-8]. CeO₂ was recently identified as a cheaper potential alternative active phase in view of its remarkable stability, though it requires higher operating temperatures [9]. As revealed by XRD and XPS analyses, when using an appropriate over-stoichiometry of oxygen in the feed gas (O₂:HCl > 0.75), the bulk of ceria was unaffected, and only the surface got chlorinated under reaction condition. The mechanism of HCl oxidation over CeO₂ was suggested to involve the following elementary steps: (i) hydrogen abstraction from HCl by basic surface O atoms to form hydroxyl groups leaving chlorine atoms on the surface, (ii) reaction of the hydroxyl groups with new incoming HCl molecules and/or hydroxyl group recombination on the surface to form water, (iii) water desorption, (iv) reoxidation of the surface via dissociative adsorption of O₂, and (v) recombination of chlorine atoms evolving as gas-phase Cl₂ [9]. Several of these steps rely on the existence of anionic oxygen vacancies that accommodate dissociated reactants. Based on the above mechanism, adsorbed Cl, OH, and H₂O are the major species populating the surface. These may occupy coordinatively unsaturated cationic sites or lattice O sites by replacement.

This manuscript attempts to address two novel aspects of the Deacon reaction over CeO₂. First, we investigate the chlorine uptake under reaction conditions and follow the kinetics of the dynamic chlorination and dechlorination processes depending on the oxygen over-stoichiometry of the feed mixture. Second, we examine the coverage of Cl and OH under various reaction conditions and relate them with reactivity. We show how convincing coverage-rate correlations break down when product inhibition is included in the experiments and conclude that the observed correlations are associated with the main part of the surface bearing little relevance for the reactivity.

5.2 Experimental

5.2.1 Catalysts

CeCl₃ (Alfa Aesar, ultra dry, 99.9%) was used as received. CeO₂ (Aldrich, nanopowder, 544,841) was calcined in static air at 1173 K for 5 h prior to use. This sample is referred to as CeO₂-A. CeO₂-R was synthesized by thermal decomposition of cerium(III) nitrate hexahydrate (Aldrich, 99.99%) in air by ramping to 1173 K (2 K min⁻¹) and holding for 3 h. CeO₂-A and CeO₂-R possessed BET surface areas of 21 and 5 m² g⁻¹, respectively, after catalytic testing. For the EPR experiments, CeO₂-A was treated in O₂:HCl = 0.75 at 703 K for 3 h. This sample is denoted as CeO₂-D.

5.2.2 Basic characterization

Powder X-ray diffraction (XRD) was measured in a PANalytical X'Pert PRO-MPD diffractometer. Data were recorded in the $10\text{-}70^\circ$ 2θ range with an angular step size of 0.017° and a counting time of 0.26 s per step. N_2 sorption at 77 K was measured in a Quantachrome Quadrasorb-SI gas adsorption analyzer. The samples were degassed in vacuum at 473 K for 12 h prior to the measurement.

5.2.3 *In situ* Prompt Gamma Activation Analysis (PGAA)

In situ PGAA [10] was utilized to measure the Cl uptake of ceria during HCl oxidation. The technique is based on the detection of element-specific gamma rays emitted upon the capture of neutrons by the nucleus. The investigated volume, in our case, a tubular micro-reactor (catalyst bed volume $\sim 0.3\text{ cm}^3$), was probed, and the amounts of Cl and Ce were quantified. PGAA was carried out under atmospheric pressure condition at the cold neutron beam of the Budapest Neutron Centre. A Compton-suppressed high-purity germanium crystal was used to detect the prompt gamma photons. Molar ratios (Cl:Ce) were determined from the characteristic peak areas corrected by the detector efficiency and the nuclear data of the observed elements. The gas-phase Cl signal (HCl , Cl_2) was subtracted; thus, all Cl:Ce ratios reported here correspond only to the catalyst itself. The quartz reactor (8 mm i.d.) was placed into the neutron beam and surrounded by a specially designed oven having openings for the incoming and outgoing neutrons and for the emitted gamma rays toward the detector. These openings were covered by thin aluminium foils to minimize heat losses. Two ceria samples ($\text{CeO}_2\text{-A}$, $\text{CeO}_2\text{-R}$) were investigated. As both revealed the same trends, only the more detailed investigation on $\text{CeO}_2\text{-R}$ is presented in the PGAA section, while results on $\text{CeO}_2\text{-A}$ are collected in the Supporting Information (SI). 0.8 g of $\text{CeO}_2\text{-R}$ (sieve fraction 0.1-0.32 mm) was loaded into the reactor. The reaction feed, at a constant total flow of $166.6\text{ cm}^3\text{ STP min}^{-1}$, was supplied by mass flow controllers and employed HCl (4.5), O_2 (5.0) N_2 (5.0), and Cl_2 (4.0). Various feed compositions, $p(\text{O}_2)$, $p(\text{HCl})$, and $p(\text{Cl}_2)$, and reaction temperature were investigated. Details are provided at the appropriate sections. The Cl_2 production was monitored by iodometric titration. The percentage of HCl conversion was determined as $X_{\text{HCl}} = (2 \times \text{mole Cl}_2 \text{ at the reactor outlet} / \text{mole HCl at the reactor inlet}) \times 100$. Further details on the technique and representative spectra are provided in the SI.

5.2.4 Catalytic evaluation

The gas-phase oxidation of hydrogen chloride was studied at ambient pressure in a set up described elsewhere [11]. The catalyst (sieve fraction = 0.4-0.6 mm) was loaded in the tubular reactor (8 mm i.d.) and pretreated in N_2 at 703 K for 30 min. Thereafter, the reaction gases were introduced at a total flow of $166\text{ cm}^3\text{ STP min}^{-1}$. CeCl_3 was tested at 703 K or 723 K, $\text{O}_2\text{:HCl} = 2, 4, \text{ or } 9$, and a catalyst weight of 0.5 g. Separated 5 h tests were carried out with fresh loads of CeCl_3 for each $\text{O}_2\text{:HCl}$ ratio and temperature. Used samples were collected for *postmortem* characterization after rapidly cooling down the reactor to room temperature in a flow of N_2 . Activity data were collected for $\text{CeO}_2\text{-A}$ after 1 h on stream under all conditions applied to CeCl_3 to serve as reference. The influence of Cl_2 co-feeding on the rate of HCl oxidation over $\text{CeO}_2\text{-A}$ was studied by introducing fixed amounts (2, 3, 4, and $5\text{ cm}^3\text{ STP min}^{-1}$) of Cl_2 to the inlet feed at 703 K and $\text{O}_2\text{:HCl} = 9$ (notice HCl flow is $16.6\text{ cm}^3\text{ STP min}^{-1}$), over 0.25 g of catalyst. Data were taken after 1.5 h on stream under each condition. Cl_2 quantification and calculation of the HCl conversion were performed as described in the above section.

5.2.5 *In situ* Fourier Transform Infrared Spectroscopy (FTIR)

A specially designed homemade cell was used to investigate Deacon catalysts under reaction conditions [12]. For *in situ* FTIR experiments, 42 mg CeO₂-A was pressed into a self-supporting disk (31.8 mg cm⁻²). The sample was placed in the sample holder, which serves as an internal furnace as well. The pellet was pretreated *in situ* by heating it in synthetic air up to 723 K (10 K min⁻¹). Spectra were recorded with a Varian-670 FTIR spectrometer (resolution = 4 cm⁻¹). In most cases, 512 scans were averaged to achieve a satisfactory signal-to-noise ratio. Mass flow controllers were used to supply the reaction feed (total flow = 100 cm³ STP min⁻¹). The effect of $p(\text{O}_2)$, $p(\text{HCl})$, and temperature was investigated under Deacon conditions. In the O₂ partial pressure-dependent series, the HCl flow was kept constant at 10 cm³ STP min⁻¹, and $p(\text{O}_2)$ was varied to give the following feed composition sequence O₂:HCl:N₂ = 9:1:0, 4:1:5, 2:1:7, 1:1:8 and 0.5:1:8.5. During the measurement of the HCl partial pressure dependence, the O₂ flow was kept constant at 20 cm³ STP min⁻¹, and HCl flow was varied as follows: 10, 6, 3, and 1 cm³ STP min⁻¹. In the partial pressure variation experiments, the temperature was kept at 703 K. The temperature dependence was investigated by reducing the temperature stepwise, 20 K per step, between 703 and 623 K using a feed of O₂:HCl:N₂ = 9:1:0.

5.2.6 Electron Paramagnetic Resonance (EPR) experiments

The X-band EPR experiments were performed in vacuum (1×10^{-4} - 8×10^{-5} mbar) at 77 K on a Bruker ESP 300E spectrometer equipped with the microwave bridge Bruker ER 042 MRH E. A Bruker ER 4116DM resonator operating in the TE 102 mode ($\nu \approx 9.5$ GHz) was used. All spectra were recorded with a modulation frequency of 100 kHz and microwave power of 2 mW with modulation amplitude of 1G. Measurements were performed with 70 mg of non-chlorinated (CeO₂-A) and 140 mg of chlorinated (CeO₂-D) samples in a quartz tube of 3 mm inner diameter. EPR spectra of both samples were collected after the following pretreatment procedure. After degassing, the sample was heated up (10 K min⁻¹) in vacuum to the desired temperature (523, 623 and 723 K). The temperature was kept constant for 20 min; then, the sample was cooled down to room temperature. O₂ adsorption was carried out at RT by dosing 1 mbar O₂ during 5 min. Afterward, the cell was outgassed, and the sample cooled down to 77 K for collecting EPR spectra. This procedure was repeated for every treatment temperature. Computer simulations of EPR line-shapes with Bruker Simfonia software were used to calculate spectral parameters. All spectra were normalized by the sample masses for semiquantitative comparison of the signal double integrals after different treatments.

5.3 Results

5.3.1 Kinetics of chlorination and dechlorination

Previous HCl oxidation experiments over CeO₂ assessed the role of feed oxygen concentration on the stability of the catalyst [9]. It was found that no rapid deactivation occurred above a feed O₂:HCl ratio of 0.75. Post-reaction XRD measurements identified CeCl₃·6H₂O in the samples undergoing deactivation, suggesting that bulk chlorination and the corresponding phase transition induced activity loss. Furthermore, *in situ* activity restoration was possible applying high O₂ feed over-stoichiometry. Herein, using *in situ* PGAA, we evaluated the kinetics of chlorination/dechlorination of CeO₂-R under HCl oxidation conditions. Since PGAA probes the whole catalyst volume, the bulk of ceria is included in the experimentally determined Cl:Ce ratios. The BET surface area of CeO₂-R is only 5 m² g⁻¹ (the average particle radius is ~80 nm), and hence, the Cl:Ce ratios are small. Later, we will show that Cl occupation limited to the surface of CeO₂-R gives rise to a Cl:Ce ratio of ~0.01 and higher numbers necessarily imply subsurface and bulk Cl contributions. It should be mentioned that by the term “surface chlorination” we do not discriminate between *cus* Ce occupation or surface lattice O replacement.

Three series of experiments were performed (Fig. 5.1A). First, a reaction feed of O₂:HCl = 1:1 was set, and the activity together with the Cl:Ce ratio was followed over time. Then, the oxygen content was increased stepwise, leading to feeds with a O₂:HCl ratio of 2:1, 4:1, and 9:1. In the second series, directly after the first, we started with an O₂:HCl ratio of 0.5:1 and stepwise increased the oxygen content up to a ratio of 9:1. In the third series, directly after the second, a stoichiometric (0.25:1) feed was applied, and the oxygen content was again raised stepwise up to the ratio of 9:1. Fig. 5.1B compiles the evolution of chlorine uptake and its effect on the reactivity in the three series. The first data point (1:1), taken after equilibration for 1 h, corresponds to ~0.02 Cl:Ce and 4% HCl conversion. The sample continuously adsorbed chlorine, and the Cl:Ce increased up to 0.067 over the 6 h of measurement without any indication of the Cl uptake to cease. Concomitantly, the sample lost approximately 15% of its initial activity. Increasing the feed oxygen content gave rise to activity increase in line with the positive, approximately +0.5, formal order of $p(\text{O}_2)$ [9]. No further rise of Cl:Ce was observed in the first set, and dechlorination was negligible in the feed of 9:1. In the second series of the experiment, strong chlorination was again evidenced at 0.5:1 and 1:1 feed ratios, and chlorination stopped at 2:1. Note, among the three series, all repeated conditions resulting in a significantly higher Cl:Ce ratio gave rise to lower HCl conversion. This time, with more than doubled Cl content, the 9:1 feed was capable to induce dechlorination with simultaneous activity recovery. Essentially, similar observations could be made for the third measurement series, with the difference that the 9:1 feed enabled strong dechlorination with significant activity recovery. Note that even if dechlorination was far from complete (Cl:Ce = 0.125), the conversion level was fully restored. In fact, it was slightly even higher than in the first two series. As the whole experiment took more than 32 h, the sample at 9:1 feed worked essentially without deactivation, underlining the remarkable stability of the catalyst. Since mere surface Cl occupation leads to a Cl:Ce ratio of ~0.01, the sample under all these conditions contains much Cl below the surface. The results described suggest that (i) chlorination at low oxygen over-stoichiometry indeed gives rise to deactivation, but (ii) dechlorination at high oxygen over-stoichiometry can clean up the relevant surface sites without the necessity of removing all subsurface/bulk Cl from the material. Fig. 5.1C depicts an example of the temporal evolution of Cl:Ce. The data illustrate that chlorination occurs continuously with a constant rate. When analyzing the chlorination rate at 1:1 feed composition as a function of the pre-chlorination degree in the three series, only little variation was found. Thus, the chlorination rate is not much affected by the pre-chlorination degree. However, despite the continuous chlorination, no further deactivation over time was observed at 1:1 feed in the second and third series. Comparing the chlorination rate as a function of the oxygen content in the feed (Fig. 5.1D), we found that a lower oxygen content preferentially facilitates chlorination, and that sustained chlorination is absent at O₂:HCl ≥ 2. Dechlorination was not observed in the 4:1 feed, and

among the feed stoichiometries probed, only 9:1 was effective in this respect. As opposed to chlorination, dechlorination was strongly influenced by the pre-chlorination degree. Whereas almost no dechlorination was found in the first series, the estimated thickness change was -2.2 and -4.8 \AA h^{-1} in the second and third series, respectively.

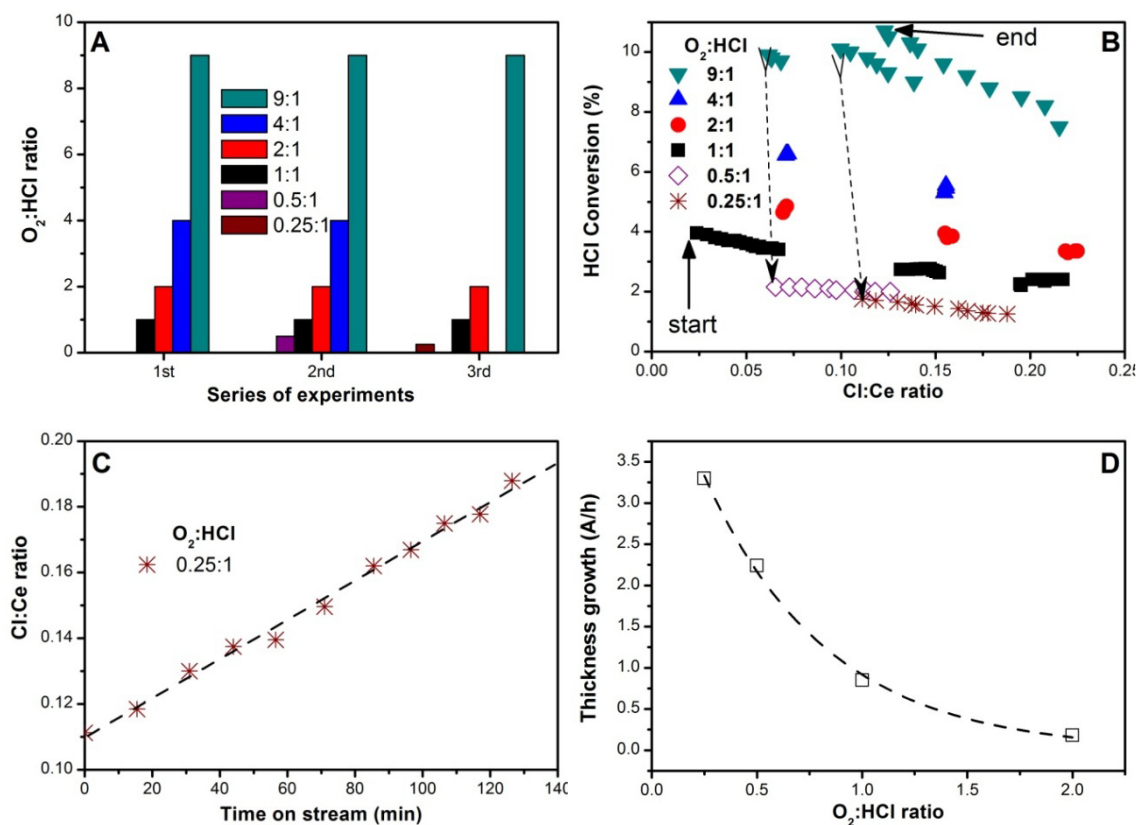


Figure 5.1 Series of chlorination/dechlorination experiments over $\text{CeO}_2\text{-R}$ at 703 K by *in situ* PGAA. (A) Map of experiments with three series. Various $\text{O}_2\text{:HCl}$ feed ratios (10% HCl, 2.5–90% O_2 balanced in N_2) were probed. Measurements were performed from left to right consecutively, however, for different time periods. (B) Evolution of HCl conversion and Cl uptake (as Cl:Ce) in the experiments. The first data point is at 4% conversion. The lines guide the eyes to follow the order of experiments. (C) An example of Cl uptake over time-on-stream with a feed of $\text{O}_2\text{:HCl} = 0.25:1$. (D) Thickness growth (\AA/h) of chlorinated shell as a function of the feed oxygen content. The rate of Cl uptake was evaluated in a simple geometric model (with particle radius of 82 nm) and assuming a homogeneous growth of the chlorinated surface shell toward the particle core. The thickness growth describes the speed of the chlorinated front moving towards the core of the ceria particle.

As chlorinated CeO_2 could be rapidly transformed back into pure CeO_2 by applying a high oxygen excess [9], it was investigated whether rejuvenation of the oxide could be possible also starting with a pure chloride phase. Therefore, bulk CeCl_3 was exposed to feeds of different $\text{O}_2\text{:HCl}$ ratio at 703 K, and the used samples were analyzed by XRD (Fig. 5.2). At $\text{O}_2\text{:HCl} = 2$, the HCl conversion level was very low ($\sim 2\%$) throughout the 5 h test, and only traces of cerium(IV) oxide were detected in the sample after reaction. By using the same feed composition but a 20 K higher temperature, the initially low HCl conversion progressively increased, nearly reaching the level exhibited by our reference $\text{CeO}_2\text{-A}$ sample under identical reaction conditions ($\sim 22\%$). In this case, the original chloride phase almost fully transformed into CeO_2 . Using higher feed $\text{O}_2\text{:HCl}$ ratios (4 and 9) rapidly led to a HCl conversion level, which even surpassed that expected for CeO_2 under the same conditions. The used samples were

pure ceria. These data indicate that the active CeO_2 phase can be *in situ* generated from CeCl_3 by action of gas-phase O_2 , and that the kinetics of its formation is faster for higher oxygen excess. The overshooting of the HCl conversion values for CeCl_3 rejuvenated at $\text{O}_2:\text{HCl} = 4$ and 9 compared to CeO_2 can be partially rationalized considering that the decomposition of the chloride to produce the oxide releases Cl_2 . This process is fast and complete for these samples, while slower and only partial for CeCl_3 exposed to lower $\text{O}_2:\text{HCl}$ ratios. Furthermore, as the surface area of these materials is 2-3 times larger than that of CeO_2 used as reference (Table 5.1), they are supposed to contain a higher amount of active surface ensembles per gram of catalyst. The reaction rate per m^2 of surface after 5 h on stream is in a similar range to that of pure ceria for all rejuvenated samples, indicating a high degree of recovery of the reactivity (Table 5.1). Comparing this rejuvenation experiment with the dechlorination study by PGAA, the low stability of CeCl_3 under Deacon conditions can be clearly inferred. Subsurface Cl in O vacancy position within the oxide phase has a higher stability against dechlorination; nevertheless, both dechlorination experiments revealed the same trends.

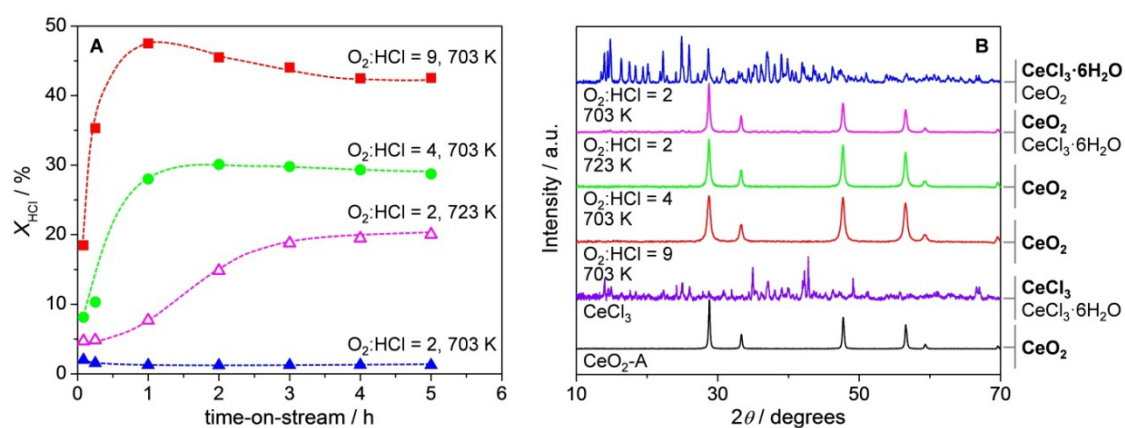


Figure 5.2 Rejuvenation of the CeO_2 phase from CeCl_3 under Deacon conditions. (A) HCl conversion *versus* time-on-stream over CeCl_3 at various $\text{O}_2:\text{HCl}$ ratios and temperatures. Other conditions: 10 vol.% HCl and 20-90 vol.% O_2 balanced in N_2 , space time = $11.2 \text{ g h mol}^{-1}$, total volumetric flow = $166 \text{ cm}^3 \text{ STP min}^{-1}$, and 1 bar. (B) XRD patterns of fresh $\text{CeO}_2\text{-A}$, fresh CeCl_3 , and CeCl_3 samples resulted from the catalytic tests. The right panel lists the crystalline phases identified in the samples, with the predominant phase in bold: CeO_2 (JCPDS 73-6328), CeCl_3 (JCPDS 77-0154), $\text{CeCl}_3 \cdot 6\text{H}_2\text{O}$ (JCPDS 01-0149).

The two CeO_2 samples ($\text{CeO}_2\text{-R}$, $\text{CeO}_2\text{-A}$) investigated in this work exhibited similar intrinsic reactivity and chlorine uptake as measured by *in situ* PGAA. As we shall see in the next section, product Cl_2 inhibits the reaction, and therefore, a linear activity scaling by the BET surface area is not attained; nevertheless, the similarity of the two CeO_2 samples is still clear. Furthermore, the evolution of *in situ* Cl:Ce ratios derived as a function of reaction conditions was essentially identical, as described in the next section and shown in Fig. S 5.1. Thus, the samples behave similarly in HCl oxidation.

Table 5.1 Comparison of characterization and activity for the ceria catalysts. Notice, the two CeO₂ catalysts exhibit similar intrinsic reactivity.

<i>Catalyst</i>	S_{BET} after Deacon ($m^2 g^{-1}$)	<i>Rate</i> ($mol Cl_2 g^{-1} min^{-1}$)	<i>Rate</i> ($mol Cl_2 m^{-2} min^{-1}$)	<i>Cl:Ce</i>	<i>Cl:Ce</i> normalized by S_{BET}
CeCl ₃ ^b (O ₂ :HCl = 9; 703 K) ^a	57	3.1×10^{-4}	5.4×10^{-6}	-	-
CeCl ₃ ^b (O ₂ :HCl = 4; 703 K)	43	2.1×10^{-4}	4.9×10^{-6}	-	-
CeCl ₃ ^b (O ₂ :HCl = 2; 703 K)	2	9.2×10^{-6}	4.6×10^{-6}	-	-
CeCl ₃ ^b (O ₂ :HCl = 2; 723 K)	26	1.5×10^{-4}	5.8×10^{-6}	-	-
CeO ₂ -R ^c (O ₂ :HCl = 9; 653 K)	5	2.2×10^{-5}	4.4×10^{-6}	0.0125	2.5×10^{-3}
CeO ₂ -A ^c (O ₂ :HCl = 9; 653 K)	21	7.1×10^{-5}	3.4×10^{-6}	0.045	2.1×10^{-3}

^a Conditions applied.^b Rate measured after 5 h on stream.^c During PGAA

5.3.2 Surface coverage analysis

Important mechanistic information may be obtained when combining different complementary *in situ* techniques [13-15] able to follow the changes of different adsorbed species and intermediates on the surface of the catalyst at work. As we have seen in the chlorination section, *in situ* PGAA is well suited to quantify the chlorine uptake of ceria, and thus, we can utilize the technique also to estimate the evolution of the Cl coverage as a function of the reaction conditions. One of the most suited complementary techniques to PGAA is *in situ* FTIR spectroscopy, affording to monitor the dynamic changes of the hydroxyl groups under reaction conditions. For the FTIR experiments, CeO₂ was activated *in situ* using synthetic air at 703 K for 90 min. After this pretreatment, two main bands at 3700 and 3620 cm⁻¹ were observed, which are assigned to mono-coordinated and doubly coordinated hydroxyl groups, respectively [16]. These two bands vanished when introducing a mixture of O₂:HCl = 9:1 at 703 K, with the concomitant development of two signals, the main one falling at 3730 cm⁻¹ and a shoulder located at 3676 cm⁻¹ [12]. Furthermore, a very broad band near 3500 cm⁻¹, likely related to surface water, was also observed. Since the mono-coordinated band at 3730 cm⁻¹ showed to quickly respond to changes in reactants concentrations and temperature, the integral area of this peak, obtained from fitting the absorbance spectra, was used to correlate the abundance of mono-coordinated OH groups with the catalyst reactivity under different reaction conditions. More details on the *in situ* FTIR experiments are published elsewhere [12].

The effect of $p(\text{O}_2)$ on the concentration of OH species, referenced to the one observed in a feed of $\text{O}_2:\text{HCl} = 9:1$, is illustrated in Fig. 5.3A. The amount of OH groups decreased when reducing the O_2 content in the feed, suggesting that sites to facilitate HCl adsorption need to be created by dissociative O_2 adsorption. In the case of the $p(\text{HCl})$ dependency (Fig. 5.3B), the OH concentration was maximum at the lowest feed HCl concentration (1 vol.%), and steadily decreased by increasing the feed HCl content. This apparently counterintuitive result will be discussed later with the corresponding surface Cl evolution. Further, the influence of the reaction temperature on the OH concentration was also studied. It appeared that the abundance of OH progressively diminished along with temperature from 703 to 623 K (Fig. 5.3C).

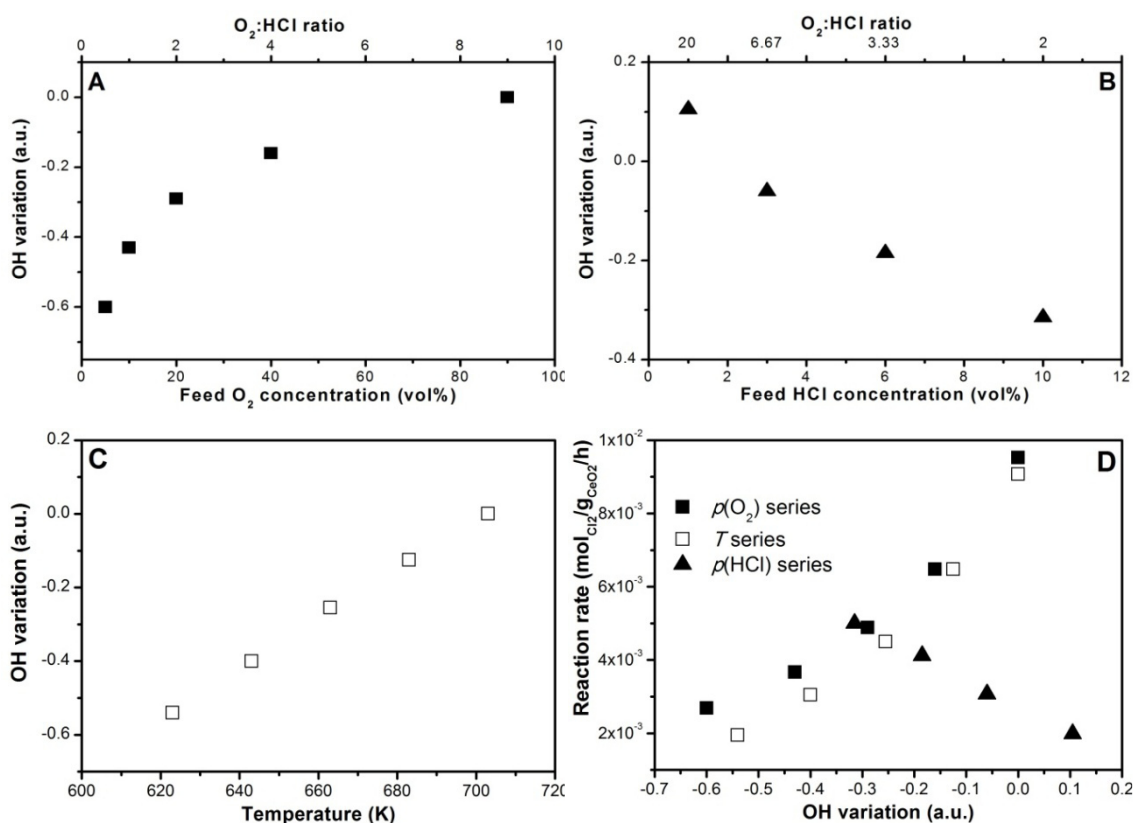


Figure 5.3 Evolution of the intensity of the mono-coordinated OH band at 3730 cm⁻¹ as a function of (A) $p(\text{O}_2)$, (B) $p(\text{HCl})$, (C) temperature as measured by *in situ* FTIR on CeO₂-A. The absorbance spectra were fitted, and the area variation referenced to the condition $\text{O}_2:\text{HCl} = 9:1$ at 703 K was plotted. (D) Reaction rate measured in parallel by iodometric titration, *versus* the intensity of the OH band under different conditions.

The correlation between the reaction rate (mol g_{CeO₂}⁻¹ h⁻¹) and the abundance of OH groups on the surface for the above variation of parameters is summarized in Fig. 5.3D. Obviously, changes in temperature and $p(\text{O}_2)$ determined the same trend, in the sense that the highest rate was achieved at the conditions (high temperature or oxygen-rich feed) that give rise to the highest OH coverage. This indicates that these two parameters may act in a similar fashion. In contrast, variation of $p(\text{HCl})$ revealed an opposite behavior. In fact, the highest Cl₂ productivity was achieved by using reaction conditions (high $p(\text{HCl})$ feed) under which the lowest surface OH concentration is observed.

Fig. 5.4 compiles the activity data *versus* the Cl uptake measured by *in situ* PGAA when varying $p(\text{O}_2)$, T , $p(\text{HCl})$, and $p(\text{Cl}_2)$. All these experimental series started with an oxidizing treatment in pure oxygen at 723 K for 2 h. This enables to remove essentially most of the chlorine from the material. Preexperiments indicated the effect of the studied variables on the Cl

content, and thus, all of these series shown here were performed in such a way that the first measurement should induce the smallest Cl uptake and the last measurement the largest.

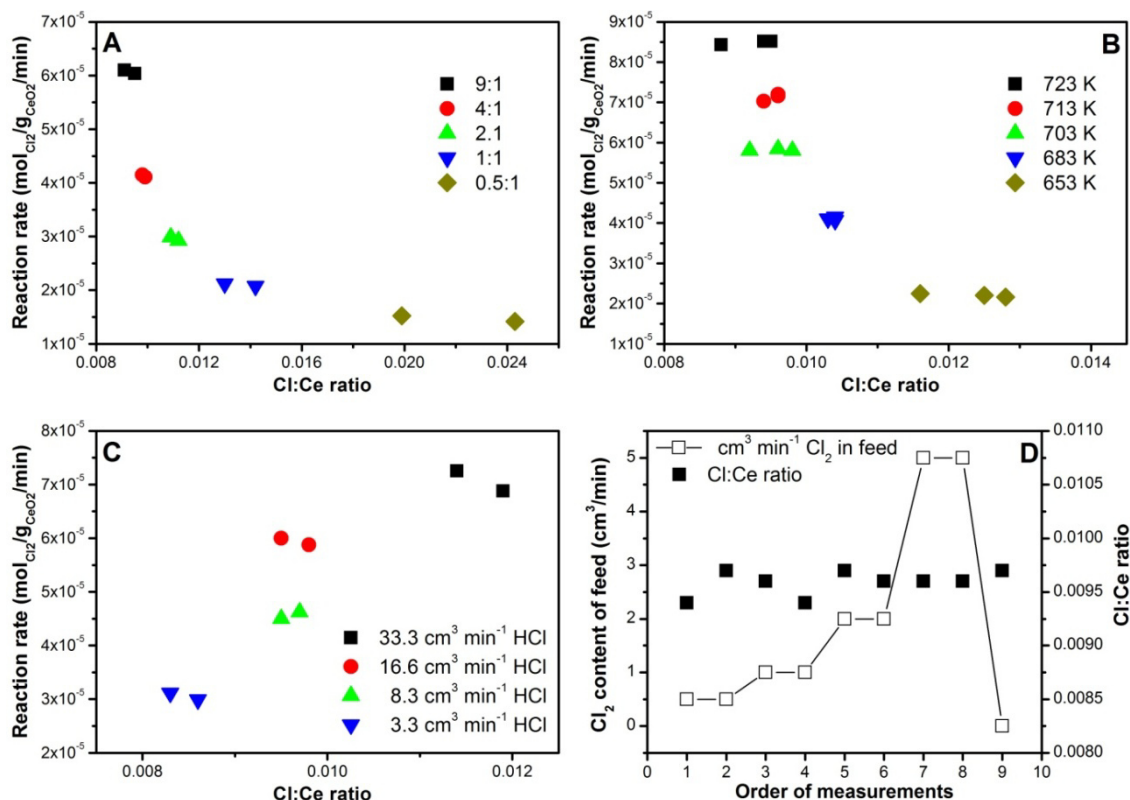


Figure 5.4 *In situ* PGAA experiments on CeO₂-R showing the reaction rate evolution as a function of Cl:Ce ratio under various conditions. In (A), the feed oxygen content (at 703 K), in (B) the temperature (at O₂:HCl = 9:1) and in (C), the feed HCl content (at 703 K) was varied. (D) Cl:Ce ratio as a function of various amounts of Cl₂ co-dosed to a 9:1 feed at 703 K. In SI, corresponding $p(\text{O}_2)$ and T dependences on CeO₂-A are shown to be identical to those given here. Table 5.1 suggests that over CeO₂-R and CeO₂-A, both reactivity and Cl uptake are similar when normalized to the corresponding BET surface area.

Fig. 5.4A depicts the effect of $p(\text{O}_2)$. The highest oxygen-containing feed (O₂:HCl = 9:1) led to the highest reactivity and to the lowest Cl uptake. Decreasing the oxygen over-stoichiometry lowered the reactivity and in parallel increased the Cl content. As shown in Fig. 5.1B, a 1:1 feed led to a continuous increase in the chlorine content in the solid. This is seen here too, as the second measurement resulted into a clearly higher Cl:Ce ratio. The effect was even stronger in the 0.5:1 feed, in agreement with Fig. 5.1D. Therefore, by decreasing the partial pressure of O₂, the Cl coverage increases slightly until the point where the chemical potential of surface Cl is high enough to induce its diffusion into the subsurface and later gives rise to a phase transition from the oxide to the chloride. The transition from purely surface to subsurface and bulk chlorination with this sample was in the Cl:Ce range of ~ 0.01 -0.012. The effect of the temperature on the OH coverage was very similar to that of $p(\text{O}_2)$. This is one-by-one transferable to the Cl coverage. High temperature results in higher reaction rate and concomitantly in a lower Cl content. As the T decreases, Cl:Ce slightly increases until at a certain temperature (653 K in this particular case) subsurface population kicks in. The trends in $p(\text{O}_2)$ and T can be overlaid very well and suggest that in these experiments the Cl coverage is a key (negative) parameter governing reactivity. This simple situation however changes for the influence of $p(\text{HCl})$, as it can be deduced from Fig. 5.4C. In a much diluted HCl-poor feed,

the reactivity gets higher by increasing the inlet HCl concentration. This applies until a certain point, above which the rate drops by a further increase of $p(\text{HCl})$ [9]. Note that in this experiment (Fig. 5.4C), we only monitored the increasing activity branch. Since the $\text{O}_2:\text{HCl}$ ratio in the $p(\text{O}_2)$ series gave rise to decreasing Cl:Ce, $p(\text{HCl})$ is expected to show an opposite behavior. This is indeed the case, as higher $p(\text{HCl})$ increases the Cl coverage. Therefore, due to the concomitant activity increase, the Cl coverage cannot be regarded per se as the sole negative factor reducing reactivity. Looking back at the lower OH intensity in the infrared spectra with increasing $p(\text{HCl})$, as higher $p(\text{HCl})$ will build up a higher Cl coverage, the steady-state situation should plateau at a lower OH coverage, assuming that OH recombination and water evolution are more facile than Cl_2 desorption. This likely explains the apparently counterintuitive trend in OH abundance. The situation gets even more complex when considering the effect of product co-feeding. Fig. 5.4D shows the effect of various amounts of Cl_2 present in the standard feed of $\text{O}_2:\text{HCl} = 9:1$ on the Cl uptake. The result clearly suggests that $p(\text{Cl}_2)$ does not contribute under these oxygen-rich conditions to the Cl uptake as the Cl:Ce ratio scatters around the same ~ 0.096 value. When Cl_2 is completely switched off, no effect is observed, indicating that the Cl uptake from $5 \text{ cm}^3 \text{ min}^{-1}$ Cl_2 flow was within the error bar of the measurement. This is at odds to the inhibition experiment described in the next paragraph.

The rate of chlorine production over $\text{CeO}_2\text{-A}$ was measured upon progressively increasing the amount of Cl_2 added to the feed mixture of $\text{O}_2:\text{HCl} = 9$. A negative near linear correlation was found between the reaction rate and the inlet concentration of Cl_2 (Fig. 5.5), indicating that molecular chlorine has a moderately strong inhibiting effect on the reactivity of the catalyst. In view of the PGAA data, this result cannot be rationalized on the basis of an increase in the surface Cl coverage in measurable quantities.

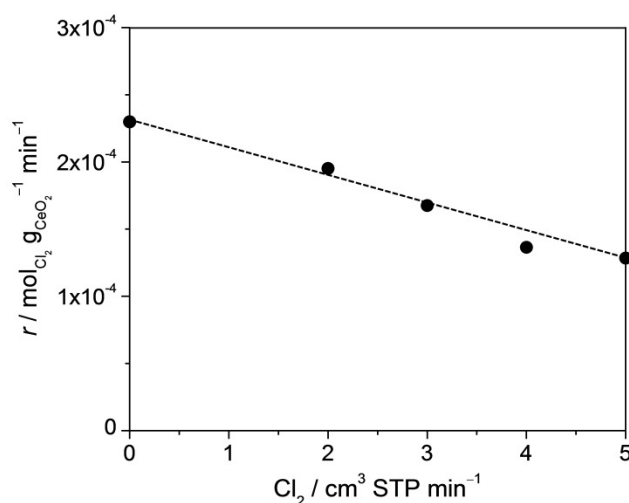


Figure 5.5 Influence of Cl_2 co-feeding on the rate of HCl oxidation over $\text{CeO}_2\text{-A}$. Conditions: $\text{O}_2:\text{HCl} = 9:1$, 703 K, space time = 5.6 g h mol^{-1} , total volumetric flow = $166 \text{ cm}^3 \text{ STP min}^{-1}$, 1 bar, and dwelling time under each condition = 1.5 h.

5.3.3 EPR experiments of O_2 adsorption

Ceria, owing to its character to reversibly exchange lattice oxygen, plays an important role in many oxidative catalytic processes. Thus, it is expected that surface chlorination influences its reducibility. Oxygen vacancies formed on the surface of the catalyst can be quantitatively investigated by means of EPR spectroscopy [17-20]. O_2 can be used as probe molecule for this purpose, because it binds to defects forming paramagnetic superoxide species, O_2^- .

EPR spectra of fresh ($\text{CeO}_2\text{-A}$) and chlorinated ($\text{CeO}_2\text{-D}$) ceria were collected, the samples being subjected to mildly reducing treatments in vacuum ($\sim 10^{-5}$ mbar) at different temperatures

within 523–723 K followed by O₂ adsorption at 298 K, in order to form the EPR-active superoxide species. By comparing the spectra of the samples before and after chlorination, significant changes in the signals' shape and intensities were observed (Fig. 5.6). The EPR spectra of CeO₂-A show a signal with quasi-axial line shape (Fig. 5.6A), which is assigned to superoxide species (O1-type) [21] having equivalent O atoms and lying parallel to the surface [20]. The corresponding *g* values are listed in Table S5.1 and agree well with literature values. The EPR spectra of CeO₂-D exhibit a signal with a rhombic shaped (Fig. 5.6B), with *g_x* shifted slightly toward higher values, which is again consistent with literature data for a chlorinated sample [22]. As opposed to *g_x*, the *g_y* and *g_z* values are essentially unaffected upon chlorination. Note that according to the so-called ionic model of the Mⁿ⁺ – O₂⁻ radicals, the *g_x* tensor value must lie very close to the free electron *g* value (*g_e* = 2.0023), bearing in mind that the *x* axis is considered to be normal to the O–O–Mⁿ⁺ plane [23]. Thus, a plausible interpretation of the *g_x* shift is a somewhat higher degree of covalent character in the Ce⁴⁺ – O₂⁻ bond induced by the substitution of lattice O atoms by Cl [24].

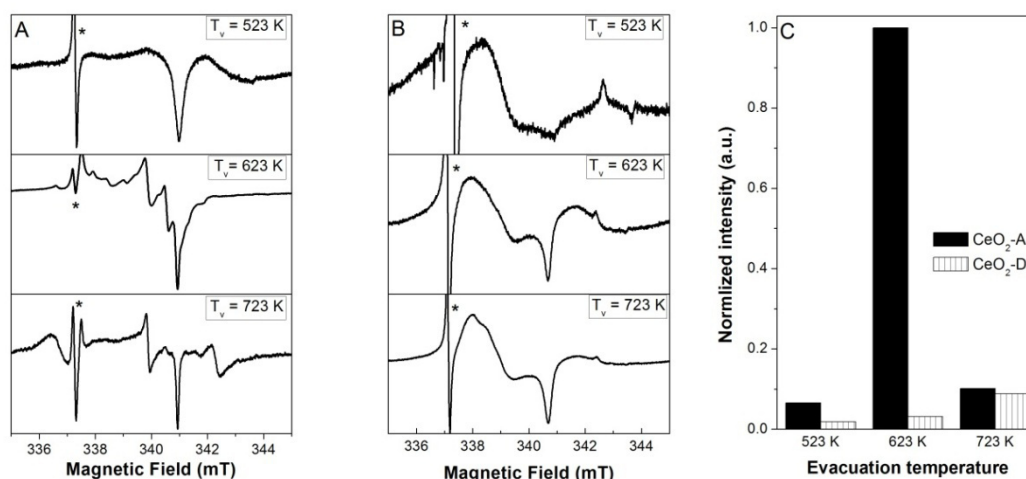


Figure 5.6 EPR signals of superoxide species produced by O₂ adsorbed at RT on pre-reduced samples (A) CeO₂-A and (B) CeO₂-D. Signal marked with * is due to highly EPR-active Mn²⁺ impurities in the ceria. (C) The amount of superoxide was quantified by double integration of signals assigned to superoxides.

The amount of paramagnetic species produced on the samples was obtained from the double integration of the signals. Fig. 5.6C shows that a maximum amount of superoxide species was formed over CeO₂-A as a function of the reduction temperature, and that outgassing at higher temperature dropped the superoxide intensity. Intuitively, one would expect even more reduced sites at higher temperature, and hence the formation of more superoxide species. However, at high temperatures, oxygen vacancies can diffuse into the bulk, since this is energetically more favored compared to being trapped at the surface [25], and thus, less superoxide could form. Additionally, at higher *T*, vacancies may cluster, and upon O₂ adsorption, these can be filled by O₂ dissociation, thus impeding the formation of superoxides. The chlorinated sample generally produced fewer superoxide species and exhibited a much smaller effect on temperature changes. No maximum was found in this case, and the highest superoxide signal intensity was observed after pretreatment at 723 K. Hence, we can conclude that chlorination inhibits facile vacancy formation, and thus lowers the propensity of ceria to activate oxygen.

5.4 Discussion

A relatively simple catalytic reaction, HCl oxidation over CeO_2 , has been investigated, and we focused our attention (1) on the chemical changes occurring on the surface and in the near-surface region of ceria, and (2) on the quantification of surface species under multiple steady states; with the hope to correlate both (1) and (2) with reactivity. PGAA experiments following chlorination and dechlorination kinetics have clearly indicated the detrimental role of subsurface/bulk chlorination on the reactivity. It is likely that this has its origin in the high surface Cl coverage necessary for facilitating Cl diffusion into the bulk and concomitant removal of lattice O in the formation of water. Losing lattice O/vacancy dynamics by extended near-surface chlorination hinders oxygen activation. EPR experiments have shown that the number of surface O vacancies enabling the formation of superoxide species upon O_2 adsorption drastically diminishes for the chlorinated sample. This implies that oxygen activation during HCl oxidation is a critical elementary step when the Cl surface coverage is high. Our recent characterization of the acid/base properties of ceria after HCl oxidation indicated that sites with basic character were essentially eliminated from the surface of chlorinated CeO_2 [12]. That is, most of the lattice O sites have been exchanged by Cl, and the OH groups formed are rather acidic. Notice, HCl activation is thought to require basic sites to abstract H. Therefore, it is not surprising to see that $p(\text{O}_2)$ has a clear negative effect on the Cl uptake and a concomitant positive influence on reactivity. Higher O_2 over-stoichiometry will liberate chlorinated sites by dissociative O_2 adsorption to enable HCl dissociative adsorption. This gives rise to less site blocking by Cl and a higher population of OH groups.

Remarkably, Cl and OH population changes were, as a rule, complementary upon variation by the reaction conditions ($p(\text{O}_2)$, $p(\text{HCl})$, and T). Higher temperature and $p(\text{O}_2)$ as well as lower $p(\text{HCl})$ decreased Cl and increased OH coverage. This indicates that the major role of temperature is to diminish site blocking by Cl. On the contrary, increasing $p(\text{HCl})$ gives rise to higher Cl coverage and parallel increase in reactivity, though only in the range where no subsurface and bulk chlorination occurs. This influence of the partial pressure of HCl points to a significantly more complex role of the coverage with Cl containing species, which may be divided into two contributions: one major part being detrimental, as discussed, most probably by site blocking, whereas a small but certain part is “reactive”. Surface sites binding Cl after dissociation less strongly can contribute to the latter group. Further, during HCl oxidation, lateral interactions at high coverages may give rise to lower heat of adsorption of reactants that can accelerate the reaction. Such lateral interactions for adsorbed HCl may be operative in increasing reactivity at high HCl partial pressures.

Molecular chlorine was predicted to have a weak effect on surface chlorination [9]. Only at high $p(\text{Cl}_2)$ and very low $p(\text{O}_2)$, surface Cl will stabilize in a lattice O vacancy or at the cus Ce^{4+} site. This is in perfect agreement with our PGAA observation, as extra Cl_2 product co-feeding in the range investigated (up to $5 \text{ cm}^3 \text{ STP min}^{-1} \text{ Cl}_2$ next to $16.6 \text{ cm}^3 \text{ STP min}^{-1} \text{ HCl}$) was not able to induce any increase of the Cl:Ce ratio. On the other hand, Cl_2 gives rise to strong inhibition, as the same amount ($5 \text{ cm}^3 \text{ STP min}^{-1}$) of Cl_2 reduced reactivity by $\sim 45\%$. The way products can inhibit reaction is most often related to site blocking by adsorption. Further, the heat of adsorption of reactants may be modulated by other adsorbates (promoters and poisons), but interaction of Cl_2 with ceria is weak and dissociation leads to surface Cl; hence, inhibition by the modification of the surface electronic structure is not likely. Since Cl_2 inhibition is not persistent and turning off Cl_2 product feeding restores reactivity quickly, complex restructuring phenomena are also not likely, and rather inhibition is expected to occur by competitive adsorption and site blocking. As, however, this was not observable within the uncertainty ($\sim 2\%$) of the experiment, one can conclude that the number of sites critically involved in the reaction should be very small (in the range of few percent). Consequently, most surface sites probed in the *in situ* spectroscopic (FTIR and PGAA) experiments correspond to either sites holding spectators or function only as buffer. The reactivity of most surface sites is thus likely negligibly low, and only very few high-energy sites can effectively contribute to the observed catalytic turnover. Nevertheless, nearby sites, temporarily storing surface species may supply

adsorbates to the high-energy site, which may effectively catalyze recombination and desorption of products. Then, the convincing correlations found in the *in situ* FTIR and PGAA experiments (Fig. 5.3 and Fig. 5.4) do *not* correspond to the relevant active surface sites, but rather describe the equilibration of the major nonreactive surface units with the reactants and the adjustment to the reaction conditions. Although *in situ* or *operando* studies deserve the attention of the catalysis community and usually represent a step up from standard works with reactivity and *ex situ* characterization, the experiments described here suggest that one should at least exercise some caution when deriving strong conclusions from a limited set of *in situ* (*operando*) experiments. Investigating a larger set of variables may override frivolously derived correlations and conclusions.

5.5 Conclusions

Ceria is a catalyst with high industrialization potential for HCl oxidation. We have investigated various aspects of this reaction system. Subsurface and bulk chlorination gives rise to deactivation, and we studied the kinetics of this as well as the inverse dechlorination process. In line with the negative role of chlorination, the rate of chlorination is higher with lower oxygen over-stoichiometry (but is independent of the pre-chlorination degree), whereas dechlorination is facilitated at high oxygen partial pressures. At the limit, CeCl_3 transforms to CeO_2 under reaction condition.

The surface coverage of the two most abundant species Cl and OH was followed under multiple steady-state conditions as a function of $p(\text{O}_2)$, $p(\text{HCl})$, $p(\text{Cl}_2)$, and T without the influence of subsurface chlorination. The feed oxygen content and the temperature remove some surface Cl and increase the OH population with concomitant reactivity enhancement. Hence, in these experiments, OH positively and Cl negatively correlates with the reactivity. On the other hand, in oxygen-rich feeds, higher $p(\text{HCl})$ gives rise to increased activity, but also to higher coverage of Cl containing species (and less OH), and therefore, here, an opposite trend is observed. Lastly, Cl_2 strongly inhibits the reaction, but no measurable increase of the Cl uptake was found. This latter result leads us to the conclusion that essentially all of the surface probed in the *in situ* experiments correspond to the main part of the surface bearing little relevance to the reactivity. This complex set of experiments highlights the importance of investigating a broad field of reaction parameters before deriving strong but artificial surface-reactivity correlations.

5.6 Supporting Information

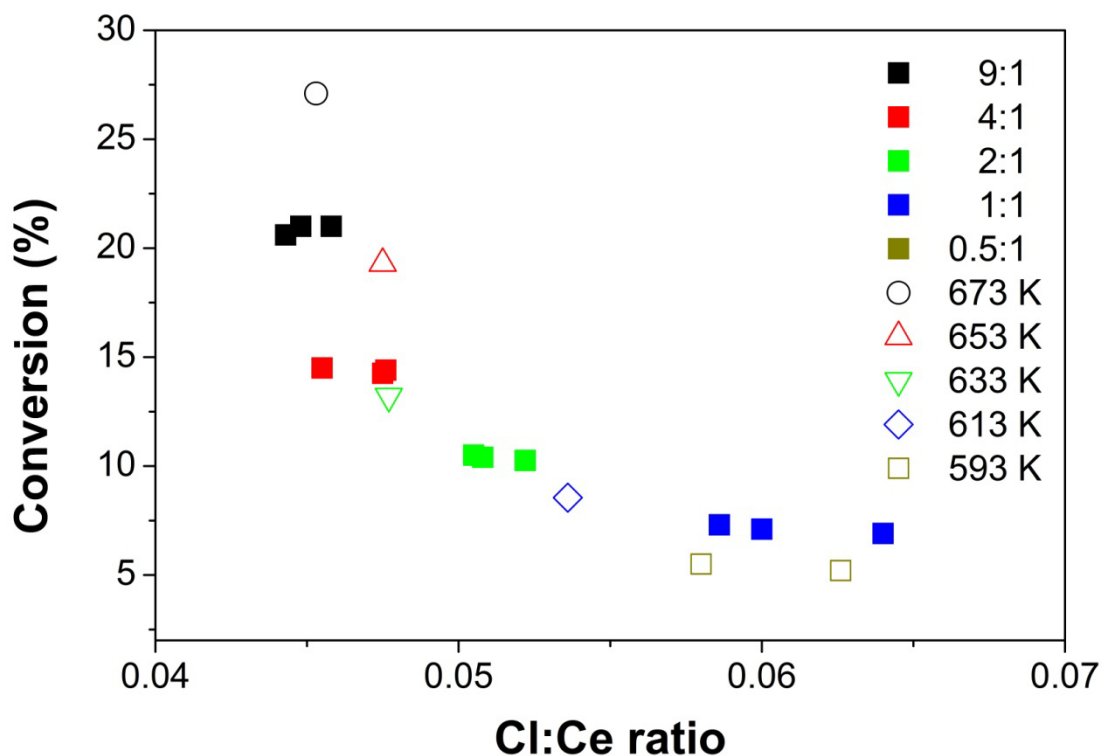


Figure S 5.1 *In situ* PGAA experiments on CeO₂-A showing the reaction rate (conversion) evolution as a function of Cl/Ce ratio under various conditions: varying the feed oxygen content at 703 K (O₂:HCl= 9:1, 4:1, 2:1, 1:1 and 0.5:1), and the temperature at O₂:HCl = 9:1 ($T = 673$ -593 K).

Table S 5.1 Characteristics of the EPR signals for CeO₂-A and CeO₂-D obtained upon oxygen adsorption at 298 K.

Sample (Outgassing Temperature)	Signal	<i>g</i> Tensor		
		g_x	g_y	g_z
CeO ₂ -A (523 K)	O1-Typ	2.01 (2.0146)	2.01	2.03
CeO ₂ -A (623 K)	O1-Typ	2.02 (2.017)	2.01 (2.011)	2.03 (2.031)
CeO ₂ -A (723 K)	O1-Typ	2.02 (2.017)	2.01	2.03
CeO ₂ -D (523 K)	OCl	2.02 (2.022)	2.01 (2.0116)	2.03 (2.028)
CeO ₂ -D (623 K)	OCl	2.02 (2.0215)	2.01 (2.0117)	2.03 (2.028)
CeO ₂ -D (723 K)	OCl	2.02 (2.0215)	2.01 (2.0116)	2.03 (2.028)

Prompt Gamma Activation Analysis

Prompt gamma activation analysis (PGAA or PGNAA) is a nuclear analytical technique for non-destructive determination of elemental and isotopic compositions. The sample (this time the catalyst *in operando*) is irradiated in a neutron beam and the gamma-rays from the radiative neutron capture are detected. In principle all elements can be analyzed except helium. Contrary to the conventional neutron activation analysis (NAA), the irradiation and the detection are here simultaneous. Both neutrons and gamma-rays are highly penetrating, therefore – in contrast to many instrumental elemental analysis techniques – the average composition of the illuminated volume is obtained. Whenever a nucleus captures a neutron, a compound nucleus is formed with excitation energy between 6 and 11 MeV. The nucleus reaches its ground state, by emitting 2–4 gamma rays in a short sequence. This radiation is characteristic, i.e. the energy values of the gamma rays identify the nuclide, and their intensities are proportional to the number of atoms. The probability of a reaction is characterized by a quantity called cross section. This nuclear data are available for all stable elements in a form of an analytical library [1]. Using this library we can relate the count rate of the analytical peak to the quantity of the element without using a standard. The energies and intensities of the peaks are independent of the chemical state of the material. Every step of the measurement and the evaluation can be described with statistical methods, and the uncertainties of the concentrations can be readily estimated from one measurement.

The experiments were done at the PGAA facility [2-3] of the Budapest Research Reactor. The neutrons are guided here to the experimental positions by curved supermirror neutron guides to decrease the background coming from the reactor core. The thermal-equivalent neutron flux at the PGAA sample position is $7.7 \times 10^7 \text{ cm}^{-2} \text{ s}^{-1}$. The standard measurement geometry was modified to accommodate this special setup. The sample chamber was removed and the flow-reactor (quartz tube, internal diameter 8 mm) with the thermal insulation was placed directly into the beam. The oven had openings for the incoming and outgoing neutrons and for the emitted gamma rays. These openings were covered by thin aluminum foils to minimize heat losses. The reaction feed, at constant total flow, was supplied by mass flow controllers. The Cl_2 production was monitored by iodometric titration.

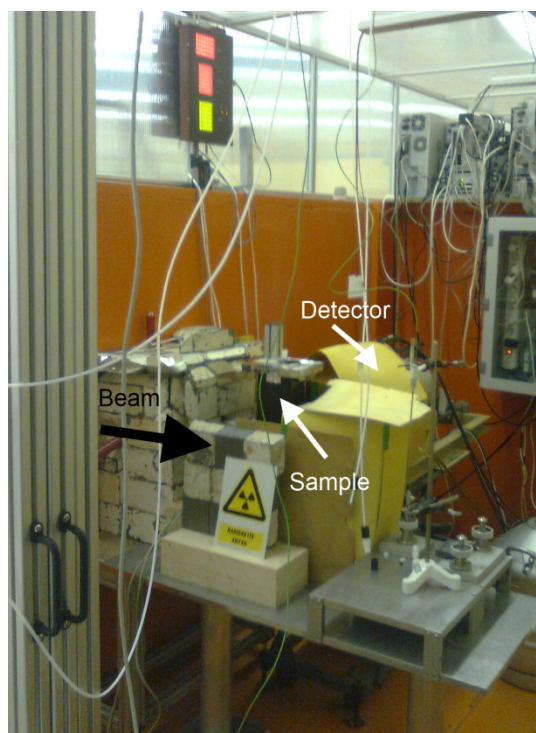


Figure S 5.2 A photo of the *in situ* PGAA experiment.

The detector system of the PGAA facility consists of an n-type high-purity germanium (Canberra HPGe 2720/S) main detector and a BGO Compton-suppressor, surrounded by a 10 cm thick lead shielding. The sample-to-detector distance was 275 mm. The BGO annulus and catchers around the HPGe detect most of the scattered gamma photons, in order to reduce the baseline of the spectra. An analogue spectroscopy amplifier combined with an ADC and an Ethernet-based multichannel analyzer (Canberra AIM 556A) collects the counts.

The detector calibration (counting efficiency [4] and nonlinearity [5]) was completed for this counting geometry with a set of sealed radioactive sources and neutron capture lines of chlorine. For most of the energy range the efficiency curve was better than 1% accurate.

A PGAA spectrum of the CeO_2 catalyst is shown in Figure S 5.3. The spectrum contains several hundreds of peaks. As the elements have more than one peak, the internal consistency of the mass determination can be validated [6]. With propagation of the uncertainties, the mass of the element can be determined with a better statistical precision [7].

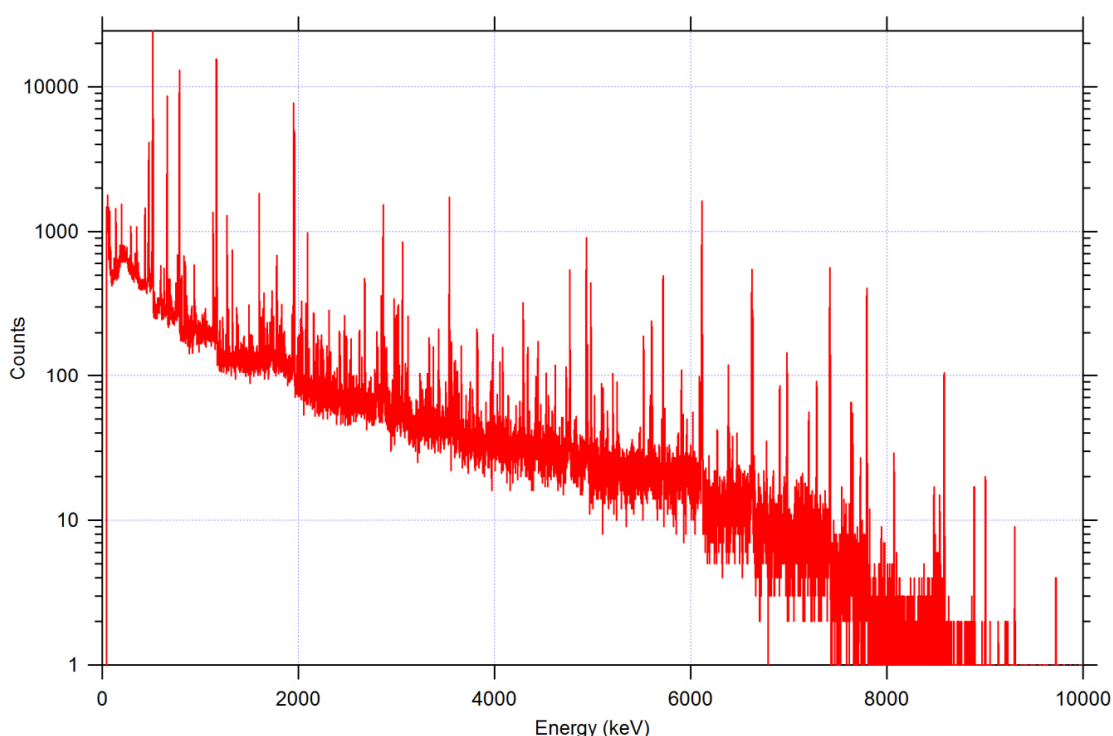


Figure S 5.3 A typical PGAA spectrum of the CeO_2 catalyst.

The peaks were evaluated with the spectroscopy software Hypermet-PC [8-9]. The program uses weighted nonlinear least square fit method to determine the peak areas and peak positions.

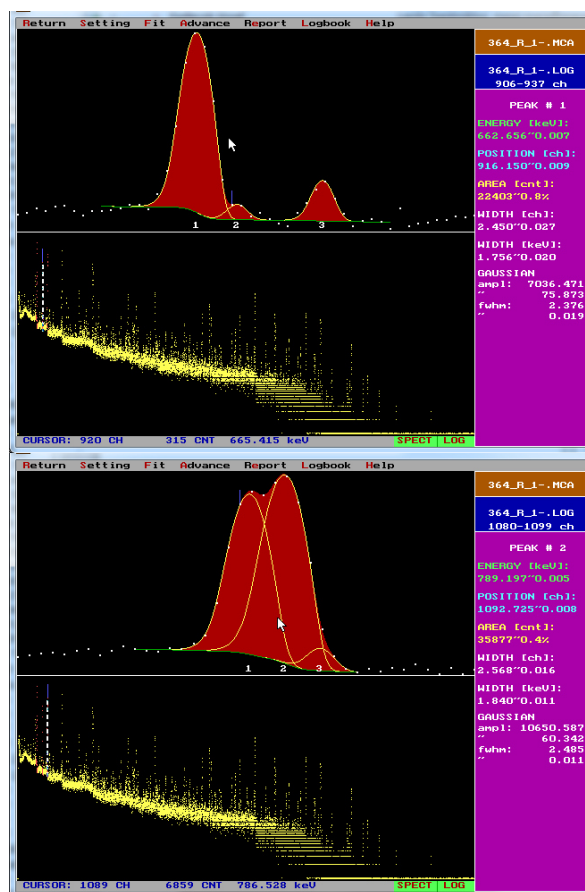


Figure S 5.4 Peak fitting of the Ce (top) and Cl lines (bottom). The panel in purple displays the uncertainties of the fitted quantities.

For the quantification the analytical library by Révay et al. [1] was used. In Table S 5.2, selected data of the elements of interest are summarized.

Table S 5.2 Peak energies, cross-sections and count rates of primary lines for Ce and Cl.

Element	Peak Energy	Unc.	Cross-section (barn)	Unc. %	Count (cps)	Rate	Unc
Cl	517.75	0.013	7.4	0.9	25.8		0.75
Ce	662.745	0.037	0.478	1.2	9.31		2.29
Cl	787.144	0.018	3.435	1.0	9.73		0.65
Cl	789.293	0.016	5.405	1.0	15.1		0.52
Cl	1953.19	0.029	6.5	0.8	11.6		0.66
Cl	1961.418	0.027	4.18	0.9	7.61		0.81

SI References:

- [1] Zs. Révay, R.B. Firestone, T. Belgya, G.L. Molnár: Catalog and Atlas of Prompt Gamma Rays in Handbook of Prompt Gamma Activation Analysis with Neutron Beams, (G.L. Molnár ed.), Kluwer Academic Publishers, Dordrecht/Boston/New York, 2004, pp. 173–364.
- [2] L. Szentmiklósi, T. Belgya, Z. Révay, Z. Kis: Upgrade of the Prompt-Gamma Activation Analysis (PGAA) and the Neutron Induced Prompt-gamma Spectroscopy (NIPS) facilities at the Budapest Research Reactor, *J. Nucl. Radioanal. Chem.*, 286 (2010) 501-505.
- [3] Zs. Révay, T. Belgya, L. Szentmiklósi, Z. Kis: Recent developments in prompt gamma activation analysis in Budapest, *J. Radioanal. Nucl. Chem.* 278 (2008) 643.
[4] G.L. Molnar, Z. Révay, T. Belgya: Wide energy range efficiency calibration method for Ge detectors, *Nucl. Instrum. Meth. A* 489 (2002) 140.
- [5] B. Fazekas, Zs. Révay, J. Östör, T. Belgya, G.L. Molnár, A. Simonits: A new method for determination of gamma-ray spectrometer nonlinearity, *Nucl. Instr. Meth. A* 422 (1999) 469.
- [6] Zs. Révay: Determining Elemental Composition Using Prompt-gamma Activation Analysis, *Analytical Chemistry*, 81 (2009) 6851-6859.
- [7] Zs. Révay: Calculation of uncertainties in prompt gamma activation analysis, *Nucl. Instrum. Meth A* 564 (2006) 688.
- [8] B. Fazekas, J. Östör, Z. Kis, G. L. Molnár, A. Simonits: The new features of Hypermet-PC, in: Proc. 9th International Symposium on Capture Gamma-Ray Spectroscopy and Related Topics, Budapest, Hungary, October 8-12, 1997, p. 774. (G.L. Molnár, T. Belgya, Zs. Révay Eds.) Springer Verlag, Budapest/Berlin/Heidelberg
- [9] Z. Révay, T. Belgya, G.L. Molnár: Application of Hypermet-PC in PGAA, *J. Radioanal. Nucl. Chem.*, 265 (2005) 261-265.

5.7 References

- [1] M. M. Schubert, M. J. Kahlich, H. A. Gasteiger, R. J. Behm, *J. Power Sources* 84, 1999, 175.
- [2] L. J. Burcham, L. E. Briand, I. E. Wachs, *Langmuir* 17, 2001, 6174.
- [3] F. C. Meunier, *Catal. Today* 155, 2010, 164.
- [4] T. Hibi, H. Abekawa, K. Seki, T. Suzuki, T. Suzuta, K. Iwanaga, T. Oizumi, EP936184, 1999.
- [5] A. Wolf, L. Mleczko, O. F. Schlüter, S. Schubert, EP2026905, 2006.
- [6] J. Pérez-Ramírez, C. Mondelli, T. Schmidt, O. F. -K. Schluter, A. Wolf, L. Mleczko, T. Dreier, *Energy Environ. Sci.* 4, 2011, 4786.
- [7] H. Over, *J. Phys. Chem. C* 116, 2012, 6779.
- [8] D. Teschner, R. Farra, L.-D. Yao, R. Schlögl, H. Soerijanto, R. Schomaecker, T. Schmidt, L. Szentmiklósi, A.P. Amrute, C. Mondelli, J. Pérez-Ramírez, G. Novell-Leruth, N. López, *J. Catal.* 285, 2012, 273.
- [9] A. P. Amrute, C. Mondelli, M. Moser, G. Novell-Leruth, N. Lopez, D. Rosenthal, R. Farra, M. E. Schuster, D. Teschner, T. Schmidt, J. Pérez-Ramírez, *J. Catal.* 286, 2012, 287.
- [10] Zs. Révay, T. Belgya, L. Szentmiklósi, Z. Kis, A. Wootsch, D. Teschner, M. Swoboda, R. Schlögl, J. Borsodi, R. Zepernick, *Anal. Chem.* 80, 2008, 6066.
- [11] A.P. Amrute, C. Mondelli, J. Pérez-Ramírez, *Catal. Sci. Tech.* 2, 2012, 2057.
- [12] R. Farra, S. Wrabetz, M. E. Schuster, E. Stotz, N. G. Hamilton, A. P. Amrute, J. Pérez-Ramírez, N. López, D. Teschner, *Phys. Chem. Chem. Phys.* 15, 2013, 3454.
- [13] X. T. Gao, S. R. Bare, J. L. G. Fierro, M. A. Banares, I. E. Wachs, *J. Phys. Chem. B* 102, 1998, 5653.
- [14] L. Burcham, G. Deo, X. Gao, I. Wachs, *Top. Catal.* 11-12, 2000, 85.
- [15] G. Le Bourdon, F. Adar, M. Moreau, S. Morel, J. Reffner, A. S. Mamede, C. Dujardin, E. Payen, *Phys. Chem. Chem. Phys.* 5, 2003, 4441.
- [16] A. Badri, C. Binet, J.-C. Lavalley, *Faraday Trans.* 92, 1996, 4669.
- [17] M. Gideoni, M. Steinberg, *J. Solid State Chem.* 4, 1972, 370.
- [18] A. Aboukais, E. A. Zhilinskaya, J.-F. Lamonier, I. N. Filimonov, *Colloids Surf., A* 260, 2005, 199.
- [19] M. Che, J. F. J. Kibblewhite, A. J. Tench, M. Dufaux, C. Naccache, *J. Chem. Soc., Faraday Trans. 1* 69, 1973, 857.
- [20] A. Martínez-Arias, J. C. Conesa, J. Soria, *Res. Chem. Intermed.* 33, 2007, 775.
- [21] J. Soria, A. Martínez-Arias, J. C. Conesa, *Faraday Trans.* 91, 1995, 1669.
- [22] J. Soria, J. C. Conesa, A. Martínez-Arias, *Colloids Surf., A* 158, 1999, 67.
- [23] M. Anpo, M. Che, B. Fubini, E. Garrone, E. Giamello, M. Paganini, *Top. Catal.* 8, 1999, 189.
- [24] J. Soria, A. Martínez-Arias, J. M. Coronado, J. C. Conesa, *Top. Catal.* 11-12, 2000, 205.
- [25] M. V. Ganduglia-Pirovano, J. L. F. Da Silva, J. Sauer, *Phys. Rev. Lett.* 102, 2009, 026101.

Chapter 6: Promoted ceria: a structural, catalytic and computational study

Ramzi Farra, Max García-Melchor, Maik Eichelbaum, Maike Hashagen, Wiebke Frandsen, Jasmin Allan, Frank Girgsdies, László Szentmiklósi, Núria López, Detre Teschner

Abstract

The role of trivalent (La, Sm, Gd, and Y) and tetravalent (Hf, Zr, and Ti) dopants in the catalytic, structural, and electronic properties of ceria was investigated. Promoted ceria catalysts were synthesized by coprecipitation with ammonia and tested in HCl and CO oxidation. Ceria catalysts exhibit a medium high reactivity and excellent stability in HCl oxidation. The intrinsic reactivity of ceria in HCl oxidation can be improved by a factor of 2 when doping with Hf and Zr in appropriate quantities, whereas trivalent dopants are detrimental. Although both oxidation reactions rely on the existence of oxygen vacancies, the order of reactivity in HCl and CO oxidation is not completely parallel. The effects of promoters on the electronic conductivity and the vacancy formation energy were studied by contactless conductivity experiments using the microwave cavity perturbation technique and by density functional theory calculations. Furthermore, transport properties were also assessed on the basis of theoretical calculations. The order of oxygen vacancy formation energy follows well the order of conductivity (polaron mobility) (trivalent > tetravalent > undoped) observed under inert and oxidizing conditions. This implies that none of these properties correlates with the reactivity. On the other hand, reducing conditions strongly enhanced the conductivity of Hf- and Zr-doped ceria. In HCl oxidation, only the balanced reduction of both Cl and O vacancy formation energies allows for an enhanced reactivity. Promoters give rise to lattice contraction–expansion modifying vacancy formation energies, adsorption properties, and surface coverages.

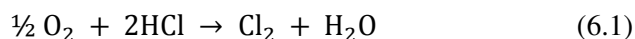
Acknowledgements

We thank ERC-StG'10, MINECO for support through project CTQ2012-33826/BQU and BSC-RES for generously providing computational resources. We thank Patrick Kast for allowing us to use his reactor setup for CO oxidation.

6.1 Introduction

Ceria is widely utilized in various catalytic processes as a support, as an additive, and as the active phase of the reaction. However, even when used as a support, it is not merely an inactive carrier. Because of the relative ease with which ceria can be reduced and the mobility of its lattice oxygen ions, it is an efficient material in redox reactions. Hence, ceria is a key component as an oxygen ion-conducting solid electrolyte in solid oxide fuel cells [1,2] and in automotive exhaust catalysis [3]. Further, it can be applied in SO₂ oxidation [4,5], in Diesel soot oxidation [6], in water-gas shift (WGS) [7,8] and preferential oxidation of CO (PROX) reactions [9,10], in oxidative halogenations [11] and in HCl oxidation [12,13]. In most of these reactions, the facile formation and annihilation of oxygen vacancies and reduced ceria sites likely play a crucial role. It is typically believed that in catalytic oxidations using ceria, the molecule to be oxidized takes oxygen from the oxide lattice, thereby creating oxygen vacancies on the surface. Reactant oxygen from the gas phase can subsequently replenish the vacancy and reoxidize the Ce³⁺ sites. Because this process of filling vacancies by oxygen is exothermic, particular attention has been focused on vacancy formation [14–20]. The local structure of surface and subsurface oxygen vacancies and vacancy clusters was revealed by scanning tunneling microscopy [14], while density functional theory (DFT) calculations suggested that the vacancy formation energy is structure sensitive [15–17] and that metals present as dopants [21–25] or adsorbed on top affect this parameter [26]. The most stable CeO₂(111) surface has a comparatively high vacancy formation energy (1.9–2.7 eV), whereas removal of oxygen from facets with a higher surface energy, e.g., (110), (100), and (310), is easier. Vacancy density was also experimentally found to be dependent on particle shape and, accordingly, the surface type exposed [27]. Consequently, surface reactions, such as CO oxidation, were also found to be structure sensitive over ceria [28–30]. The addition of promoters (dopants) has been frequently used to improve a certain target property of ceria. For example, ionic conductivity is much enhanced by trivalent dopants such as Gd and Sm [31], whereas reducibility and oxygen storage capacity are facilitated by the incorporation of Zr or Hf into the cubic structure [22,32,33]. Furthermore, addition of Zr improves the structural integrity of ceria, preserving the cubic phase. Promoters also were found to enhance the reactivity of ceria in CO oxidation [34,35]. The role of Zr and La doping of Pt/CeO₂ in the WGS reaction was also recently investigated [36,37].

Our interest in ceria stems from its medium high reactivity and excellent stability in HCl oxidation (Deacon process, eq 6.1) [12,13].



This reaction involves reactive HCl adsorption by proton abstraction with surface lattice oxygen, the formation of surface Cl, the recombination of surface species to produce gas-phase chlorine and water, and subsequent reoxidation of the surface by dissociative oxygen activation. Therefore, adsorption and recombination steps replenish or generate surface vacancies. Most Cl species substitute surface lattice O sites, which are tightly bound Cl species. Using *in situ* surface analysis, we recently concluded that HCl oxidation is also structure sensitive and only minority sites are responsible for the reactivity [38]. In this work, promoted ceria catalysts prepared by coprecipitation are evaluated and compared in HCl and CO oxidation. We show that in HCl oxidation the intrinsic reactivity of ceria, when using an Hf or Zr dopant in appropriate quantities, can be enhanced by a factor of ~2, whereas trivalent dopants are detrimental. Moreover, the structure, conductivity, and the surface Cl coverage of promoted samples were investigated to reveal the key physicochemical properties of these materials. Mechanistic details of promoted ceria were assessed by DFT calculations of the vacancy formation energy in removing Cl or O from the surface, as well as the vacancy and electron transport barriers for various doped ceria materials.

6.2 Experimental and computational methods

6.2.1 Preparation of catalysts

Doped ceria catalysts (Table 6.1) were synthesized by coprecipitation of guest and host precursors (nitrates or chlorides) from the aqueous phase with an NH_3 solution, followed by aging of the precipitate in the mother liquor and calcination after washing and drying. Controlled coprecipitation was performed in an automated laboratory reactor system (Mettler-Toledo LabMax) where the pH of 9 and the temperature (318 K) were controlled by *in situ* probes. The following precursors were used: $\text{Ce}(\text{NO}_3)_3 \cdot 6\text{H}_2\text{O}$, $\text{La}(\text{NO}_3)_3 \cdot 6\text{H}_2\text{O}$, $\text{Sm}(\text{NO}_3)_3 \cdot 6\text{H}_2\text{O}$, $\text{Gd}(\text{NO}_3)_3 \cdot 6\text{H}_2\text{O}$, $\text{Y}(\text{NO}_3)_3 \cdot 4\text{H}_2\text{O}$, HfCl_4 , ZrCl_4 , and TiCl_4 . Catalysts with different doping cations and concentrations were prepared according to the following procedure: A 200 cm^3 solution of a mixture of host and guest components (0.2 M Ce^{4+} and the corresponding concentration of the guest) was dosed into a reactor filled with 400 cm^3 of bidistilled water within 25 min, while the pH value was adjusted to 9 by simultaneous addition of appropriate amounts of an ammonia solution (10 wt %). The precipitate was subsequently aged at the same temperature for 60 min while being stirred in the mother liquor. A typical LabMax protocol is shown in Figure S 6.1 of the SI. No variation in pH was observed during the aging period. Thereafter, the precipitate was filtered, washed (three times with bidistilled water, once with ethanol, and finally with acetone), and dried. The resulting wet cake was covered and dried overnight at 373 K. The dried material was ground in a mortar to achieve better homogeneity before the calcinations step. Calcination (5 K min^{-1}) was performed in flowing air ($100 \text{ cm}^3 \text{ min}^{-1}$) at 973 K for 5 hours.

6.2.2 Basic characterization

The powder X-ray diffraction (XRD) measurements were performed on a STOE STADI P transmission diffractometer equipped with a primary focusing germanium monochromator (Cu $\text{K}\alpha_1$ radiation) and a linear position sensitive detector, and on a STOE Theta/theta Bragg-Brentano diffractometer equipped with a DECTRIS MYTHEN1K one-dimensional silicon strip detector (Ni-filtered Cu radiation). XRD data were evaluated by total pattern analysis using TOPAS [39]. An empirically obtained convolution accounted for the instrumental contribution to the peak profiles, while the sample contribution was described according to the Double-Voigt approach [40]. Crystallite sizes were calculated from the $1/\cos(\theta)$ Voigt function and are given as $L_{\text{Vol}}\text{-IB}$ values (volume-weighted mean column length based on integral breadth), i.e., without making further assumptions about crystallite shapes or size distributions, while strain contribution ϵ_0 was derived from the $\tan(\theta)$ Voigt component. Scanning electron microscopy (SEM) images were captured on a Hitachi S-4800 field emission scanning electron microscope at a working voltage of 1.5 kV. The microscope was equipped with an EDAX system with a Sapphire Si(Li) detecting unit, which was used for elemental analysis by energy dispersive X-ray spectroscopy (EDX). Nitrogen adsorption was conducted at 77 K on a Quantachrome Autosorb-6B analyzer. Prior to the measurement, the samples were outgassed in vacuum at 423 K for 5h.

6.2.3 Contactless conductivity experiments using a microwave cavity perturbation technique

The *in situ* microwave cavity perturbation technique (MCPT) setup, which was described in detail recently [41], allows the measurement of the electrical conductivity of (powder) samples in a fixed-bed flow-through reactor at temperatures up to 773 K in various gas atmospheres with on-line probing of reactants and products for the simultaneous deduction of kinetic reaction data. More details of the setup and data evaluation are provided in the Supporting Information. For this investigation, the 0.1–0.315 mm sieve fractions of undoped CeO_2 and CeO_2 doped with 5% Hf, Zr, La, and Sm were measured in a quartz tube reactor with a 3 mm inner diameter placed in the center of the microwave X-band cavity resonating in the TM_{110} mode at 9.2 GHz. The length of the catalyst bed was 10 mm, and a $20 \text{ cm}^3 \text{ min}^{-1}$ flow of different inert, reducing,

and oxidizing gas mixtures was applied. Every sample was first dehydrated in N_2 at 623 K for 30 min, then cooled to 303 K, and heated again to 623 K at a rate of 10 K min^{-1} , followed by isothermal treatments at 623 K in N_2 and H_2/N_2 and O_2/N_2 mixtures.

6.2.4 *In situ* Prompt Gamma Activation Analysis (PGAA)

In situ PGAA was utilized to measure the uptake of Cl of (promoted) ceria during HCl oxidation. The technique is based on the detection of element-specific γ -rays emitted upon excitation of the nucleus with cold neutrons. The investigated volume, in our case a tubular quartz microreactor, was probed, and the amounts of Cl, Ce, and dopants were quantified. PGAA was conducted at the cold neutron beam of the Budapest Neutron Centre. For further details, see the Supporting Information.

6.2.5 Catalytic tests

The gas-phase oxidation of hydrogen chloride was studied at ambient pressure in the same quartz microreactor that was used for the *in situ* PGAA experiment. The catalyst (sieve fraction of 0.1–0.315 mm) was loaded in the reactor (8 mm inside diameter) and pretreated in N_2 at 703 K for 30 min. Thereafter, the reaction gases were introduced at a total flow rate of $166\text{ cm}^3\text{ min}^{-1}$. Catalysts were tested in the temperature range of 623–703 K and at different O_2 :HCl ratios. The flow of HCl was always constant at $16.6\text{ cm}^3\text{ min}^{-1}$, and the oxygen flow was balanced with N_2 . Used samples were collected for postreaction characterization after the reactor had been rapidly cooled to room temperature in a flow of N_2 . Stability testing was performed with CeHf-10 for 100 h. Cl_2 quantification and calculation of the HCl conversion were based on iodometric titration. CO oxidation over ceria and promoted ceria samples was conducted at ambient pressure in a fixed-bed microreactor using 0.2 g of catalyst (sieve fraction of 0.1–0.25 mm). The catalyst was diluted and well-mixed with 0.4 g of SiC (sieve fraction of 0.25–0.335 mm) to minimize hot spot formation. The reaction temperature was controlled by a K-type thermocouple inserted directly into the catalyst bed. The sample, loaded into a U-shaped stainless steel tube (4 mm inside diameter) with glass-lined tubing, was pretreated in flowing 5% O_2 in He (total flow of $100\text{ cm}^3\text{ min}^{-1}$) at 660 K for 1 h and cooled to $\sim 400\text{ K}$ in an O_2 /He atmosphere. The gas was switched to the reaction mixture (1% CO and 1% O_2 in He; total flow of $100\text{ cm}^3\text{ min}^{-1}$) at 400 K, and the reactor was held at this temperature for 5 min for stabilization. Conversion *versus* temperature curves (light-off profiles) were collected by increasing the temperature at a rate of 2 K min^{-1} until the temperature reached 660 K and monitoring CO conversion. Furthermore, with CeHf-5 and CeLa-5, a cooling experiment was performed to check for deactivation or hysteresis of the reactivity. Additionally, O_2 -dependent experiments were also conducted with these two samples at 550 K. A Rosemount Analytical X-STREAM on-line multicomponent gas analyzer was used for measuring the volume percentage of CO, O_2 , and CO_2 in the effluent gas stream, which uses a nondispersive infrared analyzer for detecting CO and CO_2 , and a paramagnetic analyzer for O_2 . After each experiment, the reactor tube was cleaned with aqua regia, and a blind test was performed to ensure and verify the lack of cross contamination. The blank reactivity at the maximal temperature (660 K) was always $<2\%$ CO conversion.

6.2.6 Computational details

All the calculations were carried out using the Vienna ab initio simulation package (VASP, version 5.3.2) [42,43]. As the electronic structure of CeO_2 is a strongly correlated system, the Perdew–Burke–Ernzenhof (PBE) gradient-corrected functional [44] was employed and the self-interaction error was mitigated through the addition of a U Hubbard-like term following the approach of Dudarev et al. [45]. The effective U parameter ($U_{eff} = 4.5\text{ eV}$) was chosen on the basis of the satisfactory results reported in previous theoretical studies. [18,46] In all the calculations, core electrons were represented by the projector-augmented wave (PAW) [47] method, with cores $[Kr]4d^{10}$, $[Kr]4d^{10}4f^{14}$, $[Ar]3d^{10}$, $[Kr]4d^{10}$, $[Kr]4d^{10}4f^5$, $[He]$, and $[Xe]$ for Ce, Hf, Zr, La, Sm, O, and Cl atoms, respectively, whereas the valence ones were expanded in

plane waves with a cutoff energy of 500 eV. Ceria has a fluorite structure, and the calculated lattice constant (a_{calc}) obtained with a dense $7 \times 7 \times 7$ Monkhorst–Pack [48] k-point mesh was 5.497 Å ($a_{\text{exp}} = 5.412$ Å), which is in very good agreement with previous theoretical studies [46,49]. The M-doped CeO_2 ($M = \text{Hf}, \text{Zr}, \text{La}, \text{and Sm}$) bulk structures with a concentration of dopant of $\sim 6\%$ were modeled as $2 \times 2 \times 2$ cubic supercells as shown in Figure 6.1a, and fully optimized using a $3 \times 3 \times 3$ Monkhorst–Pack k-point mesh. The M-doped CeO_2 catalysts employed for the study of the Deacon reaction were constructed using the optimized lattice constants of the doped bulk structures described above and considering its two lowest surface energy facets, (111) and (110) (see Figure 6.1b). The (111) surfaces were simulated as periodically repeated slabs of three O–Ce–O trilayers with a vacuum space of 15 Å between them. The geometry optimizations of these (111) surfaces were performed using a surface periodicity of $p(3 \times 3)$ unit cells and a $3 \times 3 \times 1$ Monkhorst–Pack mesh for the k-point sampling. During these optimizations the five outermost layers were allowed to fully relax, whereas the four bottom layers were kept fixed in their bulk positions. On the other hand, the (110) surfaces were constructed as slabs of five layers thick separated with a vacuum space of 15 Å. In this case, geometries were optimized using a $p(3 \times 3)$ periodicity and a $2 \times 3 \times 1$ Monkhorst–Pack mesh and fully relaxing the top three layers. In all geometry optimizations, total energies converged better than 10^{-5} eV in the self-consistent field and the structures were relaxed with an energy threshold of 10^{-4} eV.

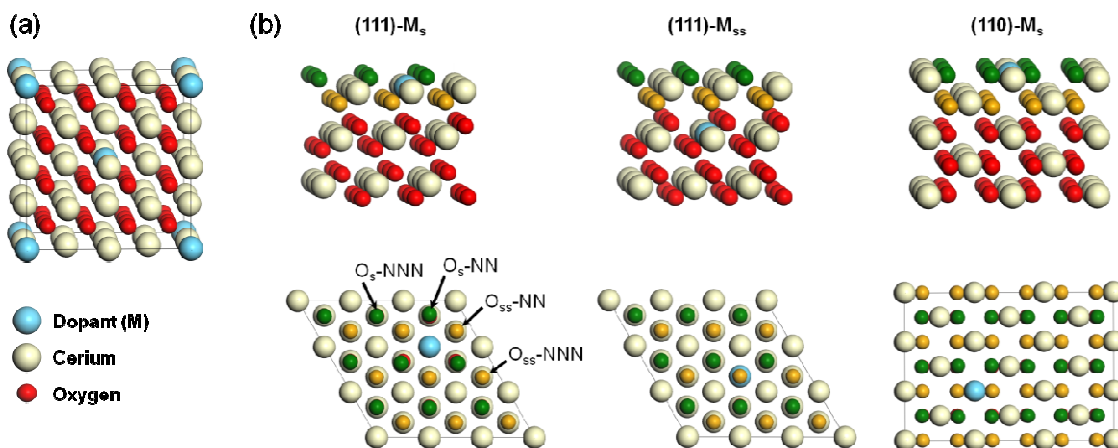


Figure 6.1 Side view of the M-doped CeO_2 bulk structures (a) and side and top views of the different M-doped CeO_2 (111) and (110) surfaces (b) employed for the DFT calculations.

Spin polarization was employed when needed, and a careful analysis of the localization of the excess of charge was performed [50]. In these calculations, a ferromagnetic spin state for the localized electrons was imposed. Some test calculations (see Table S 6.1) showed that the difference between the ferromagnetic and antiferromagnetic spin states is very small, in agreement with previous theoretical works [18,20,51]. With this setup, the vacancy formation energy for the clean (111) surface is 2.36 eV, in good agreement with data in the literature for the same charge localization (2.22 eV) [52]. Some tests regarding charge localization, geometric distortions induced, and comparison to previous calculations [18,20] can be found in the Supporting Information (Tables S 6.2–S 6.4). For trivalent dopants, the configuration with a $M^{3+}\text{-O}^\bullet$ character was investigated following the results from ref [25].

6.3 Results

6.3.1 HCl oxidation

Promoted and unpromoted catalysts prepared by coprecipitation were tested in HCl oxidation (Table 6.1). First, catalysts with a 5% dopant concentration were investigated in a standard reaction mixture (703 K and 9:1 O₂:HCl ratio). The addition of the tetravalent dopants, Zr and Hf, improved the reactivity of ceria, whereas trivalent dopants were clearly detrimental. Second, Hf- and Zr-modified catalysts with a dopant concentration in a range of 1–20% were prepared and tested in HCl oxidation. The results pointed out that 10% Hf and 10 or 20% Zr represent the optimal dopant concentration. All materials suffered slight deactivation, typically in the range of ~3–5%, within the first 5 h on the reaction stream. To assess the long-term stability of the catalysts, we selected the best material, CeHf-10, and tested its reactivity evolution over 100 h on stream (Figure 6.2a). Deactivation slows over time, and the catalyst is essentially stable after 80–90 h, with an overall 15% loss of initial reactivity. Kinetic investigations were also conducted to compare the promoted samples; the temperature dependence was explored for all catalysts, whereas selected materials were tested for *p*O₂ partial pressure dependence. The temperature dependence of the catalyst bed was evaluated for a 9:1 O₂:HCl reaction mixture in the range of 643–703 K. The apparent activation energy of the catalysts varies in the range of 55–78 kJ mol⁻¹, with most samples scattering around 60 kJ mol⁻¹. The highest value was observed with CeTi-5, followed by the materials with trivalent dopants. Although the range of the apparent activation energy is small, the data indicate a weak Constable–Cremer relation (compensation phenomenon) [53,54], that is, a linear correlation between the apparent activation energy and the logarithm of the apparent pre-exponential factor (Figure S 6.3a). A similar compensation phenomenon was recently observed with a RuO₂-based HCl oxidation catalyst, by modulating the surface coverage of rate-limiting surface species [55]. The oxygen pressure dependence (Figure S6.3b) was measured with selected samples by varying the O₂:HCl ratio from 1 to 9 at 703 K. All investigated catalysts revealed an apparent oxygen order of ~0.4, in line with results reported for ceria catalysts [13,38]. However, as HCl oxidation is associated with strong product inhibition [38,56] the apparent order of 0.4 would be significantly higher (close to 1) [56] when products were co-fed into the reaction mixture to minimize the effect of varying product concentrations. Hence, O₂ activation is a critical elementary step with promoted ceria materials, as well [12].

One unfortunate consequence of product inhibition is that the observed HCl conversion does not linearly scale with the catalyst weight used to load the reactor. This is illustrated in Figure 6.2b with the example of CeHf-10, where the obtained level of HCl conversion is plotted as a function of catalyst weight (and surface area) loaded into the reactor. The dependence can be best described as a 0.5 order function, typical for product inhibition when two products (Cl₂ and H₂O here) impede the reaction with an order of -1 [57]. Thus, the intrinsic reactivity of catalysts cannot be estimated and compared directly by surface area normalization and the space time yield and reaction rate values will depend on catalyst loading (total surface area). Note that all recent HCl oxidation catalysts seem to be affected by product inhibition. This was verified and discussed for RuO₂ [56], and also for ceria [38]. Here we show that the same product inhibition occurs with the best doped sample (CeHf-10), and therefore, this behavior is rather general. However, knowing the 0.5 order dependence on catalyst weight (and surface area), we can use for each catalyst the observed HCl conversion level to estimate an equivalent surface area (SA^{Eq}) of the reference CeHf-10 that gives the same HCl conversion. When comparing this equivalent surface area to the actually used one (SA^{Act}), one can estimate the efficiency and, consequently, the intrinsic reactivity of these materials in comparison to each other. Intrinsic reactivity will be further analyzed in the Discussion.

Table 6.1 Samples with their codes, BET surface areas, and Cl₂ space time yields under standard conditions

sample	sample code ^a	$S_{BET} (m^2 g^{-1})$		
		fresh	used in HCl oxidation	Space time yield ^b (g Cl ₂ g _{cat} ⁻¹ h ⁻¹)
CeO _x	CeO ₂ (14766)	55.5	47.2	2.1
Ce _{0.95} La _{0.05} O _x	CeLa-5 (14687)	52.0	45.1	1.4
Ce _{0.95} Sm _{0.05} O _x	CeSm-5 (14676)	46.9	44.9	1.6
Ce _{0.95} Gd _{0.05} O _x	CeGd-5 (14650)	31.1	27.9	1.2
Ce _{0.95} Y _{0.05} O _x	CeY-5 (14679)	45.8	39.4	1.8
Ce _{0.95} Ti _{0.05} O _x	CeTi-5 (16097)	36.4	30.5	2.1
Ce _{0.99} Zr _{0.01} O _x	CeZr-1 (15225)	34.3	48.6	2.7
Ce _{0.975} Zr _{0.025} O _x	CeZr-2.5 (15228)	55.6	46.2	2.6
Ce _{0.95} Zr _{0.05} O _x	CeZr-5 (15232)	62.3	49.0	2.8
Ce _{0.9} Zr _{0.1} O _x	CeZr-10 (15289)	68.4	49.4	3.0
Ce _{0.8} Zr _{0.2} O _x	CeZr-20 (15291)	64.1	48.3	3.0
Ce _{0.99} Hf _{0.01} O _x	CeHf-1 (14728)	71.8	51.7	2.0
Ce _{0.975} Hf _{0.025} O _x	CeHf-2.5 (14730)	87.1	55.4	2.8
Ce _{0.95} Hf _{0.05} O _x	CeHf-5 (14685)	64.1	53.4	3.0
Ce _{0.9} Hf _{0.1} O _x	CeHf-10 (14762)	90.1	49.8	3.1
Ce _{0.8} Hf _{0.2} O _x	CeHf-20 (14764)	39.0	41.6	2.5

^a Internal (FHI) sample codes in bracket.

^b Reaction conditions: 703 K, O₂:HCl = 9, flow 166 cm³ min⁻¹, catalyst weight 0.25 g. STY after 2 h on stream.

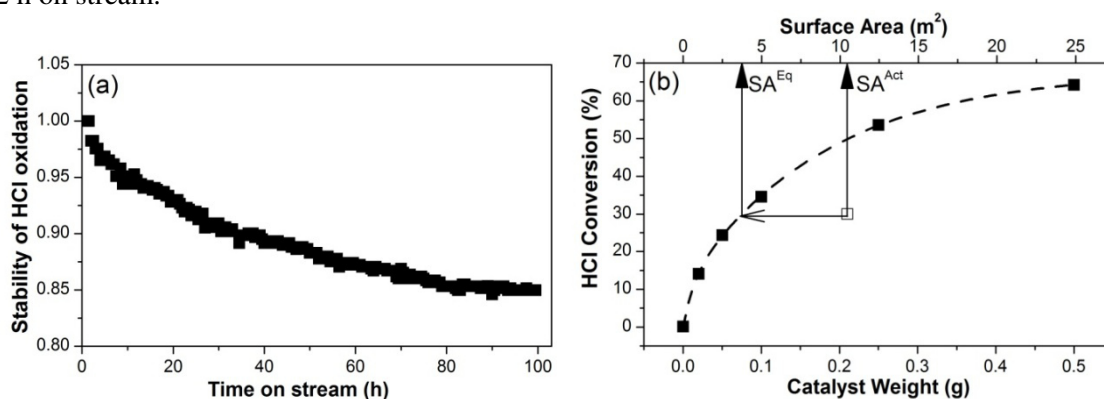


Figure 6.2 (a) Stability test. Normalized HCl conversion over CeHf-10 vs time on stream. Conditions: 703 K, 9:1 O₂:HCl ratio, catalyst weight of 0.25 g. (b) HCl conversion (■) over CeHf-10 vs the reactor loading expressed in weight and surface area. Conditions: 703 K, 9:1 O₂:HCl ratio. A hypothetical other catalyst (□) is also shown. The intrinsic reactivity of the samples (i.e. the efficiency to provide a certain number of turnovers to occur) is compared on the basis of the actual surface area (SA^{Act}) of the sample and the equivalent surface area (SA^{Eq}) by SA^{Eq}/SA^{Act}. Please note that the fit shown (---) does not correspond to the 0.5 order power fit because of the slowly approaching equilibrium above 60 % HCl conversion. Instead, a mathematically better fitting can be

obtained for the whole 0–64 % conversion range using an Exponential Decay 2 function (in Origin Pro), which is shown here and was used to calculate SA^{Eq} .

6.3.2 CO oxidation

CO oxidation is a widely employed test reaction for characterizing ceria-based materials. It requires reactant adsorption, O vacancy formation, and replenishment, and thus, some elementary steps are common to HCl oxidation. As HCl oxidation was enhanced by Hf and Zr promotion and inhibited by trivalent (including Sm and La) doping, we selected these four doped catalysts and the unpromoted ceria to test these materials in CO oxidation. To study the reactivity of the catalysts, we adopted the often utilized methodology of recording the light-off curves for CO oxidation. The light-off profiles for a 1:1:98 O₂:CO:He feed mixture are compiled in Figure 6.3a. CO conversion is essentially zero at 400 K, and the onset of reactivity is in the range of 470–520 K. Although the reactivity of the samples is not vastly different, markedly, Hf-promoted CeO₂ and Zr-promoted CeO₂ are the most reactive samples, and doping with Sm, particularly at low levels of conversion, is the least efficient. For an easier comparison, Figure 6.3b provides the temperatures at which the catalysts reach 20, 50, and 90% CO conversion. CeSm-5 lags ~20 K behind CeHf-5 at lower levels of conversion, while the reactivity of CeSm-5 rapidly improves above 600 K. CeO₂ and CeLa-5 are equally active up to ~590 K, while at higher temperatures CeLa-5 is slightly more reactive. Above 55% conversion, the undoped ceria was the least reactive sample. The apparent activation energy (evaluated from the smooth conversion range of ~5–40%) was calculated to be between 64 and 86 kJ mol⁻¹ (Figure S 6.4); the lowest value was found with CeHf-5 and the highest with CeSm-5. Interestingly, the Arrhenius plot of CeSm-5 (Figure S 6.4a) reveals an increase in the slope at ~560–570 K (near 15% CO conversion), suggesting a change in surface state likely due to surface segregation. A similar but slightly less pronounced effect was found with CeLa-5 (not shown). Despite the narrow range of apparent activation energies, the values fit to a compensation plot (Figure S 6.4b; the compensation phenomenon is discussed in the supporting information). Repeated light-off experiments were performed with CeHf-5 and CeLa-5 (as an example of +4 and +3 promoted samples, respectively), and the sample was subsequently cooled to see how the reactivity evolves during cooling. The CO conversions in the heating and cooling sections almost perfectly overlap for CeHf-5 (Figure S 6.4c), whereas there is a slight activation for CeLa-5; that is, the latter shows slightly higher CO conversion in the cooling experiment. Furthermore, after the samples had been cooled to 550 K, we varied the O₂ content (1, 2, 5, and 10% vs 1% CO) of the reaction feed. The results indicate a very minor dependence on O₂, the formal reaction order of O₂ being 0.07 for CeHf-5 and 0.11 for CeLa-5 (Figure S 6.4d).

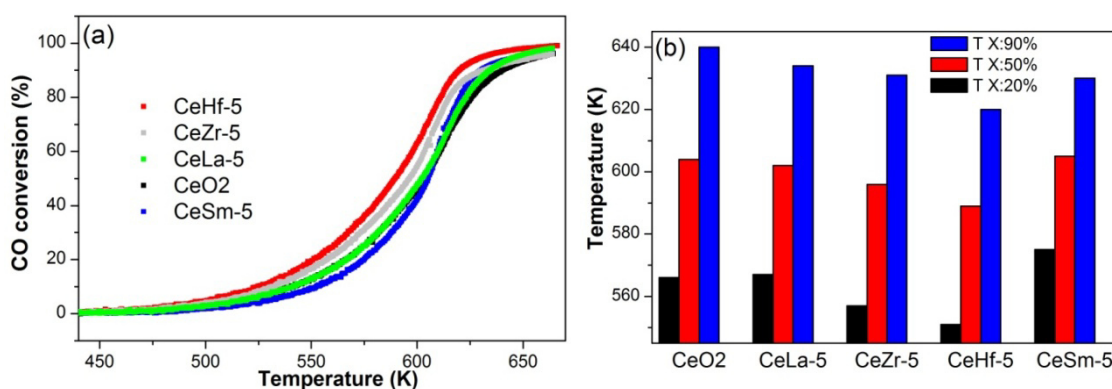


Figure 6.3 (a) CO oxidation light-off profiles of selected catalysts at a 1:1:98 O₂:CO:He mixture, and (b) temperatures allowing 20, 50, and 90% CO conversion. Catalyst weight of 0.2 g and flow rate of 100 cm³ min⁻¹.

6.3.3 Structural characterization of promoted ceria

The BET surface areas of all catalysts in their as synthesized form as well as after HCl oxidation are listed in Table 6.1. The BET values range from 31 to 90 m² g⁻¹, typically around 45–65 m² g⁻¹, and after HCl oxidation, most catalysts undergo a slight loss of surface area. The morphology of selected samples was investigated by SEM and is exemplified in Figure 6.4. SEM revealed that the primary nanoparticles (<50 nm) agglomerated into much larger secondary particles, forming a porous structure. Although the shape of nanoparticles is irregular and often not discernible, it is worth mentioning that several nanoparticles possess an elongated, needlelike structure. The morphology seems to be conserved after HCl oxidation (100 h stability test with CeHf-10). EDX experiments were conducted with the Hf-doped catalysts to estimate the amount of Hf introduced into the structure. The analysis confirmed that the nominal Hf concentration was reached in these materials; moreover, after a 100 h stability test with CeHf-10, the same ~10% Hf concentration was observed, indicating that the dopant was not leached and removed upon HCl oxidation. PGAA experiments (under HCl oxidation, *vide infra*) assessed the promoter concentration of selected catalysts and confirmed that the nominal concentration of dopants was established during preparation.

The XRD pattern of the unpromoted CeO₂ suggests the sole presence of face-centered cubic fluorite structure (lattice constant $a = 5.412 \text{ \AA}$). Upon introduction of 5% dopant into the ceria, the materials remain single-phase and consequently accommodate the strain caused by the modified size of the dopant cations. The lattice parameter of the 5% dopant samples correlates approximately with the ionic radius of the guest ion considering an 8-fold coordination given by the host structure (Figure 6.5a); the larger trivalent cations expand the lattice, whereas contraction occurs with Hf and Zr dopants. CeTi-5 gives rise to deviation from this trend, as its lattice parameter ($a = 5.413 \text{ \AA}$) is significantly larger than expected from the size of the Ti⁴⁺ cation. Although no second crystalline phase could be identified with CeTi-5 either, the deviation indicates that the difference in the ionic radii of Ce and Ti could not be accommodated by decreasing the lattice parameter, and rather phase separation and or segregation occurred. If amorphous, the Ti-rich phase would be invisible in XRD analysis. As the performance of the catalyst was not exceptional, we have not investigated this point further. The lattice parameter correlates also with the guest ion concentration (Figure 6.5b), monotonically decreasing with an increasing Hf and Zr content. We need to note here, however, that the diffraction peaks of the 20% samples are slightly asymmetric toward higher 2θ , and fitting suggests the presence of a second cubic phase (see the pattern of CeHf-20 in Figure S 6.5). These additional phases can be attributed to c-HfO₂ and c-ZrO₂ doped with Ce, as their lattice parameters are shifted up with respect to the corresponding pure phases. After HCl oxidation, however, no second phase was observed in CeZr-20. Most samples evidence a slight lattice expansion upon HCl oxidation, indicative of increased O vacancy formation (CeO_{2-x} where $x \sim 0.003$) with minor Ce reduction. The cubic phase without disintegration can accommodate much higher vacancy concentrations, even before vacancy ordering starts [31]. The accumulation of vacancies in the bulk of ceria particles during HCl oxidation may occur when nascent surface vacancies are displaced by subsurface oxygen atoms rather than by adsorption from the gas phase.

The contribution of strain, ϵ_0 , to the peak profiles was generally found to be non-negligible but poorly defined, i.e., with comparably large estimated errors. Nevertheless, the overall trend suggests an increase in strain with a higher dopant concentration (Figure S 6.6a). This seems plausible from crystal chemistry, as a substitution with differently sized ions should cause local deviations in the d spacings. The crystallite sizes show a slight inverse volcano-type trend but are all found to fall into the same regime of ~ 10–15 nm (Figure S 6.6b). It should be noted that these diffraction-based crystallite sizes cannot be directly compared to the BET surface areas, because the diffracting crystallite domains usually do not represent the primary particles.

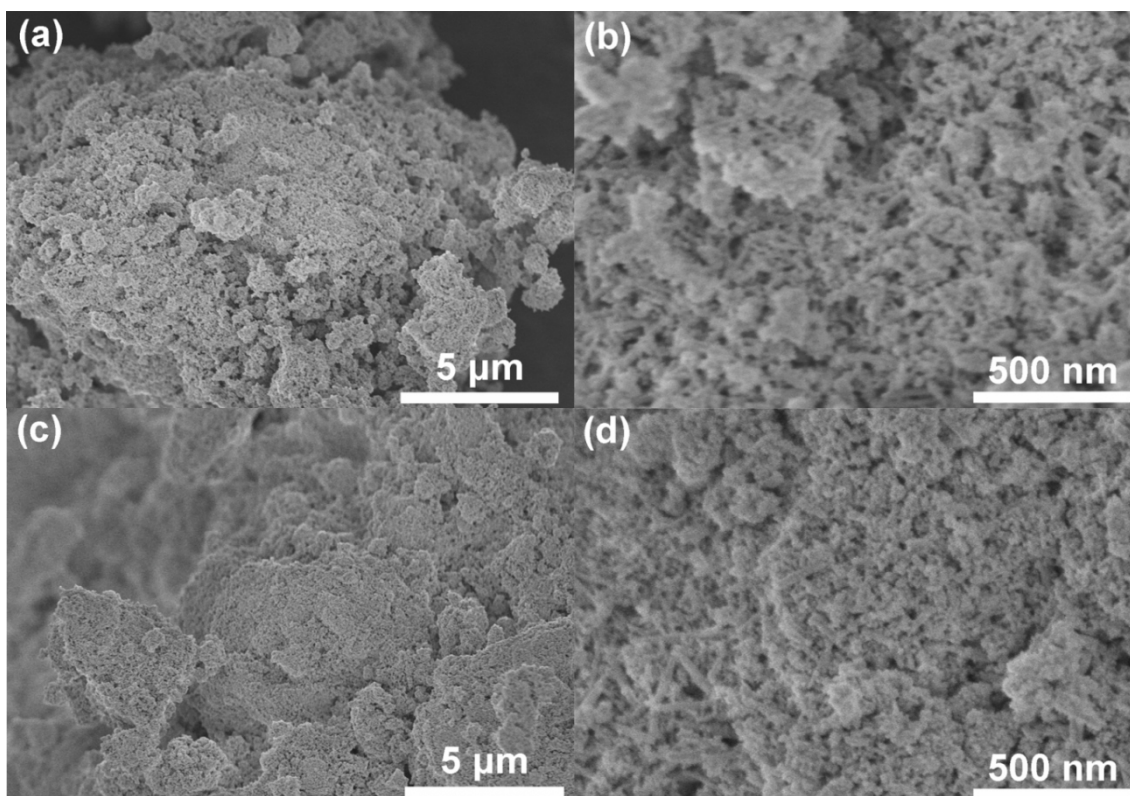


Figure 6.4 SEM of CeHf-10 as prepared (a and b) and after a 100 h stability test in HCl oxidation (c and d).

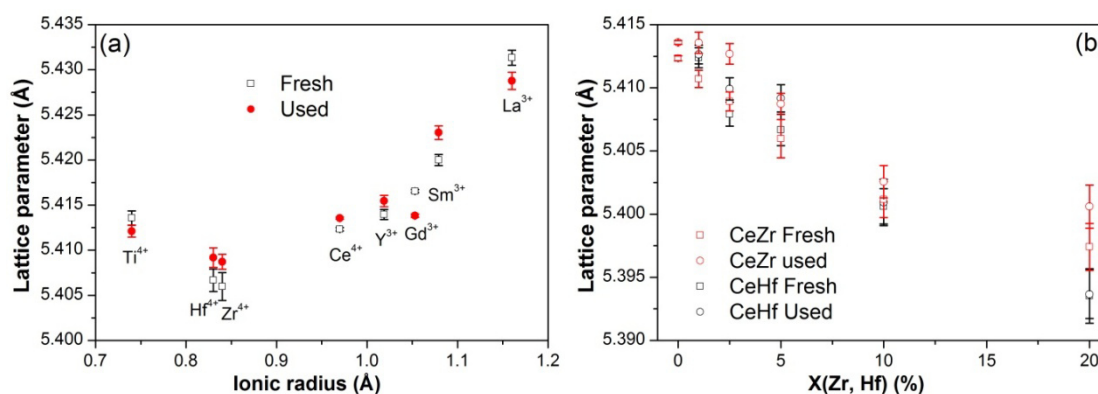


Figure 6.5 (a) Plot of the lattice parameter as a function of effective ionic radius of the guest ion for fresh materials and those used in HCl oxidation. The ionic radius is an effective radius of Shannon [71], with a coordination number of 8. (b) Plot of the lattice parameter as a function of guest ion concentration of Zr and Hf. Error bars correspond to ± 3 times the estimated standard uncertainties.

6.3.4 Contactless conductivity experiments using the microwave cavity perturbation technique

Contactless microwave conductivity measurements were performed by applying the microwave cavity perturbation technique to pure CeO₂ and selected samples with a 5% dopant concentration in a fixed-bed flow-through reactor. This way, absolute conductivity values of powder samples under operation conditions are accessible without problems typically arising because of electrode-sample contact resistance in conventional electrical conductivity studies [41]. The results are shown in Figure 6.6, and the most important data are summarized in Table 6.2. At room temperature, a very low conductivity in the range of 10⁻⁹ S cm⁻¹ was

measured for pure CeO_2 . After doping, however, much larger conductivities were observed. While the tetravalent dopants Hf and Zr caused an increase to $4 \times 10^{-8} \text{ S cm}^{-1}$, the trivalent ions induced an even larger increase to $2 \times 10^{-7} \text{ S cm}^{-1}$ (La) and $2 \times 10^{-5} \text{ S cm}^{-1}$ (Sm). When the samples were heated to 623 K, the conductivity improved for all samples as expected for semiconductors. While for pure CeO_2 a value of $\sim 1 \times 10^{-6} \text{ S cm}^{-1}$ was measured, doping with tetravalent ions increased the conductivity to $5 \times 10^{-6} \text{ S cm}^{-1}$ (Zr) and $2 \times 10^{-5} \text{ S cm}^{-1}$ (Hf). With trivalent ions, even higher values of $8 \times 10^{-5} \text{ S cm}^{-1}$ (La) and $3 \times 10^{-4} \text{ S cm}^{-1}$ (Sm) were obtained. Notably, samples doped with Hf and Zr reached already at around 473 K (Zr) and 533 K (Hf) a rather constant conductivity value, which did not increase further upon the sample being heated to 623 K.

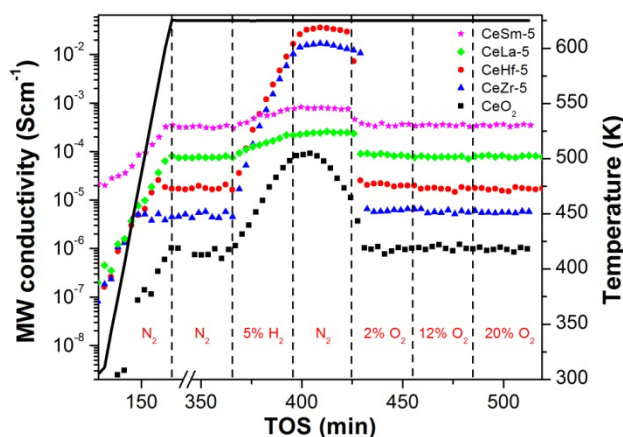


Figure 6.6 Microwave (MW) conductivity at 9.2 GHz of undoped and doped CeO_2 powder samples in different gas mixtures as indicated, with N_2 as the residual gas. As for CeO_2 , between 170 and 350 min time on stream (TOS) the sample was treated in mixtures containing 2–20% O_2 in N_2 (not directly labeled), but no conductivity changes were observed.

Table 6.2 Steady-state microwave conductivity data for selected doped and undoped CeO_2 measured under different conditions as shown in Figure 6.6.

Sample	E_H / eV	$\sigma_e (303 \text{ K}) / \text{S cm}^{-1}$	$\sigma_e (623 \text{ K}) \text{ in } \text{N}_2 / \text{S cm}^{-1}$	$\sigma_e (623 \text{ K}) \text{ in } \text{H}_2 / \text{S cm}^{-1}$
CeO_2	0.32	$\approx 10^{-9}$	1×10^{-6}	9×10^{-5}
CeLa-5	0.19	2×10^{-7}	8×10^{-5}	2×10^{-4}
CeSm-5	0.12	2×10^{-5}	3×10^{-4}	8×10^{-4}
CeZr-5	0.14	4×10^{-8}	5×10^{-6}	2×10^{-2}
CeHf-5	0.15	4×10^{-8}	2×10^{-5}	4×10^{-2}

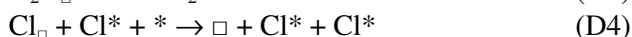
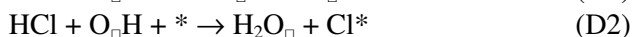
At 623 K, the CeO_2 sample was exposed to air, but no conductivity changes could be recognized. This treatment was followed by an exposure to a gas mixture of 2% H_2 in N_2 . Here, an increase in conductivity to $9 \times 10^{-5} \text{ S cm}^{-1}$ (i.e., an increase of a factor of 90) was determined. Further conductivity rise was still observed after we had switched back to the inert N_2 atmosphere. However, this initial increase turned into a rapidly decreasing conductivity after a few minutes. This effect is due to bulk diffusion processes, e.g., due to migration of oxygen to the surface to compensate for the large number of surface defects. A final treatment in N_2 containing different concentrations of O_2 accelerated the conductivity decrease up to a then constant value of $\sim 1 \times 10^{-6} \text{ S cm}^{-1}$, which is similar to the conductivity observed during the first measurement cycle in N_2 . Similar trends were observed for all investigated doped samples, but with enormous relative differences between trivalent and tetravalent dopants. While for CeO_2 doped with tetravalent ions the conductivity increased in H_2 by more than 3 orders of magnitude (factors of 4000 for Zr and 2000 for Hf), the values increased only slightly for La (factor of 2.5) and Sm (factor of 2.7). Hence, in H_2 and N_2 , the conductivity of the tetravalent-doped samples

exceeds that of the trivalent-doped samples by up to 2 orders of magnitude. In summary, doping with 5% Zr, Hf, Sm, or La increased the conductivity throughout the whole studied temperature range between 303 and 623 K, with the largest effect measured for trivalent dopants (Sm > La > Hf > Zr). In contrast, the effect of reducing gases, i.e., the difference in conductivity between H₂ and O₂ atmospheres, is largest for tetravalent ions and smallest for trivalent ions (Zr > Hf ≫ La ≈ Sm).

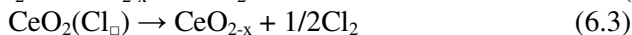
6.3.5 DFT calculations

As expected, calculations showed that the bulk structure doped with the trivalent cations (La and Sm) gives rise to the expansion of the cubic lattice constant (~0.3 and ~0.1%, respectively), while the samples doped with tetravalent cations Hf and Zr result in its contraction (~0.5 and 0.4%, respectively). Thus, the lattice parameters decrease as follows: CeLa > CeSm > Ce > CeZr ≈ CeHf (in line with experiments).

The Deacon process on CeO₂ was described as involving surface oxygen and vacancies sites being able to trap the incoming HCl as OH and Cl (and finally as water; steps D1-D3), the activation of Cl from lattice positions (D4) with concomitant desorption (D5), and the surface reoxidation step (D6) [12].



where \square denotes an anionic vacant or occupied site and * a Ce on-top site. The catalytic activity of the surface can thus be summarized as its ability to maintain oxygen atoms on the surface and expel Cl atoms from lattice positions; these two descriptors are the oxygen and chlorine vacancy formation. We computed the energy required for these two processes as follows:



where in the second case the Cl atom is occupying a lattice position, just as oxygen in the first one. For the O and Cl vacancy formation descriptors, we split the contributions according to *geometric* and *electronic* factors as both appear when an impurity is present.

To analyze *geometric contributions*, the vacancy formation energies for oxygen and chlorine lattice atoms were calculated without any dopants but as a function of the lattice constant, within a range of ±10% of the ideal CeO₂, a_{CeO_2} , for the lowest-energy surface, (111) (Figure 6.7). According to the calculations, the elimination of Cl from the lattice is nearly constant, whereas the removal of O is strongly affected by the contraction and expansion of the lattice (a/a_{CeO_2}). In particular, in the far contracted region (yellow), oxygen is so difficult to remove from the surface that no Cl is available to produce Cl₂. Conversely, in the far expanded region (blue), oxygen is easily removed from the surface and no oxygen is left on the surface to make the reaction evolve. In slightly contracted cells ($a/a_{\text{CeO}_2} \approx 0.98$), the Cl and O vacancy formation curves cross, and this indicates that at this lattice value the two energies are well balanced.

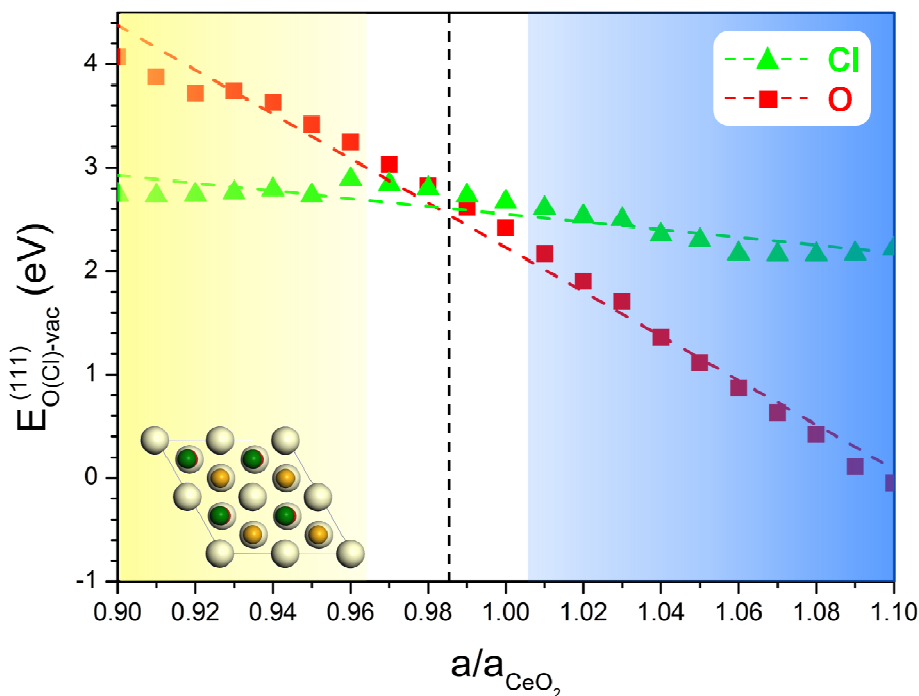


Figure 6.7 Calculated formation energies for oxygen and chlorine surface defects as a function of the x and y -lattice expansion in an undoped $p(2 \times 2)$ $\text{CeO}_2(111)$ surface.

Electronic effects were analyzed for the (111) and (110) surfaces, now including dopants explicitly. First the segregation of dopants was investigated (Table 6.3). On the basis of the segregation energies, in the (111) surface there is almost no preference of the impurity for the surface or subsurface positions, except for La, which prefers to be on the surface. On the other hand, impurities on the (110) surface are slightly favored.

Taking the dopant distribution into account, we next calculated the oxygen and chlorine vacancy formation energies for different positions close to and far from the dopant M and for M sitting in the surface or subsurface position [only surface M was considered for (110) surfaces; Figure 6.8]. All dopants reduce the energy penalty for forming oxygen and chlorine vacancies. The effect on oxygen vacancy formation is in good agreement with previous results [22,58,59].

The oxygen vacancy formation energies on the (111) surface are ~ 2.4 eV for the native CeO_2 , with those of CeHf and CeZr being ~ 1.5 eV for the nearest neighbor defect and ~ 0.6 eV with the La and Sm impurities. This effect is maintained for next nearest neighbors in the case of La and Sm, in line with previous calculations with lower-valence dopants [59], and also if the dopant is in the subsurface region. For the open (110) surface, the effect is less pronounced as the reference CeO_2 value is 1.45 eV, with tetravalent cations around 0.7 eV and trivalent cations around ~ 0.4 eV.

Table 6.3 Segregation energies, E_{seg} in eV, for M -doped- CeO_2 (111) and (110) surfaces.

M	$E_{\text{seg}}^{(111)}$	$E_{\text{seg}}^{(110)}$
Hf	0.08	-0.10
Zr	0.09	-0.10
La	-0.41	-0.29
Sm	0.00	0.00

The effect on the Cl vacancy formation energies is much smoother. The reference value is ~ 2.7 eV for the $\text{CeO}_2(111)$ surface but it is reduced by almost 1 eV for the tetravalent cations on the surface and by 0.3 eV for trivalent La and Sm. For the (110) surface, the reduction in the vacancy formation energy is smaller than for the compact surface and accounts for 0.4 eV for the tetravalent M cations (in the nearest neighbor position) and 0.3 eV for trivalent cations (in the next nearest neighbor position). Finally, Cl is large enough that it cannot easily penetrate into the lattice, and hence, the surface vacancy formation energies are the relevant cases.

Considering the geometric and electronic contributions described above, it follows that for the trivalent ions there is an extra electronic contribution that makes oxygen vacancy formation less energy demanding than for tetravalent ions. The reason for this lowest energy requirement for trivalent dopants is the fact that upon forming the defect only one electron is left per oxygen vacancy, and the other is stabilized by the dopant. This means for trivalent cations that there is no significant energy penalty due to electronic repulsion, as is the case for tetravalent cations, where two electrons are located in the vacancy. However, there is also a clear electronic contribution for tetravalent dopants, as the geometric contribution would rather dictate an increase in the oxygen vacancy formation energy. The low O vacancy formation energy in the trivalent systems is not accompanied by a significant decrease in the the chlorine energy. This suggests that under HCl oxidation conditions the whole surface of ceria with trivalent dopants is chlorinated, and therefore, reaction (D1) cannot take place efficiently.

6.3.6 *In situ* PGAA

The chlorine coverage is one decisive parameter of reactivity, and we have conducted *in situ* PGAA experiments to evaluate the surface uptake of Cl under HCl oxidation conditions of selected catalysts. In Figure 6.9a, the normalized intrinsic reactivity (see the description above) is shown as a function of Cl uptake [expressed as the $\text{Cl}/(\text{Ce} + \text{M})$ ratio] at 703 K in a 9:1 O_2 :HCl reaction mixture. For the sake of convenience, the intrinsic reactivity of 1 corresponds to CeO_2 . The experiments indicate the lowest level of Cl uptake for undoped CeO_2 , the highest level of uptake for catalysts with trivalent dopants, and a weak volcano-shaped trend. The higher level of chlorination upon trivalent doping is in good agreement with the DFT prediction.

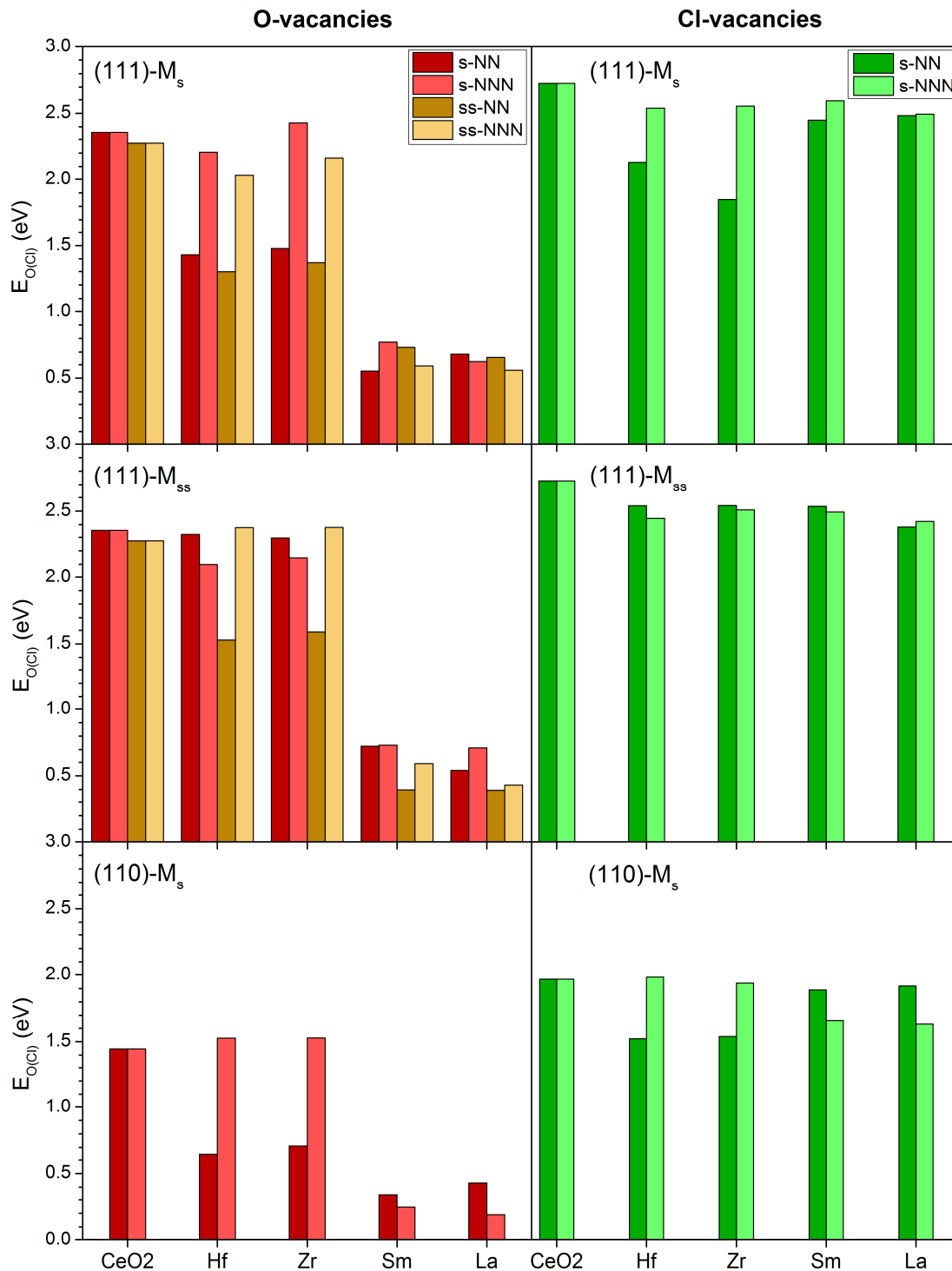


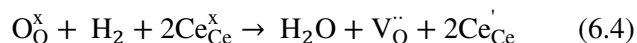
Figure 6.8 O and Cl vacancy formation energies with respect to gas-phase oxygen or chlorine (E_O or E_{Cl}), for the different undoped CeO_2 and M-doped surfaces. The relative positions of the dopant and the vacancy are indicated as follows: s for surface position, ss for subsurface position, and NN and NNN for the vacancy being the nearest and next nearest neighbor to M, respectively. See Figure 6.1 for further details.

6.4 Discussion

Oxidative redox reactions over ceria catalysts require the formation of surface oxygen vacancies, and the creation and transport of vacancies can be effectively modulated by dopants. Because the maximal conductivity and the lowest apparent activation energy of conduction in doped ceria materials are usually reached in the 5–10% dopant concentration range [60,61], we first prepared 5% doped catalysts and evaluated them in HCl oxidation. Zr and Hf promoted the HCl oxidation reactivity of CeO₂, whereas trivalent dopants (La, Gd, Sm and Y) were detrimental. Concentration optimization identified 10% Hf- and 10–20% Zr-doped ceria as the best catalysts among the materials tested. The slight deactivation revealed by the stability test fits well to an inverse observation of strongly bound OH buildup (in a similar time frame) [62] that, because of its extended stability, would block a part of the active surface units and thereby act as a deactivating agent. Furthermore, CO oxidation was utilized as a test reaction, and we found that similar to HCl oxidation Hf and Zr dopants enhance the CO oxidation rate, in good agreement with a previous literature report [35]. The best reactivity was observed with CeHf-5, whereas the worst performance (<55% CO conversion) was found with CeSm-5. Doping with La gave no improvement in reactivity below 590 K, which is at odds with an earlier report of La-doped alumina-supported ceria [34]. Because HCl oxidation is severely product-inhibited, the similarities in the two reactions may suggest that CO₂ could also act as an inhibiting agent via strongly bound carbonate species. This would be in line with the observations of Wu et al. [30] showing that the majority of carbonate species are spectators in CO oxidation. This aspect may initiate further studies. Although both reactions require the formation of surface vacancies, the reactivity ordering in the two reactions does not completely follow the same line (the possible reasons are discussed in the supporting information). We therefore assessed various physicochemical properties of the catalysts to improve our understanding of the requirements of a good ceria-based HCl oxidation catalyst.

In particular, the electronic conductivity was investigated using a microwave cavity perturbation technique at 623 K, slightly above the temperature of the onset of HCl oxidation and in the temperature regime of CO oxidation. Under inert or oxidizing conditions, dopants give rise to a much enhanced conductivity compared to that of CeO₂, the trivalent dopants being the most effective. On the contrary, under reducing conditions Hf and Zr promote very high conductivity, whereas trivalent-doped materials exhibit only minor modulation. This dependence of electronic conductivity on reaction conditions can be rationalized in terms of the number of mobile charge carriers under certain conditions (*vide infra*).

It is generally accepted that electron transport in the n-type semiconductor ceria can be described by a small polaron transport process, i.e., by a thermally activated hopping mechanism [31,63,64]. Under reducing conditions, ceria tends to lose oxygen to the ambient atmosphere, accompanied by the creation of oxygen vacancies and a change in the oxidation state from 4 to 3 of an adjacent cerium ion. This can be written using the Kröger-Vink notation as



where $\text{O}_\text{O}^{\times}$ represents an oxygen lattice site (i.e. O^{2-}), $\text{Ce}_{\text{Ce}}^{\times}$ is a normal cerium atom in a cerium site (i.e. Ce^{4+}), $\text{V}_\text{O}^{\cdot\cdot}$ is a doubly positively charged vacancy in an oxygen site, and Ce'_{Ce} is a single negatively charged cerium (i.e. Ce^{3+}) in a cerium site.

Hence, electronic conductivity σ_e can be expressed as

$$\sigma_e = [\text{Ce}'_{\text{Ce}}]e\mu \quad (6.5)$$

where $[\text{Ce}'_{\text{Ce}}]$ is the concentration of charge carriers (located at a Ce atom), e is the elementary charge, and μ is the mobility defined by

$$\mu = \left(\frac{A}{T}\right) \exp\left(\frac{-E_H}{k_B T}\right) \quad (6.6)$$

where A is a constant (further described in ref [63]), E_H is the activation energy for the electron hopping process, and k_B is the Boltzmann's constant.

Hence, by plotting $\log(\sigma_e T)$ versus the reciprocal temperature ($1/T$), we determined the hopping transport activation energies for all studied samples (see Figure S 6.2 as an example). As a result, a value of 0.32 eV was obtained for the pure CeO₂ sample. This value is well in the range of 0.4 eV found by Mogensen et al. [31], and 0.2 eV measured by Naik and Tien [64] for nearly stoichiometric CeO₂. This rather low activation energy furthermore indicates that with the microwave technique electronic conduction is measured rather than ionic charge transport, the latter having typical activation energies of ≥ 0.7 eV. In such cases, ionic mobility measures not only vacancy hopping but also vacancy formation (or association with dopants) [31,65,66]. From the computational point of view, the difference in energy between charge distributions that can be linked to the electronic mobility is found to be 0.27 eV. This is the difference in energy between two identical structures where the electrons are either close to and far from to the vacancy site (E_{pol} in Table S 6.1). This is in agreement with previously reported values [18]. Moreover, the mobility of oxygen vacancies implies also the redistribution of charge in nearby Ce atoms, thus inducing charge mobility. Oxygen vacancy hopping shows a diffusion barrier with a concomitant charge redistribution of 0.34 eV.

The presence of trivalent dopants affects the initial number of carriers, assuming a single phase, as follows:



Therefore, in inert or oxidizing atmospheres, the doping reaction (eq 6.7) controls the numbers of carriers. Indeed, experiments show that the conductivity decreases in the following order: trivalent > tetravalent > CeO₂. Under reducing conditions, oxygen vacancy generation plays an important role, and thus, both eqs 6.4 and 6.7 should be taken into account. Under heavy reduction conditions, eq 6.4 will be the dominating term as reduction is eased for all samples. Upon vacancy formation, tetravalent dopants generate twice the number of charge carriers as trivalent ions; thus, the electronic conductivity shall be larger for M^{4+} . Compared to that of pure ceria, significantly lower activation energies were determined for the doped ceria samples in the microwave conductivity experiment, with 0.15 eV for Hf, 0.14 eV for Zr, 0.19 eV for La, and 0.12 eV for Sm. In this case, the computed differences between the charge distributions (associated with a moving polaron) are between 0.09 eV for La and 0.17 eV for Hf. For a homogeneous distribution of vacancies, vacancy hopping with electron redistribution implies also low barriers of ~ 0.14 and ~ 0.22 eV for Hf and La, respectively. More details about these calculations are given in Figure S 6.7 and Table S 6.1. Comparing the HCl oxidation results with the O vacancy formation energy and the electronic conductivity under inert and oxidizing conditions, it becomes clear that these properties do not at all correlate with reactivity. It is intriguing that the vacancy formation energy of the catalysts is not followed in CO oxidation either. On the other hand, reducing conditions increase the electronic conductivity of CeZr-5 and CeHf-5, which are indeed better catalysts. Also, the lattice parameter seems to qualitatively follow the reactivity in HCl oxidation, lattice contraction being beneficial and expansion detrimental. To quantitatively visualize the effect of the lattice parameter, we compared the normalized intrinsic reactivity of all samples and plotted them as a function of the lattice parameter determined after reaction. This is shown in Figure 6.9b, where again the intrinsic reactivity of 1 corresponds to CeO₂. There is a weak trend of decreasing lattice parameter providing better reactivity, and the effect peaks near 5.4 Å (CeHf-10, CeZr-10, and CeZr-20). Greater lattice contraction does not seem to be advantageous, though we need to keep in mind that CeHf-20 was biphasic. The fact that the most efficient support for ceria was found to be ZrO₂ is not surprising, considering that nanoclusters of ceria on the ZrO₂ carrier could be compressively strained or part of Zr might be incorporated into the ceria clusters. Because HCl oxidation is a surface process, it is not per se evident why a bulk property (lattice parameter) should directly correlate with the catalytic rate. Nevertheless, one might envisage that the strained lattice extends onto the surface, giving rise to modified adsorption strength.

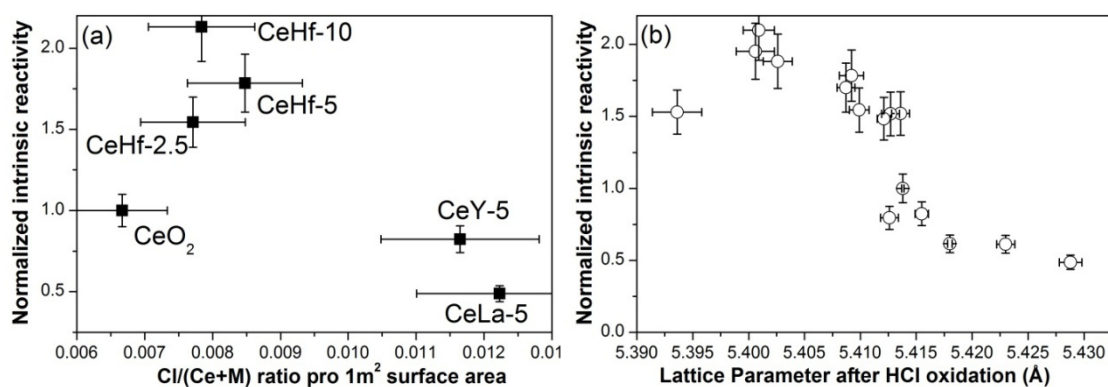


Figure 6.9 Intrinsic reactivity as a function of (a) the Cl uptake pro surface area as measured by *in situ* PGAA and (b) the lattice parameter after HCl oxidation. The normalized intrinsic reactivity is based on the description provided in the legend of Figure 6.2b; however, the numbers are scaled to provide CeO₂ an intrinsic reactivity value of 1. Error bars assume for the lattice parameter ± 3 times the estimated standard uncertainties and for Cl uptake and normalized intrinsic reactivity $\pm 10\%$ of the actual value. The $\pm 10\%$ error is an estimate of the convoluted error of reactivity + the BET value and the PGAA accuracy + the BET value.

With regard to the effect of surface coverage with chlorine, *in situ* PGAA indicated that intermediate coverages give rise to better reactivity. Although in our previous work [38] we concluded that most of the Cl uptake was related to the part of the surface that is not relevant for HCl oxidation, nevertheless, the trends of Cl uptake observed as a function of experimental parameters (T and partial pressure of reactants) were thought to be still valid for the small portion of the surface responsible for the catalytic reaction. Likewise, the Cl uptake of this experiment traces the overall surface, mostly not directly involved in HCl oxidation, but the volcano-type Cl uptake may still be relevant and could suggest that an intermediate Cl coverage of the active surface units could give rise to the largest reactivity. The comparison of Cl and O vacancy formation energies suggests that the highest activity shall be observed for the systems with the concomitant reduction of the vacancy formation energies for Cl and O. This is most effectively achieved for tetravalent ions. In comparison, trivalent ions are very effective at forming oxygen vacancies, but this ends up with the chlorination of the surface. Additionally, Hu and Metiu [67] have shown that doping ceria with trivalent La gives rise to a stabilization of on-top Cl adsorption (one Cl on Ce and another Cl on O) because of a strong interaction between the Lewis acid and Lewis base Cl atoms in Cl–Ce and Cl–O bonds, respectively. Such stabilization is admittedly not beneficial for desorbing Cl₂ from the surface and will hinder reactivity.

Studt et al. [68] using DFT calculations evaluated various rutile oxide surfaces in HCl oxidation and found that the dissociative adsorption energy of O₂ is a good descriptor of the reactivity. Recently, Over and Schomäcker [69] compiled experimental reactivity data and suggested a similar volcano dependence as a function of the same descriptor. In general, dissociation of molecules on surfaces is thought to be strongly structure sensitive because of the productlike late nature of the transition state [70]. Although no O₂ adsorption occurred at 173 K on nanocrystals of ceria with controlled morphology (octahedra, cubes, and rods) after calcination, the O₂ chemisorption was structure sensitive on the prereduced nanocrystals [27]. Therefore, our observation [38] that only a small portion of the surface is responsible for the reactivity (structure or defect sensitivity) is overall in line with the predictions of the descriptor. The dissociative adsorption of oxygen can be seen as the inverse process of O vacancy formation, and therefore, the oxygen adsorption energy is a strong function of dopants. Nevertheless, one needs to be aware that the strong variation of the vacancy formation energy is not compatible with the much less pronounced effect in reactivity. In summary, there are other parameters (shape of the doped catalyst, surface concentration of dopants, etc.) not considered here that

might also play an important role in HCl oxidation; nevertheless, our observations suggest that lattice contraction using dopants with smaller ionic radii is beneficial. Clearly, the reduced O vacancy formation energy alone does not guarantee a good catalyst, and only the balanced reduction of both Cl and O vacancy formation energy allows for an enhanced reactivity.

6.5 Conclusions

We have studied the role of trivalent and tetravalent promotion on the structural, electronic, and catalytic properties of ceria. In particular, our interest was to improve the reactivity of ceria in HCl oxidation. This can be effectively achieved upon promotion with 10% Hf and 10–20% Zr; on the other hand, trivalent dopants are clearly detrimental. There is a weak trend of a decreasing lattice parameter of the cubic structure providing better reactivity, the effect peaking near 5.4 Å, whereas lattice expansion upon trivalent doping is undesirable. We find also a weak volcano behavior between the surface Cl coverage and the reactivity, indicating that intermediate Cl coverages are preferred. Although both HCl oxidation and CO oxidation rely on the existence of oxygen vacancies, the orders of reactivity in these reactions are not completely identical, suggesting that CO oxidation might not always be appropriate as a test reaction for other redox reactions. The oxygen vacancy formation energy and the electronic conductivity of promoted catalysts were assessed under inert or oxidizing conditions, and neither of these properties correlates with the reactivity in HCl oxidation. DFT calculations indicate that only the balanced reduction of both Cl and O vacancy formation energy allows for an enhanced reactivity.

6.6 Supporting Information

6.6.1 Details to *in situ* PGAA

In situ Prompt Gamma Activation Analysis (PGAA) is a technique recently implemented for studying catalysts in action [1]. It is based on the radiative neutron capture of nuclei, enabling the quantification of most elements in the investigated volume, in our case, inside a Deacon micro-reactor. PGAA at atmospheric pressure condition was carried out at the cold neutron beam of the Budapest Neutron Centre. For the experiments, a quartz tube reactor was placed into the neutron beam, and the reactor tube was surrounded by a specially designed oven having openings for the incoming and outgoing neutrons and for the emitted gamma rays. These openings are covered by thin aluminium foils for decreasing heat losses. 0.25 g of doped and undoped CeO₂ with the sieve fraction of 0.1-0.315 mm was loaded into the reactor. Various gas feeds, at constant 166.7 cm³ min⁻¹ total flow, were supplied by mass flow controllers. HCl (4.5), oxygen (5.0) and nitrogen (5.0) were used. The standard reaction condition was set to O₂:HCl:N₂ = 9:1:0 at 703 K, and the reaction was monitored by iodometric titration. A Compton-suppressed high-purity germanium crystal was used to detect the prompt-gamma photons. Molar ratios, Cl/(Ce+M), (M: dopant) were determined from the characteristic peak areas corrected by the detector efficiency and the nuclear data of the observed elements [2].

6.6.2 A typical LabMax protocol

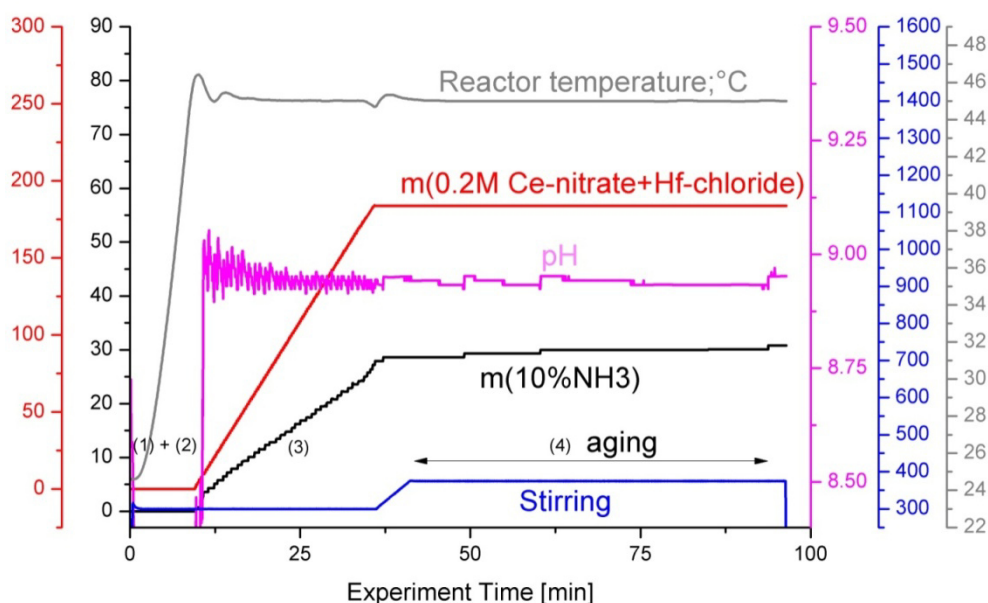


Figure S 6.1 A typical LabMax® protocol on the example of the synthesis of Ce_{0.95}Hf_{0.05}O₂. The protocol reads as follows; (1) increasing the reactor temperature till 45 °C; (2) basification to pH = 8.95; (3) addition of metal salt solution (7 cm³ min⁻¹) while keeping the pH constant at 9 by adding appropriate amounts of ammonia solution (10 wt.%); (4) aging for 1 hour accompanied by increasing the rotation speed to 375 rpm.

6.6.3 Microwave conductivity setup

The setup for the *in situ* microwave cavity perturbation technique (MCPT) was described in detail earlier [3]. In short, a quartz tube plug-flow reactor with 4 mm outer and 3 mm inner diameter was placed in the center of a cylindrical X-band TM₁₁₀ cavity resonating at 9.2 GHz. The reactor was connected upstream to a gas delivery manifold and downstream to a gas chromatograph. The reactor itself was inserted into an evacuated double-walled quartz Dewar

for heating of the sample by a preheated stream of N_2 without heating up the resonator. The temperature at the sample was controlled by a K-type thermocouple located inside the reactor. The resonator was kept at 293 K by external piezoelectric cooling elements. The conductivity of the sample was obtained by measuring the resonance curve in reflection mode with a vector network analyzer (Agilent PNA-L). The resonance frequency and quality factor of the resonator were deduced by an automatized parallel resonant circuit fit routine based on the transmission line theory [4]. From the difference of the reciprocal quality factors with and without sample the imaginary part of the powder permittivity, $\epsilon_{2,powder}$, was determined after the protocol described in Ref.3. The bulk permittivity, $\epsilon_{2,bulk}$, was calculated by applying the effective medium model after Landau-Lifshitz-Looyenga [5]. The microwave conductivity, σ_e , of the sample was calculated after $\sigma_e = \epsilon_{2,bulk} \epsilon_0 \omega_b$, with ϵ_0 being the vacuum permittivity and ω_b being the angular resonance frequency of the empty resonator.

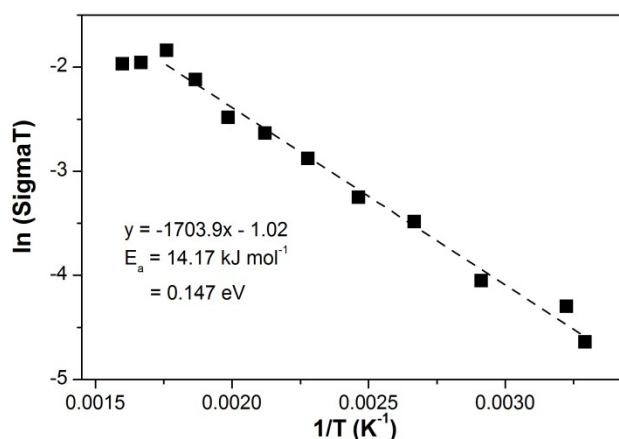


Figure S 6.2 Ln(SigmaT) plot as a function of inverse temperature for CeHf-5, as deduced from the temperature dependent MW conductivity experiment.

6.6.4 Additional HCl oxidation results

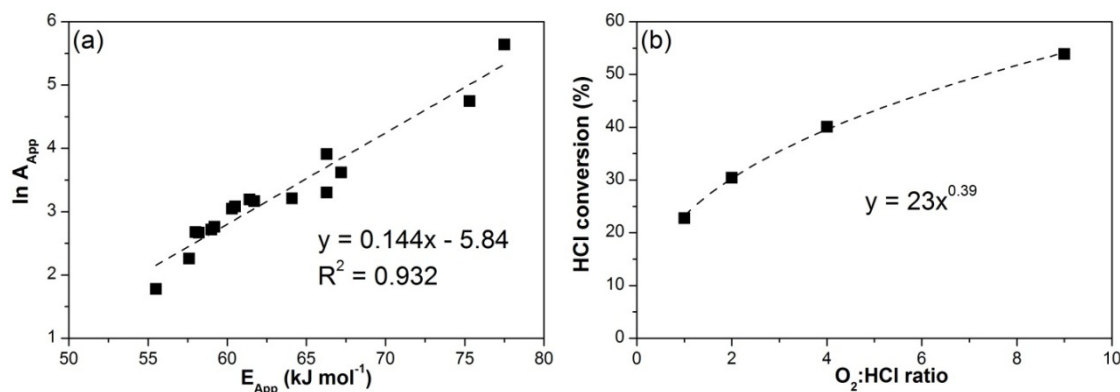


Figure S 6.3 (a) Constable-Cremer relationship for HCl oxidation over doped and undoped CeO_2 catalysts. The Arrhenius parameters were determined in the temperature range of 643–703 K with a reaction mixture $O_2:HCl:N_2 = 9:1:0$ and a catalyst loading of 0.25 g. The rate was plotted as “mol Cl_2 $g^{-1} min^{-1}$ ” in the Arrhenius diagram. (b) Oxygen partial pressure dependence (at constant HCl and total flow rate) with CeHf-10 at 703 K.

6.6.5 Detailed CO oxidation results

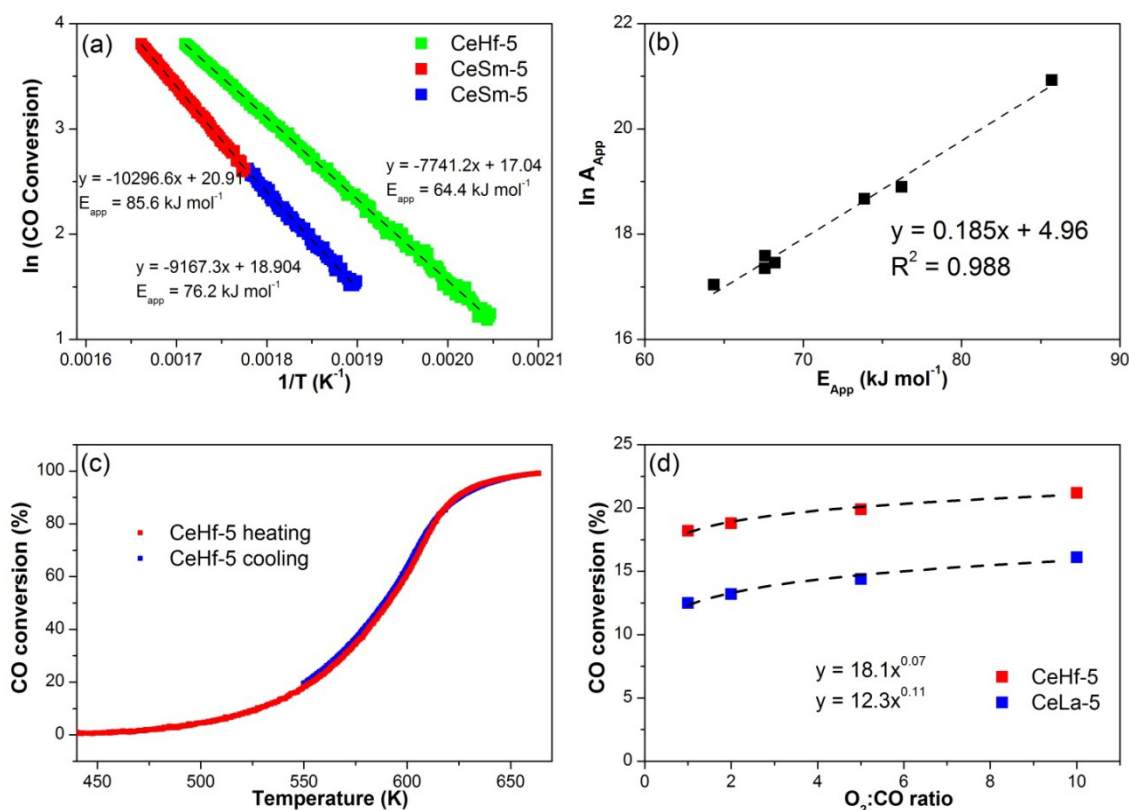


Figure S 6.4 (a) Arrhenius plot for CO oxidation ($\text{CO}:\text{O}_2:\text{He} = 1:1:98$) over CeSm-5 and CeHf-5. (b) Constable-Cremer relationship for CO oxidation over the studied catalysts. The Arrhenius parameters were determined in the smooth conversion range of $\sim 5\text{--}40\%$ with excellent linear fit. The rate was plotted as “CO conversion” in the Arrhenius diagram. (c) CO conversion in heating and cooling section showing very little difference in reactivity over CeHf-5. At 550 K cooling was stopped and the feed O_2 content was varied. (d) Oxygen partial pressure dependence (at constant CO and total flow rate) with CeHf-5 and CeLa-5 at 550 K.

CO oxidation as probe reaction

Catalysts are usually characterized by various spectroscopic techniques, but catalytic reactions may also serve as a characterization tool. CO oxidation is such a test reaction, which potentially could provide valuable information about the catalyst itself. It is generally accepted that CO oxidation over ceria occurs via Mars-Van Krevelen mechanism, in which lattice oxygen atoms interact with adsorbed CO molecules and produce thereby CO_2 and an oxygen lattice vacancy (defect site).

The ease of oxygen vacancy formation is suggested to play a crucial role in determining the reactivity of the catalyst for CO oxidation. On the other hand, HCl oxidation over ceria requires also the formation of oxygen vacancies on the surface for the activation of molecular oxygen. Although the chemical potential of the reactants (HCl and CO) for producing an oxygen vacancy is not identical, and the proposed reaction mechanisms for vacancy formation in these reactions are different, it is very likely that O_2 activation is a crucial elementary step for both reactions. Therefore the abundance of oxygen vacancies on the catalyst surface is important for both HCl and CO oxidation.

We have conducted fast temperature-programmed CO oxidation experiments with different promoted ceria catalysts to see whether CO oxidation reaction can be used as probe reaction for screening the reactivity of promoted ceria catalysts in HCl oxidation. The results have shown that the reactivity trend of promoted ceria catalysts in HCl and CO oxidation reactions is not

identical. There are two plausible reasons which can explain this discrepancy. First, under reaction conditions promoted catalysts have different propensity for surface chlorination (in the case of HCl oxidation) or for building up strongly-bound carbonate species (in the case of CO oxidation). These surface species block surface sites, and affects thereby the reactivity of the catalyst. Second, under reaction conditions adsorbed species on the surface may have also an impact on the extent of surface dopant segregation, that is, under reaction conditions the concentration of the dopant on the surface (or in subsurface layers) could be a function of adsorbed species. This can lead to different vacancy formation energies and different reactivity trends of promoted ceria catalysts in these reactions. However, this point may require more investigations to point the reactant-induced changes on the near-surface state of the catalysts.

Constable-Cremer relation

In heterogeneous catalysis most of the surface catalyzed reactions are temperature-dependent and follow the Arrhenius law: $r(T) = A_{app} e^{-E_{app}/k_b T}$ where k_b is Boltzmann's constant. However, in some classes of systems with varying activation energies it has been found that changes in the apparent activation energy (E_{app}) are concomitant with changes in the pre-exponential factor (A_{app}). The pre-exponential factor is related to the reaction frequency or the overall rate of the reaction. The apparent activation energy can be determined experimentally, and it is referred as *apparent* because it is the sum of the activation barrier of the critical elementary step (the *true* activation energy) and the adsorption enthalpies of the reactants (which are in most cases exothermic).

The interrelation between the apparent activation energy and pre-exponential factor is known as the compensation phenomena or the Constable-Cremer relation. The interrelation, when observed, follows the equation:

$$\ln A_{app} = a E_{app} + c$$

where a and c are constants.

This linearity indicates that whenever the apparent activation energy changes the rate of the overall reaction rate is balanced out due to the concomitant change in the pre-exponential factor. In general the compensation effect may occur when the nature of the catalyst is modified, the reactant is changed or when the pressure of the reactants and/or products is modified.

Beside the numerous experimental observation of compensation, many investigations were devoted to find the origin of this effect. Some of them were based on theoretical simulations on model systems. The pioneering work reported by Bligaard et al. (*J. Phys. Chem B*, 2003, 107, 9325) emphasizes the key role of surface coverage in the interpretation of the compensation phenomena. They have concluded that the compensation effect is intimately linked to the underlying Brønsted-Evans-Polanyi relationship, that is, the compensation effect is related to the relationship between activation energies and the binding energy of surface intermediates.

The Brønsted-Evans-Polanyi relation indicates that the decrease in the activation energies is accompanied by a concomitant increase in the stability of the reaction intermediates on the catalyst, and hence less free sites exist on the surface, which are required for the activation of the reactants.

This implies that the stability of surface species modulates the coverage of free sites, which in turn affects both the activation energies and the pre-exponential factor, keeping in mind that the former parameter is related to the adsorption enthalpy, which is a function of the surface coverage.

The compensation effect was also observed in HCl oxidation over RuO₂ catalysts (*Nature Chemistry*, 2012, 4, 739). The surface coverage of oxygen and chlorine species was determined under reaction conditions using *in situ* prompt gamma activation analysis and temporal analysis of products. (*Nature Chemistry*, 2012, 4, 739). The results revealed that the catalyst under different reaction conditions (i.e. different temperatures) can yield the same activity, provided

that the coverage of critical species (free sites; non-chlorine coverage) is equal. This behavior suggests that compensation effect holds true in this catalytic system and hence, surface coverage modulations gives rise to a linear dependence between the apparent activation energy and the pre-exponential factor. This was verified with the aid of DFT calculations and it was concluded that surface coverage changes affect two thermodynamic parameters, namely, the surface configurational entropy associated with the number of empty sites and the adsorption enthalpy of reactants. The later correlated linearly with E_{app} whereas the former implied that lower reaction rates were brought about by crowded catalytic surfaces, which impeded the dissociative adsorption of reactants limiting the reaction.

We do find a compensation phenomenon with various doped CeO_2 catalysts in HCl oxidation and in CO oxidation, as well. Despite the relatively narrow range of E_{app} , the measurements are accurate enough to trust the observations.

In this doped CeO_2 system we did not attempt to study the reasons of this phenomenon. However, based on the above points, the reasons might be similar as discussed: variation of surface coverage likely gives rise to modulation in both Arrhenius parameters. Indeed, *in situ* PGAA experiments have shown Cl coverage variations in HCl oxidation for various doped CeO_2 catalysts. Although we can only speculate, in CO oxidation promoters could induce varied adsorption enthalpy of CO and might control the amount of strongly bound (spectator) species, giving rise to similar E_{app} and $\ln A_{app}$ modulation.

6.6.6 X-ray diffraction example; strain and size analysis

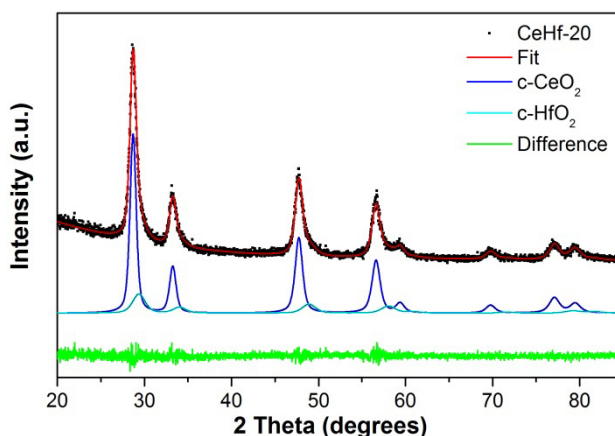


Figure S 6.5 The XRD pattern of CeHf-20 with its fitting showing the two cubic phases present.

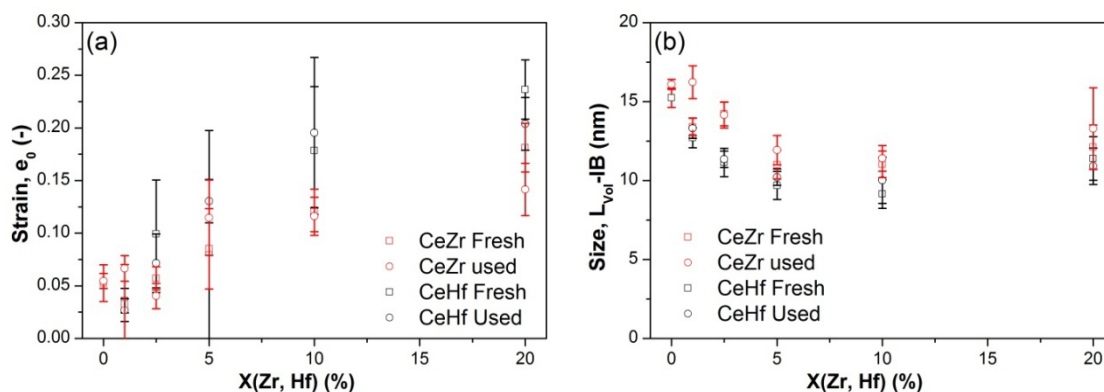


Figure S 6.6 Strain (a) and crystallite size (b) as a function of Zr and Hf dopant concentration, as derived by the Double-Voigt pattern analysis [6]. Error bars correspond to ± 3 -times the estimated standard uncertainties.

6.6.7 Additional DFT results

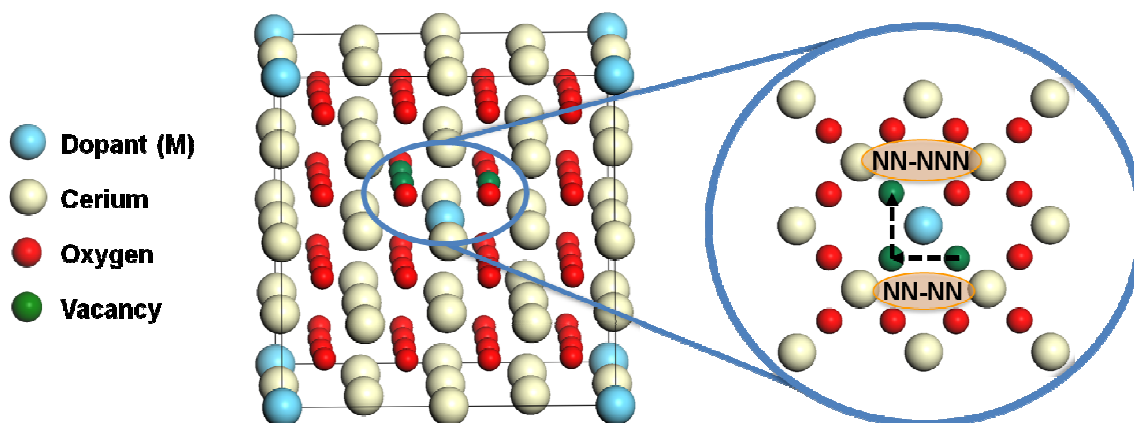


Figure S 6.7 Side and top views for the calculation of oxygen vacancy diffusion barriers in the M-doped-CeO₂(111) surface (M = Hf, La). Notice that when moving the vacancy a rearrangement of the associated electrons takes place.

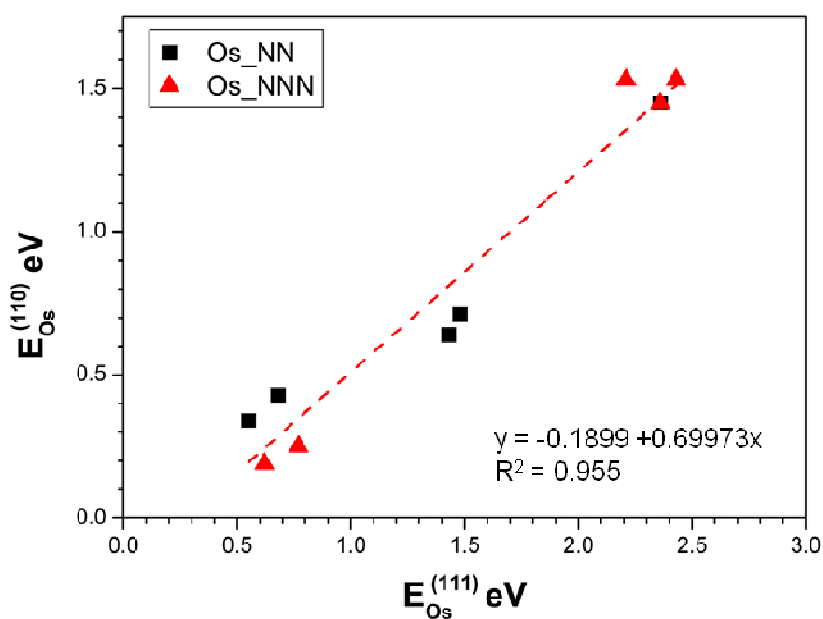


Figure S 6.8 Plot of the calculated oxygen vacancy formation energy for the M-doped-CeO₂(110) surface *versus* the M-doped-CeO₂(111) surface.

Table S 6.1 Calculated formation energy (in eV) of an oxygen surface defect in a p(3×3) CeO₂(111) surface imposing a ferromagnetic (FM) and an antiferromagnetic (AFM) spin states.

<i>O-defect</i>	$ \Delta E_{FM} - \Delta E_{AFM} $
O _s	< 0.01

Table S 6.2 Calculated formation energies of an oxygen surface defect in a p(3×3) CeO₂(111) surface, $\Delta E_{Os}^{(111)}$ in eV, with different locations of the pair of Ce³⁺ ions. In parenthesis, reported values for comparison.

<i>Ce³⁺ positions^a</i>	$\Delta E_{Os}^{(111)}$	$\Delta E_{Os}^{(111)}$ ref. [7]	$\Delta E_{Os}^{(111)}$ ref. [8] ^b
1 ₁ -1 ₁	2.36	2.22	-
1 ₁ -2 ₁	2.28	2.16	2.35
2 ₁ -2 ₅	2.07	-	2.28

^aThe notation n_m implies a cation position in the n^{th} shell of cations surrounding the defect, and m is the cationic layer counted from the surface. ^bFor a p(2×2) cell (3×3×1 k points) and cutoff 400 eV.

Table S 6.3 Calculated formation energy of an oxygen surface defect in a p(3×3) CeO₂(111) surface, $\Delta E_{Os}^{(111)}$ in eV, with and without adding a U_{eff} term for the O(2p) states.

<i>Ce³⁺ positions^a</i>	U_{eff} O(2p) states	$\Delta E_{Os}^{(111)a}$
1 ₁ -1 ₁	0.0	2.36
1 ₁ -1 ₁	7.0	1.74

^aThe energy difference of ~0.5 eV between the calculation with and without adding the U_{eff} term to O(2p) states is in good agreement with the 0.3-0.4 eV reported value in ref. [9].

Table S 6.4 Relevant distances (in Å) for the CeO₂(111) surface with no oxygen defects, and the CeO₂(111) and M_s-doped-CeO₂(111) (M = Hf, La) surfaces with an oxygen surface defect.

<i>Surface</i>	<i>O-defect</i>	<i>Ce-Ce</i>	<i>Ce-M</i>	<i>Ce-O</i>	<i>M-O</i>
CeO ₂	-	3.886 ^a	-	2.382	-
CeO ₂ -O _s	O _s	4.192 ^b 4.244 ^c 4.248 ^c	-	2.420 ^f /2.447 ^f 2.420 ^f /2.449 ^f 2.276 ^g /2.284 ^g	-
CeHf-O _s -NN	O _s -NN	4.095 ^b	4.273 ^d	2.401 ^f /2.436 ^f	2.157
CeLa-O _s -NN	O _s -NN	4.266 ^c	4.194 ^d /4.263 ^e	2.415 ^f /2.442 ^f 2.299 ^g /2.294 ^g	2.419/2.451

^aTwo Ce⁴⁺ cations. ^bTwo Ce³⁺ cations. ^cTwo Ce³⁺ and Ce⁴⁺ cations. ^dCe³⁺ and M cations. ^eCe⁴⁺ and M cations. ^fCe³⁺ cation and an adjacent oxygen atom close to the defect. ^gCe⁴⁺ cation and an adjacent oxygen atom close to the defect.

Table S 6.5 Calculated polaron energy, E_{pol} in eV, oxygen diffusion barriers, E_a in eV for different M-doped bulk structures. Notice that when moving the anions a homogeneous distribution of dopants is employed. NN: nearest neighbor, NNN: next nearest neighbor, >NNN: further away from M.

<i>Diffusion path</i>	E_{pol}	E_a NN-NN	E_a NN-NNN	E_a >NNN
CeO ₂	0.27	0.34	0.34	0.34
CeHf	0.17	0.06	0.14	0.19
CeLa	0.09	0.43	0.22	0.38

SI References

- [1] Révay, Z.; Belgya, T.; Szentmiklósi, L.; Kis, Z.; Wootsch, A.; Teschner, D.; Swoboda, M.; Schlögl, R.; Borsodi, J.; Zepernick, R. *Anal. Chem.* **2008**, *80*, 6066–6071.
- [2] Révay, Z. *Anal. Chem.* **2009**, *81*, 6851–6859.
- [3] Eichelbaum, M.; Stöber, R.; Karpov, A.; Dobner, C.-K.; Rosowski, F.; Trunschke, A.; Schlögl, R. *Phys. Chem. Chem. Phys.* **2012**, *14*, 1302–1312.
- [4] Kajfez, D. *IEEE Trans. Microw. Theory Tech.* **1994**, *42*, 1149–1153.
- [5] Landau, L. D.; Lifshitz, E. M. *Electrodynamics of continuous media*, Pergamon Press: New York, **1960**; Looyenga, H. *Physica*, **1965**, *31*, 401–406.
- [6] Balzar, D. (1999): Voigt-function model in diffraction line-broadening analysis. - *Microstructure Analysis from Diffraction*, edited by R. L. Snyder, H. J. Bunge, and J. Fiala, International Union of Crystallography, 1999.
- [7] Jerratsch, J.-F.; Shao, X.; Nilius, N.; Freund, H.-J.; Popa, C.; Ganduglia-Pirovano, M. V.; Burow, A. M.; Sauer, J. *Phys. Rev. Lett.* **2011**, *106*, 246801.
- [8] Murgida, G. E.; Ganduglia-Pirovano, M. V. *Phys. Rev. Lett.* **2013**, *110*, 246101.
- [9] Yeriskin, I.; Nolan, M.; *J. Phys. Condens. Matter*, **2010**, *22*, 135004.

6.7 References

- [1] Khartona, V. V.; Marquesa, F. M. B.; Atkinson, A. *Solid State Ionics*, **2004**, *174*, 135–149.
- [2] Fergus, J. W. *J. Power Sources*, **2006**, *162*, 30–40.
- [3] Trovarelli, A. *Catal. Rev.–Sci. Eng.* **1996**, *38*, 439–520.
- [4] Yoo, J. S.; Bhattacharyya, A. A.; Radlowski, C. A.; Karch, J. A. *Appl. Catal. B*, **1992**, *1*, 169–189.
- [5] Yoo, J. S.; Bhattacharyya, A. A.; Radlowski, C. A. *Ind. Eng. Chem. Res.* **1991**, *30*, 1444–1448.
- [6] Aneggi, E.; de Leitenburg, C.; Llorca, J.; Trovarelli, A. *Catal. Today*, **2012**, *197*, 119–126.
- [7] Fu, Q.; Saltsburg, H.; Flytzani-Stephanopoulos, M. *Science*, **2003**, *301*, 935–938.
- [8] Hilaire, S.; Wang, X.; Luo, T.; Gorte, R. J.; Wagner, J. *Appl. Catal., A*, **2001**, *215*, 271–278.
- [9] Schubert, M. M.; Plzak, V.; Garche, J.; Behm, R. J. *Catal. Lett.* **2001**, *76*, 143–150.
- [10] Pozdnyakova, O.; Teschner, D.; Wootsch, A.; Kröhnert, J.; Steinhauer, B.; Sauer, H.; Toth, L.; Jentoft, F. C.; Knop-Gericke, A.; Paál, Z.; Schlögl, R. *J. Catal.* **2006**, *237*, 1–16.
- [11] He, J.; Xu, T.; Wang, Z.; Zhang, Q.; Deng, W.; Wang, Y. *Angew. Chem. Int. Ed.* **2012**, *51*, 2438–2442.
- [12] Amrute, A. P.; Mondelli, C.; Moser, M.; Novell-Leruth, G.; López, N.; Rosenthal, D.; Farra, R.; Schuster, M. E.; Teschner, D.; Schmidt, T.; Pérez-Ramírez, J. *J. Catal.* **2012**, *286*, 287–297.
- [13] Moser, M.; Mondelli, C.; Schmidt, T.; Girgsdies, F.; Schuster, M. E.; Farra, R.; Szentmiklósi, L.; Teschner, D.; Pérez-Ramírez, J. *Appl. Catal. B*, **2013**, *132*, 123–131.
- [14] Esch, F.; Fabris, S.; Zhou, L.; Montini, T.; Africh, C.; Fornasiero, P.; Comelli, G.; Rosei, R. *Science*, **2005**, *309*, 752–755.
- [15] Sayle, T. X. T.; Parker, S. C.; Catlow, C. R. A. *Surf. Sci.* **1994**, *316*, 329–336.
- [16] Fabris, S.; Vicario, G.; Balducci, G.; de Gironcoli, S.; Baroni, S. *J. Phys. Chem. B*, **2005**, *109*, 22860–22867.
- [17] Nolan, M.; Parker S. C.; Watson, G. W. *Surf. Sci.* **2005**, *595*, 223–232.
- [18] Ganduglia-Pirovano, M. V.; Da Silva, J. L. F.; Sauer, J. *Phys. Rev. Lett.* **2009**, *102*, 026101.
- [19] Jerratsch, J.-F.; Shao, X.; Nilus, N.; Freund, H.-J.; Popa, C.; Ganduglia-Pirovano, M. V.; Burow, A. M.; Sauer, J. *Phys. Rev. Lett.* **2011**, *106*, 246801.
- [20] Murgida, G. E.; Ganduglia-Pirovano, M. V. *Phys. Rev. Lett.* **2013**, *110*, 246101.
- [21] Krcha, M. D.; Mayernick, A. D.; Janik, M. J., *J. Catal.* **2012**, *293*, 103–115.
- [22] Nolan, M. *J. Phys. Chem. C* **2009**, *113*, 2425–2432.
- [23] Nolan, M.; Parker, S.C.; Watson, G. *Phys. Chem. Chem. Phys.*, **2006**, *8*, 216–218
- [24] Yeriskin, I.; Nolan, M.; *J. Phys.: Condens. Matter*, **2010**, *22* 135004-1-8.
- [25] Nolan, M. *J. Phys. Chem. C* **2011**, *115*, 6671–6681.
- [26] Aryanpour, M.; Khetan, A.; Pitsch, H. *ACS Catal.* **2013**, *3*, 1253–1262.
- [27] Wu, Z.; Li, M.; Howe, J.; Meyer, H. M.; Overbury, S. H. *Langmuir*, **2010**, *26*, 16595–16606.
- [28] Aneggi, E.; Llorca, J.; Boaro, M.; Trovarelli, A. *J. Catal.* **2005**, *234*, 88–95.
- [29] Zhou, K.; Wang, X.; Sun, X.; Peng, Q.; Li, Y. *J. Catal.* **2005**, *229*, 206–212.
- [30] Wu, Z.; Li, M.; Overbury, S. H. *J. Catal.* **2012**, *285*, 61–73.
- [31] Mogensen, M.; Sammes, N. M.; Tompsett, G. A. *Solid State Ionics*, **2000**, *129*, 63–94.
- [32] Fally, F.; Perrichon, V.; Vidal, H.; Kaspar, J.; Blanco, G.; Pintado, J. M.; Bernal, S.; Colon, G.; Daturi, M.; Lavalley, J. C. *Catal. Today*, **2000**, *59*, 373–386.
- [33] Putna, E. S.; Bunluesin, T.; Fan, X. L.; Gorte, R. J.; Vohs, J. M.; Lakis, R. E.; Egami, T. *Catal. Today*, **1999**, *50*, 343–352.

- [34] Katta, L.; Thrimurthulu, G.; Reddy, B. M.; Muhler, M.; Grünert, W. *Catal. Sci. Technol.* **2011**, *1*, 1645–1652.
- [35] Reddy, B. M.; Bharali, P.; Saikia, P.; Khan, A.; Loridant, S.; Muhler, M. Grünert, W. *J. Phys. Chem. Lett.* **2007**, *111*, 1878–1881.
- [36] Kalamaras, C. M.; Dionysiou, D. D.; Efstathiou, A. M. *ACS Catal.* **2012**, *2*, 2729–2742.
- [37] Kalamaras, C. M.; Petallidou, K.C.; D. D.; Efstathiou, A. M. *Appl. Catal. B: Environ.* **2013**, *136-137*, 225–238.
- [38] Farra, R.; Eichelbaum, M.; Schlögl, R.; Szentmiklósi, L.; Schmidt, T.; Amrute, A. P.; Mondelli, C.; Pérez-Ramírez, J.; Teschner, D. *J. Catal.* **2013**, *297*, 119–127.
- [39] TOPAS version 4.2, copyright 1999, 2009 Bruker AXS.
- [40] Balzar, D. In *Microstructure Analysis from Diffraction*; Snyder, R. L., Bunge, H. J., Fiala, J., Eds.; International Union of Crystallography, 1999.
- [41] Eichelbaum, M.; Stöber, R.; Karpov, A.; Dobner, C.-K.; Rosowski, F.; Trunschke, A.; Schlögl, R. *Phys. Chem. Chem. Phys.* **2012**, *14*, 1302–1312.
- [42] Kresse, G.; Furthmüller, J. *Comput. Mater. Sci.* **1996**, *6*, 15–50.
- [43] Kresse, G.; Furthmüller, J. *Phys. Rev. B*, **1996**, *54*, 11169–11186.
- [44] Perdew, J.; Burke, K.; Ernzerhof, M. *Phys. Rev. Lett.* **1996**, *77*, 3865–3868.
- [45] Dudarev, S. L.; Botton, G. A.; Savrasov, S. Y.; Humphreys, C. J.; Sutton, A. P. *Phys. Rev. B*, **1998**, *57*, 1505–1509.
- [46] Fernández-Torre, D.; Košmider, K.; Carrasco, J.; Ganduglia-Pirovano, M. V.; Pérez, R. *J. Phys. Chem. C*, **2012**, *116*, 13584–13593.
- [47] Blöchl, P. E. *Phys. Rev. B*, **1994**, *50*, 17953–17979.
- [48] Monkhorst, H. J.; Pack, J. D.; *Phys. Rev. B*, **1976**, *13*, 5188–5192.
- [49] Da Silva, J. L. F.; Ganduglia-Pirovano, M. V.; Sauer, J.; Bayer, V.; Kresse, G. *Phys. Rev. B*, **2007**, *75*, 045121.
- [50] For consistency, the same localization of the excess of charge was imposed in all the spin polarized calculations. See Supporting Information for details.
- [51] Andersson, D. A.; Simak, S. I.; Johansson, B.; Abrikosov, I. A.; Skorodumova, N. V. *Phys. Rev. B*, **2007**, *75*, 035109.
- [52] Paier, J.; Penschke, C.; Sauer, J.; *Chem. Rev.* **2013**, *113*, 3949–3985.
- [53] Constable, F. H. *Proc. R. Soc. Lond. A*, **1925**, *108*, 355–378.
- [54] Cremer, E. *Adv. Catal.* **1955**, *7*, 75–91.
- [55] Teschner, D.; Novell-Leruth, G.; Farra, R.; Knop-Gericke, A.; Schlögl, R.; Szentmiklósi, L.; Hevia, M. G.; Soerijanto, H.; Schomäcker, R.; Pérez-Ramírez, J.; López, N. *Nature Chem.* **2012**, *4*, 739–745.
- [56] Teschner, D.; Farra, R.; Yao, L.; Schlögl, R.; Soerijanto, H.; Schomäcker, R.; Schmidt, T.; Szentmiklósi, L.; Amrute, A. P.; Mondelli, C.; Pérez-Ramírez, J.; Novell-Leruth, G.; López, N. *J. Catal.* **2012**, *285*, 273–284.
- [57] In a flow reactor, assuming small concentration changes of educts between bed segments, a doubled conversion and thus doubled product concentration will drive the reaction rate to the half, and as both products inhibit the reaction by -1 order, the rate decreases by factor $2 \times 2 = 4$. That is, four times weight provides twice conversion and thus we get the 0.5 order dependence on catalyst weight. Fitting the actual data points in the 0–53% conversion range suggests an order of 0.505 in very good agreement with the prediction.
- [68] Andersson, D. A.; Simak, S. I.; Skorodumova, N. V.; Abrikosov, I. A.; Johansson, B. *Appl. Phys. Lett.* **2007**, *90*, 031909.
- [59] Hu, Z.; Metiu, H. *J. Phys. Chem. C*, **2011**, *115*, 17898–17909.
- [60] Faber, J.; Geoffroy, C.; Roux, A.; Sylvestre, A; Abélard, P. *Appl. Phys. A*, **1989**, *49*, 225–232.
- [61] Inaba, H.; Tagawa, H. *Solid State Ionics*, **1996**, *83*, 1–16.
- [62] Farra, R.; Schuster, M. E.; Wrabetz, S.; Stotz, E.; Hamilton, N. G.; Amrute, A. P.; Pérez-Ramírez, J.; López, N.; Teschner, D. *Phys. Chem. Chem. Phys.* **2013**, *15*, 3454–3465.

- [63] Tuller, H. L.; Nowick, A. S. *J. Phys. Chem. Solids*, **1977**, *38*, 859–867.
- [64] Naik, I. K.; Tien, T. Y. *J. Phys. Chem. Solids*, **1978**, *39*, 311–315.
- [65] Andersson, D. A.; Simak, S. I.; Skorodumova, N. V.; Abrikosov, I. A.; Johansson, B. *PNAS*, **2006**, *103*, 3518–3521.
- [66] Shoko, E.; Smith, N. F.; McKenzie, R. H., *J. Phys. Chem. Solids*, **2011**, *72*, 1482–1494.
- [67] Hu, Z.; Metiu, H. *J. Phys. Chem. C*, **2012**, *116*, 6664–6671.
- [68] Studt, F.; Abild-Pedersen, F.; Hansen, H. A.; Man, I. C.; Rossmeisl, J.; Bligaard, T. *ChemCatChem*, **2010**, *2*, 98–102.
- [69] Over, H.; Schomäcker, R. *ACS Catal.* **2013**, *3*, 1034–1046.
- [70] van Santen, R. A.; Neurock, M.; Shetty, S. G. *Chem. Rev.* **2010**, *110*, 2005–2048.
- [71] Shannon, R. D., *Acta Cryst. A* **1976**, *A32*, 751–76

Chapter 7: Conclusions

In this work CeO₂-based catalysts have been investigated by means of various *in situ* and *ex situ* spectroscopic techniques to assess novel questions regarding key parameters rendering CeO₂ as a promising alternative to the industrially implemented RuO₂ catalyst for chlorine production.

The effect of sample pretreatments, in particular calcination, on the reactivity and structural stability has been investigated by testing the reactivity of CeO₂ samples calcined at different temperatures (in the range 573-1373 K) in HCl oxidation followed by the assessment of surface area changes of the samples. The results revealed that calcination at relative high temperatures (1273 or 1373) has a detrimental influence on the reactivity. The reason of this behavior is that samples calcined at such high temperatures have already lost a significant portion of their surface area during the calcination process. In contrast, the reactivity of the samples calcined at lower temperatures (< 1173 K) indicates no dependency to the total surface area of fresh samples. The reason of this observation is that in this case the calcination temperature was not high enough to ensure structural rigidity of CeO₂ particles under Deacon conditions. That is, exposing them to the reaction feed led to drop in the surface area indicating that substantial sintering of the CeO₂ particles occurred during HCl oxidation. Moreover, calcination of CeO₂ at mildly high-temperature (1173 K) gives rise to an optimum between stabilized surface and unacceptable loss of surface area.

Steady state kinetic experiments were conducted to assess the influence of O₂:HCl ratio on the activity. Raising the relative O₂ content in the feed mixture (O₂:HCl = 0 to 7) leads to higher HCl conversions, and the calculated reaction order of O₂ was 0.5. The comparison to RuO₂, which has a similar p_{O_2} dependence, gives the first insight concerning the importance of the oxygen-assisted chlorine evolution (re-oxidation) as a rate-limiting step in the reaction mechanism. On the other hand, upon raising the relative HCl content in the feed mixture, the Cl₂ production slightly increased at first and then progressively diminished. Low HCl concentrations limit Cl₂ production, while HCl excess causes a change in the catalyst composition that leads to activity loss. The analysis of XRD pattern of post-reaction samples treated with various O₂:HCl feeds showed that the reactivity loss for samples exposed to sub-stoichiometric Deacon feeds (O₂:HCl ≤ 0.25) is related to the formation of CeCl₃·6H₂O phase pointing to bulk chlorination as the main cause for the observed catalyst deactivation. XRD patterns of the samples treated in O₂-rich conditions (O₂:HCl ≥ 0.75) did not indicate any detectable bulk chlorination. Interestingly, the activity of chlorinated (deactivated) samples can be recovered by exposing them to O₂-rich conditions. The outcome of these results confirms that deactivation does not appear to be induced by the volatilization of the active phase in form of the metal chlorides produced during the reaction, as in some other Deacon catalysts.

To assess the degree of surface chlorination, samples exposed previously to different Deacon conditions were investigated by means of X-ray photoelectron spectroscopy. The quantitative analysis of the chlorine uptake indicates that under O₂-rich conditions chlorination is confined to the surface and possibly one subsurface layer of CeO₂ particles.

With the aid of DFT calculations conducted on the regular CeO₂ (111) surface, which is the most stable facet, the reaction profile of the HCl oxidation on CeO₂ was proposed and hence the main elementary steps involved in the reaction mechanism comprise: (i) hydrogen abstraction from HCl by basic surface O atoms to form hydroxyl groups leaving chlorine atoms on the surface, (ii) reaction of the hydroxyl groups with new incoming HCl molecules and/or hydroxyl group recombination on the surface to form surface water, (iii) water desorption, (iv) reoxidation of the surface via dissociative adsorption of O₂, and (v) recombination of chlorine atoms evolving as gas-phase Cl₂. Furthermore, DFT simulations revealed that Cl atoms on the

surface of ceria can be accommodated on the top of Ce cations (which are energetically less favored) or by occupying O-vacancy sites, and, as a result of this, Cl activation from vacancy position to surface Ce atoms is found to be the most energy-demanding step. The penetration of the Cl atoms to deeper layers is hindered by more than 2 eV, but owing to vacancy diffusion, and thus oxygen supply of the surface, ceria is prone to bulk chlorination and hence deactivation in sub-stoichiometric Deacon feeds ($O_2:HCl \leq 0.25$). Due to the high degree of surface chlorination, chlorine-oxygen competition for the available active sites can render re-oxidation as the rate-determining step.

The reaction mechanism highlights the importance of different surface species, O-basic sites, OH groups, surface Cl and vacancies, in determining the catalyst reactivity. Each of these surface species has been investigated experimentally using the proper spectroscopic analytical technique.

The proposed reaction mechanism suggests the vital role of basic sites (surface lattice O) in abstracting H atoms during the dissociative HCl adsorption. Since upon exposure to the reaction feeds the surface of ceria is prone to chlorination, the impact of surface chlorination on the acid/base properties of ceria (fresh and after reaction) was investigated by probe molecule adsorption (CO_2 , NH_3 , CO) applying micro-calorimetry, FTIR and TPD experiments. The micro-calorimetric CO_2 adsorption experiments revealed that the basic character of CeO_2 has been essentially eliminated upon reaction, which indicates that most of the surface lattice oxygen atoms are substituted by Cl atoms upon exposure of the surface to the reaction feed. This renders H abstraction during dissociative HCl adsorption also demanding, in line with the positive formal reaction order of HCl in O_2 -rich reaction conditions. On the other hand, FTIR and TPD adsorption experiments using NH_3 and CO as probing molecules revealed that the density and the strength of surface acidic functions increased significantly upon reaction.

An important feature making ceria such an interesting catalyst for a wide range of redox reactions is the exceptional reduction-oxidation properties of cerium ion, which easily switches between Ce^{4+} and Ce^{3+} . Surface O vacancies formed during reduction are required for activation of molecular oxygen and thus are expected to play a crucial role. EPR experiments were carried out on fresh and post-reaction samples using O_2 as probing molecule to assess the effect of surface chlorination on the amount of surface O vacancies. The results strongly suggest that high surface chlorination degrees inhibit oxygen activation on the surface, and only very few sites are available for re-oxidation, thus limiting Cl_2 production.

The above results indicate that the surface state under reaction conditions is not pure ceria, but rather Cl species are incorporated in the structure. Thus, we prepared and tested the stability and the reactivity of $CeOCl$ as a possible active phase for Deacon reaction using various feed compositions at 703 K. This allowed us to find out whether the sole existence of Cl and O species on the surface is enough to ensure catalytic reactivity and to assess the role of bulk oxide phase in this catalytic system. Cerium oxychloride was synthesized by the solid state reaction of cerium oxide and anhydrous cerium chloride. X-ray diffraction pattern of post-reaction samples revealed that $CeOCl$ is not stable neither in oxygen-rich nor in -lean conditions, which confirms that the sole presence of O and Cl species incorporated into the catalyst surface is not enough to achieve stable and efficient catalytic performance. Furthermore, substantial HCl conversions were only observed after complete transformation of $CeOCl$ to CeO_2 under O_2 -rich reaction feeds, which indicates that the coexistence of bulk oxide phase is a prerequisite for this catalytic system, probably by facilitating efficient O_2 activation via bulk and surface O vacancy dynamics.

Since OH and adsorbed Cl constitute the most abundant species on the surface, and because of their active involvement in many elementary steps of the proposed reaction mechanism, a quantitative assessment of their surface density under various reaction conditions was desirable. The coverage of OH and Cl under various reaction conditions were investigated by *in situ* infrared spectroscopy and PGAA, respectively. The surface coverage-reactivity correlations revealed that higher temperature and $p(O_2)$ have a positive impact on the reactivity, which

correlates with the increased OH and decreased Cl coverage. Moreover, increasing $p(\text{HCl})$ gives rise to higher Cl coverage and lower OH population with concomitant reactivity enhancement, though only in the range where no subsurface chlorination occurs. The outcome of these experiments indicates that the vital role of Cl species on the surface can be divided into the two following contributions: (i) one major part being detrimental, most probably by site blocking. (ii) a small but certain part being beneficial and regarded as “reactive”. Considering the first detrimental role of Cl (site blocking), the observation of enhanced reactivity brought about by increasing the temperature or $p(\text{O}_2)$ can be interpreted as lowering surface Cl concentration and thus opening up new sites capable of abstracting H from HCl and shifting equilibrium coverage toward higher OH density

An interesting result concerning the amount of active sites involved in the catalytic reaction was obtained by monitoring the Cl uptake while co-dosing Cl_2 into the reaction feed mixture. Cl_2 inhibits strongly the reaction, but no measurable increase of the surface Cl uptake associated with this inhibition could be observed, suggesting that only a little fraction of sites present on the catalyst surface contributes to the observed catalytic turnover.

With the aim at promoting catalytic efficiency of ceria for HCl oxidation, a series of doping elements (Ti, Hf, Zr, Gd, Sm, Y, La) was chosen and then promoted ceria catalysts with 5% dopant concentration were synthesized by co-precipitation procedure using NH_3 as precipitant. Promoted and unpromoted ceria catalysts were tested in a standard reaction mixture (703 K, $\text{O}_2:\text{HCl} = 9:1$). Steady state kinetic experiments have shown that doping with Hf and Zr improves the reactivity of ceria, whereas doping with trivalent dopants (like: La, Sm, Gd, Y) is detrimental. Dopant concentration optimization identified 10% Hf and 10-20% Zr as the best catalysts among the materials tested with an intrinsic reactivity enhancement by a factor of 2.

In order to assess the role of dopants in promoting/reducing the reactivity of corresponding doped-ceria catalysts, the structure, the conductivity, and the surface Cl coverage of promoted samples were investigated. Moreover, DFT calculations were performed to assess the effect of dopants on the vacancy formation energy in removing Cl or O from the lattice. The results revealed that the oxygen vacancy formation energy and the electronic conductivity of promoted ceria catalysts have the following order under inert or oxidizing conditions: trivalent > tetravalent > undoped, and neither of these properties correlates with the reactivity in HCl oxidation. DFT calculations indicated that in HCl oxidation over promoted ceria catalysts only the balanced reduction of both Cl and O vacancy formation energies allows for an enhanced reactivity. In addition, XRD structural analysis of promoted catalysts after reaction indicates that slight contraction in the lattice parameter of ceria brought about by doping it with Hf or Zr is concomitant with the reactivity enhancement observed, whereas lattice expansion induced by doping of ceria with trivalent elements is detrimental. These results are in line with the DFT calculations because the intersection of the O or Cl vacancy formation energy trends as a function of the lattice parameter lies in the range where the lattice exerts slight contraction.

Ceria is one the most widely applied metal oxides in heterogeneous catalysis owing to its unique oxidation-reduction properties and thus, the vacancies, as proved in this study and shown in many other redox-reactions, are key parameter determining the reactivity of ceria-based catalysts. By considering vacancy diffusion, vacancy clustering on the surface or in sub-surface layers the chemistry of ceria becomes more complicated. Therefore further experimental and theoretical studies might be helpful to address the impact of vacancy associations on the reactivity of ceria based catalysts in redox reactions, and in particular in Deacon reaction. Additionally, it has been observed in a number of catalytic systems (also here) that only a minor fraction of a catalyst surface may represent the active site. This indicates that even stronger efforts are required to identify the structure and the amount of active sites on the catalyst surface.

Finally, I hope that this work with its comprehensive methodology serves as a worthwhile example in heterogeneous catalysis research.

Appendix

Appendix A

Infrared Spectroscopy

A.1 Introduction

Infrared radiation spans a section of the electromagnetic spectrum below the red end of visible light at high frequencies and above the microwave region at low frequencies. This region is usually divided into three parts named for their relation to the visible spectrum: the near-, mid- and far-infrared. In terms of energy, the wavenumber ($= \frac{1}{\lambda}$; cm^{-1}) is usually used for the definition of the corresponding energy limits. So that it is approximately 14000-4000 cm^{-1} for the near-IR, 4000-400 cm^{-1} for mid-infrared and the 400-10 cm^{-1} for far-IR region.

Atoms within the molecules vibrate around their equilibrium positions giving rise to more or less complex vibrational modes. At absolute zero temperature, all polyatomic chemical species lie at the vibrational ground state. However, they can undergo vibrational excitation (fundamental vibrational transition) as a consequence of absorbing a specific energy quantum from an electromagnetic radiation and hence occupy higher energy vibrational states. The energy difference between two adjacent vibrational states falls in the mid- and far-IR ranges. When infrared radiation interacts with a matter, it may be absorbed, reflected or transmitted. The analysis of absorbed and transmitted radiation gives information on the vibrational structure of absorbing chemical species. An absorptive transition between two vibrational states is governed by selection-rules and they can be simplified as follows:

$$\Delta v = \pm 1 \quad (\text{A } 1)$$

$$\left(\frac{\partial \mu}{\partial Q}\right) \neq 0 \quad (\text{A } 2)$$

Equation A 1, where v is the vibrational quantum number, means that in a harmonic oscillator only transitions between adjacent vibrational states are allowed. According to the law of Boltzmann distribution most population lie in the ground state. Consequently, IR spectra at room temperature or even at relatively high temperatures are chiefly constituted of fundamental transitions, i.e transitions originating from the ground state to the first excited state, whereas transitions originating from the first excited state are much less probable. However, in case of anharmonic oscillators this condition is relaxed, so that not only fundamental transitions but also overtone or combination modes can be sometimes observed; usually with weak intensity. Equation A 2, where μ is the dipole moment and Q is the atomic displacement from equilibrium, indicates that only vibration modes associated with molecular dipole moment changes can be excited. In general, the number of normal vibration modes of a molecule (consisting n atoms) depends on its degrees of freedom and equals to $3n-6$ (or $3n-5$ for linear molecules). The $3n$ total number of degrees of freedom is reduced by six since three coordinates are required to describe the translational motion and three for the rotational one. (Linear molecules have only two coordinates describing their rotational motion). Nevertheless, and because of molecular symmetry considerations, it is not necessary that all vibrational modes are IR active, but rather only those that obey the second selection rule (change of the dipole moment). As a matter of fact, when a molecule from the gas phase adsorbs on a solid surface its symmetry is reduced upon interaction with the electric field of that surface, and thus vibrational modes which were IR silent before adsorption (in gas phase) become IR active. The asymmetric interaction between the molecule and the surface results in a perturbation of the molecule's uniform electronic distribution, which in turn induces dipole moment changes within the molecule. Therefore, the information obtained via IR spectroscopy may even increase in case of studying species adsorbed on the surface, whereby all vibrations de facto become IR active, and even homomolecular diatomic molecules like H_2 or O_2 can be observed by IR spectroscopy [1,2].

Furthermore, using transmission-absorption IR technique the concentration of IR-absorbing species adsorbed on the sample can be obtained applying the Beer-Lambert law,

$$A = \epsilon cl \quad (\text{A } 3)$$

which indicates that the absorbance A is linearly depended on the molar concentration of absorbing species c , the molar absorption coefficient ϵ and on the IR-radiation pathlength within the sample l . In case of (solid) powder samples the effect of light-scattering becomes an issue. In order to reduce this effect, solid samples must be prepared in such a way that the diameter of particles is smaller than the wavelength of the incident IR radiation.

A.2 IR spectroscopy in heterogeneous catalysis

For decades the development of new solid catalysts was based primarily upon empirical testing results. The reasons behind are surface complexity and the difficulty of finding the best means to investigate it. With respect to surface complexity, the real catalyst is a polycrystalline material; its surface consists of several planes that differ energetically from each other, and hence possess unequal chemical activities [3–5]. On the other hand, the variety of possible defects (microscopic defects: steps, cracks, corners, etc. or point defects: vacancies, interstitial atoms, substituted or inserted atoms) on the surface complicate further surface structure-reactivity correlations. It is worth to note that the surface itself can be considered as a major defect of the three-dimensional structure of the crystal. Thus, the diversity of factors contributing to surface chemical activity hinders the determination of active centers responsible for the catalytic process. Understanding molecular interactions on solid surfaces and the nature of active sites may however pave the way for designing new catalysts of superior catalytic performance. This knowledge requires the utilization of spectroscopic methods that can provide information on the molecular level about surface-adsorbate bonds, active surface centers and the structure of adsorption complexes. Infrared absorption spectroscopy is by far the most frequently used, and usually the most efficient spectroscopic method for the analysis of surface chemistry of heterogeneous catalysts [6].

A.2.1 Characterizing catalyst surfaces using probing molecules

IR absorption spectroscopy enables *in situ* monitoring of adsorbed species or intermediates under reaction conditions as well as the analysis and classification of surface adsorption centers (Brønsted and Lewis sites) using different probing molecules.

The latter use of IR-spectroscopy (analysis of adsorption centers) based on the utilization of selected probe molecules, whose IR-spectral features are a function of the specific surface centers, gives indirect information about the properties, and concentration of the surface sites.

According to Morrison's description of 'surface center' [7], the following types of surface center can be distinguished on metal oxides: 1) electron-donating oxygen ions, 2) electron-acceptor metal cations, and 3) surface functionalities. These centers bring out acid-base properties of oxide surfaces. There are two kinds of surface acidic sites, namely, Lewis and Brønsted. The Brønsted acid sites are hydroxyl groups able to provide H^+ upon interaction with bases. Lewis sites are coordinative unsaturated metal cations (cus) possessing electron affinity because of unsaturation. Strong or weak basic molecules are used for probing acid centers. Ammonia and pyridine are among the most frequently used strong bases. Although these two molecules differ in their molecular cross-sections and relative basicity, nevertheless, they both possess a pair of electrons at the nitrogen site available for donation to other species. These molecules are able to interact with both the acidic hydroxyl groups (Brønsted acids) and cus cations (Lewis acids). The spectral characteristics of the ammonia or pyridine molecules adsorbed on Lewis sites are practically different from those of ammonium or pyridinium ions resulting from the interaction with Brønsted acid sites [8]. Weak bases are also used for the determination of surface acidity. The most frequently used molecule is carbon monoxide. The heats of adsorption of CO on metal oxides is usually low. Therefore CO adsorption IR experiments must be conducted at low temperatures (77K). However, the weak interaction

energies make CO more selective than pyridine and NH_3 . CO molecules interact with both Lewis and Brønsted acid sites. Upon adsorption, downward or upward shift of the carbonyl stretching frequency relative to that of the free CO molecule (2143 cm^{-1}) gives rise information about the nature of adsorbing site (Lewis or Brønsted) as well as the oxidation state of the metal site. The $\sigma - \pi$ bonding system in CO molecule is responsible for these shifts, so that electron withdrawal forces induce the C-O bond order to increase and hence a shift in the CO vibrational frequency towards higher wavenumbers (blue-shift). In contrast, down-shift of CO signal to lower wavenumbers is caused by electron back donation from the cation site to CO. This electron goes to the anti-bonding orbital ($2\pi^*$) of CO causing the C-O bond order to decrease and hence a red-shift. The possibility of π back donation increases with increasing the electronic occupation of d orbitals and with decreasing the ionization potential of the cations [9]. The interaction between CO and hydroxyl groups (Brønsted sites) on the surface of metal oxides leads to broadening of O-H signals with a concomitant shift to lower frequencies. The magnitude of this shift is very often used to assign relative acidity strength of different hydroxyl groups available on the surface [9].

Basic sites on metal oxide surface are probed using acidic molecules. Practically, the most frequently used one is carbon dioxide, which is able to interact with both Brønsted- (OH-groups) and Lewis- (O^{2-}) basic sites. The interaction of CO_2 with OH groups leads to the formation of hydrogen carbonate species HO-CO_2 , whereas the interaction with basic oxygen ions results in the formation of different kinds of carbonate species (unidentate, bidentate and bridged species) [10]. The asymmetric $\nu_3(\text{CO})$ vibration at 1415 cm^{-1} splits into two signals upon formation of carbonate species (adsorption lowers the symmetry of CO_2). It is believed that $\Delta\nu_3$ splitting characterizes the structure of the species formed: it is about 100, 300 and 400 cm^{-1} for unidentate, bidentate and bridged species, respectively.

It is worth to emphasize that in some cases CO_2 interaction is not confined to the surface of the oxide but rather to the bulk, which results in the formation of bulk-polydentate species [10]. Thus, the use of complimentary analysis techniques is recommended (like TPD or micro-calorimetry) to support assessment of basic sites using CO_2 as probing molecule.

A.2.2 *In situ* IR spectroscopy

While using probing molecules to characterize adsorption sites on the surface of catalysts may sometimes results in surface structure-reactivity correlations, care must be taken by the interpretation of these observations, since more than one adsorption structure of the reactant may occur even on a particular kind of surface site. Therefore, monitoring of adsorbed species under reaction conditions, identifying their adsorptive structure and following their transient response to reaction condition changes give rise to more reliable surface structure-correlations and distinctive mechanistic conclusions.

In situ IR spectroscopy is best suited for this task due to its ability in giving qualitative and quantitative information about the species adsorbed on the working catalyst and by distinguishing between intermediates and spectators by following the concentration of specific adsorbed species after a controlled change of the reaction temperature or reactant pressure [11,12].

In principle, all forms of IR spectroscopy (i.e. transmission absorption, specular reflection, diffuse reflection, attenuated total reflection, emission, acoustic methods, etc.) give similar information and can be applied for *in situ* investigations. However, for practical experimental reasons the transmission-absorption technique is preferred.

A.2.2.1 Design of the *in situ* cell

Two essential requirements must be taken into consideration while constructing an efficient infrared transmission cell. First, the windows must be chosen to be IR transparent within the region of interest, able to endure relative high temperature without losing their optical properties and be chemically inert to the gas mixture applied (e.g., hygroscopic windows cannot be used if

the reaction produces water). Second, the void volume of the cell must be as small as possible to ensure best mixing of gases inside the cell, in other words the construction must approximate a micro reactor, whereby a homogeneous exposure of the catalyst to the reactants and products is assured. Several cell designs and their application on different heterogeneous catalytic systems can be found in the literature [6,13–16].

A.2.2.2 Sample preparation

In the transmission mode the catalyst powder is pressed into a self-supporting thin disk (10 to 100 mg) and placed inside a cell, where it can be securely held at a controlled temperature and exposed to reactant gases. It is necessary to assure that this mechanical treatment of the sample does not influence catalyst properties (e.g. structural changes). The catalyst particles diameter must be smaller than the wavelength of incident IR radiation, otherwise light-scattering becomes an issue. *In situ* transmission-absorption technique can be applied only if the bulk of the catalyst absorbs IR radiation weakly. In practice, not all catalysts let themselves easily be pressed into wafers. On the other hand, infrared opaque samples (e.g. carbons or metal supported oxides) cannot be investigated in the transmission mode. In such a case *in situ* DRIFT (Diffuse Reflectance Infrared Fourier Transform Spectroscopy) can be a good option.

A.2.2.3 Quantitative analysis and measurement conditions

The concentration of a particular adsorbed species (in the transmission-absorption mode) can be determined using the Beer-Lambert equation (A 3). This requires a prior knowledge of two parameters, namely, the molar extinction coefficient (ϵ) of the particular species and the density of the catalyst wafer in the beam. The former parameter can be determined by comparing the amount of the species adsorbed per surface area and the intensity of the corresponding IR-bands.

As mentioned before, transient response experiments are very informative. For instance, surface coverage changes induced by the relaxation of the system into a new steady state after perturbation (change of reaction temperature or reactant pressure) can be correlated to the reaction rate, and hence giving a reasonable proof that the species observed is the intermediate of interest. In order to correlate changes of adsorbed species with the catalyst reactivity changes, the concentration of reactants and products in the effluent gas mixture must be determined during the acquisition of spectroscopic data. Usually this is done with gas chromatography (GC) or mass spectroscopy (MS).

A.2.3 Designing and construction of *in situ* IR transmission cell for Deacon reaction

We have constructed an *in situ* transmission IR cell to investigate the transient response and evolution of OH groups on ceria catalysts at different feed compositions and temperatures. The windows and construction materials constituting the cell are chosen to endure highly corrosive conditions associated with the Deacon reaction. The cell consists of two main parts, namely the lid and the cell body. The latter is provided with two IR transparent Si windows and two 1/8 in. tubing for the inlet and outlet of the reactant gases and products. The windows are optical grade mono-crystalline Si wafers from the company UQG Optics®. The transmission spectrum of Si in the mid and far infrared regions is shown in Figure A 1. It is worth to mention that silicon and diamond windows are the only materials which offer both good IR transmission properties in the mid-IR region and high chemical resistivity towards gas feed mixtures used in the Deacon reaction. Si windows (20 mm id, 1 mm thickness) were positioned between two PTFE gaskets and sealed with chemically inert Karlez o-rings. A cross section view of the cell is depicted in Figure A 2. The inner walls of the cell body were coated with silver, which is expected to form a compact film of silver chloride upon exposure to the molecular chlorine. This chloride layer acts as protecting shell and hence passivates the silver coating. The cell body itself is made of stainless steel.

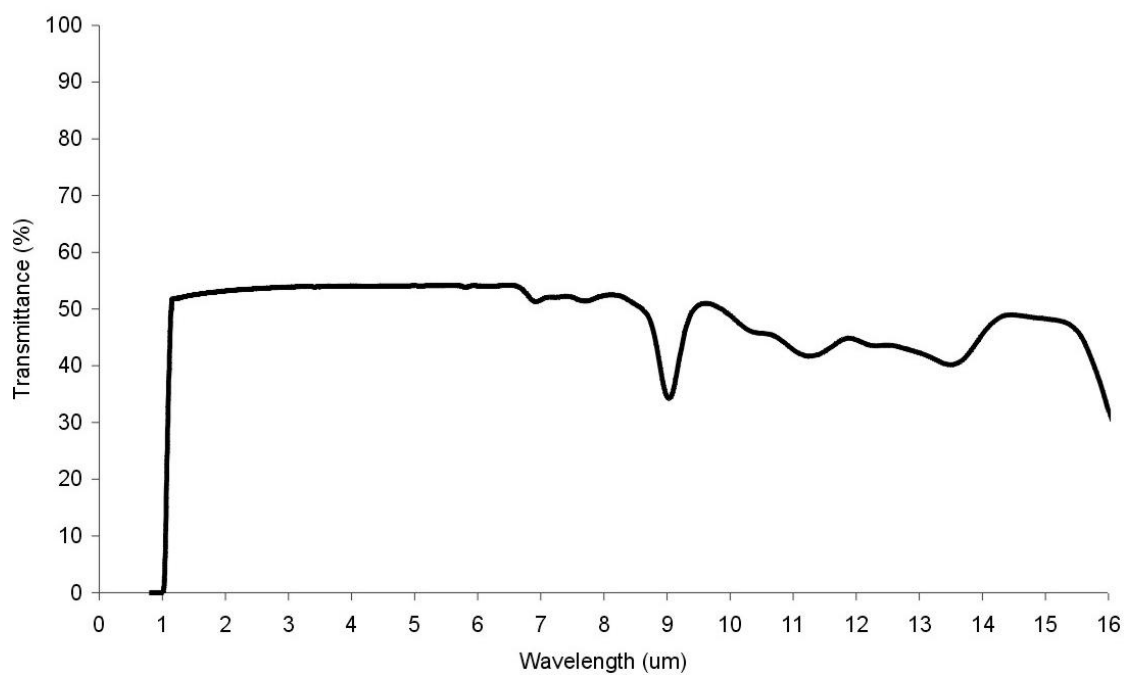


Figure A 1 The transmission spectrum of Si window in the mid and far infrared regions.

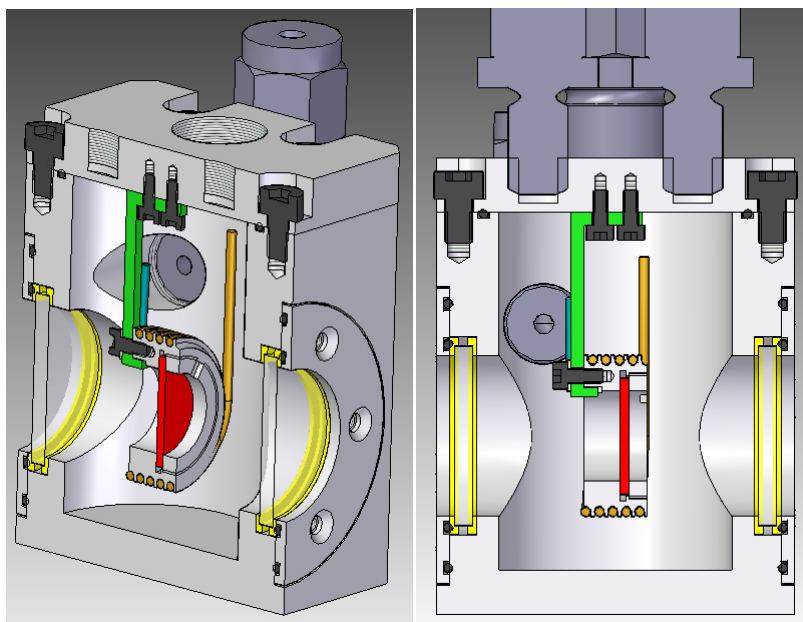


Figure A 2 Cross section views of the *in situ* transmission FTIR cell.

The second part of the cell is the lid, which is provided with a cylindrical oven operating in the temperature range from 300 to 823 K. The oven is designed to serve as a sample holder as well. The reaction temperature is monitored with a thermocouple which is placed inside a hole made in the oven and terminates at the sample pellet. The lid is made of Hastelloy C-22, which is coated afterwards with a special inert Si-based coating (Silcoalloy™ 1000). The void volume of the cell is *ca.* 20 cm³. Figure A 3 shows the lid and the heatable stage.

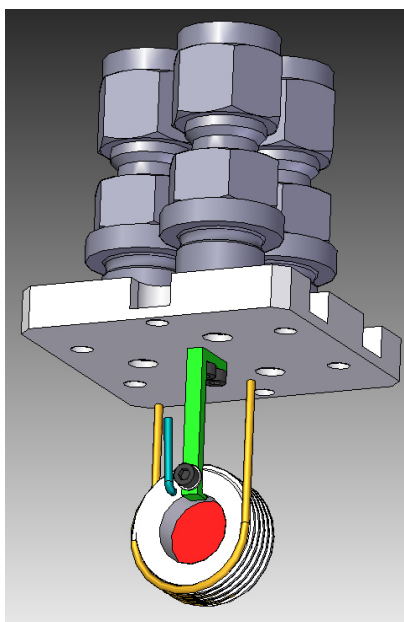


Figure A 3 The lid and the heatable stage (sample holder) of the in situ FTIR cell.

References

- [1] L. Can, K. Domen, K. Maruya, T. Onishi, *J. Am. Chem. Soc.* **1989**, *111*, 7683–7687.
- [2] C. Lamberti, A. Zecchina, E. Groppo, S. Bordiga, *Chem. Soc. Rev.* **2010**, *39*, 4951.
- [3] R. Si, M. Flytzani-Stephanopoulos, *Angewandte Chemie International Edition* **2008**, *47*, 2884–2887.
- [4] T. Sayle, S. Parker, C. Catlow, *Surf. Sci.* **1994**, *316*, 329–336.
- [5] M. Nolan, G. W. Watson, *J. Phys. Chem. B* **2006**, *110*, 16600–16606.
- [6] J. Ryczkowski, *Catalysis Today* **2001**, *68*, 263–381.
- [7] S. Morrison, *Chemical Physics of Solid Surfaces*. Plenum Press, **1977**, New York.
- [8] M. C. Kung, H. H. Kung, *Catalysis Reviews* **1985**, *27*, 425–460.
- [9] K. I. Hadjiivanov, G. N. Vayssilov, in *Advances in Catalysis*, Academic Press, **2002**, pp. 307–511.
- [10] A. M. Greenaway, T. P. Dasgupta, K. C. Koshy, G. G. Sadler, *Spectrochimica Acta Part A: Molecular Spectroscopy* **1986**, *42*, 949–954.
- [11] G. Haller, *Catal. Rev.-Sci. Eng.* **1981**, *23*, 477–504.
- [12] F. C. Meunier, *Catalysis Today* **2010**, *155*, 164–171.
- [13] G. Mirth, J. Cejka, J. Lercher, *J. Catal.* **1993**, *139*, 24–33.
- [14] G. Mirth, F. Eder, J. A. Lercher, *Appl. Spectrosc.* **1994**, *48*, 194–197.
- [15] R. F. Hicks, C. S. Kellner, B. J. Savatsky, W. C. Hecker, A. T. Bell, *Journal of Catalysis* **1981**, *71*, 216–218.
- [16] P. Basu, T. H. Ballinger, J. T. Yates, *Rev. Sci. Instrum.* **1988**, *59*, 1321.
- [17] M. Mitchell, *Adv. Chem. Ser.* **1993**, 351–375

Appendix B

Prompt Gamma Activation Analysis (PGAA)

B.1 Introduction

Prompt Gamma Activation Analysis (PGAA) is a rapidly developing chemical analytical method utilizing nuclear techniques. It is based on the radiative neutron capture of nuclei or the so-called (n,γ) reaction, in which a nucleus absorbs a low-energy neutron followed by immediate release of γ radiation. The energies of γ -rays are characteristic of the elements they have been emitted from, and the radiation intensities are proportional to the amount of elements in the sample. Therefore, qualitative and quantitative information about the sample composition can be obtained using PGAA spectroscopy. The use of neutron-capture gamma rays as a method of elemental analysis was introduced many years ago [1,2]. In fact, the PGAA spectroscopy has many unique properties which make it a powerful technique for analytical purposes. An important characteristic is that both the captured and the emitted particles (n and γ respectively) are highly penetrating, which means that even sealed samples can be investigated. In practice the entire sample or part of it (depending on the size of the sample) is illuminated by the neutron beam, and the detected gamma-radiation gives an average composition of the sample. However, neutron self-shielding within the sample may be an issue if the sample contains a nuclide with a high neutron capture cross section as a major component. This effect will reduce uniformly γ -ray intensities of all components, and thus neutron-self shielding effect may not be a problem when peak ratios are used for the determination of components' relative concentrations. Samples in any physical state and up to few grams can be analyzed. No sample preparations are required and the analytical results are independent of the chemical state of the sample, because gamma-rays originate from the excitation of the nuclei, and not from the electron shells. The PGAA technique is best suited for measuring light elements [3] (H, B, P, S, Cl, etc.), which cannot be easily measured by other conventional methods. PGAA is a non-destructive analytical tool, since the number of atoms undergoing nuclear reaction after a fairly long irradiation time (as long as one day assuming that all neutrons had been absorbed by the sample) is negligible in comparison to the number of atoms in the sample [4]. Sample irradiation and gamma-ray detection are taking place at the same time. Thus, all elements in the sample can be analyzed simultaneously, i.e. PGAA gives a multi-elemental panorama analysis. Because of all aforementioned properties, PGAA spectroscopy has been applied for the analysis of a wide variety of materials in many scientific fields, from archeology through geology to material science [4]. Recently, it has been adopted to investigate heterogeneous catalytic systems under reaction conditions [5–7]. As any analytical tool, PGAA has some weaknesses as well. The most problematic one is that some combination of elements are difficult to analyze, this is because they differ in the neutron capture cross section by several orders of magnitude (e.g. O: 0.00019 barn and Gd: 48,800 barn) [4]. Furthermore, PGAA spectra contain several hundred peaks depending on the nuclear level structure of the emitting nuclide and the number of levels between the capture state and the ground state. This large number of prompt gamma-ray lines lead to very complex gamma-ray spectra. However, peak assignment is carried out by comparing the results with known prompt gamma-ray data. Data libraries, as e.g. of the cold neutron PGAA facility in Budapest, have been established for straightforward evaluation purposes [8,9]. Neutron capture by the detector-, shielding- and constructing materials in vicinity to the sample is also a significant source of error and causes an increase of the spectrum base-line. Actually, the spectrum background has an important impact on the elements' detection limit, and therefore the lower the background the lower are the detection limits.

B.2 Neutron capture and reaction rate

It is worth noting that prompt-gamma activation analysis and the conventional Neutron Activation Analysis (NAA) are similar from the point of view of setup requirements and independency of matrix and chemical state of the sample. However, they differ in the energy range accessible. In NAA some elements produce radioactive capture products (isotope of higher mass number with a certain half-life) which decay by emitting gamma radiations. The highest energy decay line in NAA is close to 3 MeV. Some elements do not produce radioactive capture products, but all elements (except of ^4He) do emit prompt gamma radiation immediately upon neutron capture. The highest energy prompt gamma line is close to 12 MeV. Thus, the energy range of prompt gamma spectra is much wider than that of NAA. Another discrepancy is that in PGAA gamma rays are detected during sample irradiation, whereas in NAA detection of gamma-rays takes place only when the sample exposure to the neutron beam has been stopped. As mentioned before, each element (except ^4He) is capable of undergoing a nuclear reaction (n, γ) and the reaction rate is given by the equation:

$$R = n \sigma \Phi \quad (\text{B } 1)$$

where R is the reaction rate (s^{-1}), n is the number of atoms of the examined nuclide in the neutron beam, σ is the cross section for neutron capture (cm^2) and Φ is the neutron flux ($\text{cm}^{-2} \text{s}^{-1}$). The cross section unit is usually expressed in barn, where $1 \text{ barn} = 10^{-28} \text{ m}^2$. Thus, the probability of the reaction is characterized by the neutron capture cross section. This parameter is highly dependent on the neutron energy, so that for slow neutrons the energy dependence follows the $1/v$ law, that is the cross section is inversely proportional to the velocity of the neutrons. The capture cross sections of the nuclides are tabulated for neutrons having a velocity of 2200 m s^{-1} [10]. These values are considered as standards and called "thermal cross sections". The neutron capture cross section of nuclides at any other neutron velocity can be calculated as

$$\sigma(v) = \sigma_0 \frac{\sigma_0}{v} \quad (\text{B } 2)$$

Alternatively, in PGAA spectroscopy the partial gamma ray production cross section (σ_γ) is used, which is the product of the isotope's natural abundance (θ), the neutron capture cross section (σ) and the emission probability of the gamma-ray at the given energy (P_γ). The latter parameter defines the fraction of the emitted gamma photons per one neutron capture.

$$\sigma_\gamma = \theta \sigma P_\gamma \quad (\text{B } 3)$$

Consequently, the most easily determined elements are those with the highest natural abundance, cross section and gamma ray yield.

The count rate of a gamma peak at certain energy can be written using the partial gamma ray production cross section (σ_γ).

$$\rho_\gamma = \varepsilon(E_\gamma) n \sigma_\gamma \Phi \quad (\text{B } 4)$$

where ρ_γ is the count rate which can be obtained from the ratio of the net peak area to the acquisition time. $\varepsilon(E_\gamma)$ is the counting efficiency of the detector, i.e. the ratio of the number of recorded pulses to the number of gamma rays emitted by the source at a certain energy. The detector efficiency can be assessed using gamma ray sources with known activity or reaction rates.

Equation B 4 represents a simplified situation in a sense that neutrons energy distribution and γ -ray attenuation within the sample are not considered. These effects are included in the following complex equation:

$$\rho_\gamma = \int_V \int_0^\infty \frac{\mu(r)}{M} N_A \sigma_\gamma(E_n) \Phi'(E_n, r) \varepsilon'(E_\gamma, r) dE_n dr \quad (\text{B } 5)$$

where $\mu(r)$ is the mass density of the examined element as a function of position r in the sample, M is the relative atomic mass of the element, N_A is the Avogadro number: $6.022 \times 10^{23} / \text{mol}$, $\sigma_\gamma(E_n)$ is the partial gamma ray production cross section for the given gamma as a function of neutron energy, $\Phi'(E_n, r)$ is the neutron flux as a function of the energy and the position within the sample, $\varepsilon'(E_\gamma, r)$ is the counting efficiency of the detector at the given gamma energy as a function of the position within the sample.

From the point of view of energy, prompt gamma rays are produced during the capture state de-excitation process. The energy of the transitional state (or capture state) determines the energy of gamma rays emitted during de-excitation process. The transitional state energy equals the binding energy plus the kinetic energy of the neutron. The utilization of cold neutrons (i.e. kinetic energy is very small; in the meV range) gives rise to a well-defined energy of the capture state, which nearly equals the neutron binding energy. The binding energy could be as high as 11 MeV. Hence, the energy of prompt gamma rays equals that of the transition state minus the recoil-energy of the nucleus:

$$E_{\gamma} = E_T - E_R \quad (\text{B } 6)$$

where E_{γ} , E_T and E_R are the energies of the gamma ray, of the transition and of the recoil, respectively. Since the momentum is conserved, the nucleus which captures a cold neutron must receive recoil energy. The latter is inversely proportional to the mass of the irradiating atom; therefore light elements have relatively higher recoil-energies. However, it is much lower than the transition energy (< 0.1%). The smallest binding energy value is for ${}^7\text{Li}$, being 2032.8 keV and the highest one is for ${}^{47}\text{Ti}$, and being 11,626.59 keV. The excited nucleus reaches its ground stand by emitting 2-4 gamma rays in a cascade. The simplest case is the ${}^1\text{H}(n, \gamma){}^2\text{H}$ reaction; i.e. the capture of a neutron by a proton. In this case the transition state (or capture state) at 2.2 MeV can decay in only one way, by emitting a characteristic 2223.23 keV gamma-ray. More complex nuclei produce high energy capture states, which usually decay through a cascade of gamma-rays. Thus, the neutron binding energy can be calculated from the sum of all gamma rays' energies weighted by their emission probabilities,

$$S_n = \sum_i E_{\gamma,i} P_{\gamma,i} \quad (\text{B } 7)$$

where S_n is the binding energy of the neutron, $E_{\gamma,i}$ is the energy of the i^{th} gamma ray, $P_{\gamma,i}$ is its emission probability.

The determination of the absolute concentration of elements within the sample is possible using Equation B 5. However, as discussed before, this is tedious because several factors, such as the neutron beam inhomogeneity, neutron self-shielding within the sample, gamma ray attenuation and geometric effects must be taken into consideration. In practice, the amount of a specific element within the sample is determined by comparing the gamma-ray count rate of a characteristic peak of the element with the count rate of standard sample of a known mass. Both, the sample and the standard must be irradiated under the same conditions. This is called the relative approach. Alternatively, if absolute concentrations are not required, the molar ratio of two elements within the same sample can be used instead. This approach overcomes most errors caused by neutron flux fluctuations and neutron- or gamma-self shielding problems, but at the same time it requires a homogenous elemental distribution of the sample components.

The molar ratio of two elements within sample is calculated from the ratio of the corresponding peak areas as follows,

$$\frac{n_1}{n_2} = \frac{A_1/\varepsilon_1\sigma_{\gamma,2}}{A_2/\varepsilon_2\sigma_{\gamma,1}} \quad (\text{B } 8)$$

where $A(E)$ is the net peak area at the γ -ray energy E , $\varepsilon(E)$ is the counting efficiency at this energy, n is the number of atoms ($n = N_A m/M$, i.e., mass over the atomic weight, times the Avogadro number), and $\sigma_{\gamma}(E)$ is the partial γ -ray production cross section in cm^2 , i.e. the number of emitted photons with energy E for unit neutron flux.

A.3 Facilities and instrumentation

The main components of a PGAA setup are: neutron source, beam guides, detector, shielding materials and beam chopper. Each of these components will be described concisely below.

A.3.1 Neutron sources

There are several kinds of neutron sources available for PGAA spectroscopy. From the energy point of view the highest neutron energy is produced by spallation (accelerated particles beat a target, which is usually a heavy metal like mercury or lead). Fusion reactions of accelerated

deuterium with deuterium or tritium produce neutrons having a kinetic energy of about 2.5 and 14 MeV, respectively. Radioactive isotopes can be used as neutrons sources or generators for transportable applications. Research reactors are the most commonly used neutron source for PGAA, in which neutrons are produced from the fission of ^{235}U . The average energy of neutrons produced in this way is about 2 MeV. This value is still high, since the neutron capture cross section of elements in the energy range of interest is inversely proportional to the energy of neutrons. Therefore, the neutrons produced must be slowed down to reach kinetic energy values less than 0.025 eV. For this purpose neutrons pass through a moderating material, which acts as energy absorber. Neutrons lose most of their energy by repeated elastic scatterings with the moderator atoms until they get thermally equilibrated with the moderator. Liquid hydrogen (21 K at atmospheric pressure) is usually used as a moderator. The PGAA setup at Budapest Neutron Centre (BNC) is equipped with liquid hydrogen moderator, and the average energy of the particles is ~ 0.003 eV [7].

A.3.2 Neutron guides

In practice the PGAA setup is placed well away from the neutron source in order to ensure a low radiation environment and hence lowering the background of the spectra caused by stray neutrons. Therefore long-wavelength neutrons (cold neutrons) must be transported to the sample location by neutron beam guides without substantial losses. The most efficient (reflecting) neutron guides are made of nickel/titanium composites and are called “supermirrors”.

A.3.3 Detectors

The main component of the PGAA spectrometer is the detector. Its role is to convert the energy of the gamma ray to an electrical signal. There are two types of detectors which are in common use for the PGAA spectroscopy: scintillation-counters [NaI(Tl) or bismuth germinated; BGO] and semiconductor based detectors (the High Purity Germanium crystal; HPGe). The semiconductor (HPGe) detector is preferred for research purposes because of its superior energy resolution, since the energy required to create one electron-hole pair in the germanium crystal is as low as 3 eV. Cryogenic temperatures are vital for the operation of germanium detectors. There are different interaction mechanisms of gamma-rays within the detector. The most important ones are: photoelectric interaction, Compton scattering and pair production. The energy of the photon is completely absorbed during the photoelectric effect, whereas only partial energy is transferred to the electrons of the Ge crystal upon Compton scattering. In the photoelectric interaction the photons give their energy to electrons in the valance band providing these electrons with enough energy to move to the conduction band of the crystal. Consequently, electron-hole pairs are produced. The electrical field applied to the detector forces the electrons to move to the positive contact-end and the holes to the negative, creating an electrical signal. This signal is proportional to the photon energy of incoming radiation and called the Full-Energy Peak (FEP). The photons which are scattered and escaped from the detector have deposited only a part of their energy to the electrons, this energy is a continuous function of the scattering angle and causes the so called Compton continuum region below every FEP peak. In other words, the detector records an energy which is only a fraction of the energy of the incident gamma ray. Usually a sophisticated detector assembly (Compton-suppressed HPGe detector) is used to decrease the Compton continua and hence improving the FEP signals in the spectrum. The Compton-suppressed HPGe detector consists of a high resolution germanium detector surrounded by several scintillations detectors. The main detector (HPGe) and the scintillators are running in anti-coincidence mode, that is, if the photon is caught by a scintillator after being escaped from the main detector (HPGe) without depositing all of its energy, the registration of the detector signal will be ignored. The normal and Compton-suppressed spectra of ^{17}Cl with the main spectral features are illustrated in Figure B 1

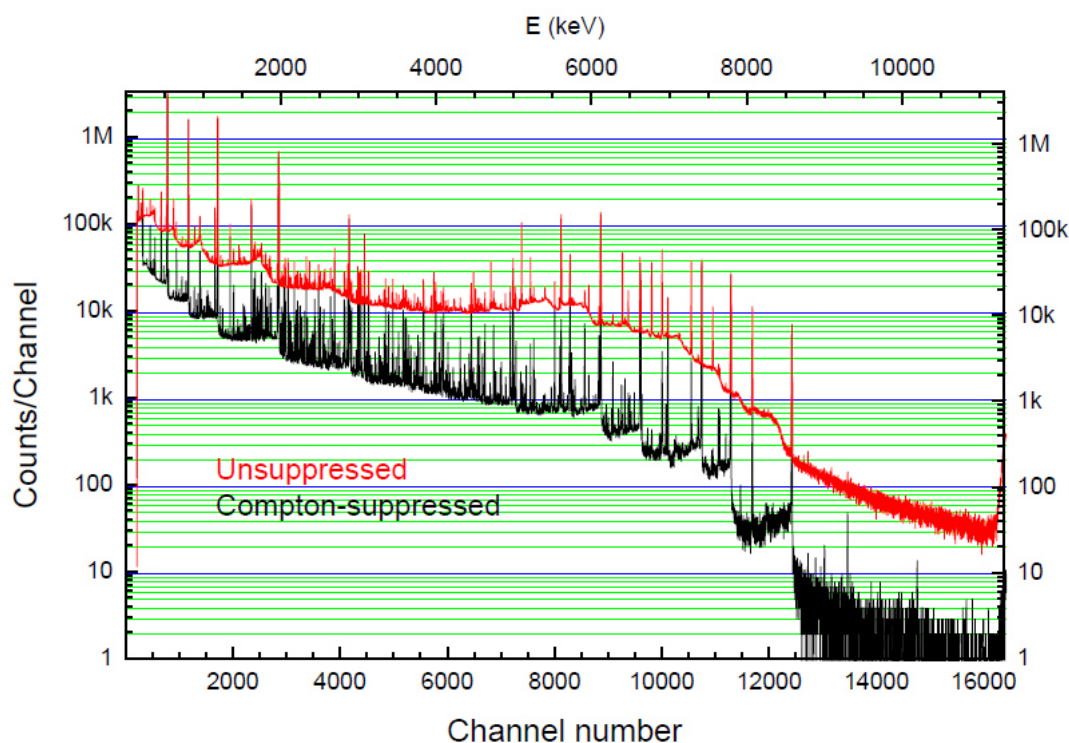


Figure B 1 Unsuppressed (red) and Compton suppressed (black) PGAA spectra of ^{17}Cl .

A.3.4 Shielding materials.

In order to protect the detector from damages by neutrons and to minimize the spectral background contribution of the peaks originated from the continuous excitation of surrounding materials by cosmic rays, a good shielding of the detector must be ensured. The perfect shielding material should absorb neutrons of all energies in a short distance, without generating gamma radiation or residual radioactive products. Only ^3He and ^6Li absorb neutrons efficiently without producing gamma rays. The Compton-suppressed HPGe detector of the PGAA facility at BNC is shielded by lead and covered by a ^6Li -containing polymer to avoid the activation of shielding materials and detectors as well.

A.3.5 Beam Chopper

Spectra obtained from un-chopped neutron beams contain signals originating from prompt and decay transitions. In order to subtract the decay contribution from the spectra (i.e. in order to get pure PGAA spectra) a beam chopper can be installed. Its function is to turn the beam on and off periodically with a frequency enabling the detector to distinguish between prompt and decay gamma rays. A rotating plastic disk partially covered with neutron absorbing material (e.g. ^6Li) can serve as a beam chopper.

A.3.6 *In situ* PGAA setup

In situ PGAA was utilized to measure the Cl uptake of ceria catalysts during HCl oxidation. PGAA experiments at atmospheric pressure conditions were carried out at the cold neutron beam of the Budapest Neutron Center. The neutrons are guided to the experimental positions by curved supermirror neutron guides. The thermal-equivalent neutron flux at the PGAA sample position is $7.7 \times 10^7 \text{ cm}^{-2} \text{ s}^{-1}$. For the experiments, a quartz reactor (8 mm i.d.) was placed into the neutron beam surrounded by a specially designed oven having opening for the incoming and outgoing neutrons and for the emitted gamma rays toward the detector. These openings were covered by thin aluminium foils to minimize heat losses. Figure B 2 shows the *in situ* PGAA setup.

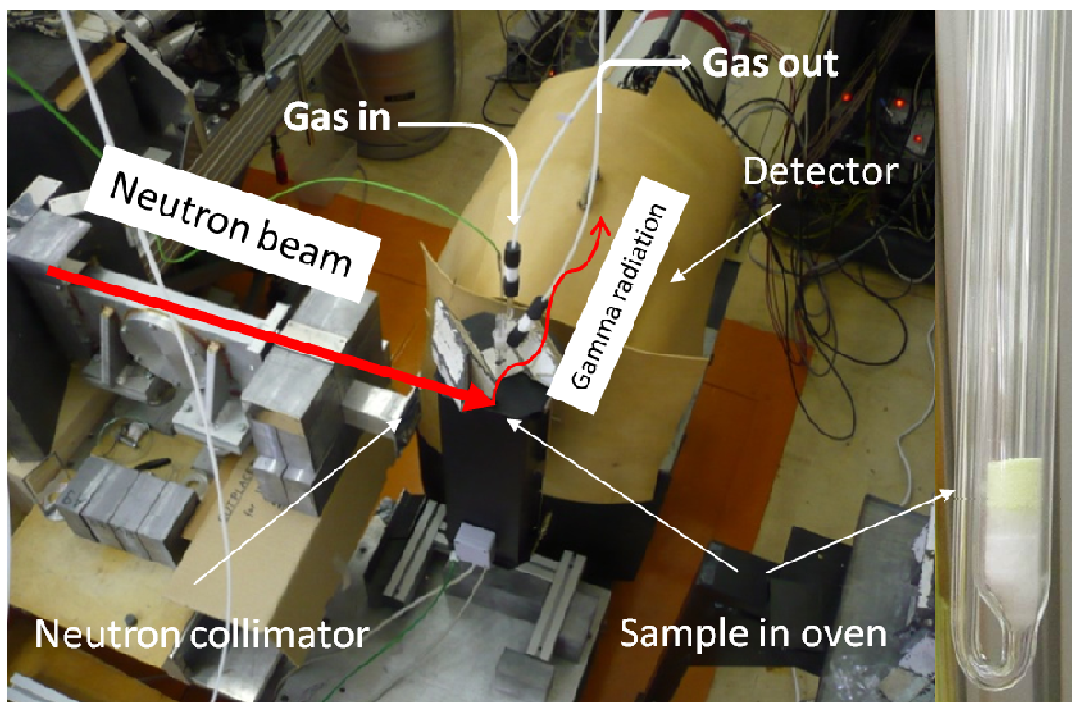
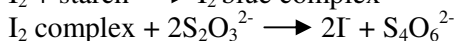
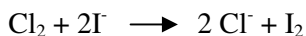


Figure B 2 A photo of the *in situ* PGAA setup.

The reaction feed, at constant total flow, was supplied by mass flow controllers. The Cl_2 production was monitored by iodometric titration. The reaction equations of the iodometric titration are as follows:



The titration was carried out at room temperature. Figure B 3 displays the titration tools.



Figure B 3 The iodometric titration tools.

The detector system of the PGAA facility consists of an n-type high-purity germanium (Canberra HPGe 2720/s) main detector and a BGO Compton-suppressor, surrounded by a 10 cm thick lead shielding. The sample-to-detector distance was 275 mm. The detector is covered by ^6Li -containing

polymer sheets to protect it from escaped or reflected neutrons. The oven is shielded by blocks of lead to ensure personal protection from emitted radiations. Shielding materials are depicted in Figure B 4.

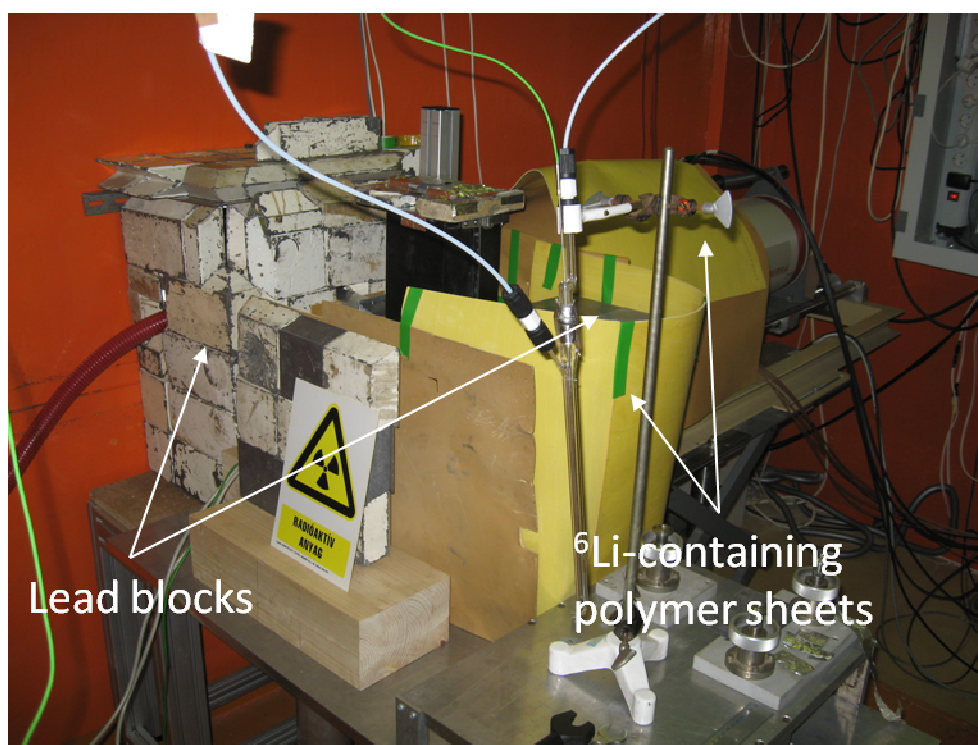


Figure B 4 Shielding materials used for the *in situ* PGAA setup.

References

- [1] T. L. Isenhour, G. H. Morrison, *Anal. Chem.* **1966**, *38*, 162–167.
- [2] T. L. Isenhour, G. H. Morrison, *Anal. Chem.* **1966**, *38*, 167–169.
- [3] R. L. Paul, R. M. Lindstrom, *J. Radioanal. Nucl. Chem.* **2000**, *243*, 181–189.
- [4] G. L. Molnár, *Handbook of Prompt Gamma Activation Analysis with Neutron Beams*, Springer, **2004**.
- [5] D. Teĉher, J. Borĉodi, Z. Kiĉ L. Szeĉtmiklĉi, Z. Rĉvay, A. Knop-Gericke, R. Schlĉgl, D. Torres, P. Sautet, *J. Phys. Chem. C* **2010**, *114*, 2293–2299.
- [6] K. Kovnir, M. Armbrüster, D. Teschner, T. V. Venkov, L. Szentmiklĉsi, F. C. Jentoft, A. Knop-Gericke, Y. Grin, R. Schlĉgl, *Surface Science* **2009**, *603*, 1784–1792.
- [7] Z. Revay, T. Belgya, L. Szentmiklĉsi, Z. Kis, A. Wootsch, D. Teschner, M. Swoboda, R. Schloegl, J. Borsodi, R. Zepernick, *Anal. Chem.* **2008**, *80*, 6066–6071.
- [8] Z. Revay, G. L. Molnar, T. Belgya, Z. Kasztovszky, R. B. Firestone, *J. Radioanal. Nucl. Chem.* **2000**, *244*, 383–389.
- [9] Z. Revay, G. L. Molnar, T. Belgya, Z. Kasztovszky, R. B. Firestone, *J. Radioanal. Nucl. Chem.* **2001**, *248*, 395–399.
- [10] S. Mughabghab, *Neutron Cross Sections: Neutron Resonance Parameters and Thermal Cross Sections, Part A: Z=1-60*, Elsevier Science, New York, **1981**.

Curriculum Vitae

Personal Data

Name	Ramzi Farra
Date of Birth:	October 11 th , 1982
Place of Birth:	Aleppo, Syria
Nationality:	Syrian

Education

since Mai 2010	PhD student at the Fritz Haber Insititute of the Max Planck Society, Department of Inorganic Chemistry (director/supervisor: Prof. Dr. Robert Schlögl), Berlin, Germany. Member of the Electronic structure group (group leader: Dr. Axel Knop-Gericke) Thesis title: "Spectroscopic studies towards the understanding of CeO ₂ -based catalysts for chlorine production"
Sept. 2009 – Mar. 2010	Diploma thesis in inorganic chemistry at Potsdam University, Potsdam, Germany (supervisor: Prof. Dr. Peter Strauch) Thesis title: "Structural interrelations of tetrabromocuprat- <i>es</i> complexes"
Aug. 2009	Final examination (Diplomahauptprüfung) in inorganic chemistry, organic chemistry, physical chemistry and environmental chemistry.
Oct. 2000	Matriculation at the University of Aleppo, Aleppo, Syria in the field of Chemistry

List of Publications

- [1] Farra, R., Girgsdies, F., Frandsen, W., Hashagen, M., Schlögl, R., and Teschner, D. Synthesis and Catalytic Performance of CeOCl in Deacon Reaction. *Catal Lett*, in press. DOI 10.1007/s10562-013-1085-4
- [2] Farra, R., García-Melchor, M., Eichelbaum, M., Hashagen, M., Frandsen, W., Allan, J., Girgsdies, F., Szentmiklósi, L., López, N., and Teschner, D. (2013). Promoted Ceria: A Structural, Catalytic, and Computational Study. *ACS Catal.* **3**, 2256–2268.
- [3] Moser, M., Mondelli, C., Schmidt, T., Girgsdies, F., Schuster, M.E., Farra, R., Szentmiklosi, L., Teschner, D., and Pérez-Ramírez, J. (2013). Supported CeO₂ catalysts in technical form for sustainable chlorine production. *Appl. Catal. B-Environ.* **132**, 123–131.
- [4] Farra, R., Wrabetz, S., Schuster, M.E., Stotz, E., Hamilton, N.G., Amrute, A.P., Pérez-Ramírez, J., López, N., and Teschner, D. (2013). Understanding CeO₂ as a Deacon catalyst by probe molecule adsorption and *in situ* infrared characterizations. *Phys. Chem. Chem. Phys.* **15**, 3454–3465.
- [5] Farra, R., Eichelbaum, M., Schloegl, R., Szentmiklosi, L., Schmidt, T., Amrute, A.P., Mondelli, C., Pérez-Ramírez, J., and Teschner, D. (2013). Do observations on surface coverage-reactivity correlations always describe the true catalytic process? A case study on ceria. *J. Catal.* **297**, 119–127.
- [6] Teschner, D., Novell-Leruth, G., Farra, R., Knop-Gericke, A., Schloegl, R., Szentmiklosi, L., Gonzalez Hevia, M., Soerijanto, H., Schomaecker, R., Pérez-Ramírez, J., and López, N. (2012). *In situ* surface coverage analysis of RuO₂-catalysed HCl oxidation reveals the entropic origin of compensation in heterogeneous catalysis. *Nat. Chem.* **4**, 739–745.
- [7] Amrute, A.P., Mondelli, C., Moser, M., Novell-Leruth, G., Lopez, N., Rosenthal, D., Farra, R., Schuster, M.E., Teschner, D., Schmidt, T., and Pérez-Ramírez, J. (2012). Performance, structure, and mechanism of CeO₂ in HCl oxidation to Cl₂. *J. Catal.* **286**, 287–297.
- [8] Teschner, D., Farra, R., Yao, L., Schlögl, R., Soerijanto, H., Schomäcker, R., Schmidt, T., Szentmiklósi, L., Amrute, A.P., Mondelli, C., Pérez-Ramírez, J., Novell-Leruth, G., and López, N. (2012). An integrated approach to Deacon chemistry on RuO₂-based catalysts. *Journal of Catalysis* **285**, 273–284.
- [9] Farra, R., Thiel, K., Winter, A., Klamroth, T., Poepl, A., Kelling, A., Schilde, U., Taubert, A., and Strauch, P. (2011). Tetrahalidocuprates(II)-structure and EPR spectroscopy. Part 1: Tetrabromidocuprates(II). *New J. Chem.* **35**, 2793–2803.

Poster Presentations and Scientific Participations

D. Teschner, R. Farra, M. Hashagen, M. Eichelbaum, W. Frandsen, J. Allan, F. Girgsdies, R. Schlögl, L. Szentmiklósi, M. García-Melchor, N. López
“The role of promoters in CeO₂ for HCl oxidation”
EuropaCat XI, Lyon, France, 2013

R. Farra, D. Teschner, R. Schlögl, L. Szentmiklósi, A. P. Amrut, J. Pérez-Ramírez
“Exploring “working catalyst” using complementary *in situ* & *ex situ* techniques; a case study of CeO₂ as HCl oxidation catalyst”
EuropaCat XI, Lyon, France, 2013

R. Farra, D. Teschner, M. Eichelbaum, M. Hashagen, S. Wrabetz, R. Schlögl, L. Szentmiklósi, A. P. Amrute, C. Mondelli, J. Pérez-Ramírez
“CeO₂ as catalyst for Deacon reaction”
46th Annual Meeting of the German Catalysis Society, Weimar, Germany, 2013

Scholar. Session: Catalysis and Materials for Hydrocarbon Conversions.
Global School for Advanced Science, Doha, Qatar, 2013

R. Farra, D. Teschner, R. Schlögl
“Deacon Reaction studied by Prompt Gamma Activation Analysis (PGAA)”
45th Annual Meeting of the German Catalysis Society, Weimar, Germany, 2012